

Report

R-23-08

November 2023



Benchmark of FLAC3D

Comparison with 3DEC and other
numerical simulation tools

Billy Fätth

SVENSK KÄRNBRÄNSLEHANTERING AB

SWEDISH NUCLEAR FUEL
AND WASTE MANAGEMENT CO

Box 3091, SE-169 03 Solna
Phone +46 8 459 84 00
skb.se

SVENSK KÄRNBRÄNSLEHANTERING

ISSN 1402-3091

SKB R-23-08

ID 2010493

November 2023

Benchmark of FLAC3D

Comparison with 3DEC and other numerical simulation tools

Billy Fälth, Clay Technology AB

This report concerns a study which was conducted for Svensk Kärnbränslehantering AB (SKB). The conclusions and viewpoints presented in the report are those of the author. SKB may draw modified conclusions, based on additional literature sources and/or expert opinions.

This report is published on www.skb.se

© 2023 Svensk Kärnbränslehantering AB

Abstract

The objective of the work that is presented in this report was to test the performance and reliability of FLAC3D. It was of particular interest to examine problems where discontinuities are included. Results from FLAC3D were compared with corresponding results generated with 3DEC and with other programs. Both version 7 and version 9 of FLAC3D were benchmarked. In version 7, the interface logic was used to model discontinuities while the zone-joint logic was used in version 9. Results from five different modelling cases were used in the comparison:

1. Single fracture model (quasi-static).
2. Multiple-fracture model (thermo-mechanical, quasi-static).
3. Thermo-mechanical model with openings and fractures (quasi-static) (FLAC3D version 7 was not included in the comparison).
4. Forsmark earthquake model (dynamic).
5. Large-scale earthquake benchmark case (dynamic) (FLAC3D version 9 was compared with programs other than 3DEC).

In all modelling cases, joint planes were included with different levels of complexity. In some cases, just one joint was included while several intersecting joints were included along with excavations in other cases.

For modelling cases with no or only a few joints, both versions of FLAC3D generate results that are practically identical to those delivered by 3DEC. In cases with several intersecting joint planes, displacement anomalies may arise locally around intersections in the FLAC3D solution when the interface logic is used. Using the zone-joint logic in FLAC3D version 9 gives more reliable and faster solutions than what is obtained in FLAC3D version 7. For the modelling cases considered here, FLAC3D version 9 generated results that differ a few percent from the corresponding results generated by 3DEC and other codes. Given the different numerical approaches in the codes, this can be regarded satisfactory. Considering this and the considerable speed increases that can be obtained when compared with 3DEC, it appears that FLAC3D version 9 with the zone-joint logic could be an attractive alternative to 3DEC for applications with a few intersecting joint planes. The results indicate that both versions of FLAC3D could be an alternative to 3DEC for problems with many joints, but without intersections.

Sammanfattning

Syftet med arbetet som presenteras i denna rapport var att testa prestandan och tillförlitligheten hos FLAC3D. Det var av särskilt intresse att undersöka fall som inkluderar diskontinuiteter. Resultat från FLAC3D jämfördes med motsvarande resultat genererade med 3DEC och med andra programvaror. Både version 7 och version 9 av FLAC3D testades. I version 7 användes interface-logiken för att modellera diskontinuiteter medan zone-joint-logiken användes i version 9. Resultat från fem olika modelleringsfall användes i jämförelsen:

1. Modell med enskild spricka (quasi-statisk).
2. Modell med multipla sprickor (termo-mekanisk, quasi-statisk).
3. Termo-mekanisk modell med öppningar och sprickor (quasi-statisk) (FLAC3D version 7 inte inkluderad i jämförelsen).
4. Forsmark jordskalvsmodell (dynamisk).
5. Storskaligt jordskalv (dynamisk) (FLAC3D version 9 jämfördes med andra program än 3DEC).

Sprickplan med olika grad av komplexitet inkluderades i alla modelleringsfall. I några fall inkluderades endast en spricka medan flera korsande sprickor inkluderades tillsammans med öppningar i andra fall.

I modelleringsfall med endast ett fåtal sprickor genererar båda versionerna av FLAC3D resultat som är praktiskt taget identiska med resultaten från 3DEC. I fall med flera korsande sprickplan kan rörelseanomalier uppstå lokalt kring sprickkorsningar då interface-logiken används i FLAC3D. Användandet av zone-joint-logiken i FLAC3D version 9 ger snabbare och mera tillförlitliga lösningar än vad som fås med FLAC3D version 7. I de modelleringsfall som undersöktes här genererade FLAC3D version 9 resultat som avviker med några få procent från motsvarande resultat genererade med 3DEC och andra program. Givet skillnaderna i de numeriska metoderna, kan detta anses tillfredsställande. När detta beaktas tillsammans med den avsevärt högre beräkningshastigheten i FLAC3D jämfört med 3DEC, framstår det som att FLAC3D version 9 med zone-joint-logiken kan vara ett attraktivt alternativ till 3DEC i applikationer som inkluderar ett fåtal korsande sprickplan. Resultaten indikerar att båda versionerna av FLAC3D kan utgöra alternativ till 3DEC för fall med många sprickplan, men utan sprickkorsningar.

Contents

| | | |
|-------------------|--|-----|
| 1 | Introduction | 7 |
| 1.1 | Background | 7 |
| 1.2 | 3DEC | 7 |
| 1.3 | FLAC3D | 8 |
| 1.4 | Objective and scope | 8 |
| 2 | Single fracture model | 11 |
| 2.1 | Model description | 11 |
| 2.2 | Results | 13 |
| 3 | Multiple-fracture model | 15 |
| 3.1 | Model geometry and properties | 15 |
| 3.2 | Stress field | 16 |
| 3.3 | Thermal load | 17 |
| 3.4 | Calculation sequence | 18 |
| 3.5 | Simulated cases | 18 |
| 3.6 | Results | 18 |
| 3.6.1 | Temperatures | 20 |
| 3.6.2 | Single_joint case | 20 |
| 3.6.3 | Double_joint case | 20 |
| 3.6.4 | Triple_joint case | 20 |
| 3.6.5 | Multiple_joint case | 28 |
| 4 | Thermo-mechanical model with openings and fractures | 35 |
| 4.1 | Model geometry, properties and stresses | 35 |
| 4.2 | Calculation sequence | 37 |
| 4.3 | Results | 37 |
| 4.3.1 | Simulation times | 37 |
| 4.3.2 | Temperatures | 38 |
| 4.3.3 | Stresses and shear displacements | 38 |
| 5 | Forsmark earthquake model | 49 |
| 5.1 | Model geometry | 49 |
| 5.2 | Initial stresses | 50 |
| 5.3 | Material properties and rupture initiation | 50 |
| 5.4 | Calculation sequence and boundary conditions | 52 |
| 5.5 | Results | 52 |
| 5.5.1 | Simulation times | 52 |
| 5.5.2 | Quasi-static results | 53 |
| 5.5.3 | Dynamic results | 55 |
| 6 | Large-scale earthquake benchmark case | 65 |
| 6.1 | Model description | 65 |
| 6.2 | Results | 66 |
| 7 | Discussion and conclusions | 73 |
| | References | 75 |
| Appendix 1 | Results from multiple-fracture model (Chapter 3) | 77 |
| Appendix 2 | Results from thermo-mechanical model with openings and fractures (Chapter 4) | 131 |
| Appendix 3 | Results from Forsmark earthquake model (Chapter 5) | 135 |
| Appendix 4 | Results from large-scale earthquake benchmark case (Chapter 6) | 141 |
| Appendix 5 | Description of TPV26 benchmark case | 159 |

1 Introduction

1.1 Background

The concept for long-term storage of spent nuclear fuel applied by the Swedish Nuclear Fuel and Waste Management Co (SKB) is the KBS-3 system in which the fuel will be encapsulated in canisters. The canisters will be emplaced in vertical deposition holes in crystalline rock at a depth of approximately 500 m below ground surface.

To carry out numerical simulations of the mechanical, thermo-mechanical and dynamic processes that take place in the repository rock is a central part of SKB's work in the design of the repository and in the long-term safety assessment. For several years, 3DEC (Itasca 2020) has been SKB's main tool for these types of rock mechanics simulations. The program has, for instance, been used for the extensive mechanical, thermo-mechanical and dynamic simulations that were performed to generate background material for the two safety assessments SR-Can and SR-Site (Fälth et al. 2010, Fälth and Hökmark 2006, Hökmark et al. 2006, 2010). One issue of great importance that is addressed in these simulations is the response of repository host rock fractures to different types of loading. Hence, 3DEC, which is a numerical code for discontinuum modelling, is well-suited for these types of simulations. However, driven by the intention to develop their modelling work and by the demands from the Swedish Radiation Safety Authority (SSM), SKB examines the possibilities to use alternative numerical simulation tools for the types of simulations listed above. One simulation program that is under consideration is FLAC3D. SKB has therefore initiated a project with the objective to compare results generated by FLAC3D (Itasca 2019) with corresponding results generated by 3DEC and other codes. The results of the software comparison are presented in this report.

FLAC3D is an established and widely used code with a documented performance in continuum analysis. One important reason for considering FLAC3D as an alternative to 3DEC is that the calculation engine in FLAC3D is more modern and faster than that in 3DEC, as will be demonstrated here. Even though 3DEC, like FLAC3D, is multi-threaded, FLAC3D is better on taking advantage of modern multi-core computer systems. As noted above, one issue of major importance here, though, is how well the response of fractures/faults can be modelled. The logic in FLAC3D for handling of discontinuities is not as robust as in 3DEC. This holds at least for FLAC3D, version 7, which is the latest officially released version at the time when this study is carried out. However, during the course of this work, a beta version of FLAC3D, version 9 was released. One important feature of this later version of the program is a new discontinuum logic, which is intended to be more robust than that in version 7. Results from both FLAC3D, version 7, and from the beta release of FLAC3D, version 9, are included here.

In the following two sections, brief descriptions of 3DEC and of FLAC3D are given.

1.2 3DEC

In this study, 3DEC version 7 (Itasca 2020) is used. The 3-dimensional Distinct Element Code, 3DEC, is developed for the simulation of the mechanical, thermo-mechanical and thermo-hydro-mechanical response (quasi-static as well as dynamic) of a fractured rock mass. The code is based on the distinct element method (Cundall 1971). A 3DEC model is comprised of blocks, which may be modelled as rigid or deformable. Deformable blocks are discretized using finite-difference zones. The boundaries between the blocks can simulate fractures/faults on which large shear- and normal displacements may take place. The blocks can also be glued together to simulate a continuum without discontinuities. Hence, 3DEC can be used to model a fractured rock mass with loose blocks that undergo large displacements/rotations or to model a practically continuous rock mass with few (or no) fractures in high compression.

3DEC contains a built-in programming language called FISH, which extends 3DEC's capability significantly by allowing the user to define functions and variables that are tailor-made to the problem at hand.

For thermal calculations, two methods are available in 3DEC. There is a numerical logic for heat transport calculations. This means that different parts of the model may have different thermal properties and that detailed temperature field simulations can be made. For the simulations of the temperature field within and around the repository, however, 3DEC's analytical thermal logic has been used. The advantage with this method is that it is fast, also when many heat sources are included and when long times are simulated. The disadvantage with the analytical method is that it implies that the thermal properties in the rock mass are homogeneous and that there are no openings. However, it has been shown that, despite of these limitations, the analytical logic can be used to simulate the temperature field in the vicinity of the repository canisters in a way that can be regarded satisfactory, given the uncertainties that are involved in the problem (Lönqvist and Hökmark 2015). Hence, the analytical logic is ideal for the application to problems related to nuclear waste repositories, in which the effects of thousands of heat sources and long simulation times are considered.

Several studies that have been carried out through the years, have shown that 3DEC generates results that are in good agreement with corresponding results generated by analytical solutions as well as with other numerical tools (Fälth et al. 2015, Hökmark et al. 2009, Lönqvist and Hökmark 2015, Probert and Claesson 1997).

1.3 FLAC3D

FLAC3D (Itasca 2019) is a three-dimensional explicit Lagrangian finite-volume program for engineering mechanics computation. The code is developed for continuum analysis of geological formations and offers a wide range of constitutive models for continuum materials. The explicit Lagrangian calculation scheme and the mixed-discretization zoning technique used in FLAC3D ensure that plastic collapse and flow are modelled accurately, also when large deformations take place. FLAC3D uses the same graphical interface as 3DEC and the built-in programming language FISH is, with exception for code-specific intrinsic functions, the same in both programs. Two versions of FLAC3D have been tested here:

- Version 7. In this version of FLAC3D, discontinuities are handled by use of so-called interface elements. This discontinuum logic is not as robust as that in 3DEC but may handle some tens of fractures. Problems may be encountered particularly at fracture intersections (Itasca 2019). FLAC3D, version 7, has a logic for numerical heat transport calculations, but lacks the type of analytical thermal logic featured by 3DEC. In the thermo-mechanical simulations performed here with FLAC3D, version 7, the temperatures and temperature increments were imported from 3DEC.
- Version 9 (beta). In addition to the interface logic, a new type of joint logic is introduced. This is called 'zone-joints' and uses two-sided contacts, which can better represent multiple joint intersections. The zone-joints are based on the PFC wall logic (Itasca 2021) where interactions between joint surfaces use PFC style contacts and contact models (Itasca 2022). Zone-joints also use an incremental formulation for normal stress and thereby resolve some of the issues with the absolute penetration problems with interfaces. It is noted here that the zone-joint logic still is under development and presently only works in small strain mode (Itasca 2022). Another new feature introduced in version 9 is the same type of analytical thermal logic as that in 3DEC.

1.4 Objective and scope

The objective of the work that is presented in this report was to test the performance and reliability of FLAC3D. It was of particular interest to examine problems where discontinuities are included. Several modelling cases were considered (Table 1-1). In the majority of these, the results from FLAC3D were compared with corresponding results generated by 3DEC. It can be noted in Table 1-1 that two different subversions of 3DEC were used. This is because some of the work was carried out during 2022 using subversion 147 while some work was done during 2023 using subversion 156. It is anticipated that this is of no importance for the conclusions of this work.

In the thermo-mechanical model with openings and fractures (Chapter 4), only FLAC3D, version 9, was tested. The reason for this is that some problems were encountered with the export of temperature data from 3DEC in combination with excavations.

In the case presented in Chapter 6, 3DEC was not used as benchmark. Instead, FLAC3D (version 9) was compared with several other simulation programs using a previously established benchmark exercise within the ‘SCEC/USGS Spontaneous Rupture Code Verification Project’ (Harris et al. 2009). Descriptions of these programs can be found at the SCEC project home page (<https://strike.scec.org/cvws/index.html>).

Table 1-1. Modelling cases and programs used.

| Case | Chapter | FLAC3D version tested | Benchmark |
|---|---------|------------------------|------------------------|
| Single fracture model | 2 | 7.147 and 9.157 (beta) | 3DEC v. 7.147 |
| Multiple-fracture model | 3 | 7.147 and 9.157 (beta) | 3DEC v. 7.156 |
| Thermo-mechanical model with openings and fractures | 4 | 9.157 (beta) | 3DEC v. 7.156 |
| Forsmark earthquake model | 5 | 7.147 and 9.157 (beta) | 3DEC v. 7.147 |
| Large-scale earthquake benchmark case | 6 | 9.157 (beta) | Several other programs |

In the following, FLAC3D (version 7) and FLAC3D (version 9, beta) are denoted “FLAC3D_7” and “FLAC3D_9”, respectively. It is furthermore implied that the interface logic is used in FLAC3D_7 and the new zone-joint logic is used in FLAC3D_9.

In all cases where 3DEC was used as benchmark, the model geometry was constructed in 3DEC and then exported to FLAC3D. The export from 3DEC and import to FLAC3D can be done using built-in commands in 3DEC and FLAC3D. All active joint planes in 3DEC can easily be activated in FLAC3D using the interface logic or the zone-joint logic. Hence, identical discretisation meshes were used in 3DEC and in FLAC3D.

In this work, mechanical, thermo-mechanical and dynamic simulations were performed. No hydro-mechanical coupling case was considered. All simulations were made in small-strain mode. In addition, it should be pointed out that 3DEC was run in deterministic mode in all modelling cases.

All simulations presented here were performed on a Windows 10 Pro computer system equipped with an AMD Ryzen Threadripper 3960X 24-Core Processor working at 3.79 GHz.

2 Single fracture model

2.1 Model description

This model was used to simulate the slip on a circular fracture subjected to a uniform load. The fracture was assumed to have uniform properties and was embedded in a linear elastic, homogeneous and isotropic continuum.

The model geometry is shown in Figure 2-1. The fracture had 100 m diameter, a dip angle of 30° , and was centrally located in a cube-shaped block with side length 700 m. The dip direction of the fracture was 180° with respect to the positive y -axis.

The circular fracture was formed by first generating a coarse grid with finite difference zones. Using FISH, gridpoints were positioned along the edge of the fracture and at the fracture centre. The coarse finite difference zone grid was then exported to disk from where it was imported again, but now as tetrahedral blocks. The blocks were then used to form a circular fracture joint plane comprising 24 triangular sectors (see Figure 2-1, left). All other joint planes in the model were joined to resemble a continuum. This block geometry was discretised with four different discretisation densities corresponding to $N = 6, 8, 16,$ and 20 discretisation edge lengths/fracture diameter (see Figure 2-1, right). The discretisation was set to be the same in the entire model volume. As noted in Section 1.4, the same model geometry was used in the FLAC3D simulations.

The fracture was assumed to respond to loads according to an idealized elasto-plastic material model with constant stiffnesses in both the normal and shear directions, and with failure according to a Coulomb criterion (Itasca 2020) (Figure 2-2). All material property parameter values are presented in Table 2-1. The components of the initial stress field are reported in Table 2-2. The pore pressure was set to 4.91 MPa. All boundaries were locked for displacements in the x -, y - and z -directions.

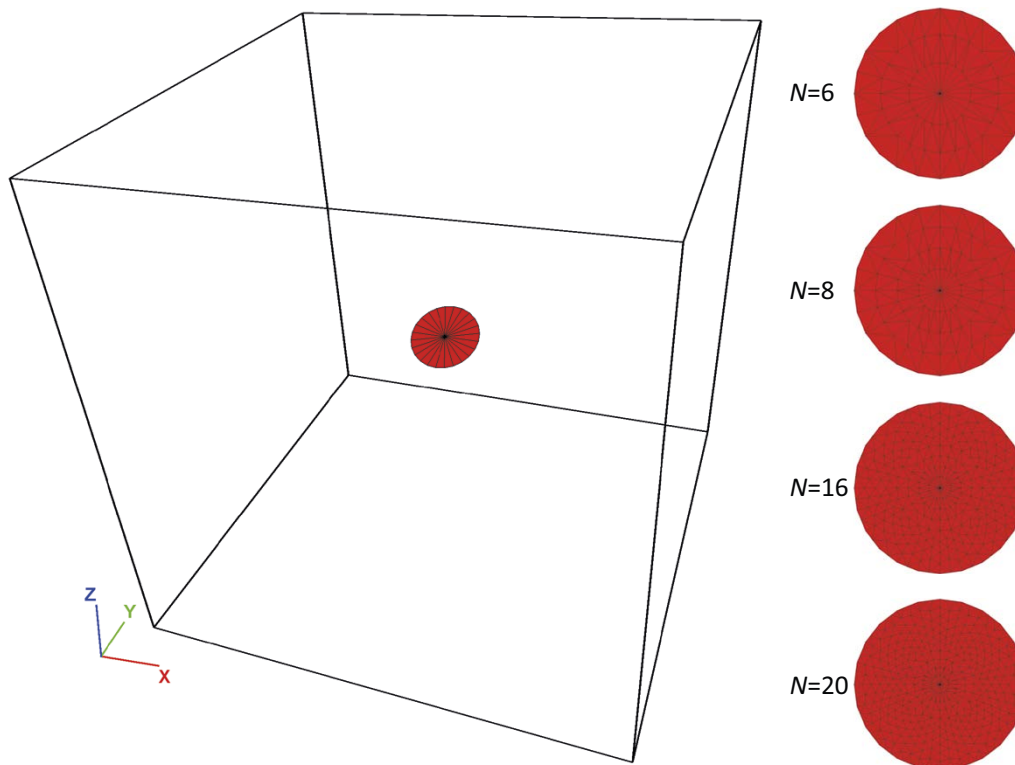


Figure 2-1. Left: Model outlines with the circular fracture plane shown in red. Right: The fracture plane discretised with four different discretisation densities corresponding to $N = 6, 8, 16$ and 20 edge lengths/fracture diameter.

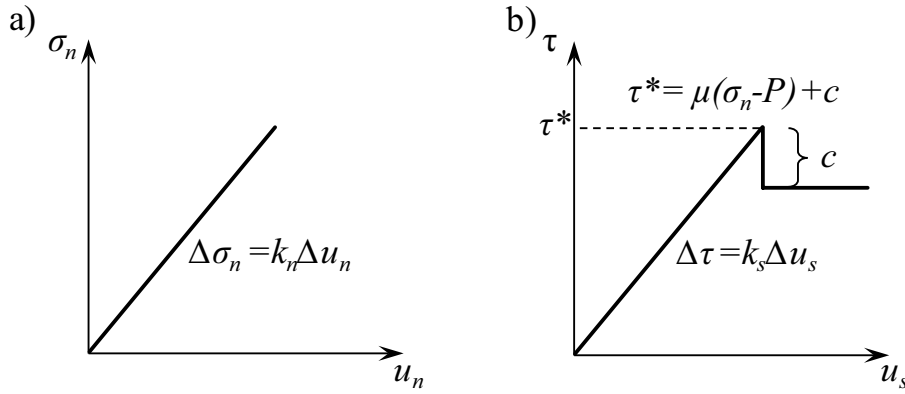


Figure 2-2. Idealised elasto-plastic joint material model. a) The normal stress σ_n is a function of the constant normal stiffness k_n and the normal displacement u_n . b) The shear stress τ is a function of the constant shear stiffness k_s and the shear displacement u_s . The shear strength τ^* is governed by a Coulomb criterion where μ , P and c are friction coefficient, pore pressure and cohesion, respectively (Itasca 2020).

For a circular fracture with radius a embedded in a homogeneous continuum with shear modulus G and Poisson's ratio ν , and for a uniform stress drop $\Delta\tau$ on the fracture surface, the displacement $u(r)$ on the fracture can be calculated according to (Segedin 1951)

$$u(r) = \frac{8(1-\nu)\Delta\tau}{\pi(2-\nu)G} \sqrt{a^2 - r^2}, \quad (2-1)$$

where r is radial position. The shear modulus is calculated as $G = E/(2(1 + \nu))$, with E being Young's modulus. The stress drop $\Delta\tau$ is the difference between the initial shear stress (τ_i) and the final shear stress (τ_f) on the slipping fault/fracture, i.e. $\Delta\tau = \tau_i - \tau_f$. Given the initial stress field, the fracture orientation and the fracture friction coefficient assumed here, the fracture stress drop becomes 5.13 MPa. For this stress drop and for the continuum properties applied here, the displacement at the centre of a 100 m diameter fracture will be 10 mm according to Equation (2-1).

Table 2-1. Material property parameter values.

| Component | Parameter | Value | Comment |
|-----------------|--|--------------------|---------|
| Rock mass | Young's modulus, E (GPa) | 70 | |
| | Poisson's ratio, ν (-) | 0.25 | |
| | Density, ρ (kg/m ³) | 2700 | |
| | Coefficient of thermal expansion, α (1/K) | 7×10^{-6} | |
| | Thermal conductivity, λ (W/(m·K)) | 2.72 | |
| | Specific heat capacity (J/(kg·K)) | 770 | |
| Fractures/zones | Friction coefficient, $\mu = \tan(30^\circ)$ | 0.58 | |
| | Cohesion, c (MPa) | 0* | |
| | Normal stiffness, k_n (GPa/m) | 200 | |
| | Shear stiffness, k_s (GPa/m) | 200 | |

* Initially, a high cohesive strength ($c_{initial} = 5.1$ MPa) was applied and then ramped down in steps. The value shown here is the final value after down-ramping.

Table 2-2. Initial stress field.

| Component | Value | Comment |
|---------------------|-------|---------|
| σ_{xx} (MPa) | 17 | |
| σ_{yy} (MPa) | 47.7 | |
| σ_{zz} (MPa) | 13.3 | |
| σ_{xy} (MPa) | 0 | |
| σ_{xz} (MPa) | 0 | |
| σ_{yz} (MPa) | 0 | |

2.2 Results

To avoid shear displacement overshoot, the fracture was assigned a high cohesion, which then was ramped down in steps with an equilibrium run between each step. The diagram in Figure 2-3 shows fracture displacements as simulated with 3DEC and with FLAC3D. The numerical results are shown along with the corresponding analytical results obtained from Equation (1-1). The results from 3DEC and FLAC3D_7 were practically identical while there was a tendency that FLAC3D_9 generated slightly larger displacements for the $N = 16$ and $N = 20$ cases. For $N = 16$ and $N = 20$, the difference between the numerically simulated displacements at the fracture centre and the corresponding theoretical value amounts to about 5 %. This kind of deviation is expected since a numerical solution cannot fully represent the discontinuity in the displacement field arising at the edge of the fracture. With further refinement of the discretisation, a numerical solution will approach the theoretical solution asymptotically.

It can be concluded that, for this modelling case, 3DEC and both versions of FLAC3D generate results that can be regarded practically identical. However, as seen in Table 2-3, FLAC3D is much faster than 3DEC. For the $N = 6$ case, FLAC3D_7 was almost 12 times faster than 3DEC and in the $N = 20$ case more than 2 times faster. Yet shorter simulation times were obtained with FLA3D_9. This version of the code was between 6 and 50 times faster than 3DEC for the present problem.

Table 2-3. Case summary.

| Case (N) | No. of elements ($\times 10^6$) | Simulation times (min) | | |
|--------------|-----------------------------------|------------------------|----------|----------|
| | | 3DEC | FLAC3D_7 | FLAC3D_9 |
| 6 | 0.6 | 15 | 1.3 | 0.3 |
| 8 | 1.4 | 20 | 2.7 | 0.7 |
| 16 | 10.8 | 67 | 26 | 7.6 |
| 20 | 21.2 | 110 | 47 | 18 |

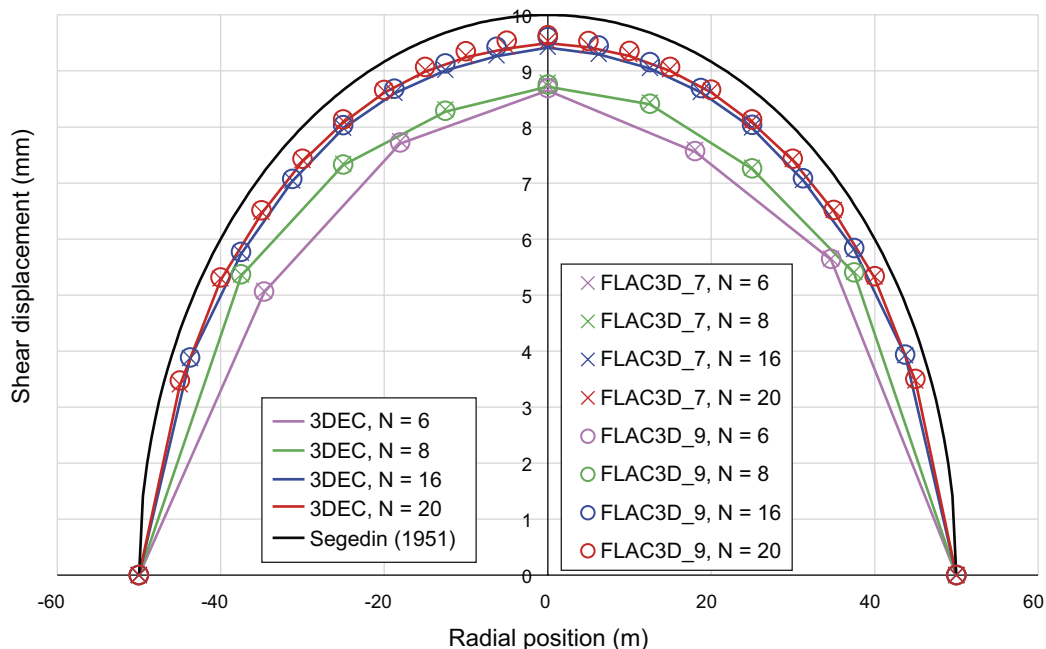


Figure 2-3. Fracture displacements as simulated with 3DEC and with FLAC3D. The results are shown along with the theoretical results obtained from Equation (2-1).

3 Multiple-fracture model

3.1 Model geometry and properties

A model containing ten intersecting joint planes (Table 3-1) was set up (Figure 3-1, Figure 3-2). The model box, in which the upper boundary represented the ground surface, had the dimensions (x, y, z) = (14, 14, 5) km. Several of the joint planes intersected the upper boundary and hence simulated surface-breaching deformation zones. The central box containing the joint planes had the dimensions (x, y, z) = (4, 4, 3) km. Within this box the discretisation edge length was set to be 150 m. The mesh was made gradually coarser toward the model boundaries. The model contained about 660 000 zones. All boundaries, except for the free upper boundary, had roller conditions. The material properties are described in Section 2.1.

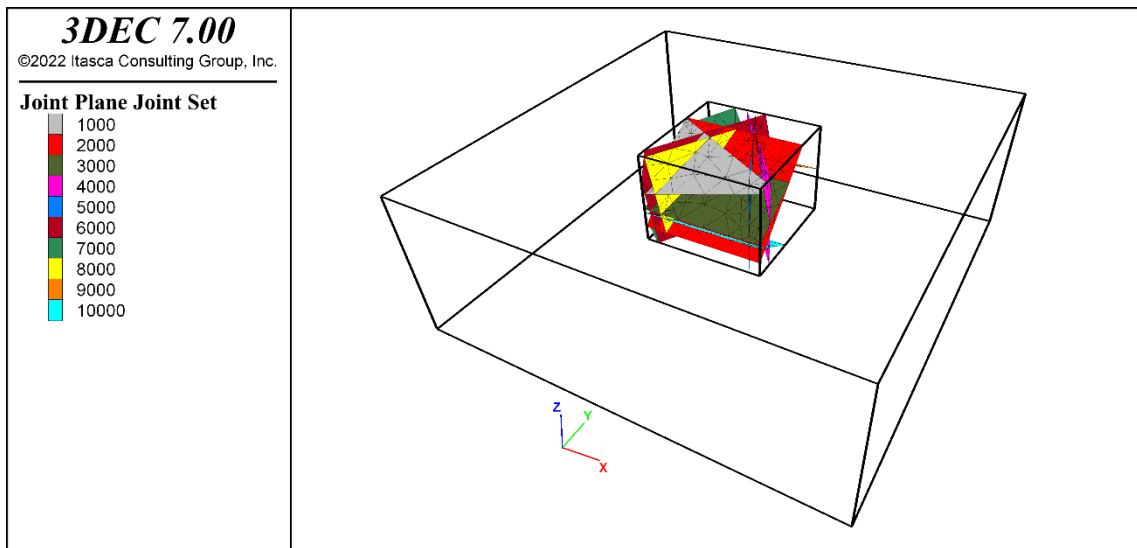


Figure 3-1. Model outlines with the centrally located joint planes shown in different colours.

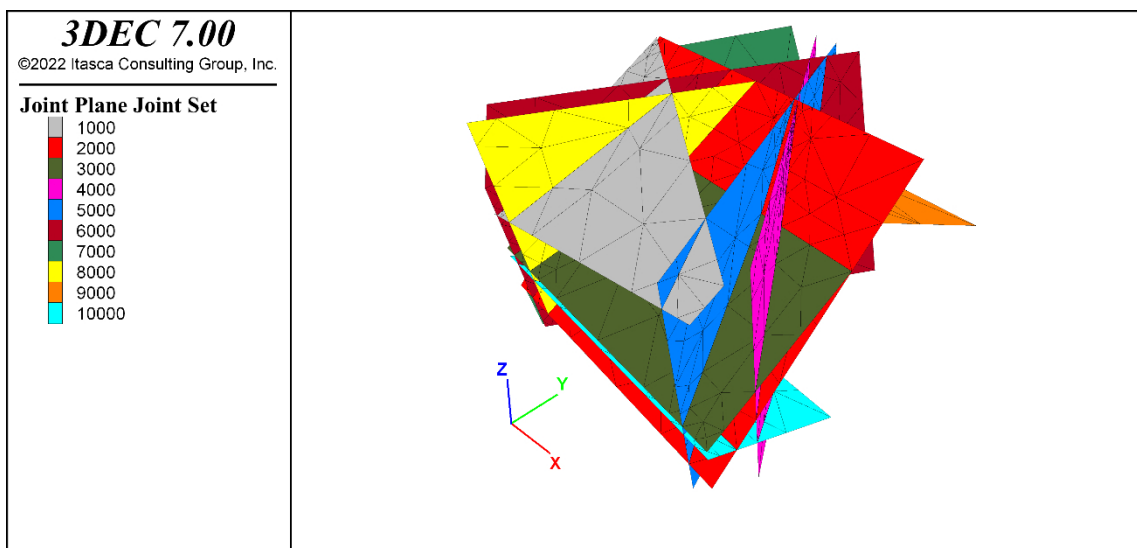


Figure 3-2. Close-up of the joint plane system.

Table 3-1. Joint plane orientations.

| Joint ID | dip | dip-direction* |
|----------|-----|----------------|
| 1000 | 30 | 210 |
| 2000 | 43 | 180 |
| 3000 | 30 | 180 |
| 4000 | 90 | 53 |
| 5000 | 90 | 65 |
| 6000 | 80 | 120 |
| 7000 | 70 | 115 |
| 8000 | 80 | 120 |
| 9000 | 30 | 0 |
| 10000 | 30 | 0 |

* With respect to positive y-axis.

3.2 Stress field

The initial stress field was defined such that optimally oriented faults are in frictional failure equilibrium. For this assumption, and given that the fault strength is governed by a Coulomb criterion, the relation between the major principal stress σ_1 and the minor principal stress σ_3 is given by (Jaeger and Cook 1979)

$$\frac{\sigma_1 - P}{\sigma_3 - P} = (\sqrt{\mu^2 + 1} + \mu)^2. \quad (3-1)$$

Here, P is the pore pressure and μ is the friction coefficient. Since Equation (3-1) involves only the major and minor principal stress components, the intermediate principal stress component, σ_2 , was constrained by (Gephart and Forsyth 1984)

$$R = \frac{\sigma_1 - \sigma_2}{\sigma_1 - \sigma_3}, \quad (3-2)$$

where R is a measure of the relative stress magnitudes. Based on Equations (3-1) and (3-2), a reverse stress field could be calculated from

$$\begin{aligned} \sigma_1 &= A(\sigma_3 - P) + P = \sigma_H \\ \sigma_2 &= \sigma_1(1 - R) + R\sigma_3 = \sigma_h \\ \sigma_3 &= \sigma_v \end{aligned} \quad (3-3)$$

with $A = (\sqrt{\mu^2 + 1} + \mu)^2$. Here, σ_3 was assumed to be vertical and to correspond to the weight of the rock overburden, i.e., $\sigma_3 = \sigma_v = \rho g d$, where ρ is rock mass density, g ($= 9.82 \text{ m/s}^2$) is the gravitational acceleration and d is depth. Further, the friction coefficient was set to $\mu = 0.7$, while $R = 0.95$ and hydrostatic pore pressure was assumed. The total principal stresses are plotted in Figure 3-3. Note that the high value of R means that σ_3 was almost equal to σ_2 , meaning that the stress field was close to being of strike-slip type. This was set to obtain low stability on gently dipping as well as on steeply dipping faults/fractures. The stresses were aligned with the model axes such that $\sigma_{xx} = \sigma_2$, $\sigma_{yy} = \sigma_1$ and $\sigma_{zz} = \sigma_3$.

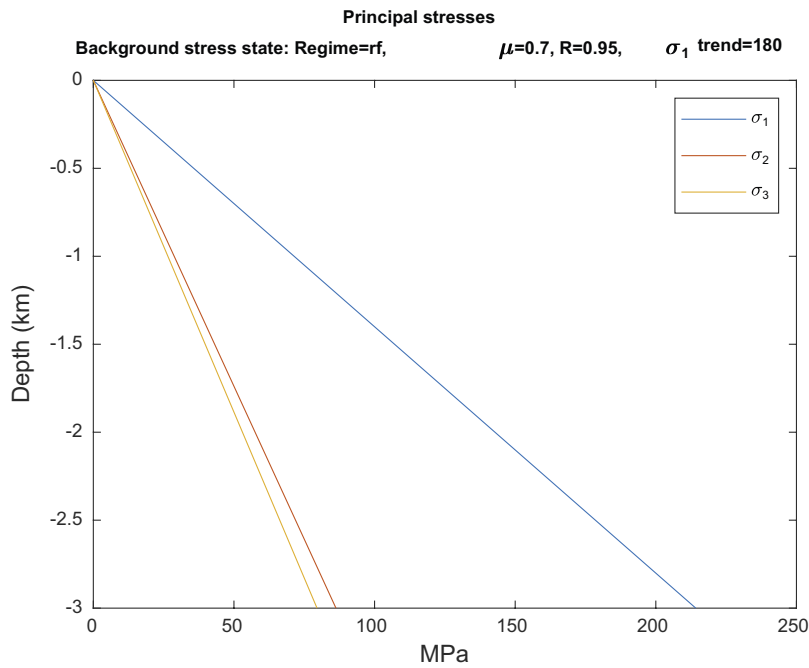


Figure 3-3. The initial total principal stresses.

3.3 Thermal load

A grid of analytical point heat sources was included in the model. The grid was located at 500 m depth close to the centre of the model and extended 1 km in the x -direction and 1.25 km in the y -direction (Figure 3-4). There were 20×20 heat sources, each with a constant heating power of 4 kW.

The analytical thermal logic is not available in FLAC3D_7. To perform the thermo-mechanical calculations in FLAC3D_7, temperatures and temperature increments were imported from 3DEC using FISH. This was not necessary in FLAC3D_9, where the analytical thermal logic is implemented.

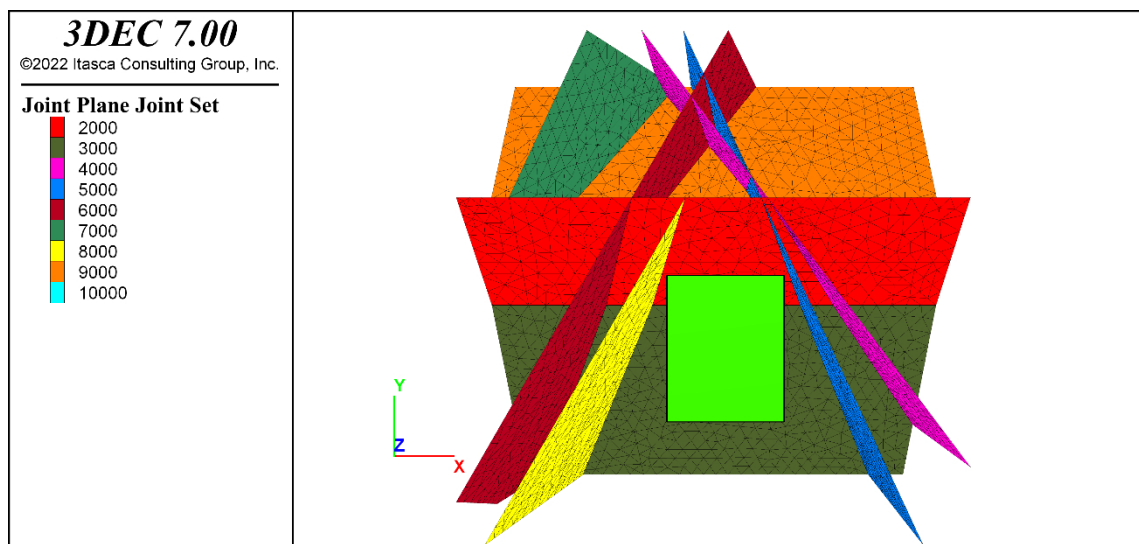


Figure 3-4. Top-down view of the model showing the location of the grid of heat sources. The grid was located at 500 m depth within the light green rectangle. Note that joint 1000 is hidden in the figure for illustrative purposes, cf. Figure 3-2.

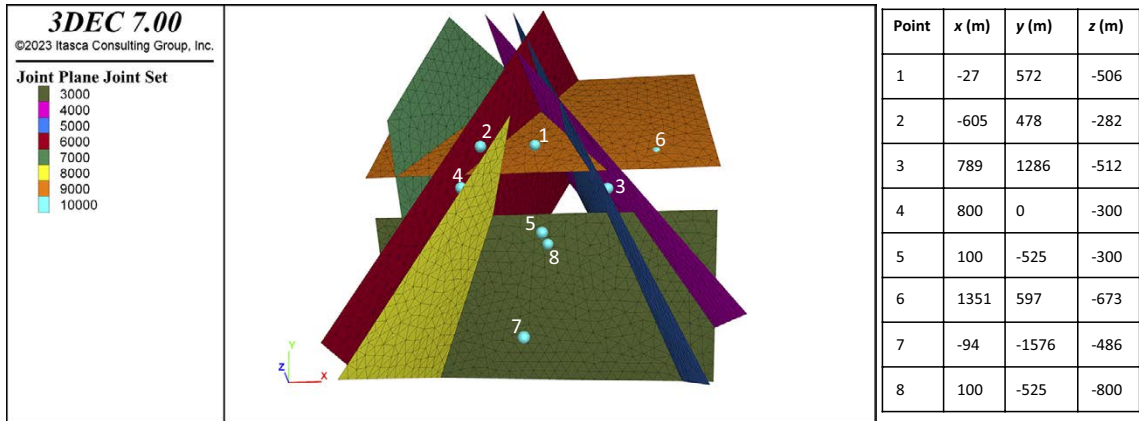


Figure 3-5. Locations of the eight points for monitoring of continuum stresses. Note that joint 1000 and 2000 are hidden in the figure for illustrative purposes, cf. Figure 3-2.

3.4 Calculation sequence

The simulation was carried out in three steps:

1. The initial stress field (Figure 3-3) was applied along with hydrostatic pore pressure and initial equilibrium was established. High cohesive strength was assigned to the joint planes to inhibit slip.
2. The cohesive strength of the joint planes was ramped down to zero in a stepwise manner. Slip was developed on the joint planes in accord with the stress field, the joint orientations, and the joint properties.
3. The heat load was applied. The thermo-mechanical response was calculated at three time instances: After 100 years, 500 years and 1 000 years of heating.

Continuum stresses at eight locations and shear displacements at two points on each joint plane were monitored during the analysis. Results were saved after simulation step 1 and 2 as well as after each of the three heating stages. The continuum stresses were calculated as the average values from zones inside a sphere with 200 m radius.

3.5 Simulated cases

Four model cases with different numbers of joint planes active were considered (Table 3-2). The same model geometry was used in all cases, but the non-used joint planes were joined and hence mechanically inactive. Here, “joined” means that the join command was used. Hence, the non-used joint planes had no active subcontacts/interface elements/zone-joints.

Table 3-2. Case summary.

| Case | Description (cf. Figure 3-2) |
|----------------|---|
| Single_joint | Joint plane 1000 active |
| Double_joint | Joint planes 1000 and 2000 active. No joint intersection. |
| Triple_joint | Joint planes 1000, 2000 and 5000 active. Intersection between the joints. |
| Multiple_joint | All ten joint planes active. |

3.6 Results

To compare code running speed, the time to complete simulation step 2 (see above) was measured, see Table 3-3. The times were partly governed by the solve ratio limit that was used. In general, it appeared that a lower solve ratio limit had to be set in FLAC3D for the velocities in the model to go down to

approximately the same level as in the corresponding 3DEC model. However, the impression was that the unbalance forces were reduced faster in FLAC3D (i.e. fewer time steps were needed). This, and the higher cycling speed in FLAC3D means that the model running times became considerably shorter with FLAC3D, at least in the cases with one, two and three joint planes.

In the Multiple_joint case with all ten joints active, the simulation time was shorter in 3DEC than in FLAC3D_7. FLAC3D_9 was much faster than both 3DEC and FLAC3D_7 in all cases (Table 3-3).

Table 3-3. Time to complete simulation step 2.

| Case | Simulation times (min) | | |
|----------------|------------------------|----------|----------|
| | 3DEC | FLAC3D_7 | FLAC3D_9 |
| Single_joint | 24 | 3.7 | 0.9 |
| Double_joint | 54 | 7.8 | 1.6 |
| Triple_joint | 90 | 17 | 2.8 |
| Multiple_joint | 247 | 295 | 15 |

Since the simulation times reported in Table 3-3, to some extent, depend on the applied solve ratio limit, an additional running time test was carried out. For each model case, the time needed to perform 500 cycles was measured. The time was taken as the average value from ten consecutive runs which were performed at the end of simulation step 2. The results, which are presented in Figure 3-6 (left), indicate that FLAC3D_7 is more sensitive to the number of joints than 3DEC is. With one joint, FLAC3D_7 was more than 3 times faster, but with ten joints it needed nearly 40 % more time than 3DEC. This shows that the interface logic in FLAC3D is not efficient for cases including several intersecting joint planes (cf. Itasca 2019).

A general observation that can be made is that FLAC3D_9 is considerably faster than both 3DEC and FLAC3D_7. For all four modelling cases, the simulation times in FLAC3D_9 were less than 20 % of those in 3DEC and between 10 % and 70 % of the times in FLAC3D_7 (Figure 3-6, left).

Notable is also that FLAC3D_9 appears to be much less sensitive to the number of joints. The run time in the Multiple_joint case was about 1.5 and 7.5 longer than in the Single_joint case for 3DEC and FLAC3D_7, respectively (Figure 3-6, right). In FLAC3D_9, the Multiple_joint run took only about 10 % longer time than the Single_joint run.

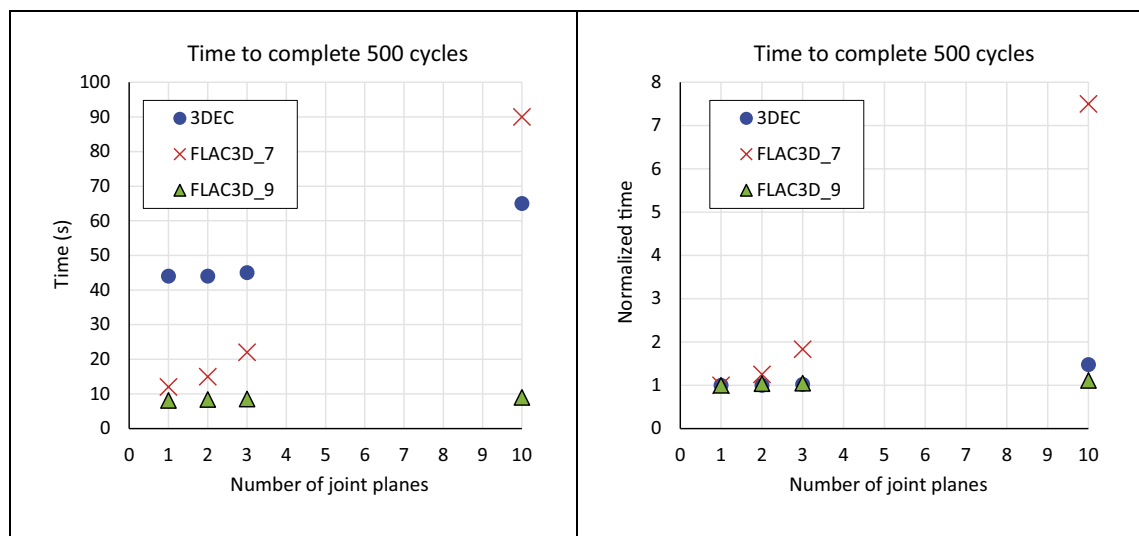


Figure 3-6. Left: Time to complete 500 cycles in the four modelling cases. The times are averages from ten consecutive runs. Right: The same results as in the left diagram but normalized to the running time of the Single joint case.

3.6.1 Temperatures

Since temperatures and temperature increments were imported from 3DEC to FLAC3D_7, temperatures were identical in these models. This is illustrated by the temperature plots in Figure 3-7 where the corresponding temperatures in FLAC3D_9 also are shown. The calculated temperatures become practically identical in 3DEC and FLAC3D_9. In fact, there are slight differences in the results (relative temperature difference $\left| (T_{FLAC3D_9} / T_{3DEC}) - 1 \right|$ of the order of 10^{-7}). Tests made here indicate that this is not related to the multithreading of the thermal logic in FLAC3D_9. Running the thermal calculation in FLAC3D_9 using different number of processor cores gives identical results. Hence, it appears that the slight differences between the 3DEC and FLAC3D_9 temperature results can be attributed to the fact that the codes are built using different programming languages (Fortran for 3DEC and C++ for FLAC3D_9). At any rate, the difference has no practical importance.

3.6.2 Single_joint case

Figure 3-8 shows evolution of principal stresses at three of the monitoring points in the inner model box (note that compressive stresses are negative in 3DEC and FLAC3D). Principal stress evolutions for all monitoring points are presented in Appendix 1. The agreement between the 3DEC stress results and the corresponding FLAC3D results is good. The stress difference (FLAC3D vs 3DEC) is typically less than 1 % for both FLAC3D versions.

Figure 3-9 shows final joint shear displacements on joint plane 1000 while evolution of joint shear displacements at two joint 1000 points is shown in Figure 3-10. The results in Figure 3-9 are repeated in Appendix 1, but with the same colour scale in all plots. About 95 % of the joint area failed in shear and/or in tension. The difference between the shear displacements generated in FLAC3D_7 and 3DEC at the different modelling steps typically amounts to some 1 %, with a maximum at 4 %. The FLAC3D_9 displacements deviate a bit more from the 3DEC displacements, with differences typically in the range 2 % to 10 %.

3.6.3 Double_joint case

Figure 3-11 shows evolution of principal stresses at three of the monitoring points in the inner model box. Principal stress evolutions for all monitoring points are presented in Appendix 1. The agreement between 3DEC results and FLAC3D results is good. The stress difference (FLAC3D vs 3DEC) is typically less than 1 % for both FLAC3D versions.

Figure 3-12 shows final joint shear displacements on joint plane 1000 while evolution of joint shear displacements at two joint 1000 points is shown in Figure 3-13. Shear displacement results for both joint planes are presented in Appendix 1. To facilitate comparison of the results, the colour scale plots are presented in Appendix 1 also with the colour scales set equal. About 95 % of the total joint area failed in shear and/or in tension. The difference between the shear displacements generated in FLAC3D_7 and 3DEC at the different modelling steps is typically in the range 0.5 % to 2 %. The FLAC3D_9 displacements deviate a bit more from the 3DEC displacements, with differences in the range 1 % to 8 %.

3.6.4 Triple_joint case

Figure 3-14 shows evolution of principal stresses at three of the monitoring points in the inner model box. Principal stress evolutions for all monitoring points are presented in Appendix 1. The agreement between 3DEC results and FLAC3D results is good. The stress difference (FLAC3D vs 3DEC) is typically less than 1 % for both FLAC3D versions.

Figure 3-15 shows final joint shear displacements on joint plane 1000 while evolution of joint shear displacements at two joint 1000 points is shown in Figure 3-16. Shear displacement results for all three joint planes are presented in Appendix 1. To facilitate comparison of the results, the colour scale plots are presented in Appendix 1 also with the colour scales set equal. About 95 % of the total joint area failed in shear and/or in tension. The difference between the shear displacements generated in FLAC3D_7 and 3DEC at the different modelling steps is typically in the range 1 % to 3 %. The FLAC3D_9 displacements deviate a bit more from the 3DEC displacements, with differences in the range 1 % to 9 %.

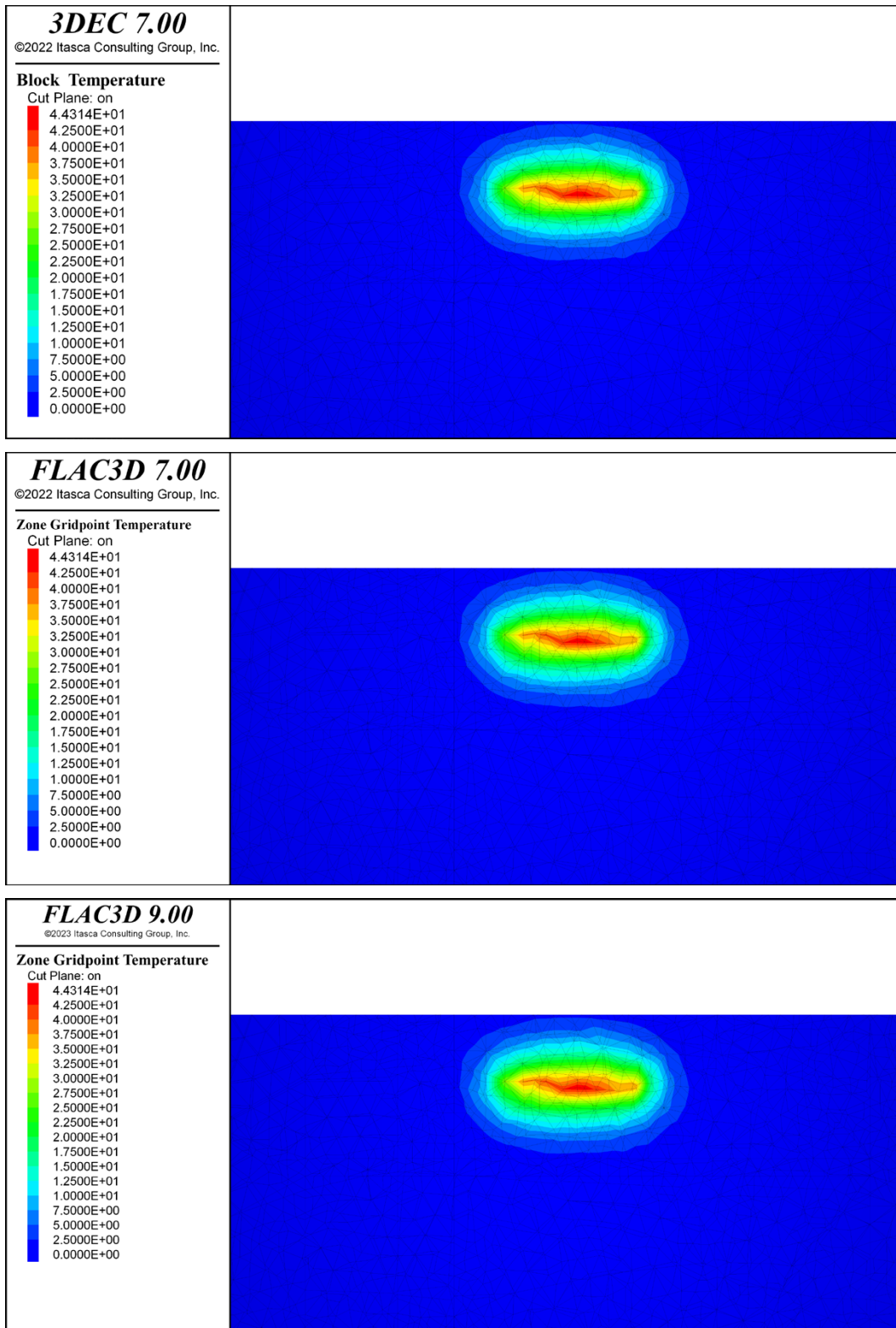


Figure 3-7. The temperature field after completed simulation shown on a vertical cross-section plane through the centre of the thermal source grid.

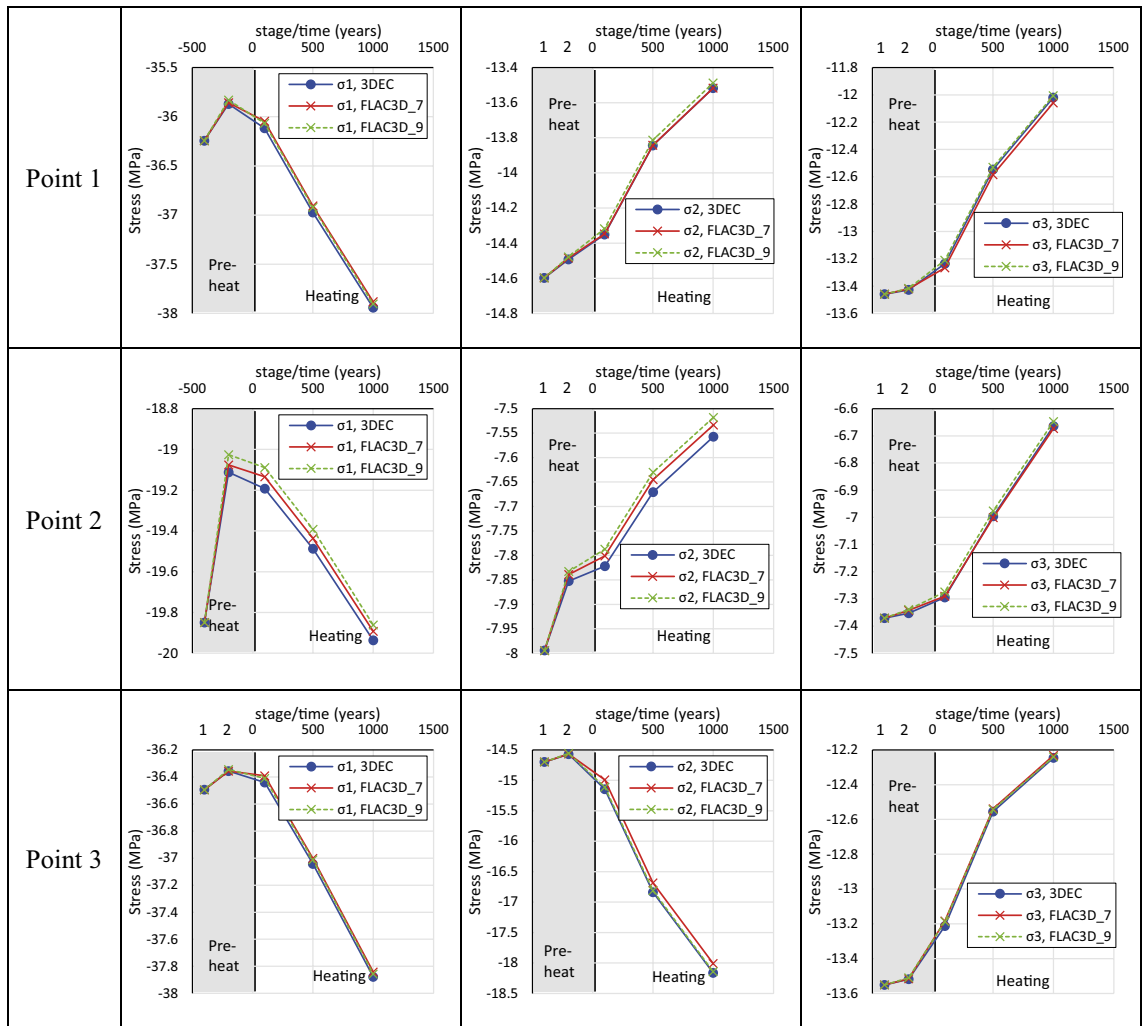


Figure 3-8. Evolution of principal stresses at monitoring points 1 to 3 in the Single joint case. Corresponding results for all eight monitoring points are presented in Appendix 1.

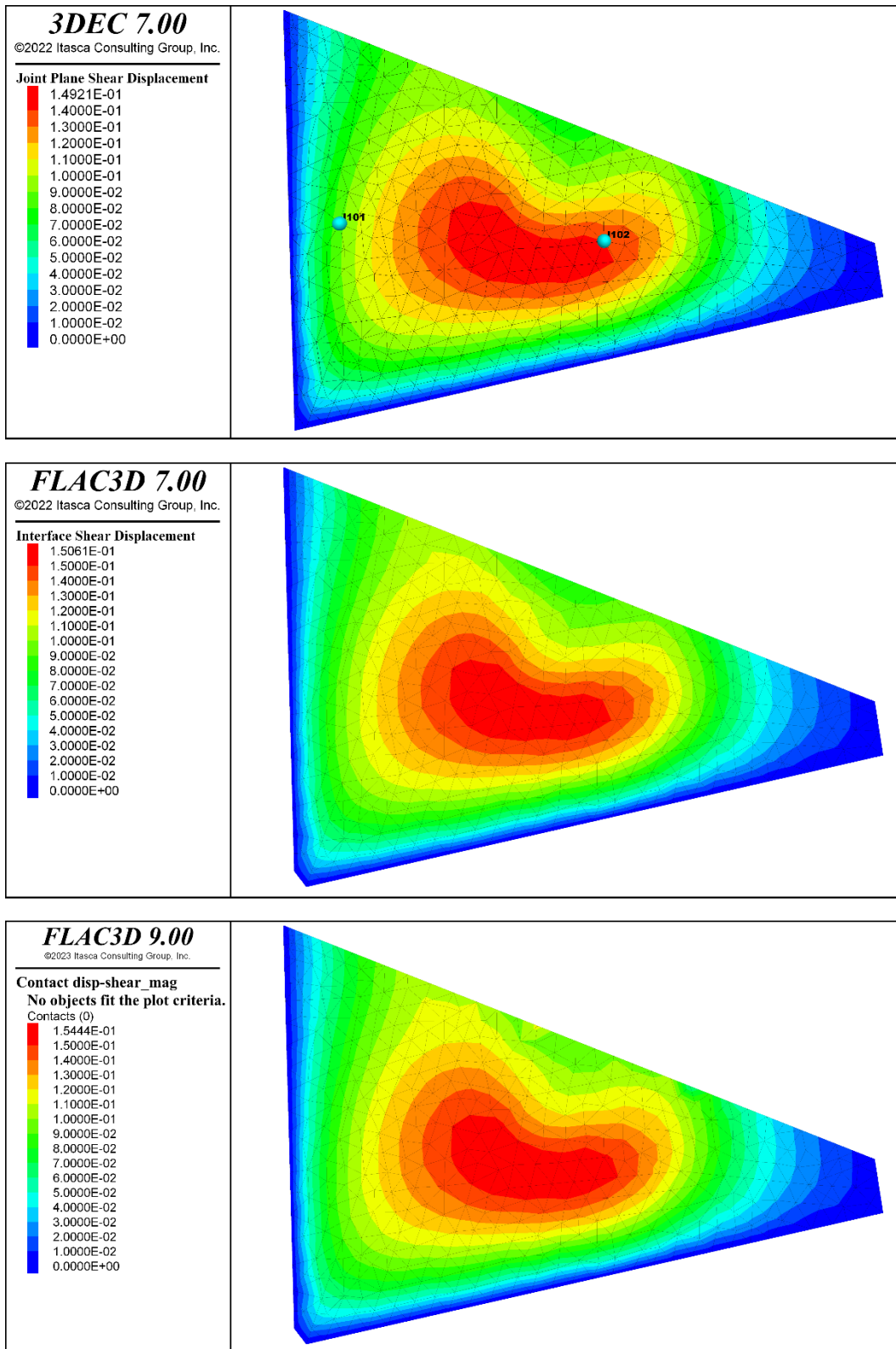


Figure 3-9. Shear displacements on joint 1000 after completed simulation in the Single joint case. Shear displacement evolution at the two points indicated in the upper plot is shown in Figure 3-10.

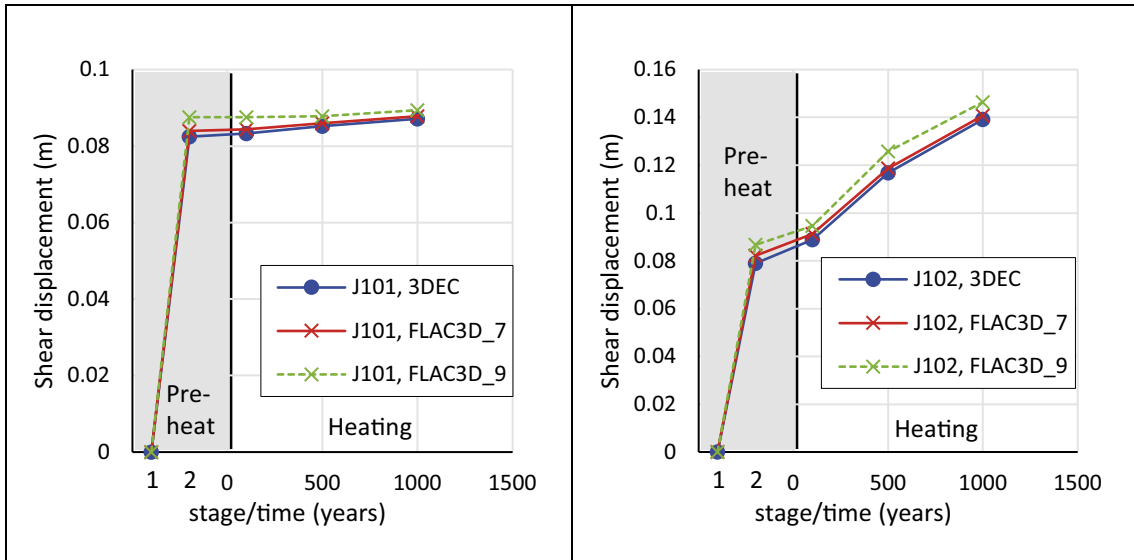


Figure 3-10. Evolution of joint 1000 shear displacement in the Single_joint case at the two points depicted in Figure 3-9, upper.

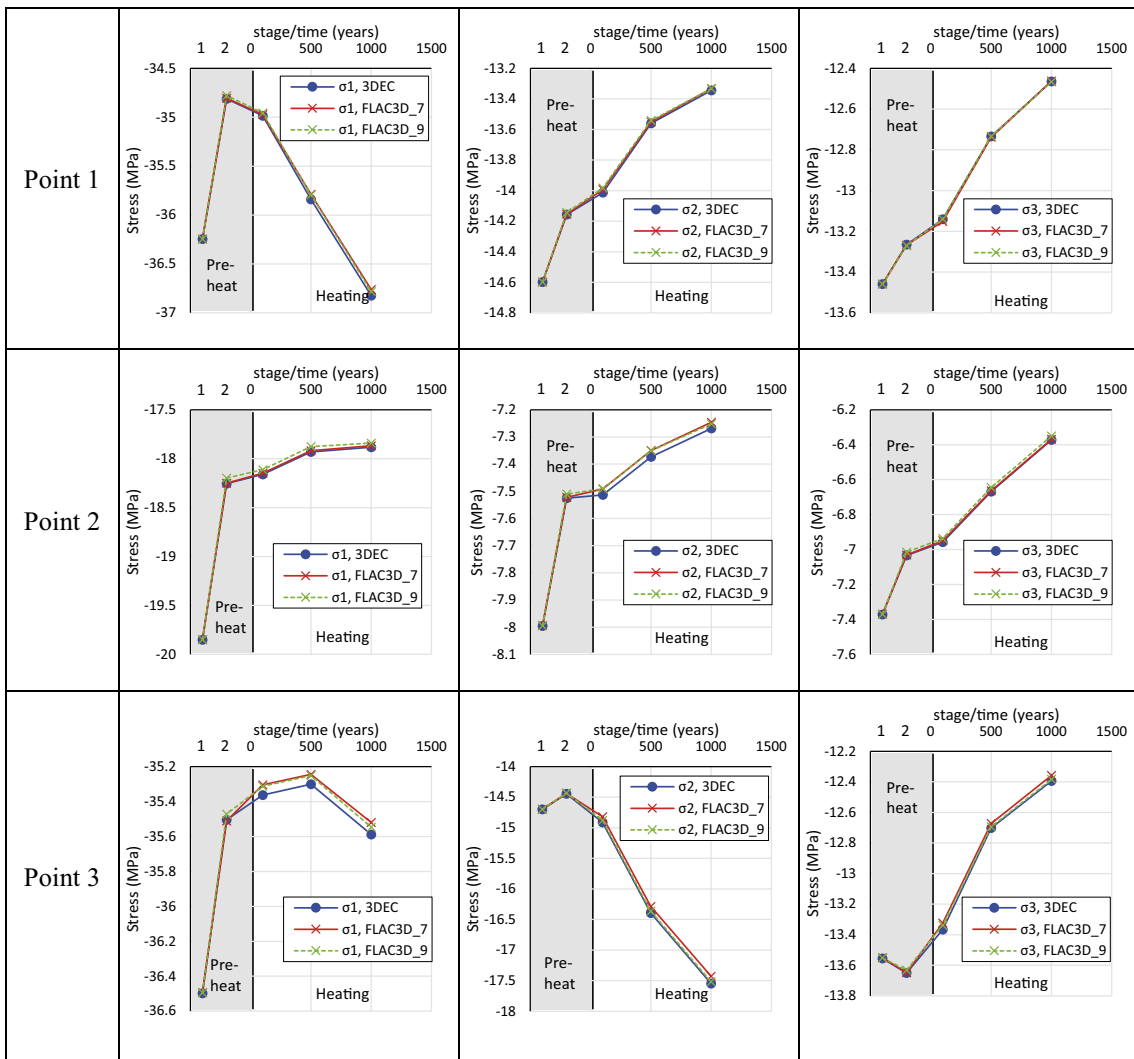


Figure 3-11. Evolution of principal stresses at monitoring points 1 to 3 in the Double_joint case. Corresponding results for all eight monitoring points are presented in Appendix 1.

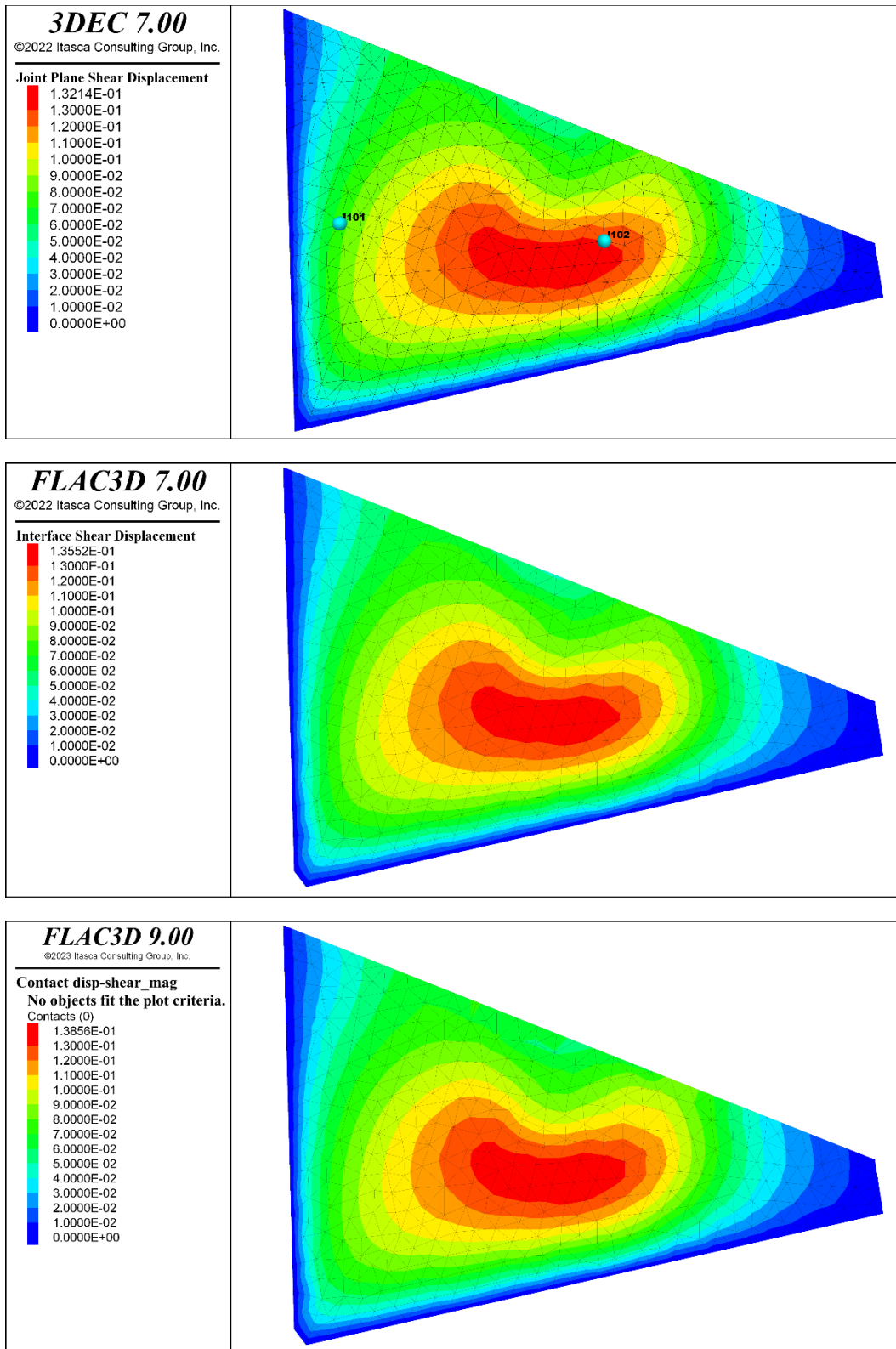


Figure 3-12. Shear displacements on joint 1000 after completed simulation in the Double joint case. Corresponding results for joint 2000 are presented in Appendix 1. Shear displacement evolution at the two points indicated in the upper plot is shown in Figure 3-13.

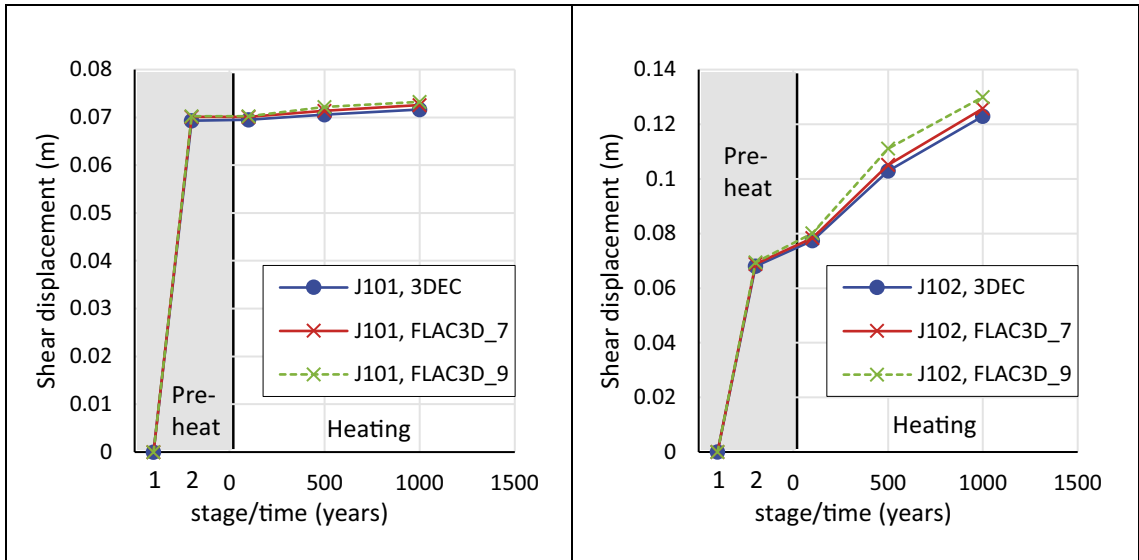


Figure 3-13. Evolution of joint 1000 shear displacement in the Double joint case at the two points depicted in Figure 3-12, upper.

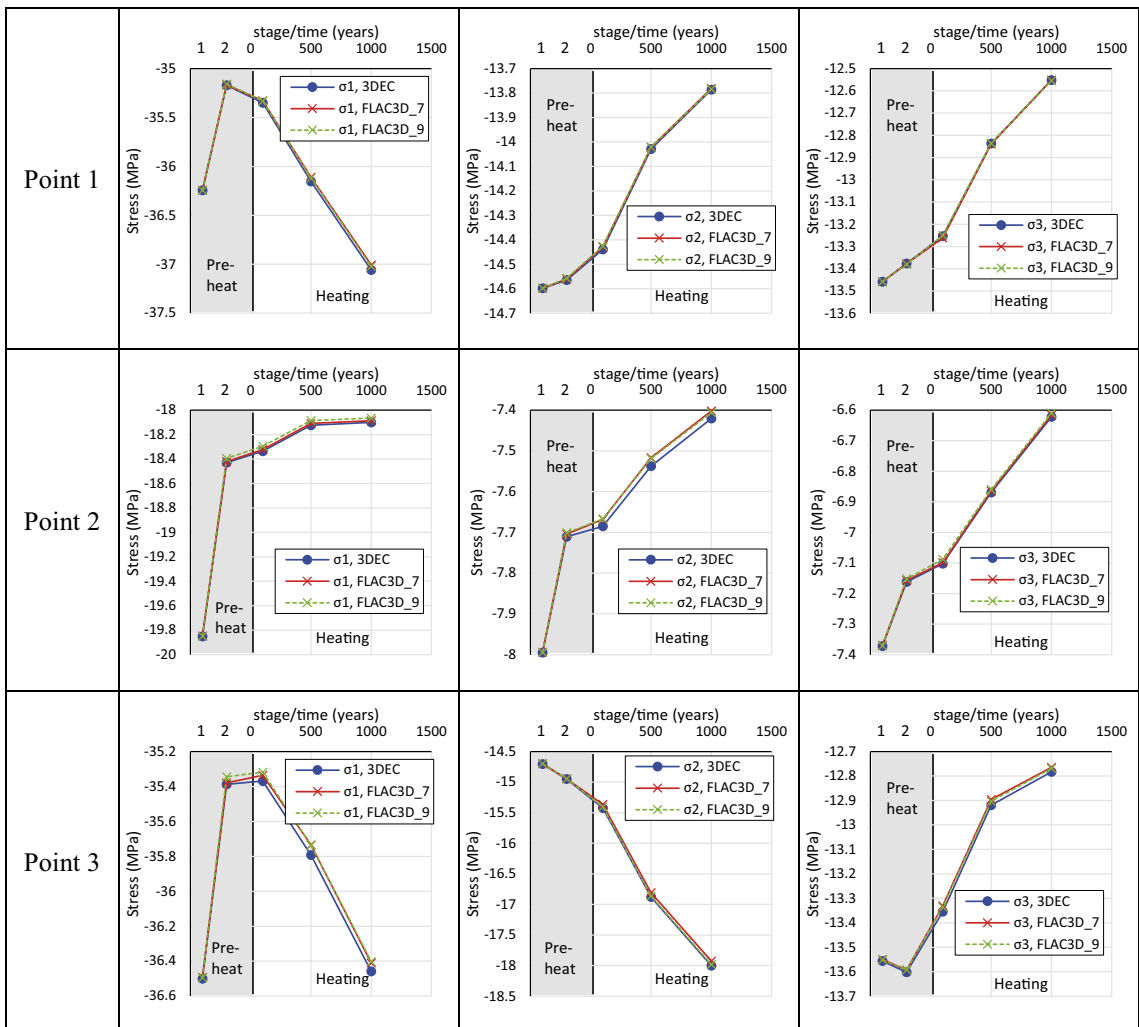


Figure 3-14. Evolution of principal stresses at monitoring points 1 to 3 in the Triple joint case. Corresponding results for all eight monitoring points are presented in Appendix 1.

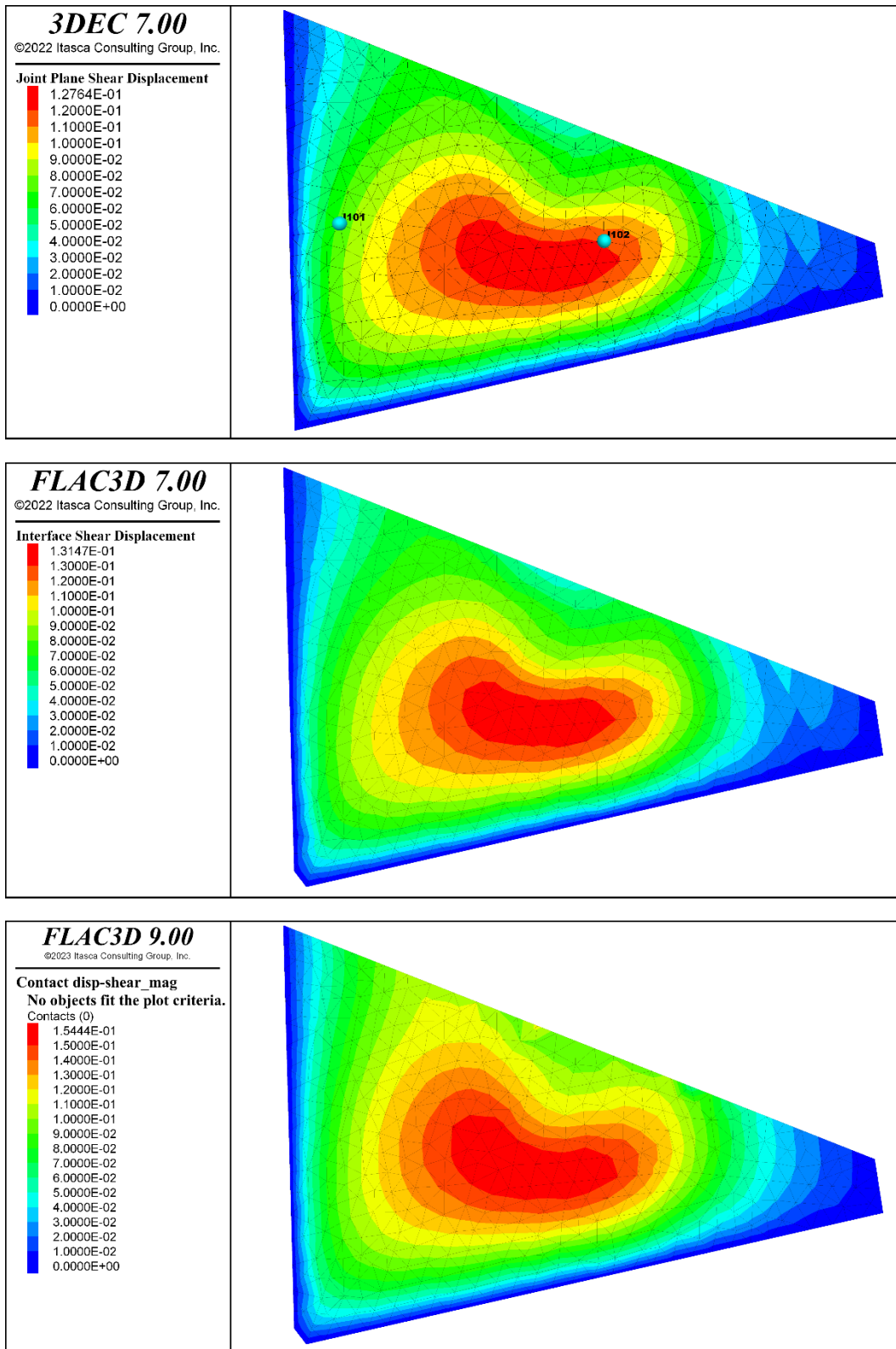


Figure 3-15. Shear displacements on joint 1000 after completed simulation in the Triple joint case. Corresponding results for joints 2000 and 5000 are presented in Appendix 1. Shear displacement evolution at the two points indicated in the upper plot is shown in Figure 3-16.

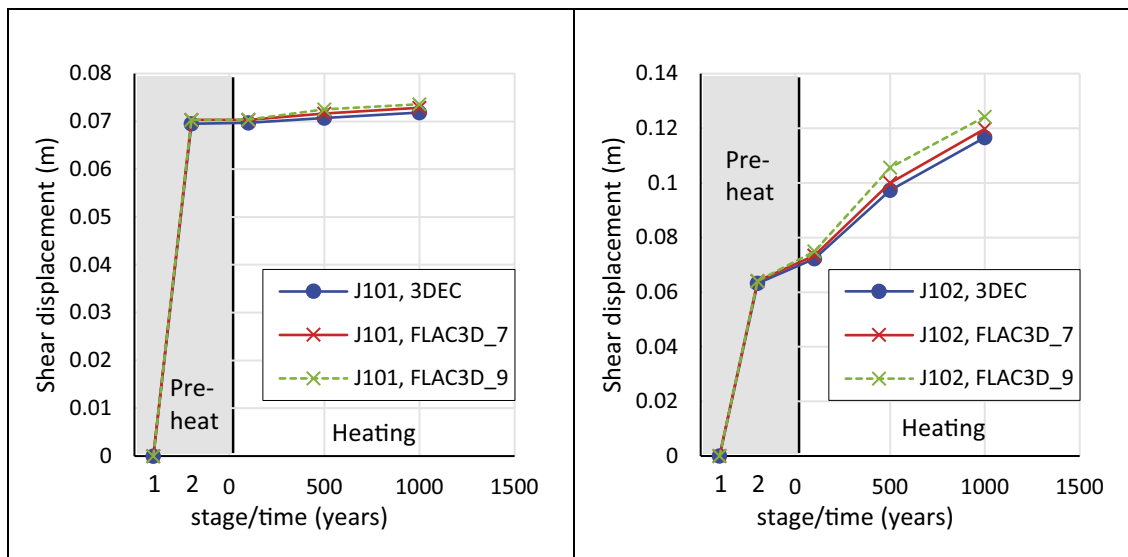


Figure 3-16. Evolution of joint 1000 shear displacement in the Triple joint case at the two points depicted in Figure 3-15, upper.

3.6.5 Multiple joint case

Figure 3-17 shows evolution of principal stresses at three of the monitoring points in the inner model box. Principal stress evolutions for all monitoring points are presented in Appendix 1. The agreement between the 3DEC stress results and the corresponding FLAC3D results is good even though the differences tend to be larger in this simulation case as compared to the Single joint, Double joint and Triple joint cases (cf. Figure 3-8, Figure 3-11 and Figure 3-14). The tendency for larger differences is most clearly seen when comparing FLAC3D_7 with 3DEC. The difference between the stresses in FLAC3D_7 and in 3DEC typically amounts to some 2 %, at most. In general, the agreement between FLAC3D_9 and 3DEC is even better, with misfits that typically amount to less than 1 % and with a maximum misfit of 1.2 %. The better agreement obtained when using FLAC3D_9 can be attributed to the fact that the zone-joint logic in FLAC3D_9 appears to work better along joint intersections than the interface logic in FLAC3D_7.

Figure 3-18 and Figure 3-19 show final joint shear displacements on joint plane 1000 and 4000, respectively. Evolution of joint shear displacements at these two joint planes is shown in Figure 3-21 and Figure 3-22. Shear displacement results for all ten joint planes are presented in Appendix 1. To facilitate comparison of the results, the colour scale plots are presented in Appendix 1 also with the colour scales set equal. About 85 % of the total joint area failed in shear and/or in tension. For several of the joints, the overall agreement in shear displacements between 3DEC and FLAC3D can be regarded acceptable, but locally, around joint intersections, there could be considerable deviations. Particularly, FLAC3D_7 may have problems with joint intersections. This is illustrated here by the joint 4000 results shown in Figure 3-19 where the overall agreement with 3DEC is fairly good, but at the intersection with joint 10000 (lower left in the contour plot), the shear displacement on one interface node becomes exaggerated in the FLAC3D_7 model. Also FLAC3D_9 shows some deviation from 3DEC, but close to the upper edge of the joint plane. Note the different colour scales in Figure 3-19. For comparison, the same results are shown in Figure 3-20, but with the same colour scale in all three plots.

The shear displacement misfit values (Figure 3-21, Figure 3-22 and Appendix 1) show that the overall agreement with 3DEC is significantly better for FLAC3D_9 than for FLAC3D_7. The largest misfit for FLAC3D_9 is found on joint 1000 with a peak at about 20 % after 500 years of heating (Figure 3-21, lower right). Besides that, the FLAC3D_9 misfit values amount to a few percent while FLAC3D_7 yields misfit values of the order of tens of percent at several instances.

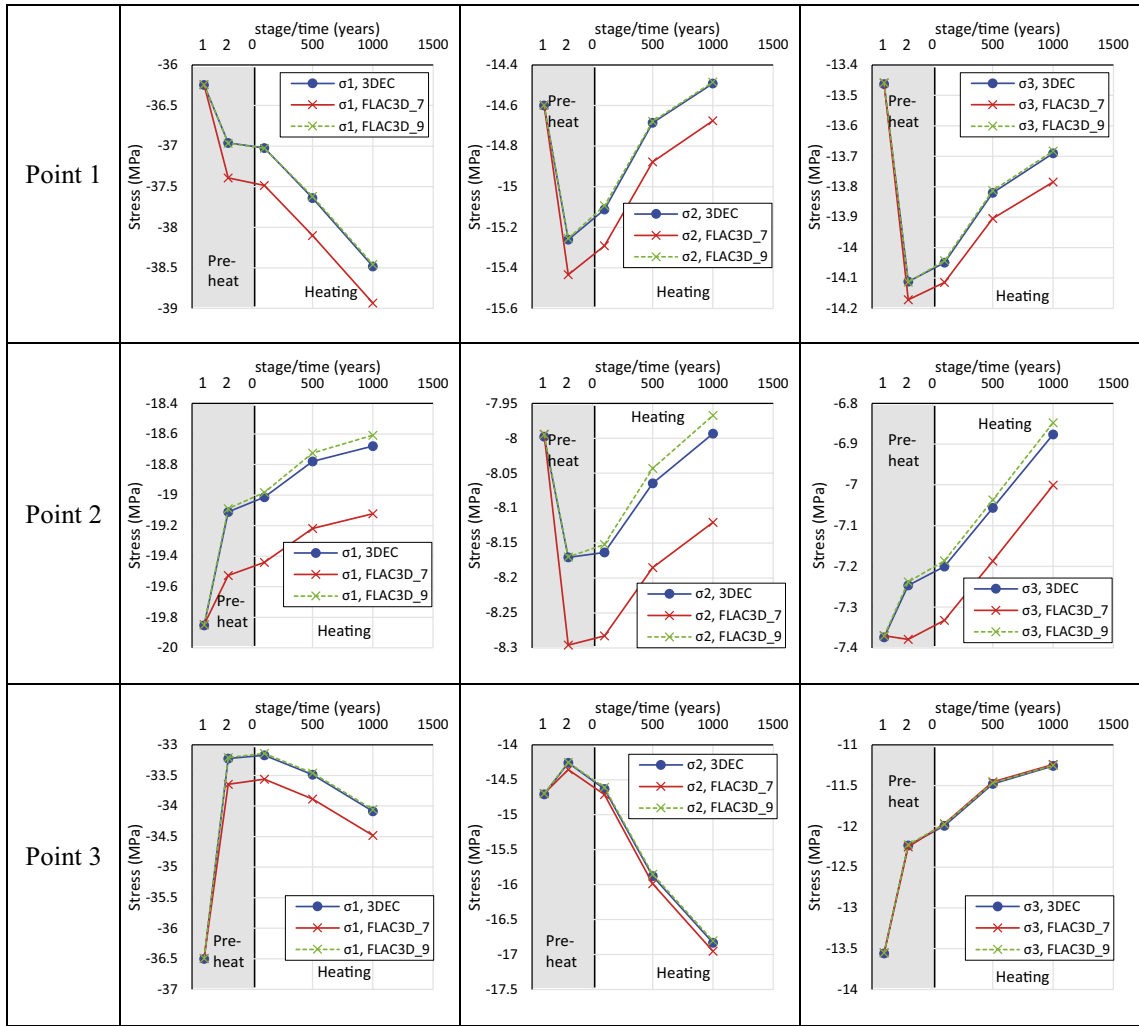


Figure 3-17. Evolution of principal stresses at monitoring points 1 to 3 in the Multiple joint case. Corresponding results for all eight monitoring points are presented in Appendix 1.

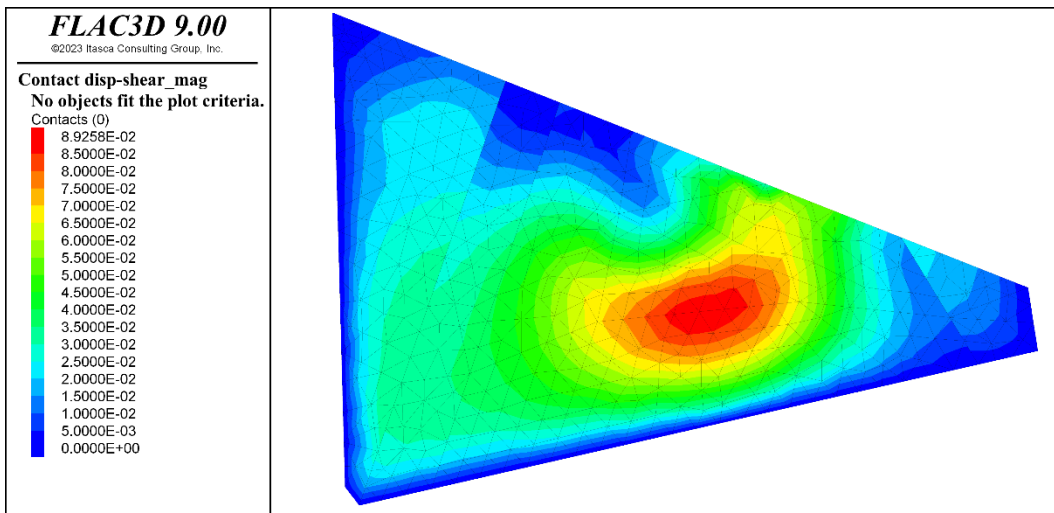
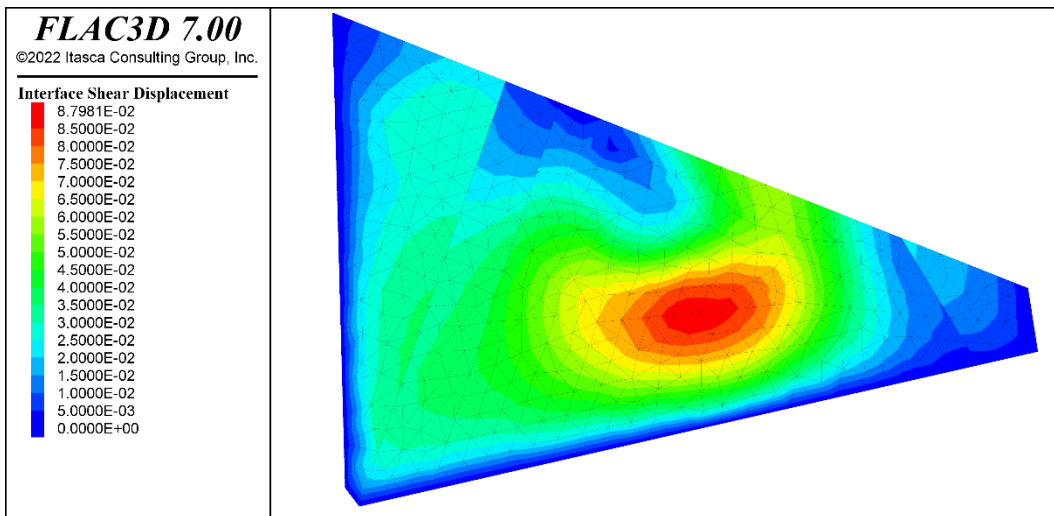
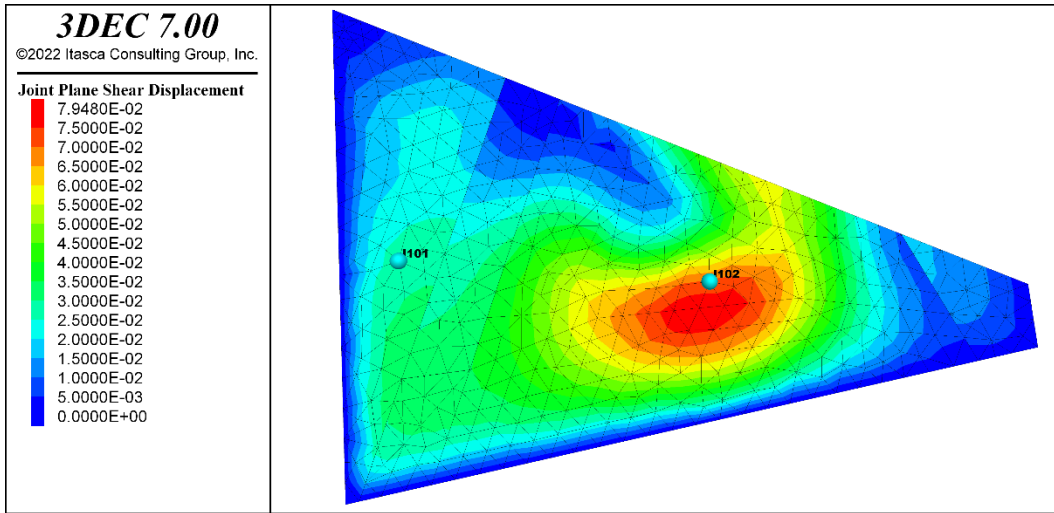


Figure 3-18. Shear displacements on joint 1000 in the Multiple_joint case after completed simulation. Corresponding results for all joints are presented in Appendix 1. Shear displacement evolution at the two points indicated in the upper plot is shown in Figure 3-21.

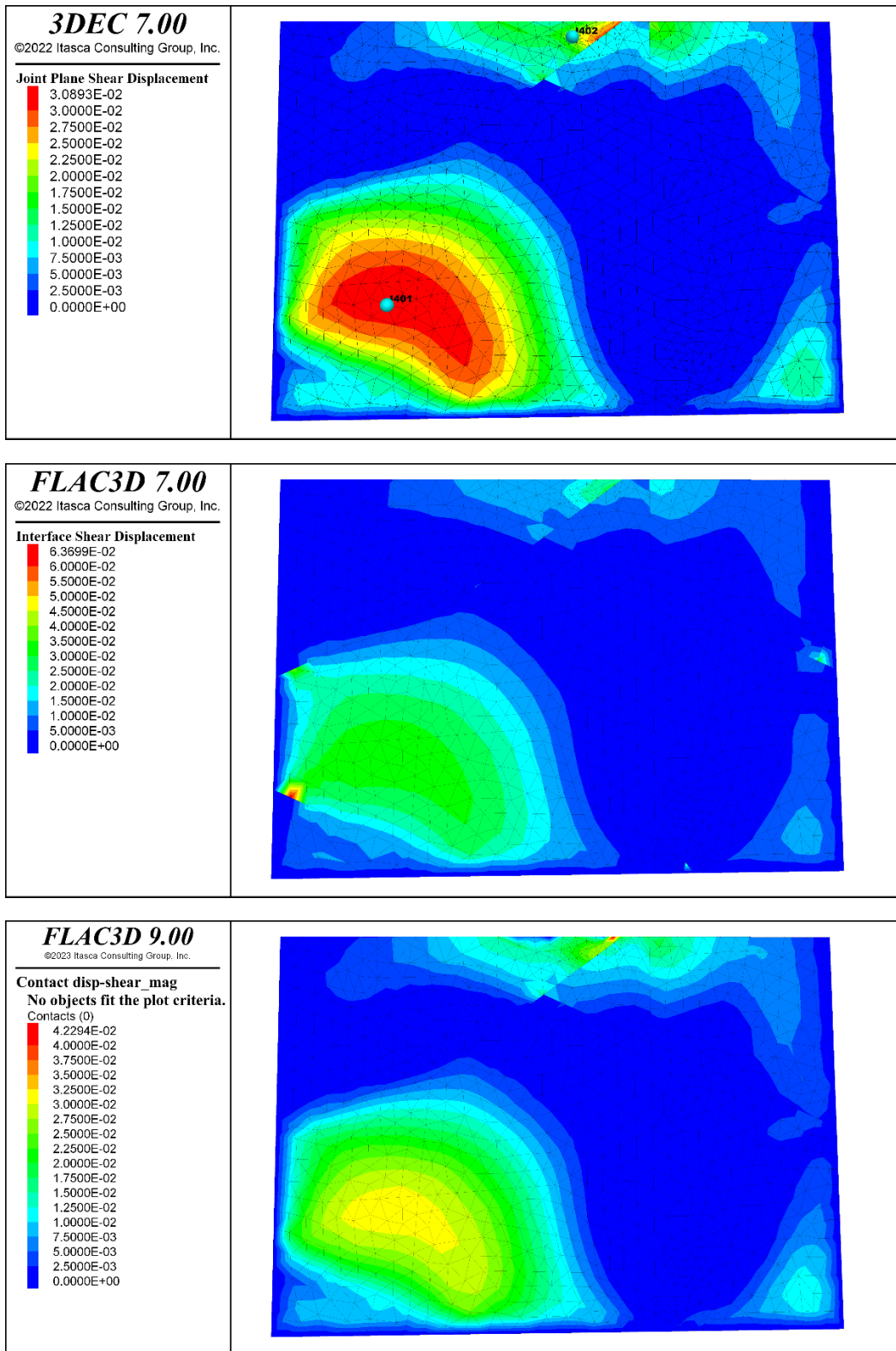


Figure 3-19. Shear displacements on joint 4000 in the Multiple_joint case. Corresponding results for all joints are presented in Appendix 1. Note the different colour scales in the plots. The same results are shown in Figure 3-20 but with the same colour scale as in the 3DEC plot. Shear displacement evolution at the two points indicated in the upper plot is shown in Figure 3-22.

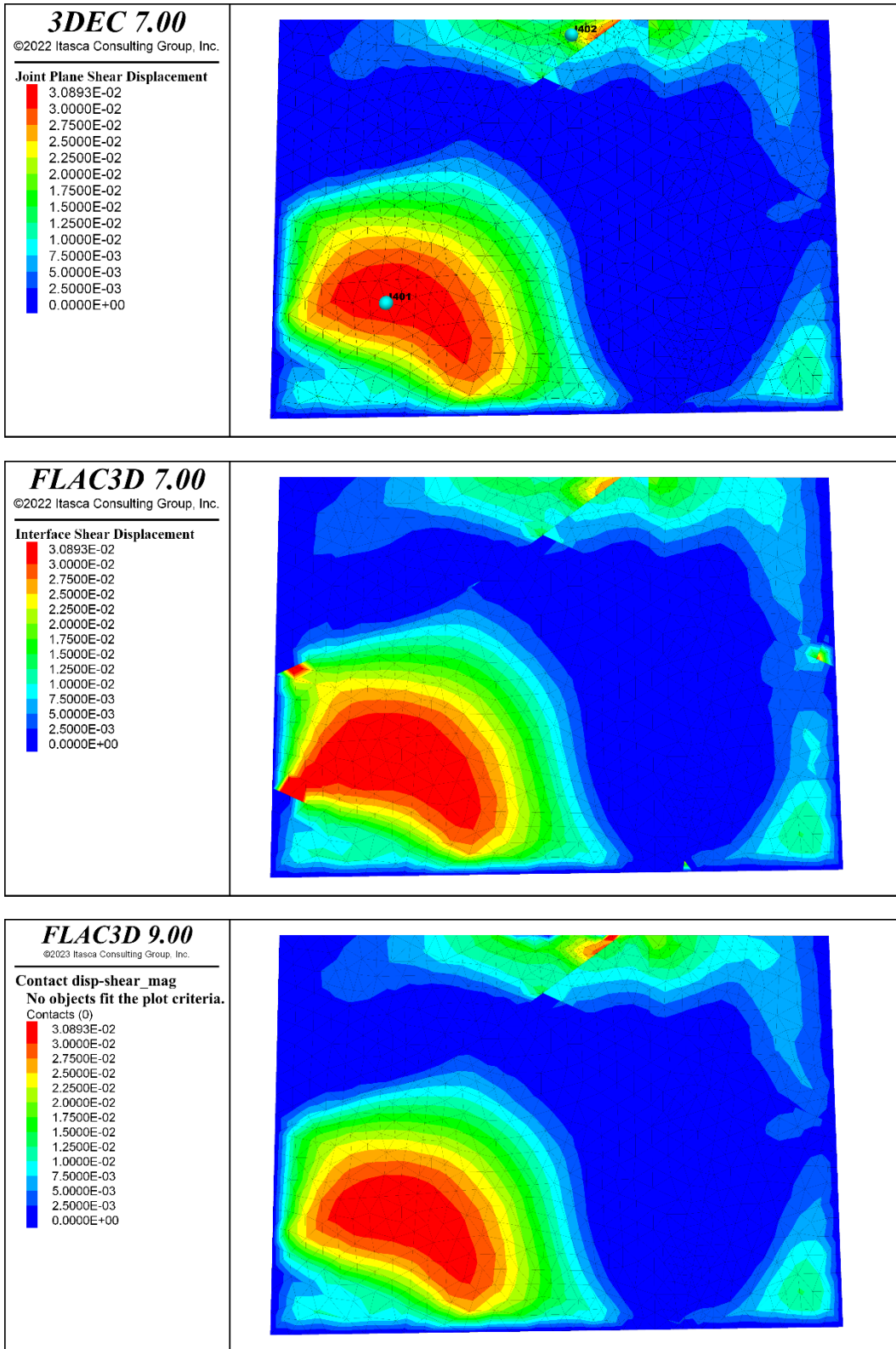


Figure 3-20. The same results as in Figure 3-19, but here the colour scales in the FLAC3D plots were set the same as in the 3DEC plot.

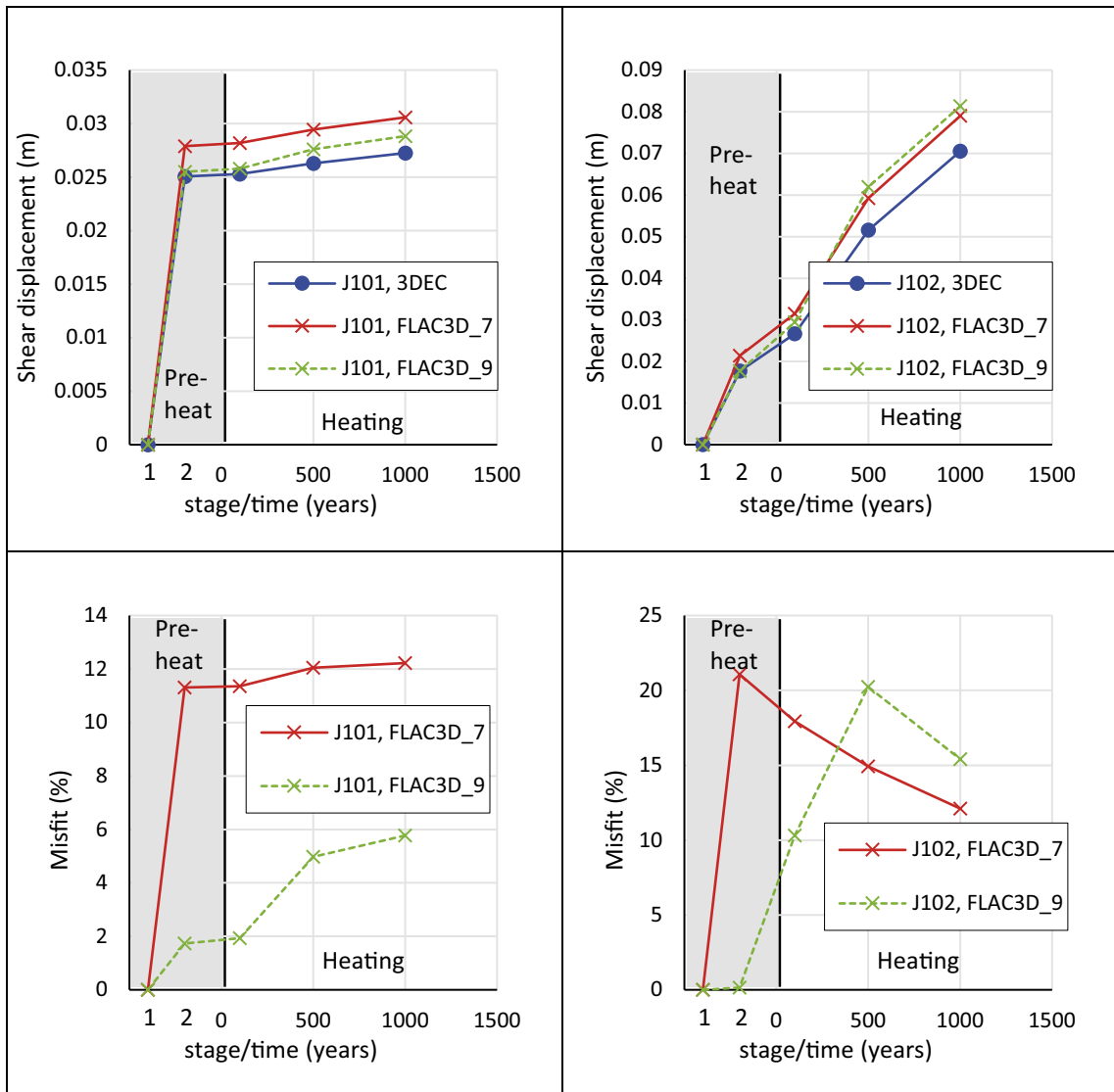


Figure 3-21. Upper: Evolution of joint 1000 shear displacement in the Multiple_joint case at the two points depicted in Figure 3-18, upper. Lower: Misfit between the FLAC3D results and the 3DEC results. Corresponding results for all joints are presented in Appendix 1.

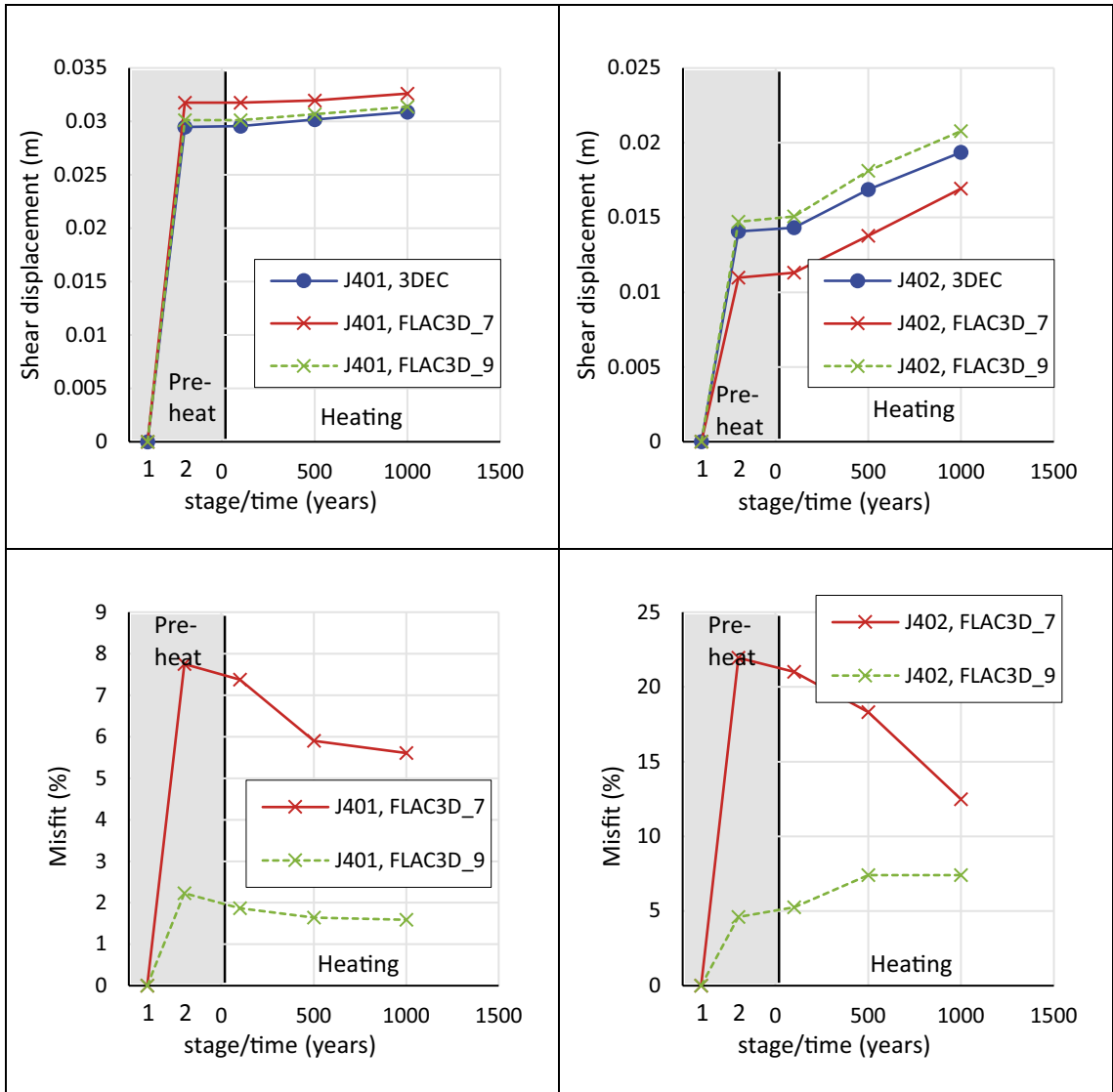


Figure 3-22. Upper: Evolution of joint 4000 shear displacement in the Multiple_joint case at the two points depicted in Figure 3-19, upper. Lower: Misfit between the FLAC3D results and the 3DEC results. Corresponding results for all joints are presented in Appendix 1.

4 Thermo-mechanical model with openings and fractures

4.1 Model geometry, properties and stresses

A model simulating a portion of a circular deposition tunnel with six deposition holes was constructed (Figure 4-1). The model (geometry, stresses and heat loads) is based on the model used in a previous thermo-mechanical simulation of the inner section of the Prototype Repository at the Äspö HRL (Fälth 2022b, Lönnqvist and Hökmark 2015). The tunnel segment is 63 m long, and its diameter is 5 m. The Prototype repository is divided in two sections, the inner and the outer section. The inner section includes four deposition holes and the outer section two holes. All deposition holes in the model were 8.1 m deep and had a radius of 0.875 m. Their positions are shown in Figure 4-1.

Four joint planes were included in the inner section, as shown in Figure 4-2. The joints were inserted in an inner volume that extended 40 m in the x -direction (along the tunnel axis), 20 m in the y -direction (perpendicular to the tunnel axis) and 22 m in the z -direction (vertical direction). The orientations of the planes are given in Table 4-1.

Here, the focus was on results from the inner section. Hence, the continuum representing the rock mass around the deposition holes in this part of the model was most densely discretised with the average edge length set to 0.25 m around the deposition holes. The model contained about 2.4 million zones.

Except for the joint friction, the material properties were the same as those in the model described in Section 2.1. To obtain a more significant and clear response of the joint planes, these were assigned a low friction angle of 15° .

As noted in Chapter 1, only FLAC3D_9 was benchmarked for this modelling case.

Table 4-1. Joint plane orientations.

| Joint ID | dip | dip-direction* |
|----------|-----|----------------|
| 1046 | 29 | 305 |
| 1061 | 68 | 270 |
| 3075 | 44 | 117 |
| 4019 | 55 | 210 |

*With respect to positive y -axis.

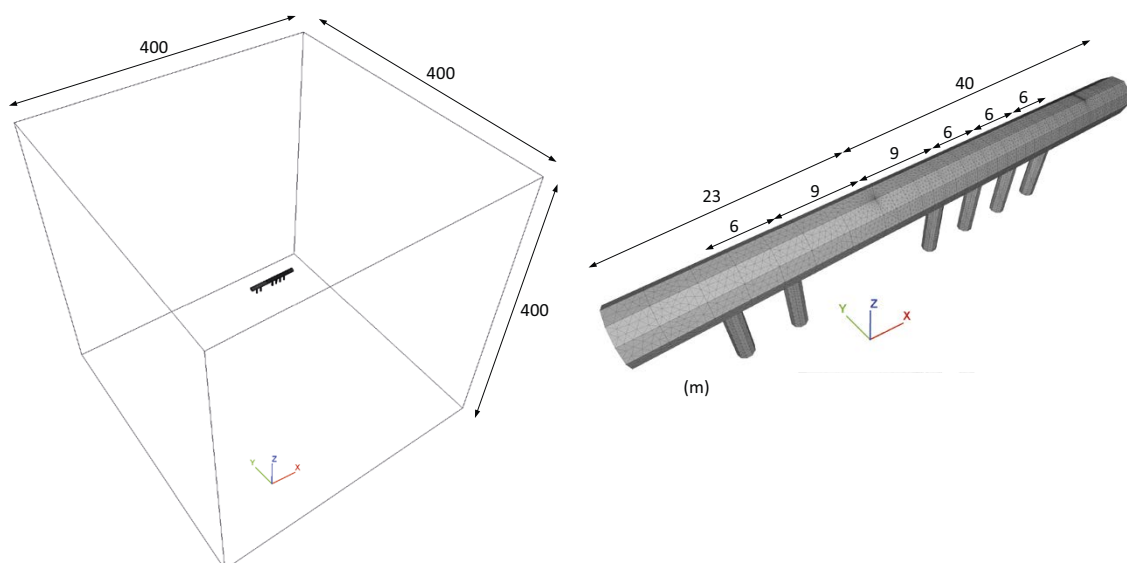


Figure 4-1. Model geometry.

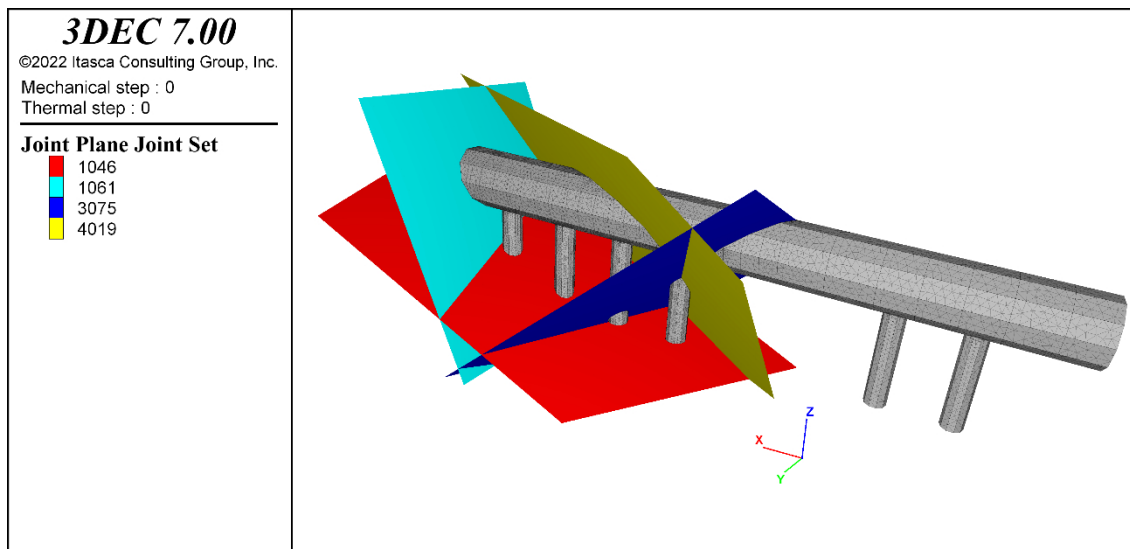


Figure 4-2. Four joint planes were included in the model. The joints intersected the inner section.

The initial stress field is reported in Table 4-2 in terms of the total principal stresses. The stress field was assumed to be homogeneous, and no effects of gravity were considered. The stress field was of reverse-type with the vertical component $\sigma_v = \sigma_x = \sigma_z$. Porewater pressure was applied on all joint planes. The pressure was set homogeneously at 4.5 MPa in the undisturbed rock. After excavation, it was set to taper off linearly over a distance of 2 m around the openings such that it was zero at the opening walls.

Table 4-2. Initial total principal stresses.

| Component | Value | Trend* |
|------------------|-------|--------|
| σ_H (MPa) | 28 | 128 |
| σ_h (MPa) | 14 | 38 |
| σ_v (MPa) | 12.8 | - |

*With respect to y-axis.

The vertical boundaries were locked for displacements in the x -, y - and z -directions while the horizontal boundaries (i.e. the boundaries with their normal parallel with the z -axis) were locked in the z -direction.

In the Prototype Experiment, copper canisters were installed in the deposition holes. The canisters were equipped with electrical heaters that simulate the heat generated by the spent nuclear fuel. In the model, the effect of these heaters was simulated by use of thermal line sources and the analytical thermal logic. A more detailed description of the thermal source model is given in Fälth (2022b) and in Lönnqvist & Hökmark (2015).

Two cases were considered:

- Elastic continuum. The joint planes were joined (using the join command) and hence made mechanically inactive. Hence, no joint planes were exported to the FLAC3D geometry.
- With fractures. All four joint planes were mechanically active.

4.2 Calculation sequence

The simulation was carried out in four steps:

1. The initial stress field according to Table 4-2 was applied along with the undisturbed pore pressure (see Section 4.1). Initial equilibrium was established.
2. The tunnel was excavated and the pore pressure was adjusted accordingly (see Section 4.1).
3. The deposition holes were excavated and the pore pressure was adjusted accordingly (see Section 4.1).
4. The heat load was applied. The thermo-mechanical response was calculated at 15 time instances: after 21, 123, 207, 291, 345, 378, 480, 555, 580, 645, 695, 1 085, 1 171, 1 450 and 1 538 days of heating. The heating scheme was based on the previous thermo-mechanical simulation of the Prototype Repository (Fälth 2022b).

To inhibit slip overshoot on the joint planes (in the case with fractures) after a load alteration, these were assigned a high cohesive strength, which then was ramped down to zero in a stepwise manner. The model was run to equilibrium after each strength reduction step. This procedure was applied after every load alteration, i.e., after the initial stress application, after each excavation step, and after each of the 15 heat load steps). Results were saved after calculation step 1, 2 and 3, and after each heat load step.

4.3 Results

4.3.1 Simulation times

The simulation times were measured (Table 4-3). It is not straight forward to find the optimal parameter values to be used to determine that static equilibrium is reached after each joint strength reduction step (see Section 4.2). To ensure a robust comparison of the results, convergence parameters that can be regarded to be strict were used. In the elastic case, static equilibrium was assumed to have been achieved when the model solve ratio was below 3×10^{-7} . In the case with fractures, it was assumed that static equilibrium was achieved when the largest joint shear velocity in the model was lower than a velocity that would give 0.015 mm shear displacement over 1 000 timesteps. Hence, the simulation times presented in Table 4-3 may not be the shortest possible.

As for the modelling cases presented earlier in this report, it can be concluded that FLAC3D_9 is considerably faster than 3DEC. The FLAC3D_9 simulation times are about 1/18 to 1/10 of the 3DEC times for the present modelling case and with the convergence parameters adopted here. Beside the faster model cycling in FLAC3D_9, it is also noted that FLAC3D_9 appears to reach equilibrium faster than 3DEC does, i.e., less number of cycles are needed (Table 4-3). Furthermore, the analytical thermal logic is multithreaded in FLAC3D_9 and hence much faster than the single-thread logic in 3DEC. No separate measurement of the difference in the thermal calculation speed was performed, though.

Table 4-3. Simulation times and number of cycles to complete simulation.

| Case | 3DEC | | FLAC3D_9 | |
|----------------|----------|--------|----------|--------|
| | Time (h) | Cycles | Time (h) | Cycles |
| Elastic | 3.0 | 28 500 | 0.29 | 6 507 |
| With fractures | 21 | 93 295 | 1.2 | 43 451 |

4.3.2 Temperatures

No temperature results are presented here. As expected, no differences in the temperatures were observed. The agreement in the temperatures calculated in 3DEC and FLAC3D_9 is verified by the results presented in Chapter 3.

4.3.3 Stresses and shear displacements

Major and minor principal stresses in the rock mass around the deposition holes in the inner section are shown in Figure 4-3 and Figure 4-4, respectively. These plots were generated in the model case with fractures. The figures show that the stresses agree well in 3DEC and FLAC3D_9. In particular, the results in Figure 4-3 show many similarities between the results from the two programs. The similarities in the results are not equally evident from the comparison of the minor principal stresses in Figure 4-4. This is mainly because there are a few zones in which the stresses deviate, which causes the colour scales to differ more. By adjusting the colour scales in the FLAC3D_9 plots (Figure 4-5), the similarities in the minor principal stress fields appear more clearly.

The stress results were also compared in more detail by calculating the relative difference in the major principal stress for all zones in the model. The relative differences were calculated the same way as for the temperatures in Section 3.6.1. Figure 4-6 (upper) shows all zones (in the model case with fractures) where the relative difference exceeded 5 % after completed simulation. These zones, which represent a small fraction of the inner model volume (Figure 4-6, lower), are located along the joint planes and mainly around the intersections between the joint planes and the excavations. In the elastic model case, the relative difference in major principal stress was below 5 % in all zones.

The stresses in the deposition hole walls shown in Figure 4-7 and Figure 4-8 are the average values from zones within a sphere with a radius of 0.2 m. The 3DEC results and the FLAC3D_9 results were practically identical. There was a minor deviation at 5 m depth in hole 1 in the case with fractures. Obviously, this is related to the short distance between the monitoring point and joint plane 1061, as indicated in Figure 4-3 and Figure 4-4.

At the end of the simulation, about 88 % of the total joint plane area had failed, i.e., undergone plastic deformation. Joint shear displacements are presented in Figure 4-9 to Figure 4-12. Corresponding colour scale plots are presented in Appendix 2, but with identical colour scales in the 3DEC and FLAC3D plots. As for the stress results, the agreement in shear displacements is satisfactory with differences between 3DEC and FLAC3D_9 of the order of 1 %.

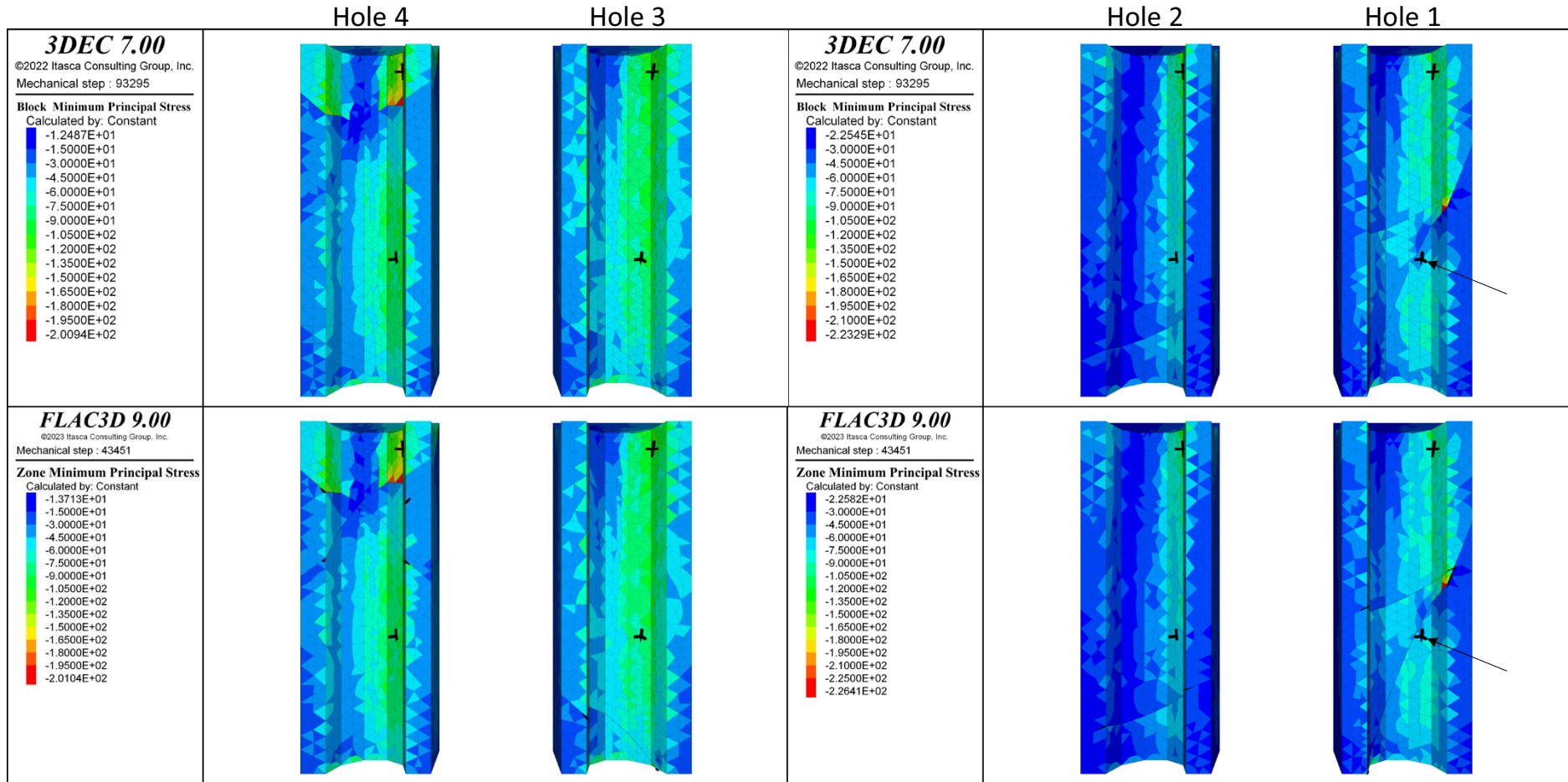


Figure 4-3. Major principal stress in the deposition hole walls in the inner section in the case with fractures (Note that compressive stresses are negative. Hence, “minimum principal stress” in figure legends). The results were captured after completed simulation. The black crosses indicate locations for monitoring of stress evolution (see Figure 4-7 and Figure 4-8). The arrows in the right plots indicate a monitoring point close to a joint plane. Note that only one half of the hole wall is visible in the plots.

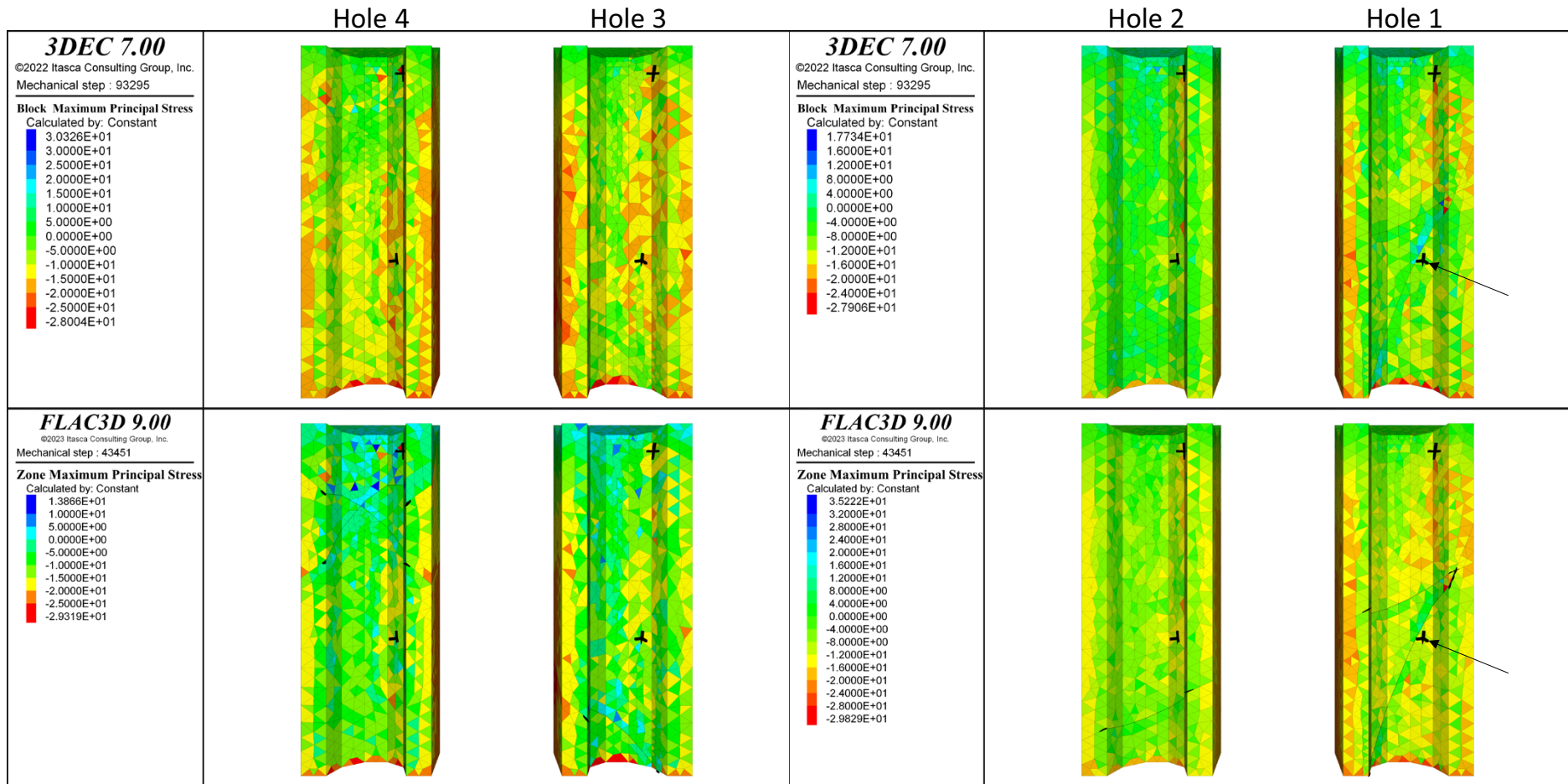


Figure 4-4. Minor principal stress in the deposition hole walls in the inner section in the case with fractures (Note that compressive stresses are negative. Hence, “maximum principal stress” in figure legends). The results were captured after completed simulation. The black crosses indicate locations for monitoring of stress evolution (see Figure 4-7 and Figure 4-8). The arrows in the right plots indicate a monitoring point close to a joint plane. Note that only one half of the hole wall is visible in the plots.

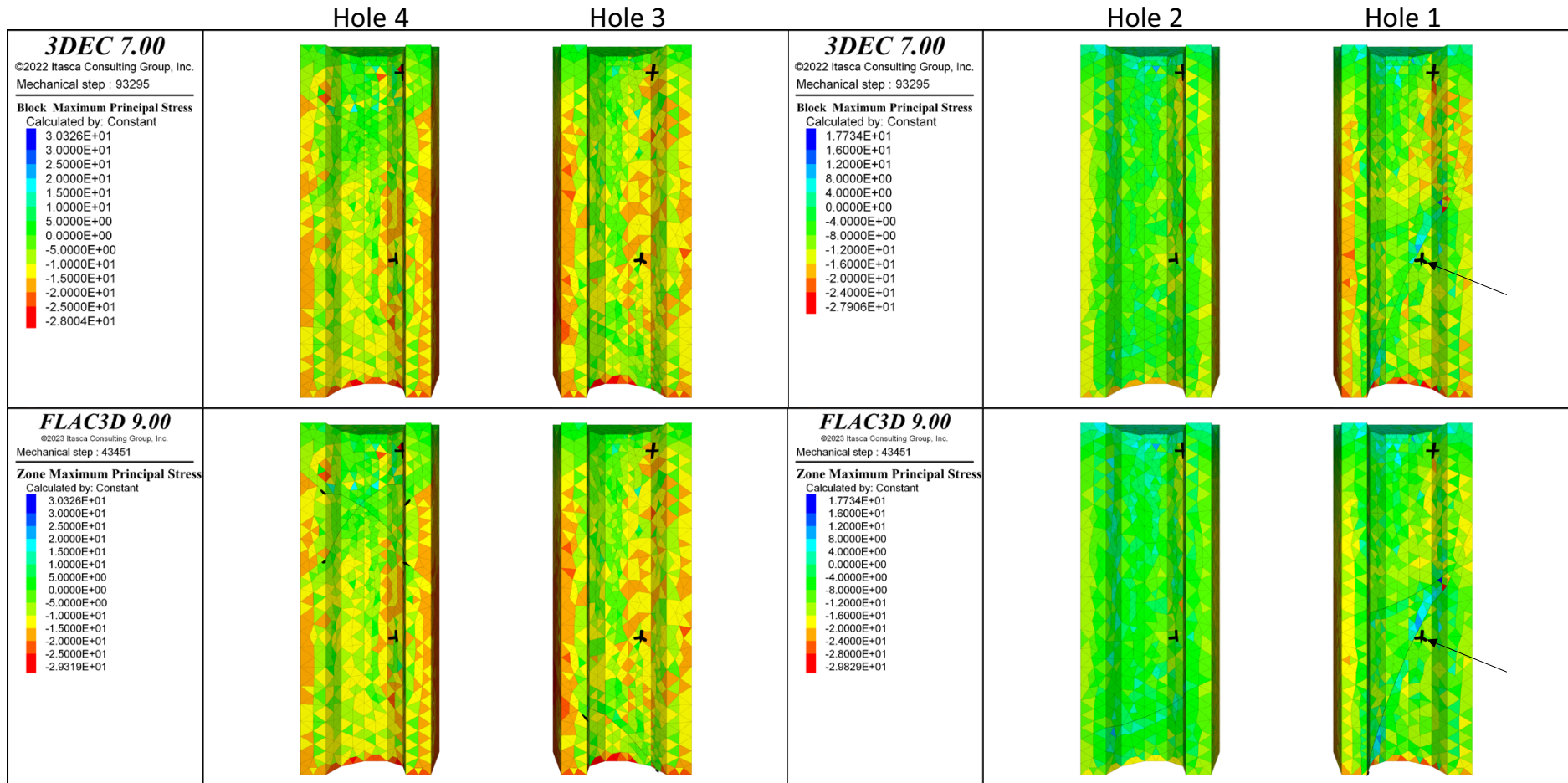


Figure 4-5. Minor principal stress in the deposition hole walls in the inner section in the case with fractures (Note that compressive stresses are negative. Hence, “maximum principal stress” in figure legends). The same results as shown in Figure 4-4 but with adjusted upper limits of the colour scales in the `FLAC3D_9` plots. The black crosses indicate locations for monitoring of stress evolution (see Figure 4-7 and Figure 4-8). The arrows in the right plots indicate a monitoring point close to a joint plane. Note that only one half of the hole wall is visible in the plots.

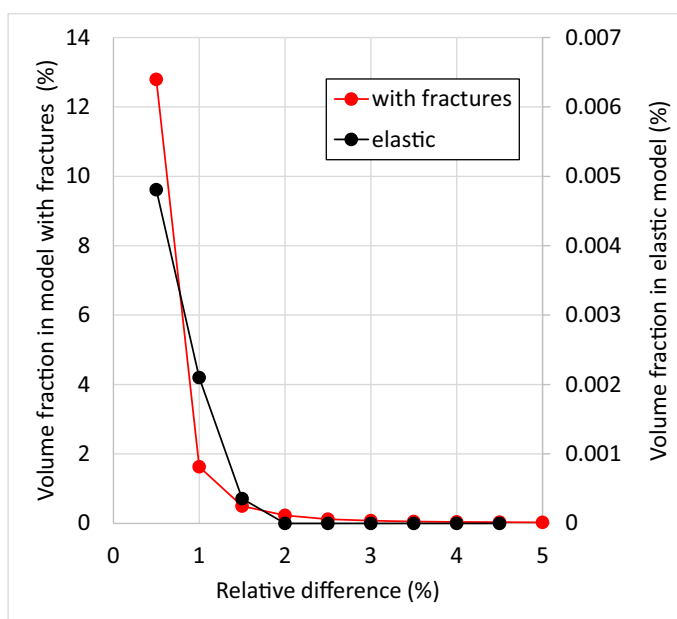
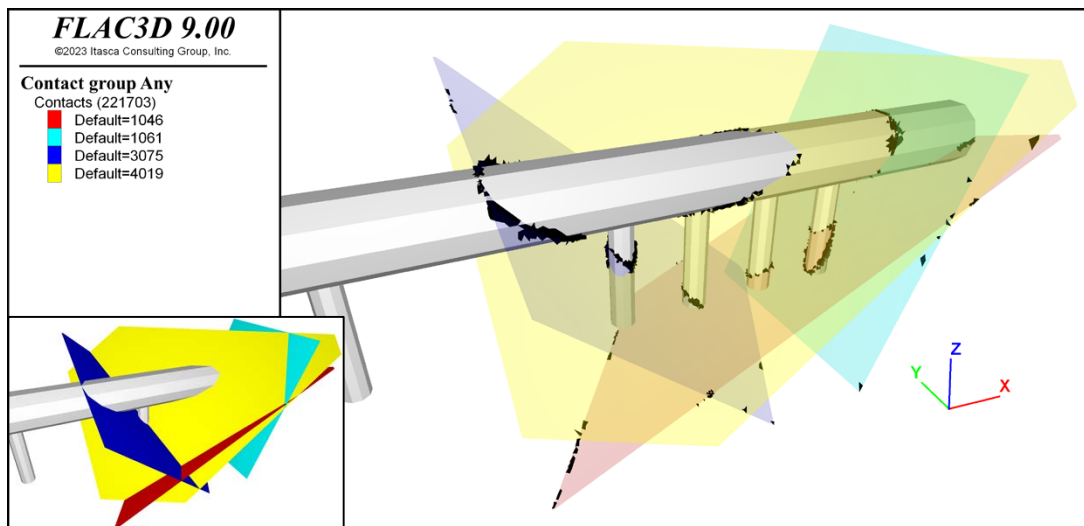


Figure 4-6. Upper: Zones with relative difference in the major principal stress above 5 % shown in black (modelling case with fractures). These zones are found along the joint planes, and mainly around the intersections with the openings. The results were captured at the end of the simulation. The joint planes are made transparent for illustrative purposes. The lower left inset is added to help the identification of the joints (cf. Figure 4-2). Lower: Model volume fraction in which the relative difference in major principal stress exceeds a given value. The reference volume used here is $40 \times 20 \times 22 \text{ m}^3$, which corresponds to the inner volume containing the four joint planes (cf. Section 4.1).

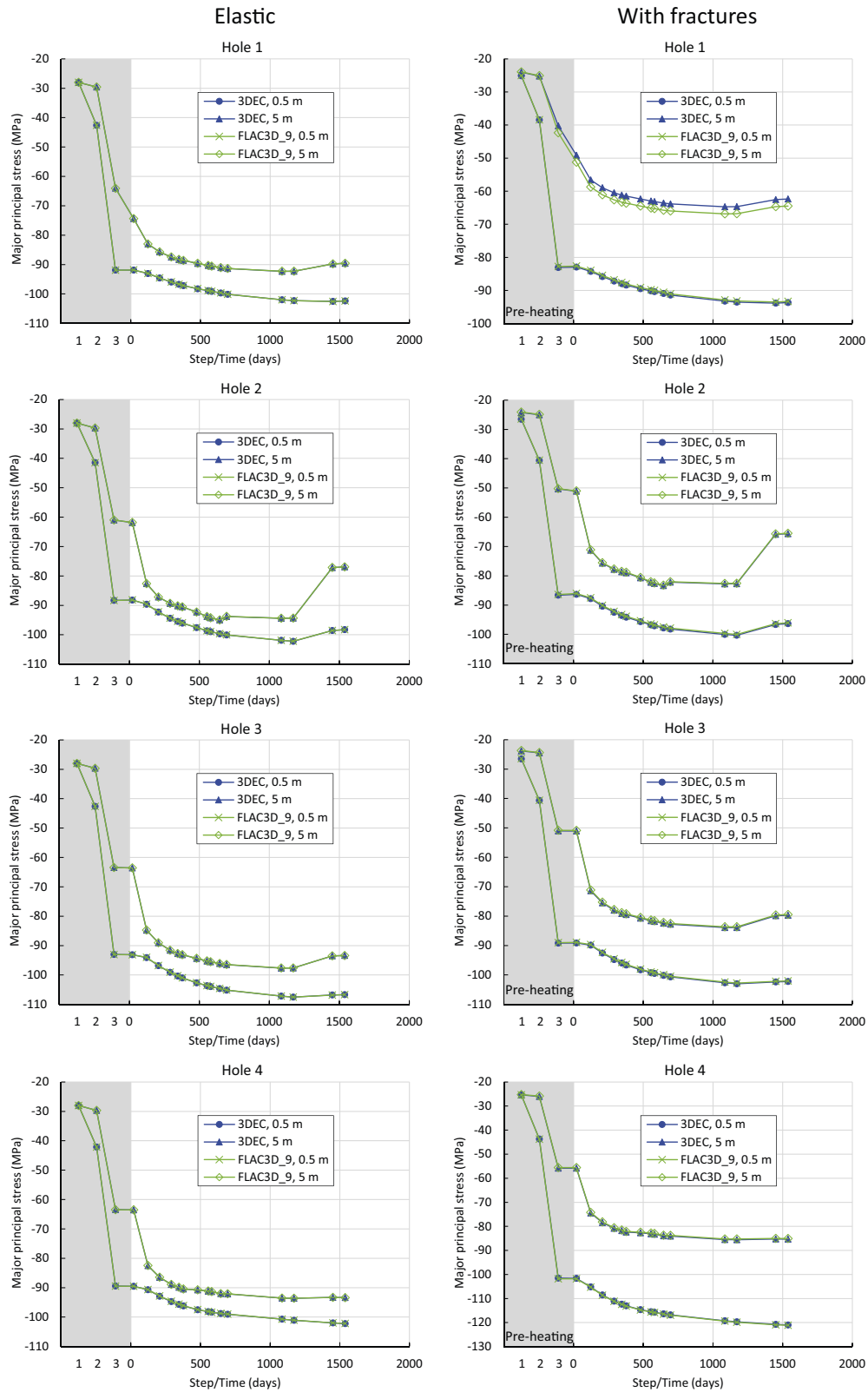


Figure 4-7. Evolution of major principal stress in the deposition hole walls in the inner section (at two depths below the tunnel floor; see Figure 4-3) (Note that compressive stresses are negative). Step #1, #2 and #3 correspond to the three first simulation steps (cf. Section 4.2). Left: Elastic continuum case. Right: Case with fractures.

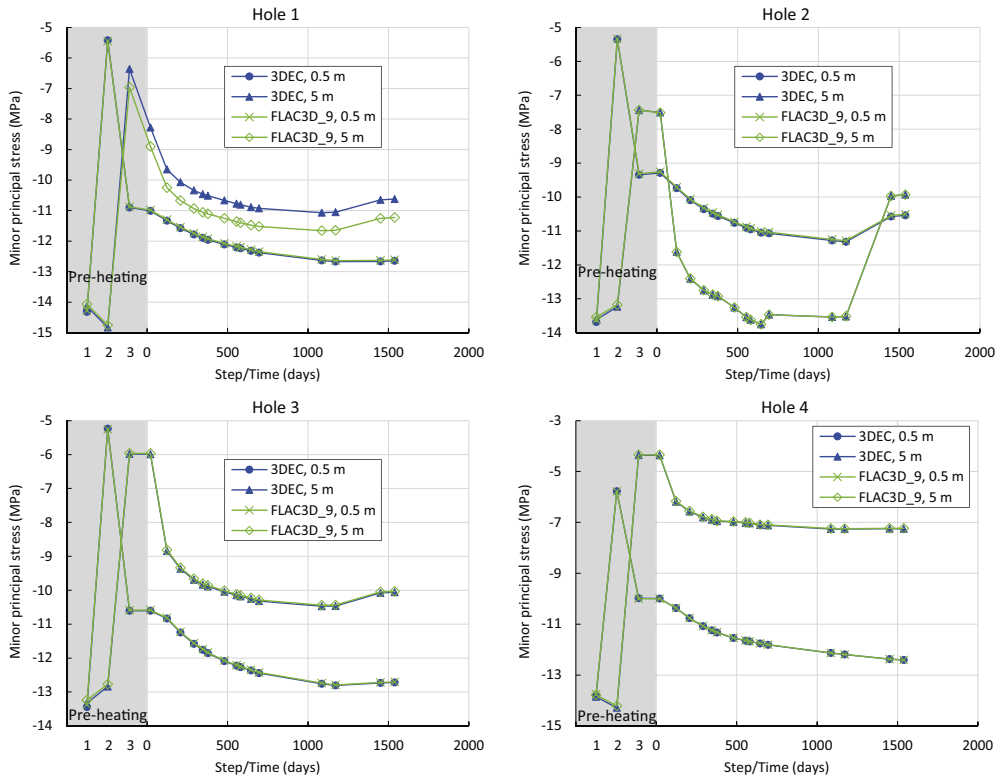


Figure 4-8. Evolution of minor principal stress in the deposition hole walls in the inner section (at two depths below the tunnel floor; see Figure 4-3) in the case with fractures (Note that compressive stresses are negative). Step #1, #2 and #3 correspond to the three first simulation steps (cf. Section 4.2).

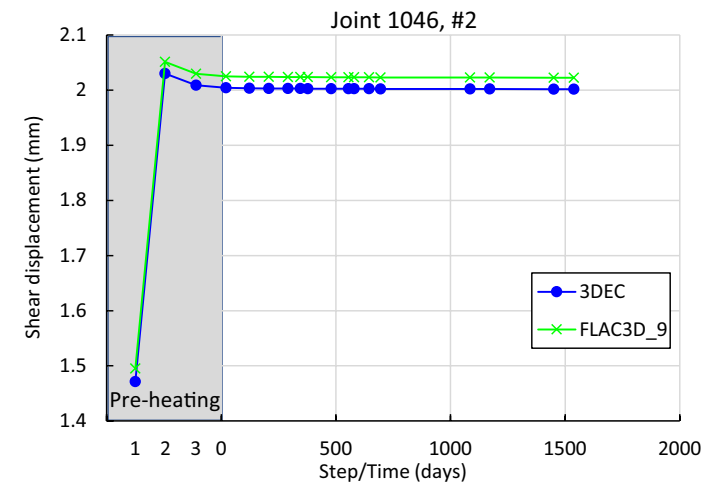
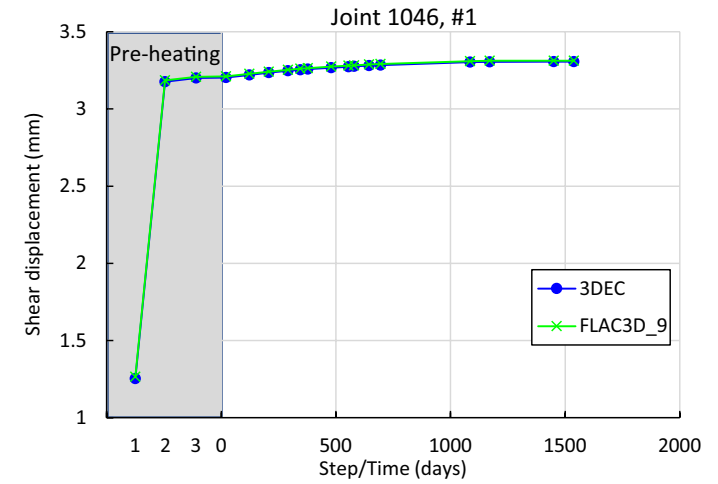
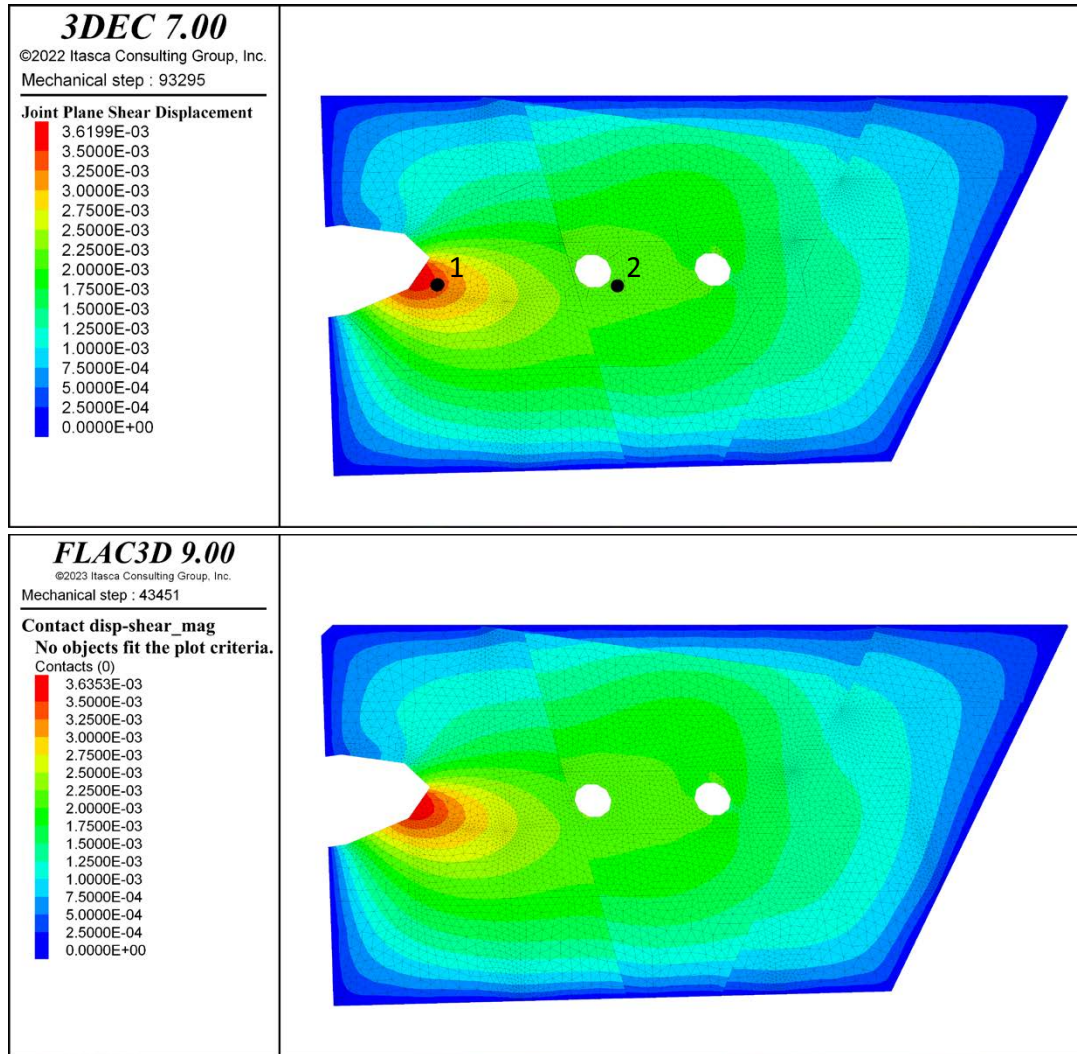


Figure 4-9. Left: Colour scale plots of shear displacement on joint 1046 after completed simulation. Right: Evolution of shear displacement at the two points depicted in the upper colour scale plot. Step #1, #2 and #3 correspond to the three first simulation steps (cf. Section 4.2).

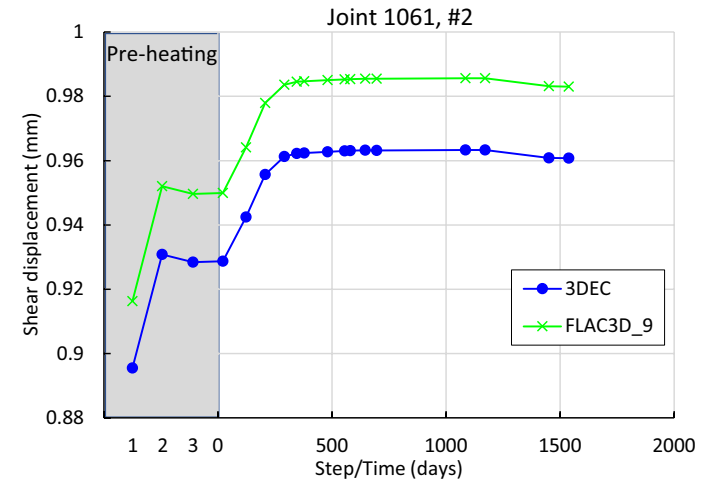
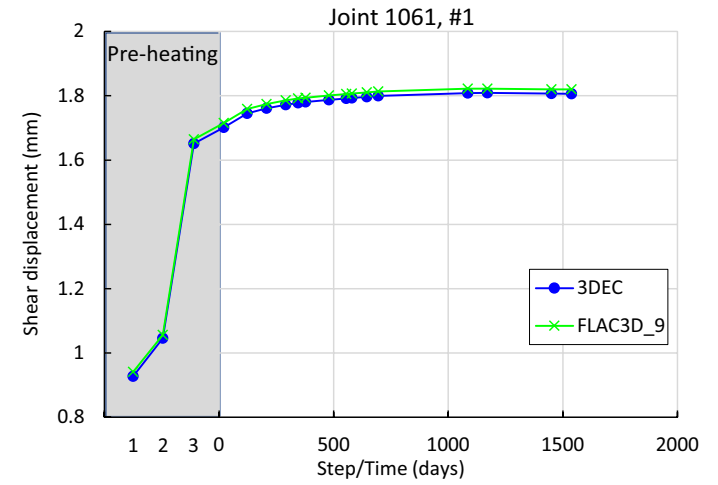
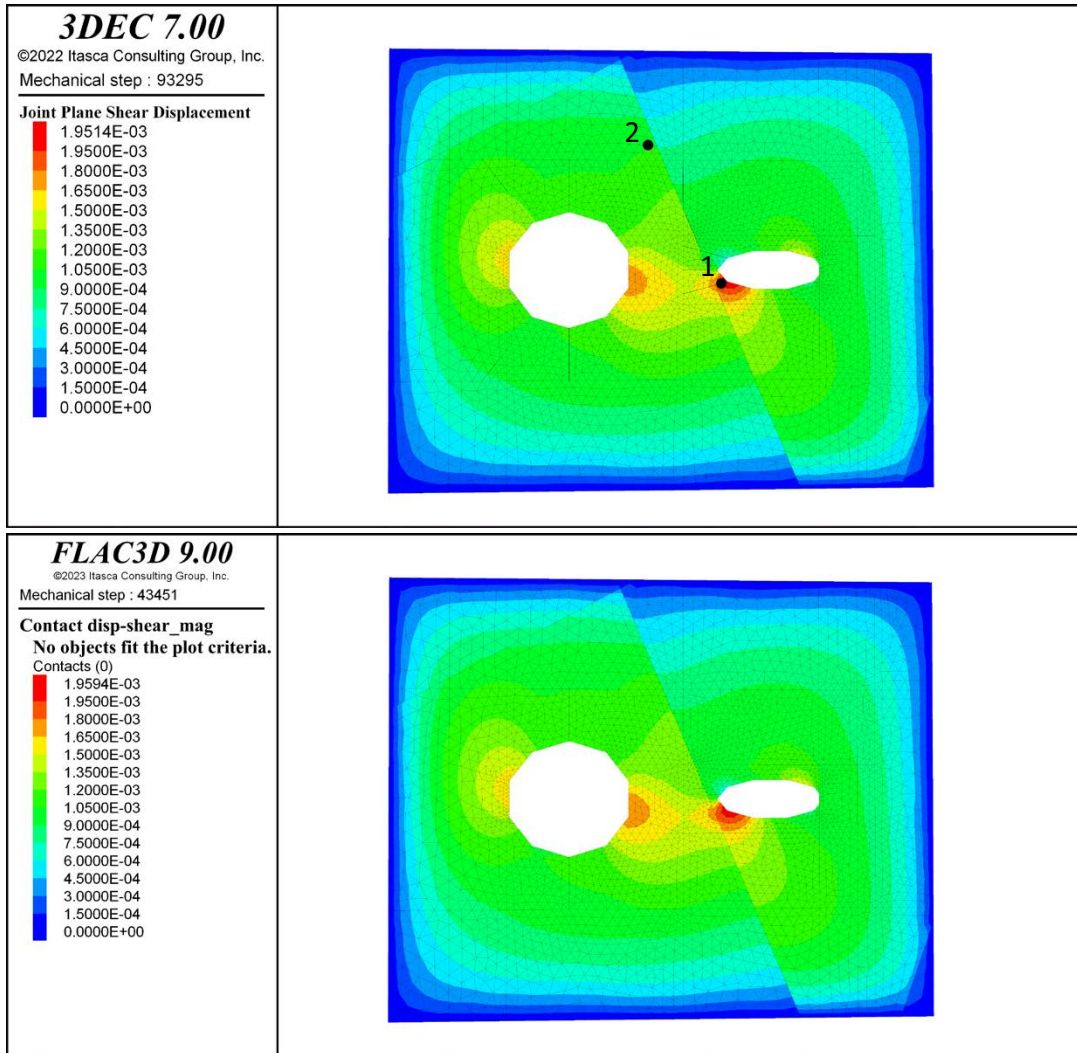


Figure 4-10. Left: Colour scale plots of shear displacement on joint 1061 after completed simulation. Right: Evolution of shear displacement at the two points depicted in the upper colour scale plot. Step #1, #2 and #3 correspond to the three first simulation steps (cf. Section 4.2).

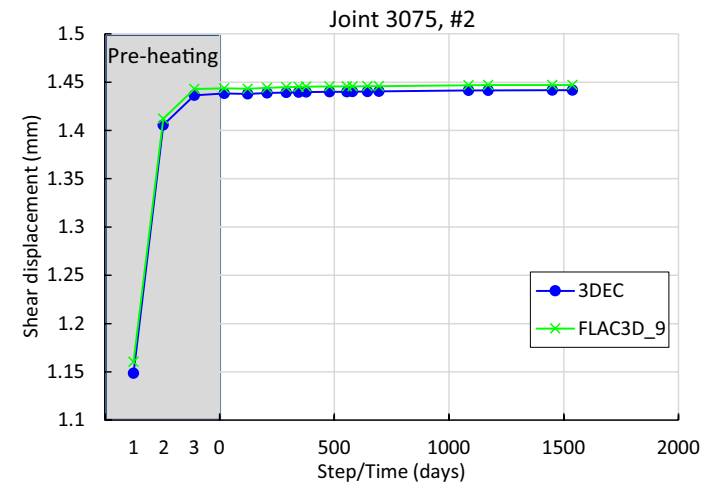
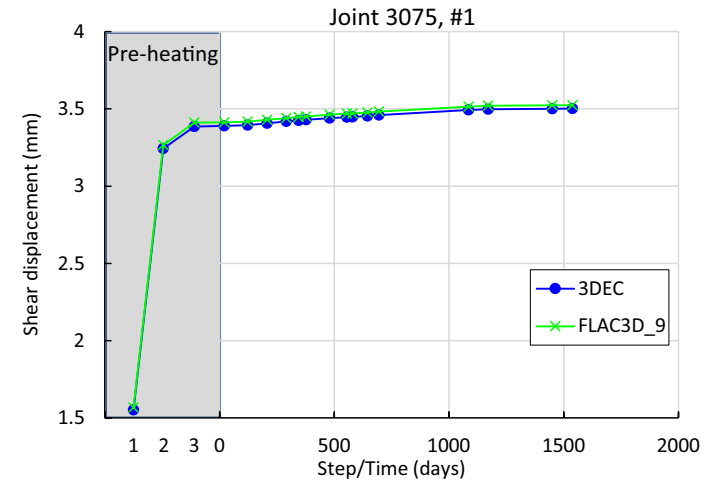
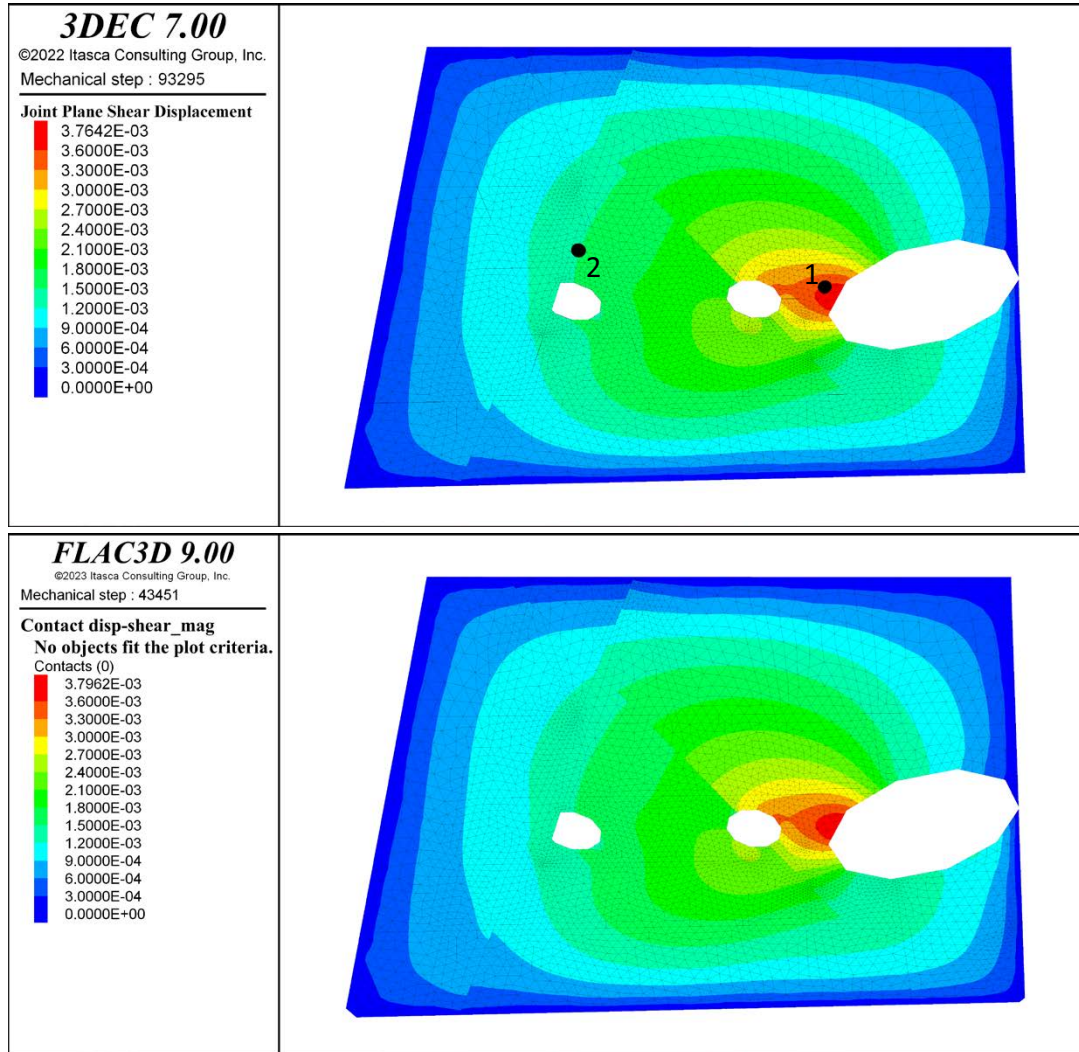


Figure 4-11. Left: Colour scale plots of shear displacement on joint 3075 after completed simulation. Right: Evolution of shear displacement at the two points depicted in the upper colour scale plot. Step #1, #2 and #3 correspond to the three first simulation steps (cf. Section 4.2).

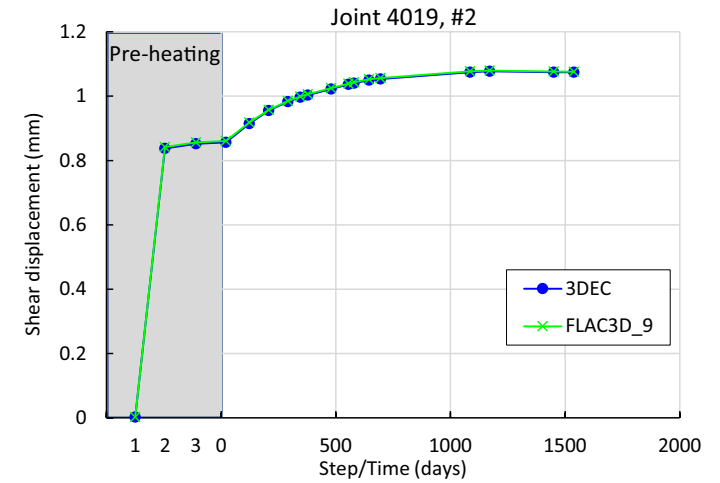
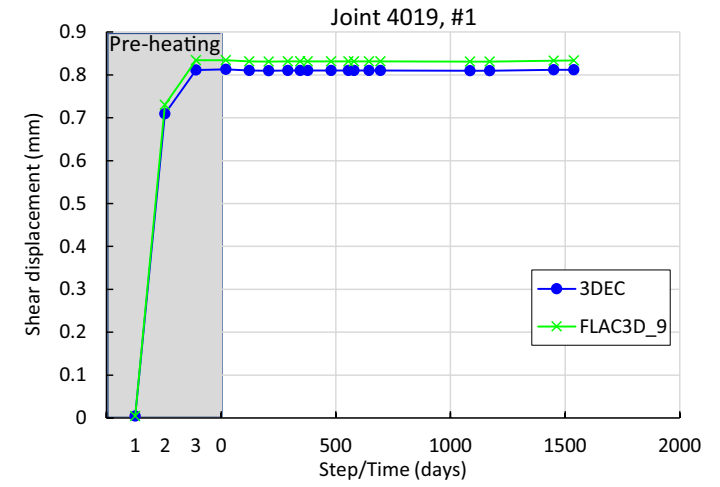
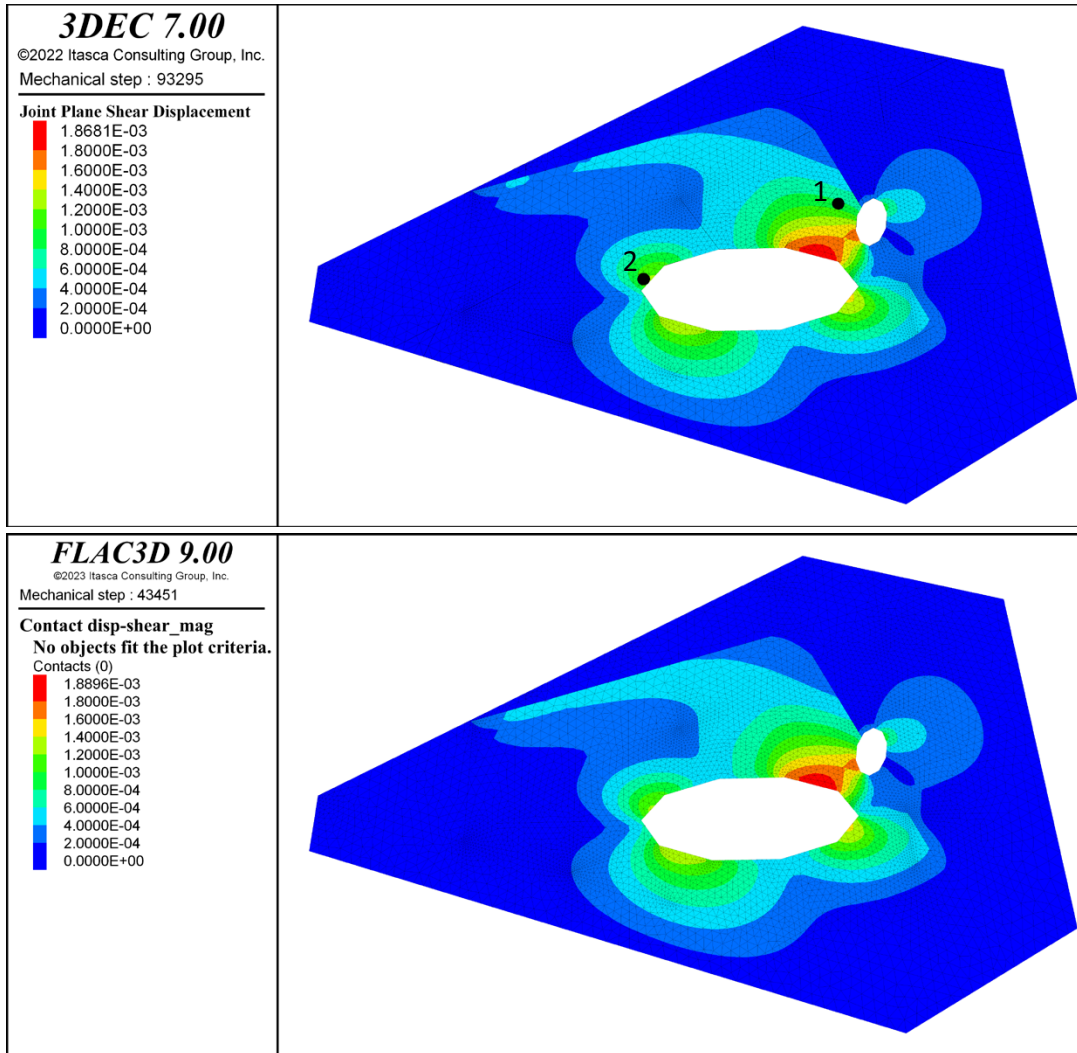


Figure 4-12. Left: Colour scale plots of shear displacement on joint 4019 after completed simulation. Right: Evolution of shear displacement at the two points depicted in the upper colour scale plot. Step #1, #2 and #3 correspond to the three first simulation steps (cf. Section 4.2).

5 Forsmark earthquake model

5.1 Model geometry

A case with a dynamic earthquake fault rupture was examined. The model geometry (Figure 5-1) was based on the geometry used in a numerical study of seismically induced secondary fracture displacements at Forsmark (Fälth 2022a).

An earthquake rupture was initiated on a joint plane representing the gently dipping Forsmark deformation zone ZFMA2. This is the green plane in Figure 5-1. The plane had dip 24° and dip direction 170° with respect to the y -axis and breaches the upper model boundary, which represents the ground surface. The surface trace length of ZFMA2 was about 4 km and its area was about 12 km^2 . The rupture initiation point was at about 900 m depth. In the footwall of ZFMA2, 53 smaller joint planes were included. On these, circular fractures (target fractures), all with 150 m diameter, were formed by assigning properties within circular regions. The target fractures had dip/dip direction $27^\circ/261^\circ$ and were located with their centres at 470 m depth. The fractures were positioned in a grid ($1.4 \times 1.5 \text{ km}$) with a centre-to-centre distance of about 200 m. The shortest target fracture centre-to-ZFMA2 distance was 280 m. The shortest target fracture centre-to-hypocentre distance was 2.7 km.

The volume around the target fractures was discretised such that there were about 9 zone edge lengths per fracture diameter. The model contained about 10 million zones.

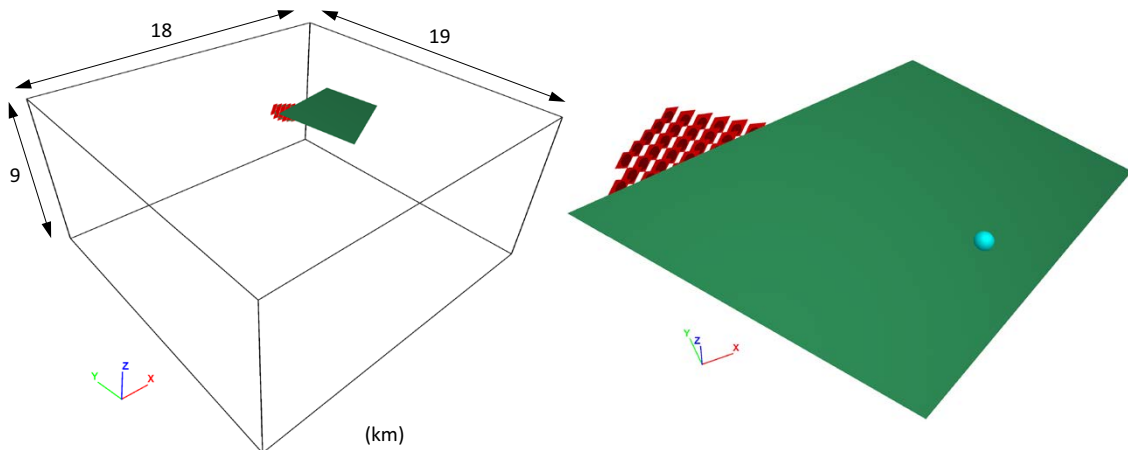


Figure 5-1. Model geometry. Left: The ZFMA2 plane (green) and the target fracture planes (red) were located centrally in the model volume. Right: Close-up of the joint planes. The turquoise dot indicates the hypocentre (centre of the nucleation region).

5.2 Initial stresses

The stress field was the sum of a background stress field based on Forsmark data and endglacial stress additions obtained from a Glacial Isostatic Adjustment (GIA) simulation of the Weichselian glacial cycle (cf. e.g. Fäth et al. 2016).

Pore pressure was applied on all joint planes. The pressure, which was constant throughout the entire simulation, i.e., time-independent, was hydrostatic with an addition of excess pressure P_e , which was set according to

$$P_e = \begin{cases} -\frac{1}{0.15}z & -0.15 \leq z < 0 \\ 1 & z < -0.15 \end{cases} \text{ MPa}, \quad (5-1)$$

where z is depth in kilometres, i.e., the excess pore pressure was set to be zero at the ground surface and then to increase linearly down to 150 m. Below 150 m depth, it was 1 MPa. The gravitational acceleration was set to 9.82 m/s^2 in the negative z -direction.

5.3 Material properties and rupture initiation

The material property parameter values are presented in Table 5-1 and are in general agreement with the values applied in a previous study (Fäth 2022a). The rock mass was assumed to be homogeneous, isotropic and continuous. The ZFMA2 deformation zone as well as the target fractures were assumed to respond to loads according to the idealized elasto-plastic material model described in Section 2.1 (Figure 2-2). The coefficient of friction on ZFMA2 during the quasi-static calculation step (cf. Section 5.4) was the same as that assigned to the target fractures. However, to obtain a well-defined and stable earthquake rupture process, a higher value was set for the static friction coefficient μ_s during the following dynamic calculation step (Table 5-1). No dynamic damping was applied in the models.

Table 5-1. Material property parameter values.

| Component | Parameter | Value | Comment |
|------------------|--|-------|---------------------------|
| Rock mass | Young's modulus, E (GPa) | 70 | |
| | Poisson's ratio, ν (-) | 0.25 | |
| | Density, ρ (kg/m ³) | 2700 | |
| | P wave velocity, V_p (km/s) | 5.6 | |
| | S wave velocity, V_s (km/s) | 3.2 | |
| Target fractures | Friction coefficient, $\mu = \tan(35^\circ)$ | 0.7 | |
| | Cohesion, c (MPa) | 0 | |
| | Normal stiffness, k_n (GPa/m) | 20 | |
| | Shear stiffness, k_s (GPa/m) | 20 | |
| ZFMA2 | Static friction coefficient, μ_s | 0.7 | During quasi-static step* |
| | | 0.78 | During dynamic step* |
| | Dynamic friction coefficient, μ_d | 0.45 | |
| | Reference slip velocity, v^* (m/s) | 0.35 | |
| | Cohesion c (MPa) | 0.5 | |
| | Normal stiffness, k_n (GPa/m) | 20 | |
| | Shear stiffness, k_s (GPa/m) | 20 | |

* See Section 5.4.

For the earthquake rupture simulation (cf. Section 5.4), it was assumed that the fault friction coefficient μ is a function of the slip velocity v , i.e., $\mu = \mu(v)$. The friction coefficient was modelled according to the velocity-weakening law proposed by Beeler et al. (2008) (Figure 5-2),

$$\mu(v) = \mu_d + \frac{\mu_s - \mu_d}{1 + \frac{v}{v^*} \left[1 - e^{-(v/v^*)^2} \right]}. \quad (5-2)$$

Here, μ_s is the static friction coefficient, which determines the peak strength of the fault, i.e., at which stress level slip is initiated. The dynamic friction coefficient μ_d determines the fault strength at high slip velocities. The third parameter v^* is a reference slip velocity, which determines how quickly the fault friction coefficient degrades from μ_s as the slip velocity increases (Table 5-1) (note that μ approaches μ_d asymptotically).

To initiate the rupture, the approach described by Bizzarri (2010) was adopted. Starting at the pre-defined hypocentre (cf. Figure 5-1) a radially expanding rupture was enforced to propagate at a constant rupture speed v_{force} within a circular nucleation region Σ_{nucl} with 750 m radius. The forced rupture velocity v_{force} was set to 50 % of the shear wave velocity V_s of the surrounding medium (cf. Table 5-1). The friction coefficient of the ZFMA2 fault plane was determined according to

$$\mu = \begin{cases} \mu_{nucl} = \min\{\mu^{VW}, \mu^{TW}\} & \forall (x, y, z) \in \Sigma_{nucl}, \\ \mu^{VW} & \forall (x, y, z) \notin \Sigma_{nucl} \end{cases} \quad (5-3)$$

where μ^{VW} (velocity-weakening) is determined by Equation (5-2) and μ^{TW} (time-weakening) is given by

$$\mu^{TW} = \begin{cases} \mu_s - (\mu_s - \mu_d) \frac{(t - t_{force})}{t_0} & t - t_{force} < t_0, \\ \mu_d & t - t_{force} \geq t_0 \end{cases} \quad (5-4)$$

Here, t_{force} is the time of rupture initiation and t_0 is the time over which the strength is ramped down from μ_s to μ_d , here set to 0.15 s. At some time during the initiation process, the ruptured area is large enough that the rupture starts to propagate spontaneously, governed by the velocity-weakening law (Equation (5-2)).

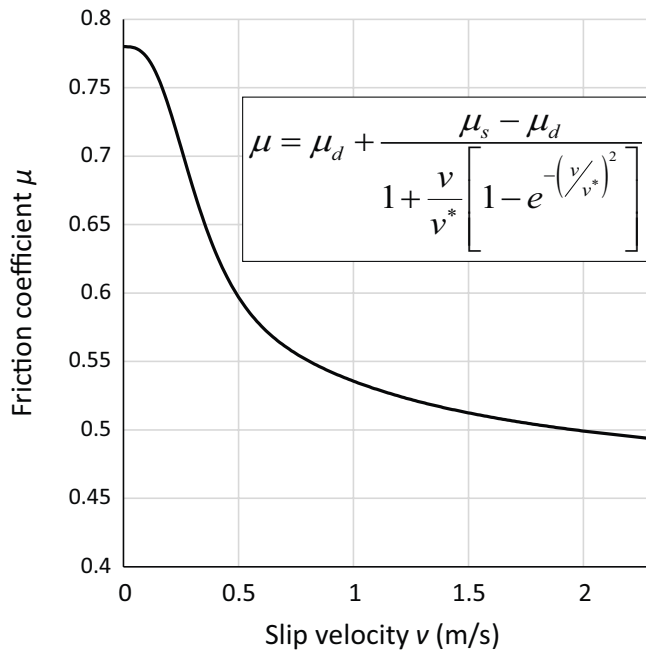


Figure 5-2. Velocity-weakening law (Beeler et al. 2008) (Equation (5-2)) with $\mu_s = 0.78$, $\mu_d = 0.45$ and $v^* = 0.35$ m/s.

5.4 Calculation sequence and boundary conditions

The simulation sequence comprised two steps.

The first step, the quasi-static simulation step, means that material properties were assigned according to Table 5-1, the initial stresses as well as pore pressure were applied, and the model was run quasi-statically until equilibrium was achieved. The vertical boundaries were locked for displacements in the x - and y -direction while the bottom boundary was locked in the z -direction. The upper boundary was free. During this simulation step the unstable parts of ZFMA2 and the target fractures slipped aseismically until all stress excess was relaxed.

The quasi-static simulation step was followed by the dynamic step when the earthquake rupture was initiated as described in Section 5.3. The vertical boundaries and the bottom boundaries were changed to be non-reflecting (quiet) boundaries while the upper boundary was kept free. The location of the rupture initiation point is shown in Figure 5-1, right. The parts of ZFMA2 that had slipped during the preceding quasi-static step were on the stability limit at the time of rupture initiation. This means that these parts were sensitive to tiny disturbances and easily started to slip as soon as the code was switched to dynamic simulation mode. To suppress this and to obtain a more distinct rupture propagation, the static friction coefficient was set to $\mu_s = 0.78$ during this calculation step.

5.5 Results

5.5.1 Simulation times

The times needed to complete the two simulation steps are presented in Table 5-2. There is a considerable difference in time to complete the quasi-static step. FLAC3D_7 completed this step about 6 times faster than 3DEC did while FLAC3D_9 was about 23 times faster than 3DEC. This can be attributed partly to the fact that the unbalanced forces appear to reduce more for each time step in FLAC3D, and partly to the faster model cycling in FLAC3D.

For the dynamic step, the critical time step determined by the programs differ. The time step determined by FLAC3D_7 was about 2.5 longer than the 3DEC time step. To facilitate the comparison of running times, partial density scaling was applied in the 3DEC model such that the time step became the same as that in FLAC3D_7. The time step used by FLAC3D_9 was yet longer – about 2.6 times the time step in FLAC3D_7.

Partial density scaling means that the user sets the desired time step and then 3DEC adds mass at critical grid points in the model such that a stable numerical solution is achieved. However, care should be taken when density scaling is applied. The more the time step is increased, the more additional mass is needed and the risk of impairing the results increases. Here, to examine the possible impact of the applied density scaling, the 3DEC model was run also without density scaling. The results generated with and without density scaling were practically identical. On average, the peak target fracture displacements differed by about 0.4 %.

The times to complete the dynamic simulation step were similar in 3DEC and FLAC3D_7, with 3DEC being about 15 % faster than FLAC3D_7. For FLAC3D_9, the simulation time is about 1/5 of the 3DEC simulation time. If the original time step had been used in 3DEC, the differences in simulation times would have been yet larger.

Table 5-2. Simulation times.

| Calculation step | Simulation times (h) | | |
|------------------|----------------------|-----------|------------|
| | 3DEC | FLAC3D_7 | FLAC3D_9 |
| Quasi-static | 7.9 | 1.3 | 0.35 |
| Dynamic | 25 | 29 | 4.9 |
| Total | 33 | 30 | 5.3 |

5.5.2 Quasi-static results

Shear displacements generated on ZFMA2 during the quasi-static calculation step are shown in Figure 5-3. The displacements are practically identical in 3DEC and the FLAC3D models, with a difference between the smallest and the largest peak displacement of about 0.2 %. Likewise, the continuum stresses are also very similar. Figure 5-4 shows the major principal stress on a vertical cross-section plane cutting through ZFMA2. The plots show that the value of the lowest stress close to the model's upper boundary differ by about 2 %, at most (cf. 3DEC and FLAC3D_7). The results in Figure 5-3 and Figure 5-4 are presented also in Appendix 3, but with identical colour scales in all plots.

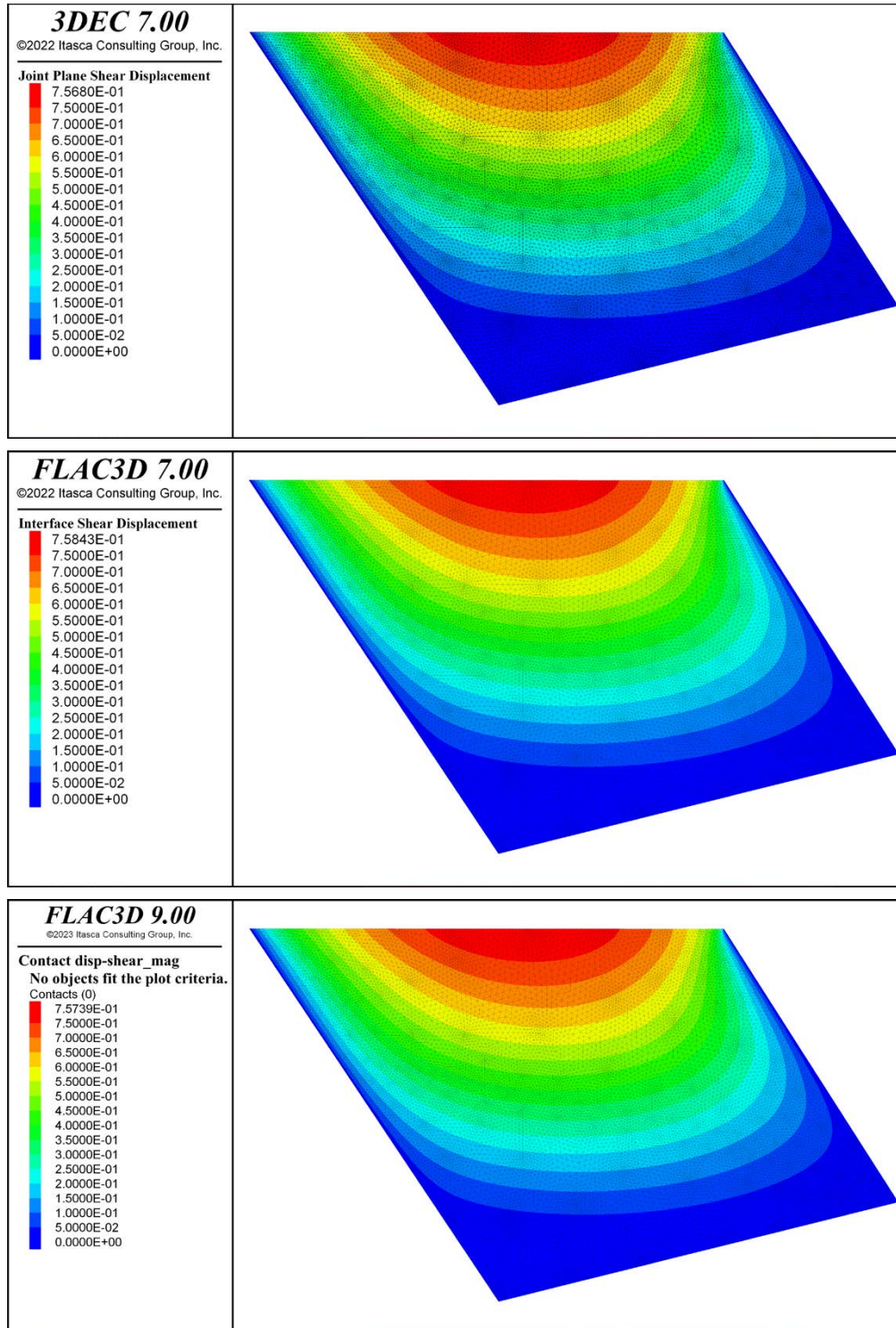


Figure 5-3. ZFMA2 shear displacements generated during the quasi-static calculation step. Upper: 3DEC. Middle: FLAC3D_7. Lower: FLAC3D_9.

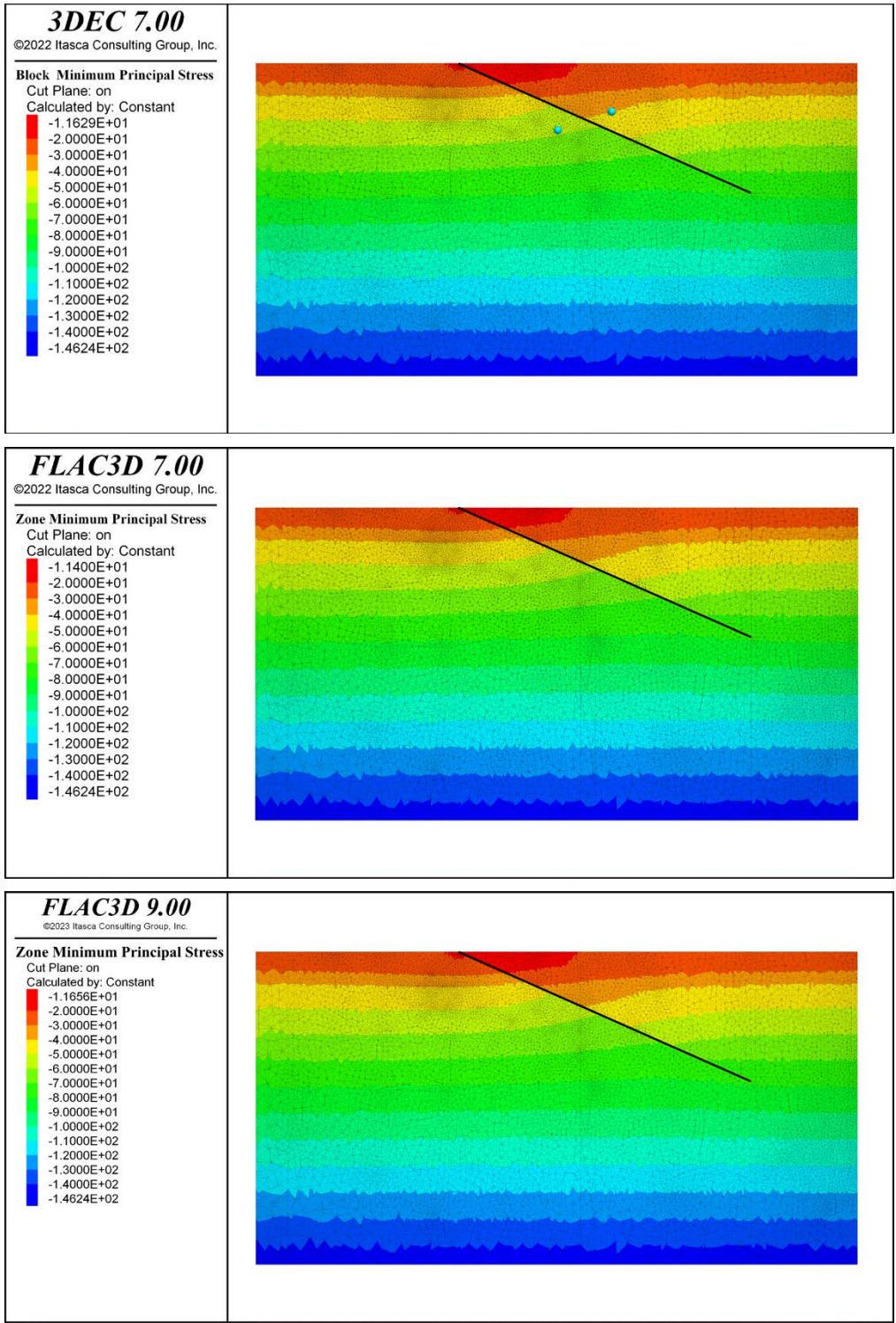


Figure 5-4. Major principal stress (MPa) in the continuum after the quasi-static calculation step. The results are shown on a vertical cross-section plane. The black line indicates the location of the ZFMA2 plane and the turquoise dots indicate positions for stress monitoring (see Figure 5-5). Upper: 3DEC. Middle: FLAC3D_7. Lower: FLAC3D_9. Note that only a portion of the model volume is shown here.

5.5.3 Dynamic results

After completed earthquake simulation, the earthquake source parameters were determined (Table 5-3). It is recalled that the stress drop $\Delta\tau$ is the difference between the initial shear stress (τ_1) and the final shear stress (τ_2) on the ruptured fault area, i.e. $\Delta\tau = \tau_1 - \tau_2$ (cf. Equation (1-1)). The average stress drop $\Delta\tau_{avg}$ in Table 5-3 is the area-weighted average value calculated from all failed subcontacts (3DEC)/interface nodes (FLAC3D_7) / zone-joints (FLAC3D_9) on ZFMA2, i.e.

$$\Delta\tau_{avg} = \frac{\sum_{i=1}^n \Delta\tau^i \cdot A^i}{\sum_{i=1}^n A^i} \quad (5-5)$$

where n is the number of failed subcontacts/interface nodes/zone-joints and A^i is the area of each subcontact/interface node/zone-joint.

The moment magnitude is calculated as

$$M_w = \frac{2}{3} \log_{10} M_0 - 6.07, \quad (5-6)$$

with

$$M_0 = G \cdot RA \cdot u_{avg}.$$

Here, G , RA and u_{avg} are the rock mass shear modulus, the rupture area and the average fault slip, respectively. All source parameters generated by 3DEC and the FLAC3D models are similar. For instance, the seismic moment M_0 and the average displacement differed by about 3 %, at most. It can be noted that the FLAC3D_9 source parameter values are closer to the 3DEC values than the FLAC3D_7 values are.

Table 5-3. Earthquake source parameters.

| Model | $\Delta\tau_{avg}$ (MPa) | M_0 ($\times 10^{16}$ Nm) | M_w | u_{avg} (m) | RA (km ²) |
|----------|-----------------------------|---------------------------------|-------|------------------|--------------------------|
| 3DEC | 1.05 | 1.93 | 4.79 | 0.0575 | 12 |
| FLAC3D_7 | 1.04 | 1.87 | 4.78 | 0.0558 | 12 |
| FLAC3D_9 | 1.06 | 1.92 | 4.79 | 0.0571 | 12 |

The co-seismic evolution of the major principal stress in the footwall and in the hanging wall of ZFMA2 was monitored. The results, which are presented in Figure 5-5, are very similar. Also, tiny details in the evolution were modelled nearly identically by the programs.

Figure 5-6 shows the evolution of shear velocity at the four locations on ZFMA2 shown in Figure 5-7. As for the near-fault stresses, there is a good agreement. At point #1 and #2, the curves are nearly identical while there are slight differences at point #3 and #4. The reason for these minor differences is not known. It is speculated that it can be due to minor numerical differences in the shear velocity calculation. In 3DEC, shear velocity is available as a regular output from the code, but in FLAC3D it had to be determined using a FISH script.

Figure 5-7 shows distributions of final shear displacement on ZFMA2. The results are similar. The largest deviations are found at some contacts close to the ground surface in the FLAC3D_9 model. If the colour scale is set the same as in the 3DEC plot (Figure 5-8), it becomes clear that the displacements at these contacts are local anomalies and that the displacement distribution in the FLAC3D_9 model, in general, is similar to that in the 3DEC model. The results in Figure 5-7 are presented also in Appendix 3 with identical colour scales for all three programs.

Distribution of peak slip velocity on ZFMA2 is shown in Figure 5-9. With the exception of some deviations close to the ground surface in the FLAC3D_7 model, the results are very similar in all three models. The results in Figure 5-9 are presented also in Appendix 3 with identical colour scales.

The similar evolutions in 3DEC and in the FLAC3D models of stresses around the ZFMA2 plane and of displacements on the ZFMA2 plane indicate that also the co-seismic load on the target fractures and the associated fracture displacements should agree well. This is confirmed by the results shown

in Figure 5-10, Figure 5-11 and Figure 5-12. Qualitatively, the target fracture shear displacement evolutions monitored close to the fracture centres are practically identical in 3DEC and FLAC3D, as illustrated in Figure 5-10. The results in Figure 5-11 are presented also in Appendix 3 with identical colour scales.

Given that the displacements on most of the fractures are small (a few millimetres), and hence sensitive to numerical disturbances, the agreement in the displacement magnitudes can be regarded satisfactory. The relative difference between the displacements generated in the 3DEC model and in the FLAC3D models is less than 6 % on about 80 % of the fractures (Figure 5-12, lower). On average, the relative difference amounts to about 4 % for both FLAC3D_7 and FLAC3D_9. The largest relative difference for FLAC3D_7 is 13 % (on fracture #25) and for FLAC3D_9 it is 9 % (on fracture #52) (Figure 5-12, upper).

Figure 5-13 shows which subcontacts (3DEC)/interfaces (FLAC3D_7)/zone-joints (FLAC3D_9) on the target fractures that have failed. The figure shows that effectively the entire target fracture areas have failed in shear.

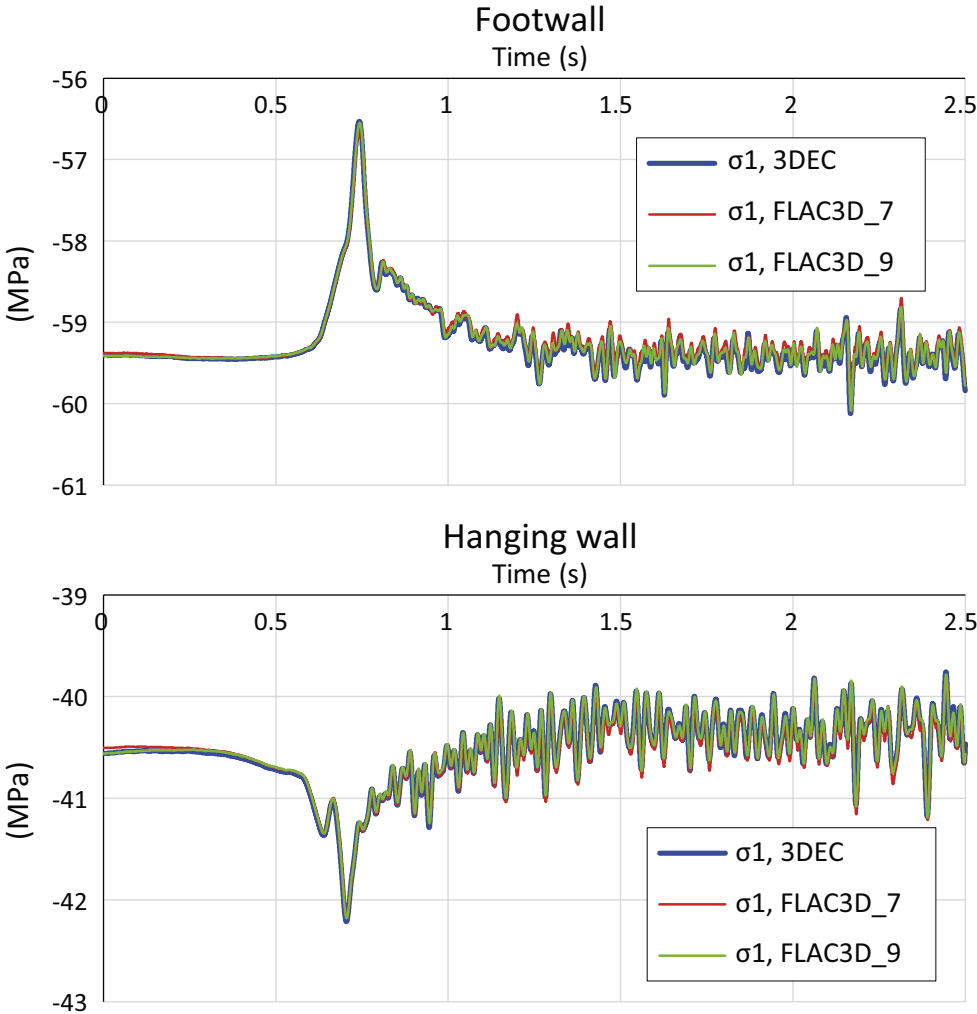


Figure 5-5. Co-seismic temporal evolution of major principal stress in the footwall and in the hanging wall of ZFMA2. See Figure 5-4 (upper) for locations of the monitoring points.

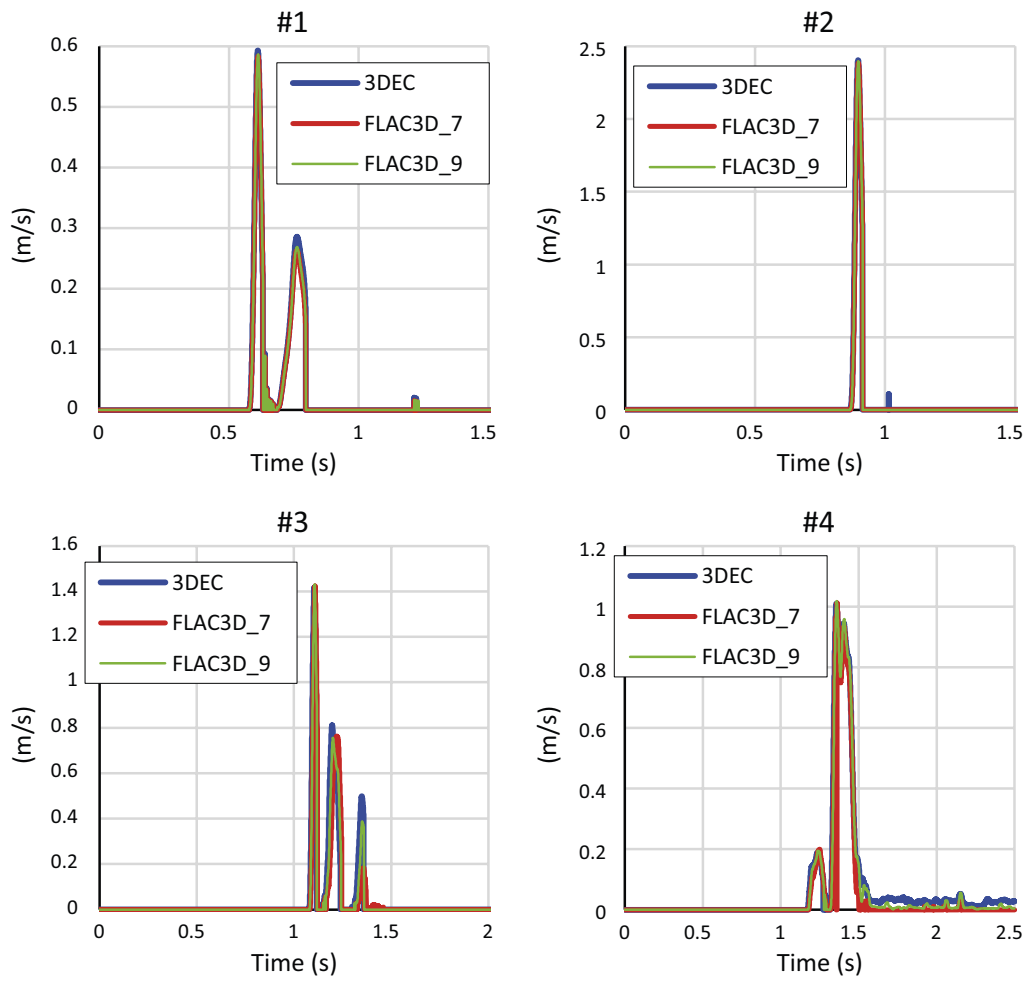


Figure 5-6. Co-seismic temporal evolution of shear velocity at four points on ZFMA2. The recording points are depicted in Figure 5-7.

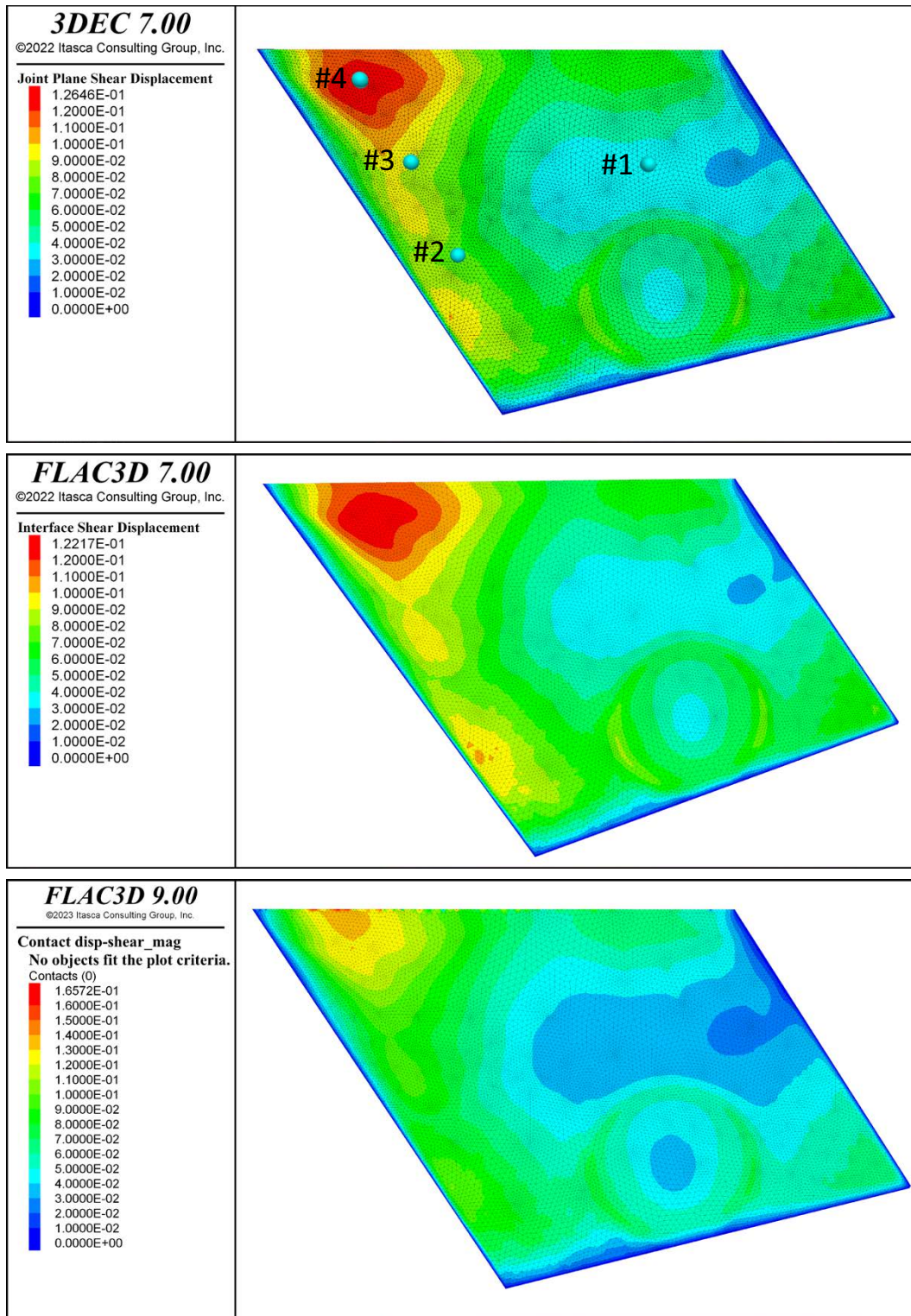


Figure 5-7. ZFMA2 final shear displacement (m) generated during earthquake rupture. Upper: 3DEC. Middle: FLAC3D_7. Lower: FLAC3D_9. The turquoise dots in the upper plot indicate locations for the monitoring of shear velocity evolution (see Figure 5-6).

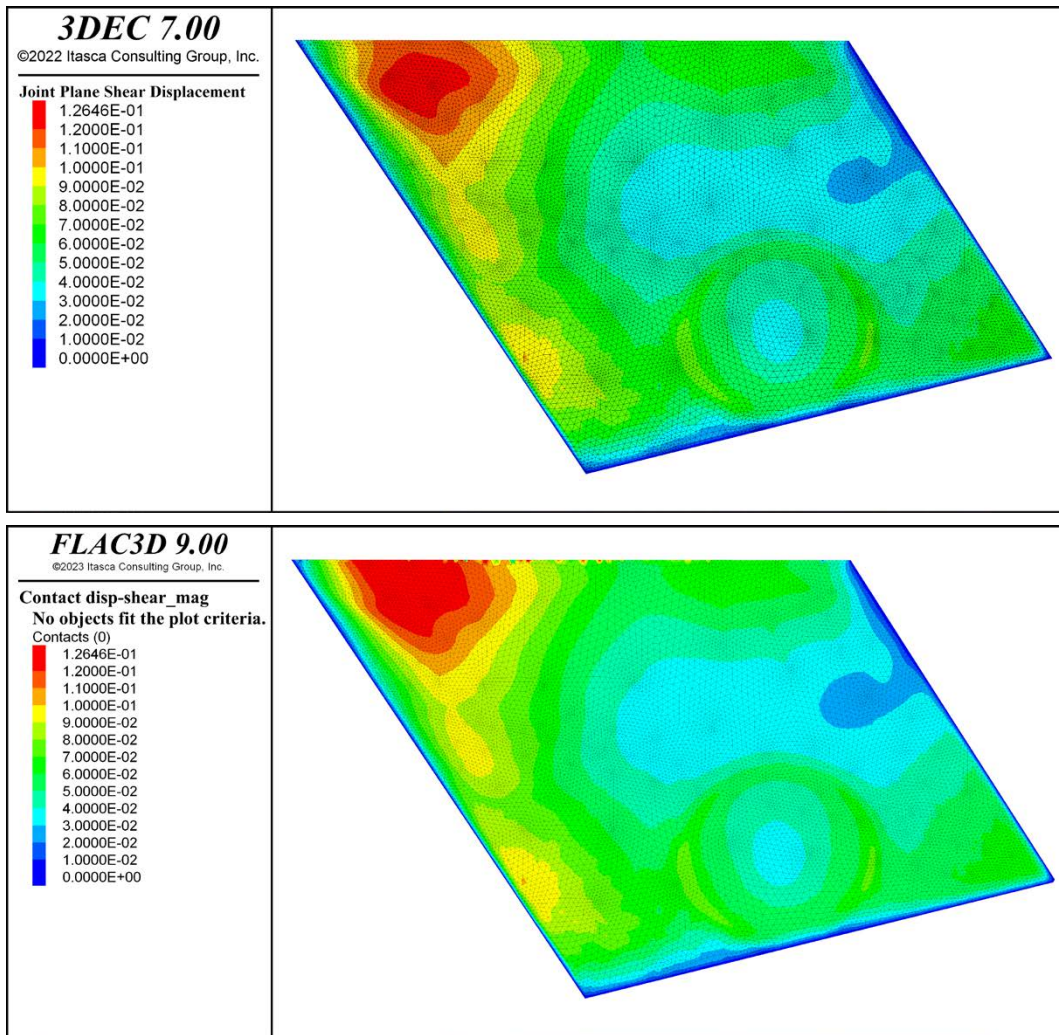


Figure 5-8. ZFMA2 final shear displacement (m) generated during earthquake rupture. Upper: 3DEC. Lower: FLAC3D_9. The same results as in Figure 5-7 but with the same colour scales in both plots.

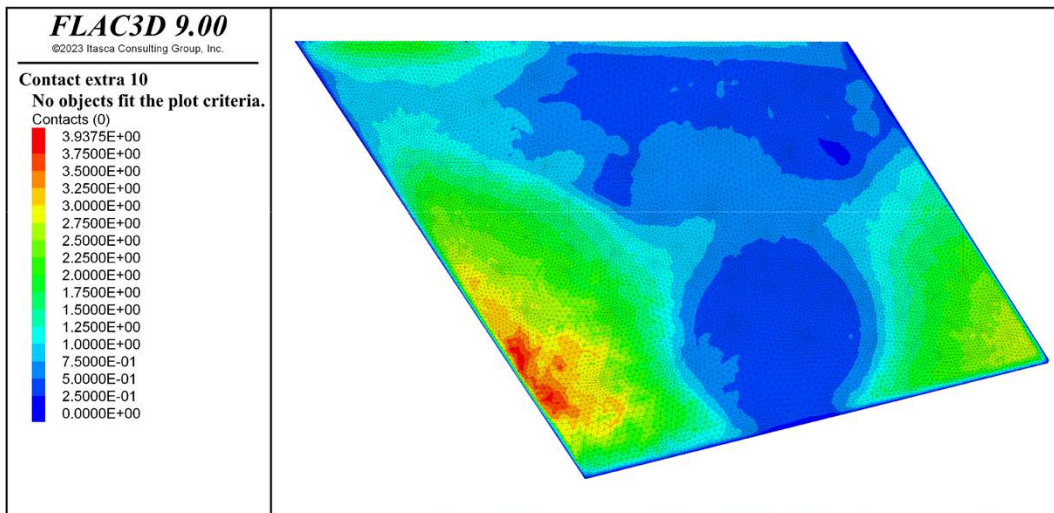
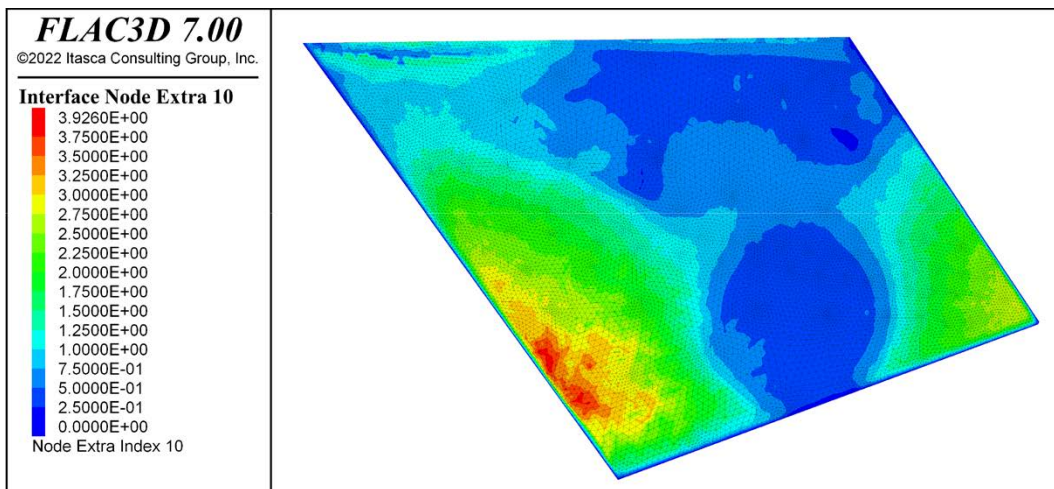
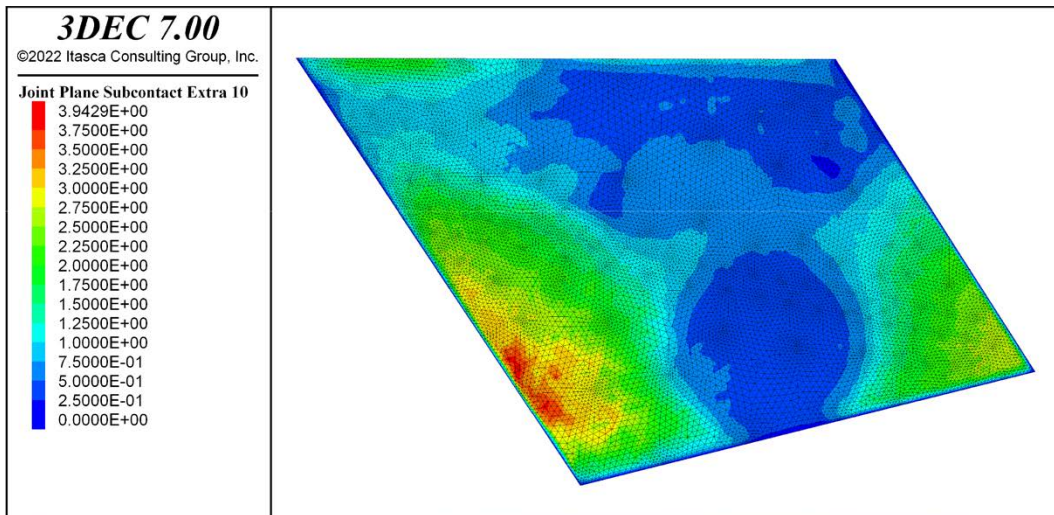


Figure 5-9. ZFMA2 peak slip velocity (m/s) during earthquake rupture.

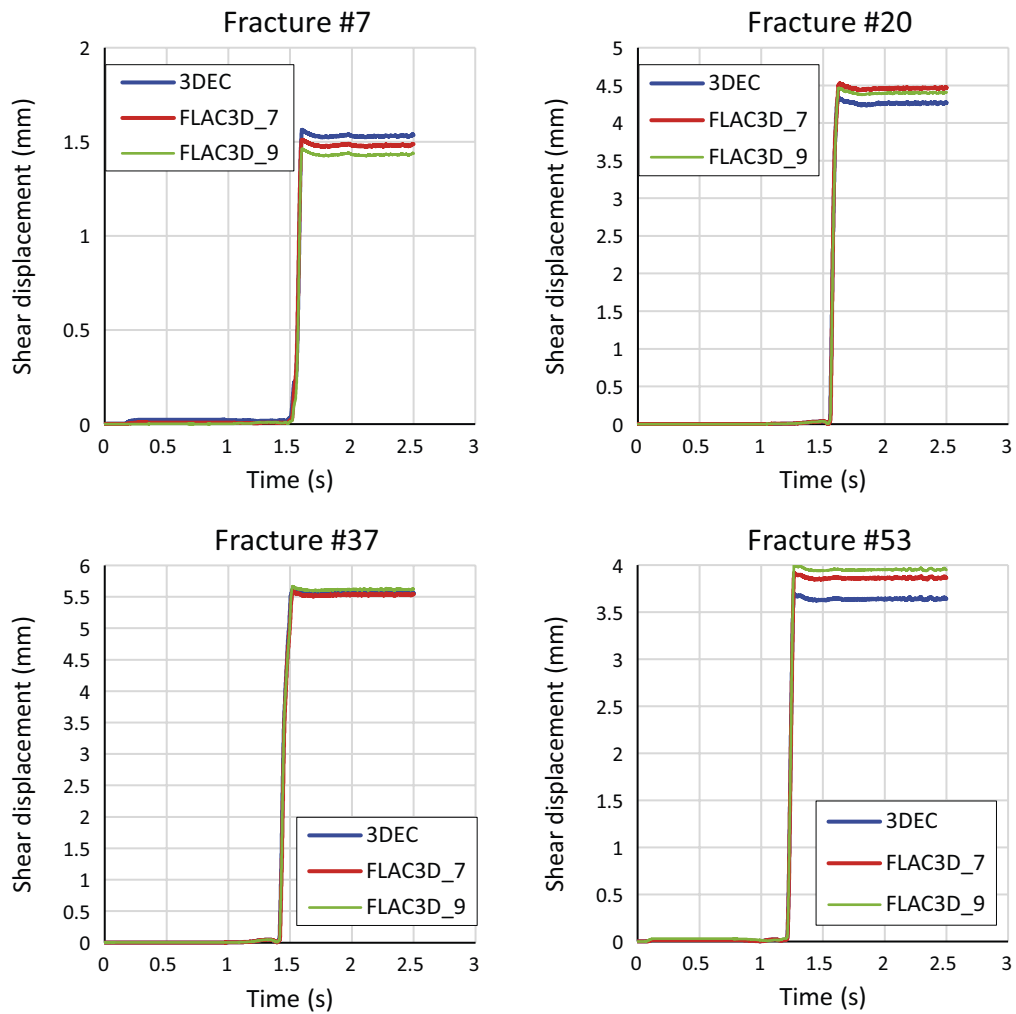


Figure 5-10. Temporal evolution of co-seismic shear displacement on four of the target fractures. The displacements were monitored close to the fracture centres. The locations of the fractures are shown in Figure 5-11, upper.

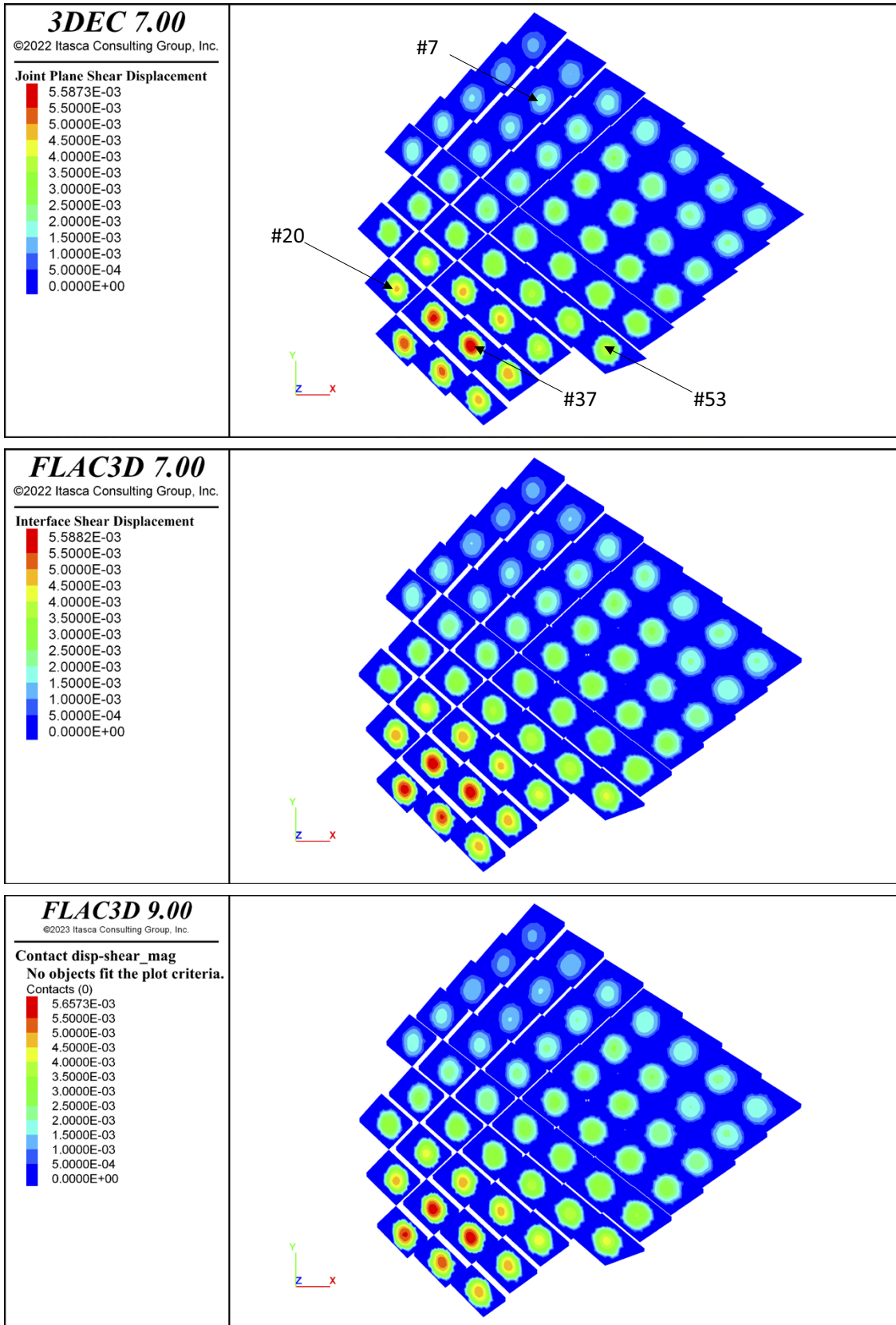


Figure 5-11. Target fracture final shear displacements (m) after earthquake rupture. Temporal evolution of shear displacements is shown in Figure 5-10 for the fractures indicated in the upper plot.

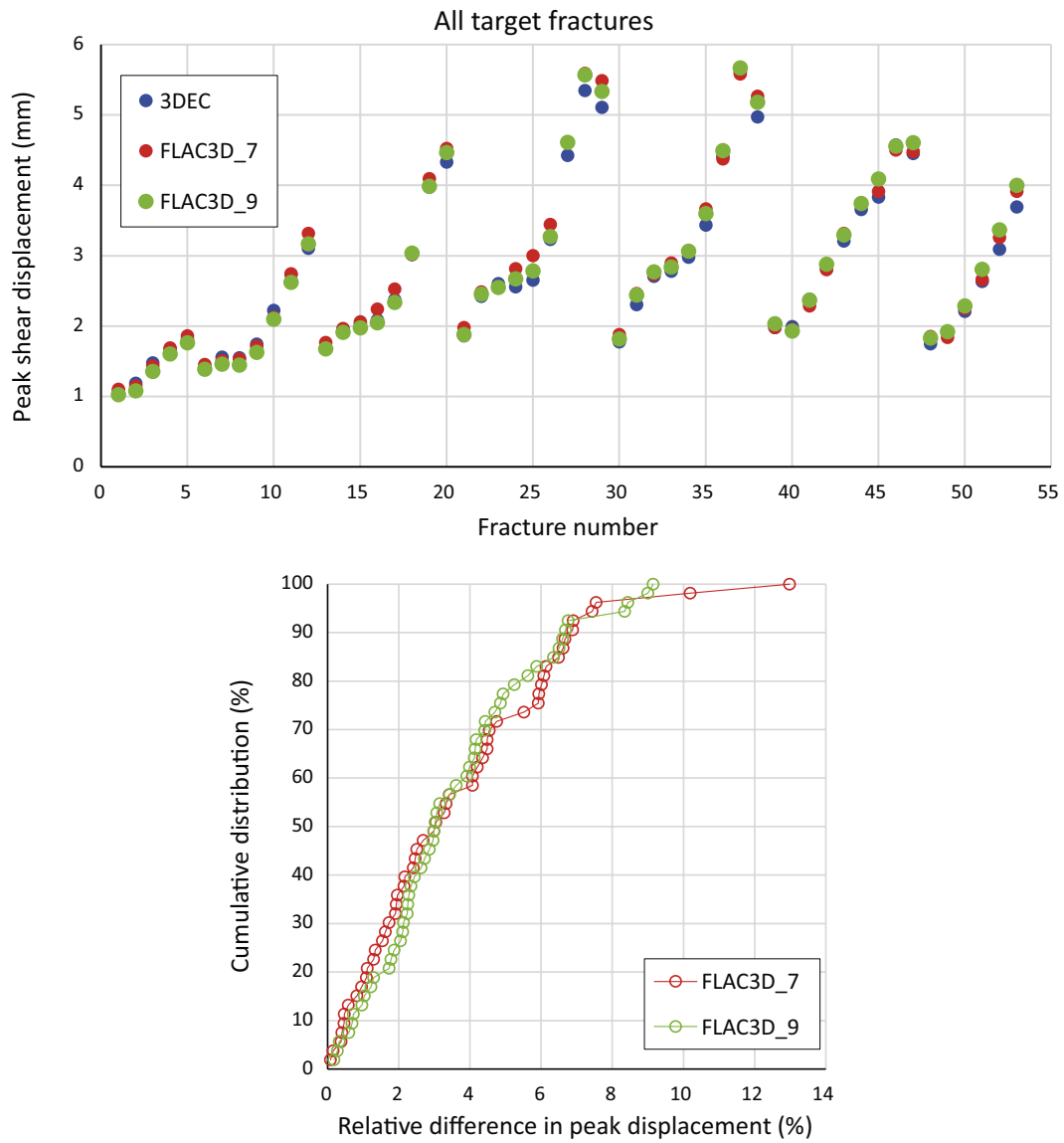


Figure 5-12. Upper: Target fracture co-seismic peak shear displacements. Lower: Cumulative distribution of relative difference between FLAC3D and 3DEC in target fracture peak shear displacement.

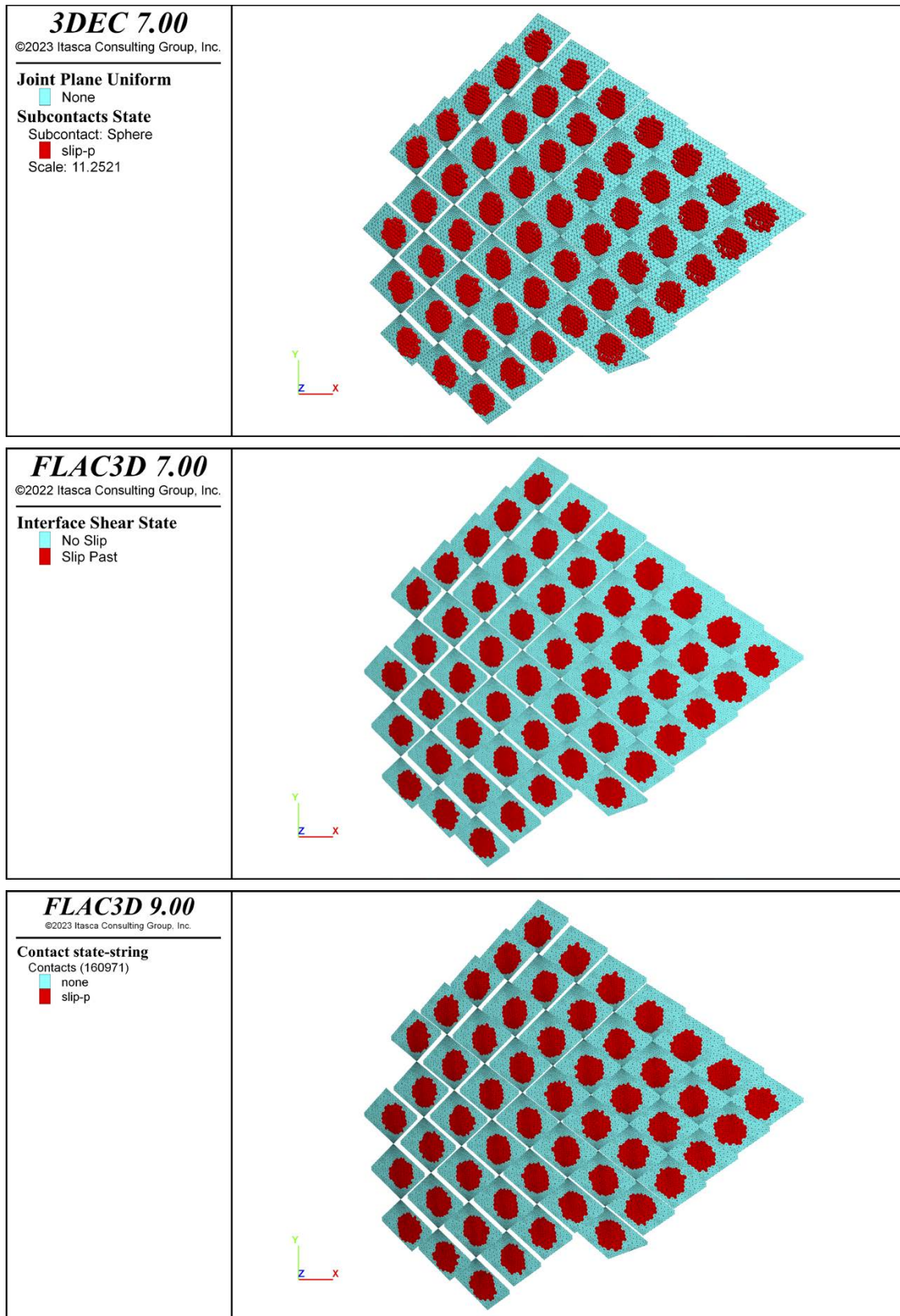


Figure 5-13. Target fracture slip indicators. Subcontacts (3DEC) / interface nodes (FLAC3D_7)/zone-joints (FLAC3D_9) shown in red have failed in shear.

6 Large-scale earthquake benchmark case

In this chapter, the simulation of a dynamically propagating large-scale earthquake source rupture is presented. The simulation is performed using FLAC3D_9. This modelling case is one of the benchmark exercises defined within the ‘SCEC/USGS Dynamic Earthquake Rupture Code Verification Exercise project’ (Harris et al. 2009). The case is called TPV26.

6.1 Model description

The earthquake rupture is propagated on a vertical right-lateral strike-slip fault. The surface-breaching fault is planar and is embedded in a linear elastic, isotropic and homogeneous continuum (Figure 6-1). The fault length (along strike) is 40 km and the fault width (along dip) is 20 km. The rupture, which is simulated by use of the linear slip-weakening law, is nucleated at 10 km depth by a forced rupture. The definition of the exercise with further details of material properties, the initial stress field and the nucleation procedure can be found at the SCEC project home page (<https://strike.scec.org/cvws/index.html>). Parts of the exercise definition are also presented in Appendix 5.

The FLAC3D_9 model volume had the dimensions $130 \times 65 \times 80 \text{ km}^3$ (Figure 6-1) and was discretized using hexahedral brick-shaped zones. The dimensions were large enough that the solution should not be impaired by potential wave reflections at the model boundary. In addition, a quiet (non-reflecting) boundary condition was applied at all model sides except for the upper, free boundary. The inner volume surrounding the fault plane was centrally located in the model volume. Within this inner volume the discretization edge length was 100 m. This densely meshed volume extended 6 km on either side of the fault plane (Figure 6-2). Outside this volume the mesh was made gradually coarser toward the boundary. The model contained 48 000 000 zones. No damping was applied in the model.

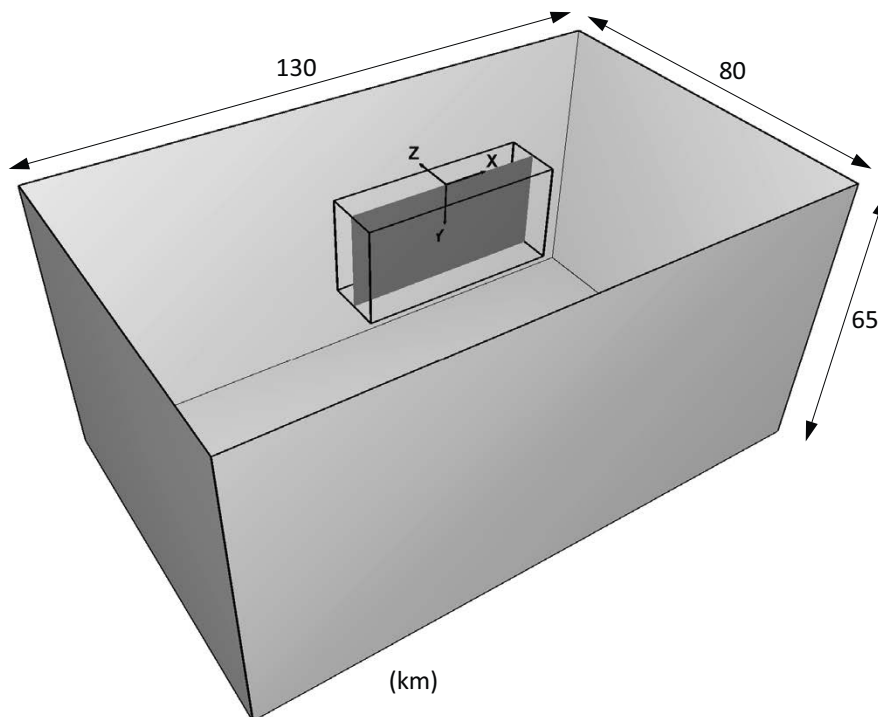


Figure 6-1. Model outlines. The fault is centrally located in the model and here represented by the dark grey plane.

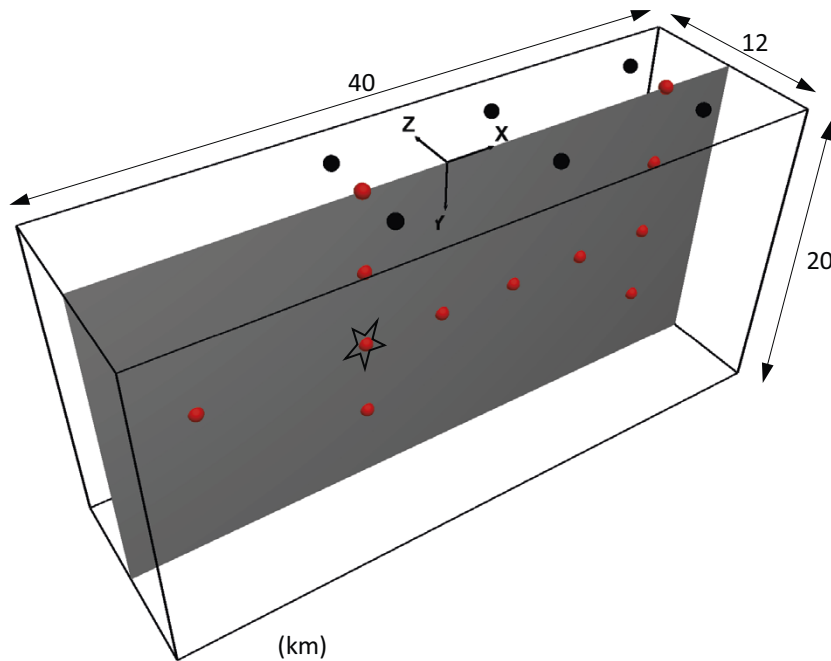


Figure 6-2. The vertical fault plane extended 40 km in the along strike (x -) direction and 20 km in the down-dip (y -) direction. The star indicates the hypocentre. The red dots indicate on-fault monitoring stations (cf. Figure 6-4) while black dots indicate off-fault surface stations (cf. Figure 6-5).

6.2 Results

The dynamic timestep determined by FLAC3D_9 is 1.15×10^{-3} s and can be regarded large. The large timestep can be attributed to the simple and hence advantageous zone mesh in combination with optimisations of the timestep calculation that have been implemented in FLAC3D_9. About 25 hours were needed to simulate 13 s of the dynamic process.

The synthetic earthquake generated a seismic moment of 4.3×10^{19} Nm, which corresponds to a moment magnitude of 7.0. Figure 6-3 (upper) shows a colour scale plot of fault rupture propagation velocity V_r normalised to the continuum shear velocity V_s . The arrows indicate the rupture propagation directions. Figure 6-3 (lower) shows fault shear displacement. Note the zero displacements on the lower part of the fault plane. This is because the initial stress field was defined such that the shear stress on the fault plane is tapered down to be zero at depths below 15 km. Hence, the rupture was gradually arrested around this depth and no slip was taking place below 17 km depth.

Shear and normal stresses as well as slip and slip velocities in the x - (horizontal) and y - (vertical) directions were monitored at the twelve on-fault stations (Figure 6-4). Displacements and velocities in the x -, y - and z -directions were monitored at the six surface stations (Figure 6-5). The results are compared with the corresponding results generated by several other authors/codes. The results from the other authors/codes were downloaded from the SCEC/USGS project home page (<https://strike.scec.org/cvws/index.html>). For most of the other codes, results generated with two different resolutions (50 m or 100 m node spacing) are available. Here, the results generated using 100 m node spacing were used in the comparison since this corresponds to the node spacing used in the present FLAC3D_9 simulation.

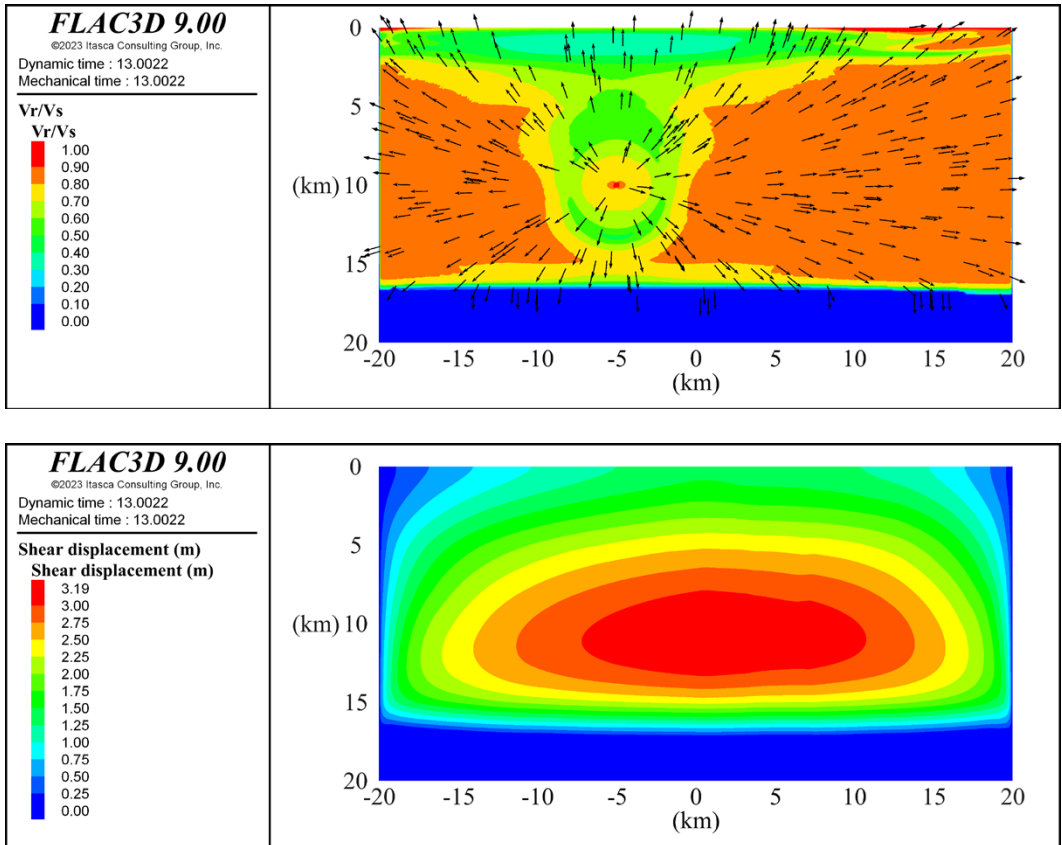


Figure 6-3. Upper: Colour scale plot of fault rupture propagation velocity normalized to the shear wave velocity of the continuum. The arrows indicate rupture directions. Lower: Colour scale plot of fault shear displacement. The stars indicate the hypocentre. The plots were generated after completed simulation (simulated time 13 s).

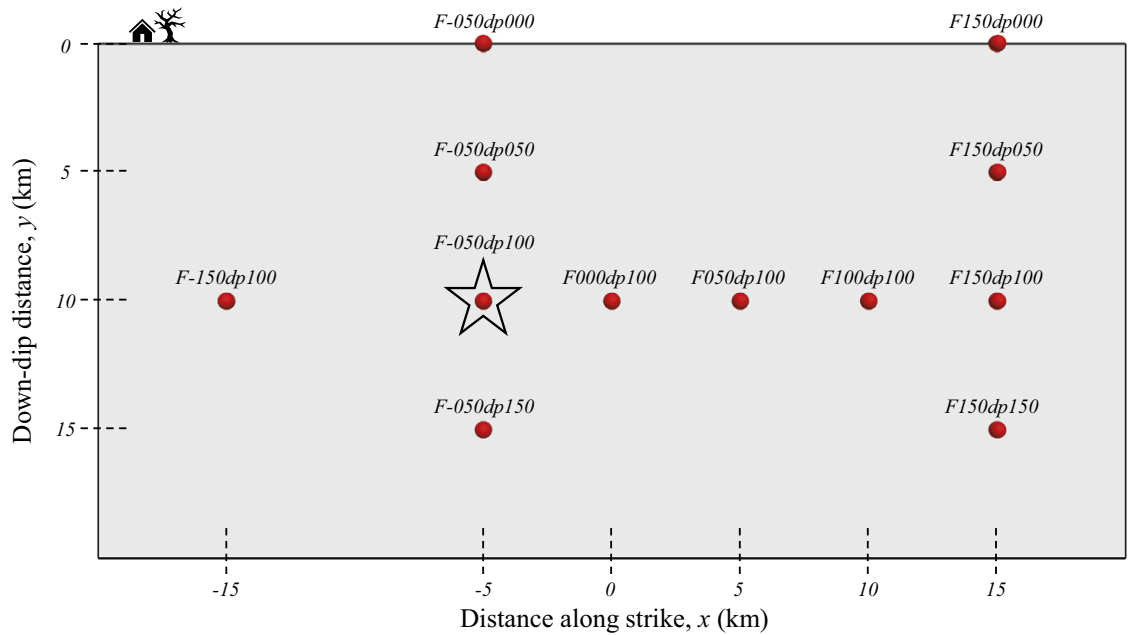


Figure 6-4. On-fault monitoring stations. The star indicates the hypocentre.

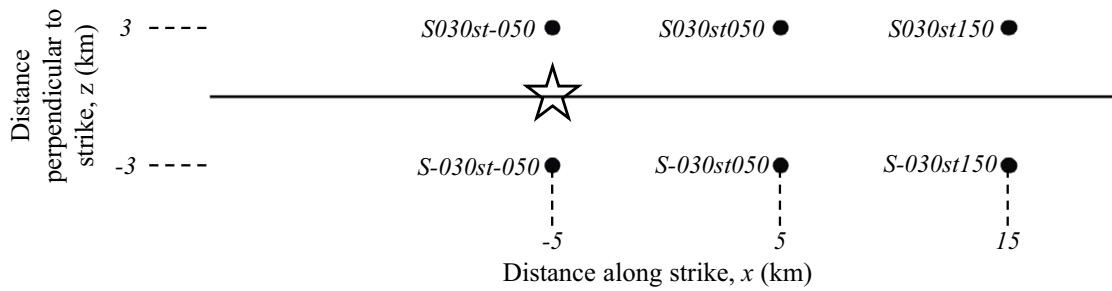


Figure 6-5. Map view showing the locations of the off-fault surface monitoring stations. The solid line indicates the fault surface trace and the star indicates the epicentre.

In Figure 6-6 to Figure 6-8 results from FLAC3D_9 are plotted along with the corresponding results from the other codes. Figure 6-6 and Figure 6-7 show evolution of slip, slip rate, and shear stress at the two on-fault stations F-050dp000 and F100dp100, respectively. These results were monitored at zone-joints on the fault plane. Figure 6-8 shows evolution of displacement and velocity at the surface station s030st050. Results from all stations are presented in Appendix 4.

In general, the results generated by FLAC3D_9 agree well with the results from the other codes. For on-fault shear displacements in the x-direction (the direction in which significant values are obtained at all stations) and for the off-fault surface displacements, the difference between FLAC3D_9 and the other codes is typically within 5 %.

For velocities and stresses, for which an exact fit is more difficult to obtain, the agreement is considered to be acceptable, given the different numerical approaches that are used in the programs. High-frequency noise is seen in the FLAC3D_9 velocity and shear stress output at some locations, mainly at the end of the time series. It is speculated here that this may be due to the coarsening of the zone mesh towards the model boundary and that it possibly would be reduced if the discretisation in the outer model volume had been finer. The noise would presumably also be reduced if damping had been applied in the model.

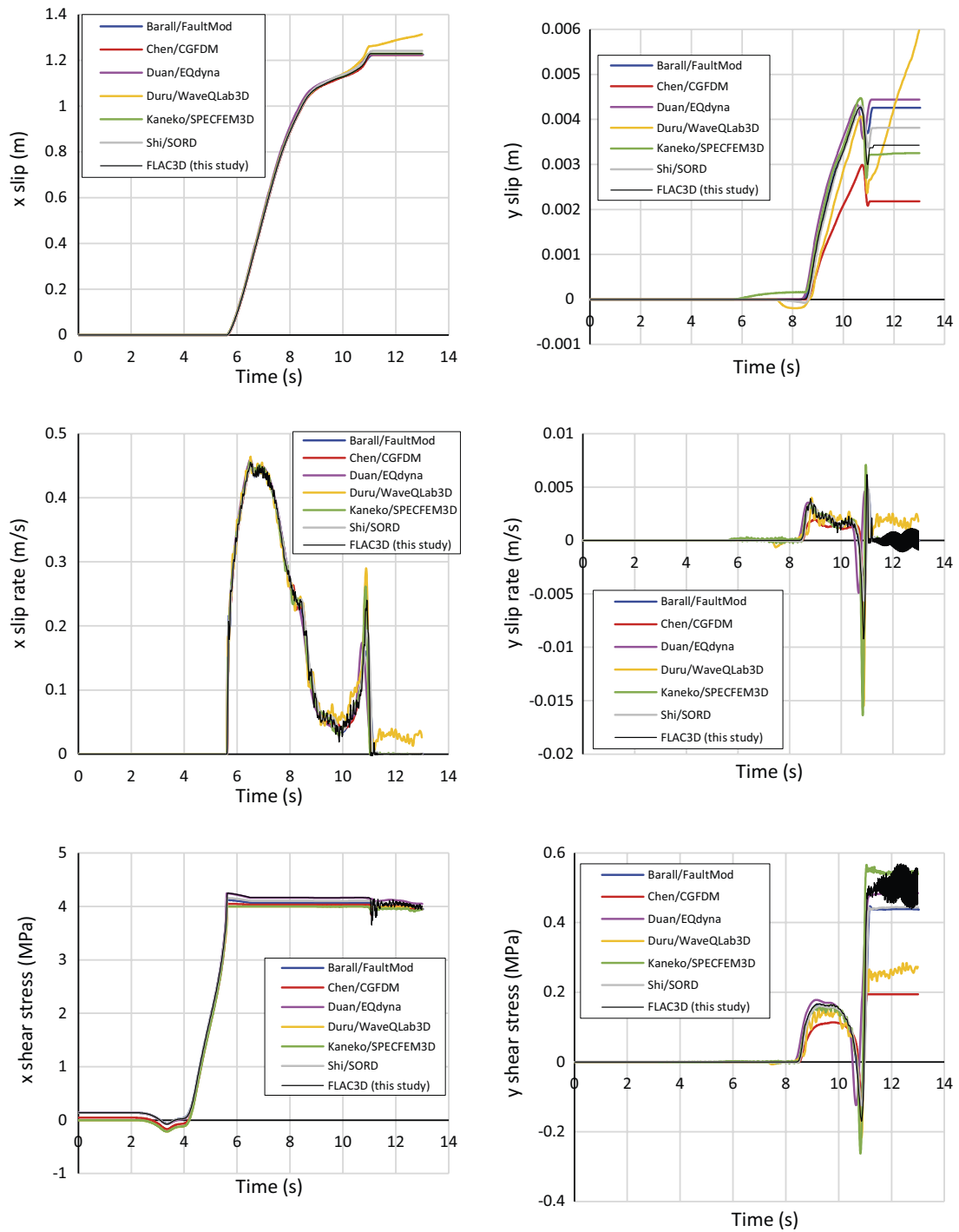


Figure 6-6. Time evolution of slip, slip rate and shear stress at the on-fault monitoring station F-050dp000 (cf. Figure 6-4). Results from FLAC3D₉ (on zone-joint) are plotted along with results from other authors/ codes. Results from all stations are presented in Appendix 4.

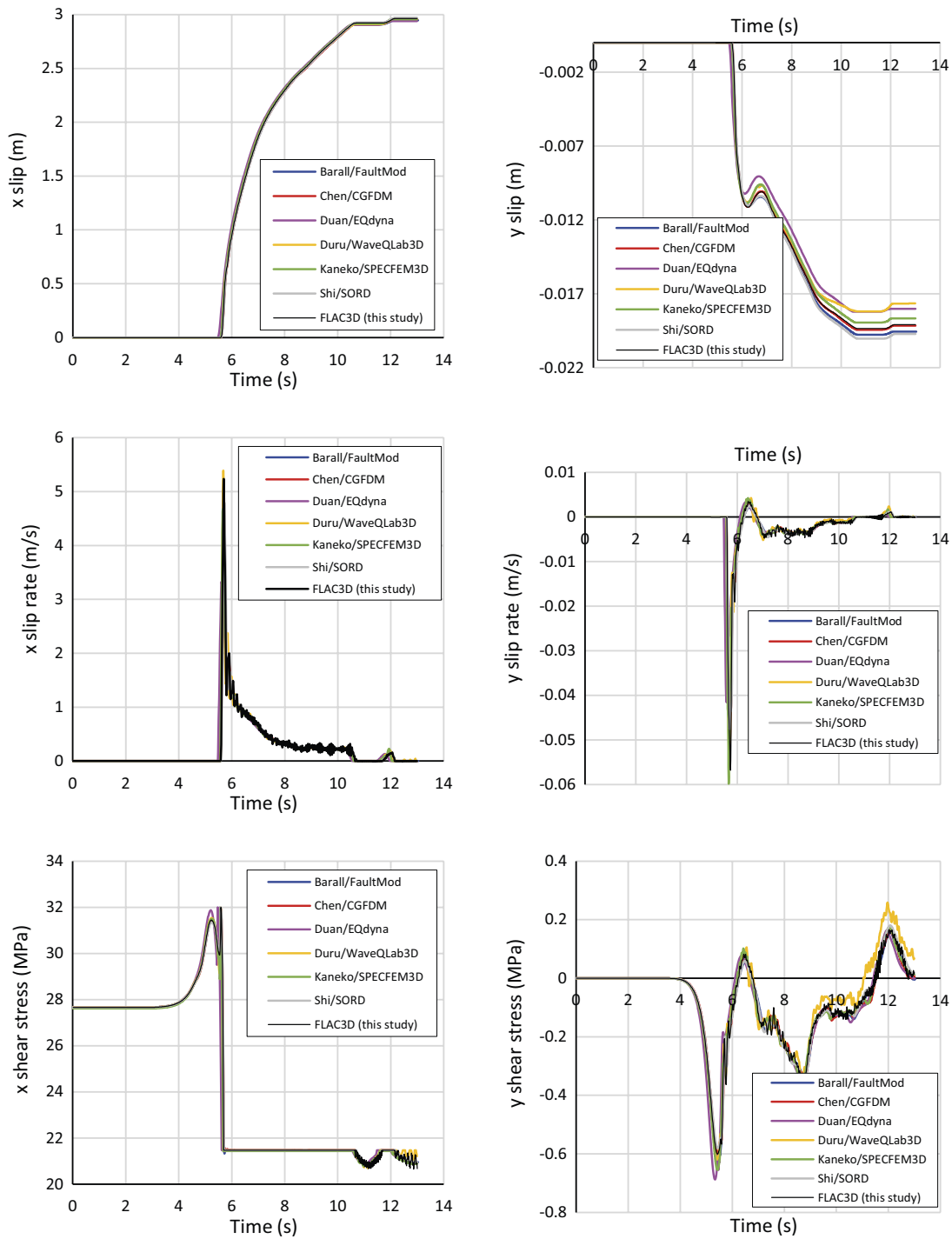


Figure 6-7. Time evolution of slip, slip rate and shear stress at the on-fault monitoring station F100dp100 (cf. Figure 6-4). Results from FLAC3D_9 (on zone-joint) are plotted along with results from other authors/codes. Results from all stations are presented in Appendix 4.

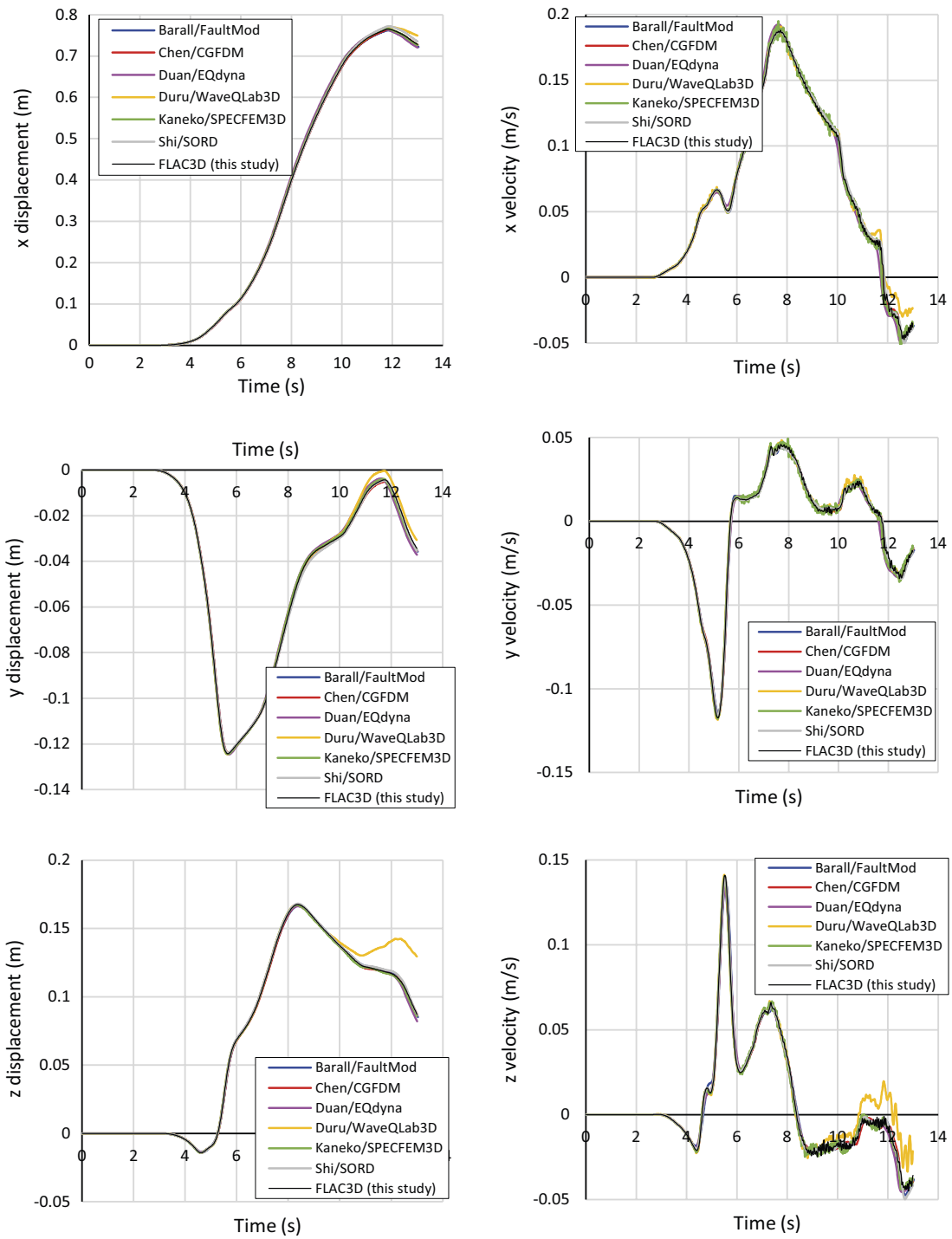


Figure 6-8. Time evolution of displacement and velocity at the off-fault surface monitoring station S030st050 (cf. Figure 6-5). Results from *FLAC3D_9* are plotted along with results from other authors/codes. Results from all stations are presented in Appendix 4.

7 Discussion and conclusions

The objective of the work that is presented in this report was to compare results generated with FLAC3D with corresponding results generated with 3DEC and with other programs. Results from five different modelling cases were used in the comparison:

1. Single fracture model (quasi-static).
2. Multiple-fracture model (thermo-mechanical, quasi-static).
3. Thermo-mechanical model with openings and fractures (quasi-static) (FLAC3D_7 was not included in the comparison).
4. Forsmark earthquake model (dynamic).
5. Large-scale earthquake benchmark case (dynamic) (only FLAC3D_9 was compared with programs other than 3DEC).

Mechanical, thermo-mechanical and dynamic simulations were performed. Even though the effects of porewater pressures were included in the conducted simulations, no hydro-mechanical coupling case was considered. In all modelling cases, joint planes were included with different levels of complexity. In some cases, just one joint was included while several intersecting joints were included along with excavations in other cases. All models were run in small-strain mode.

As noted earlier, 3DEC and FLAC3D_7 use the same graphical interface (the interface in FLAC3D_9 is a bit different). Furthermore, both the command syntax and the syntax of the built-in programming language FISH are similar in the programs. Hence, for an experienced 3DEC user, it is not too complicated to set up and run a FLAC3D model. This holds, at least for the models examined here where the model geometry was generated in 3DEC and then exported to FLAC3D.

In the comparison of results generated with 3DEC and FLAC3D, it was a great advantage that both programs could use identical model geometries with identical discretisation of the continuum. So, possible influence of continuum mesh dependence was out of question when results were compared. This is also reflected in the results, which were very similar in most cases.

By default in the interface logic (used in FLAC3D_7), each interface element node corresponds to one gridpoint along the joint (Itasca 2019). Each wall vertex in the zone-joint logic (used in FLAC3D_9) corresponds uniquely to one gridpoint along the joint (Itasca 2022). The correspondence between contact vertices/nodes and the zone gridpoints along the joint surface is like the correspondence between subcontacts and gridpoints in 3DEC (Itasca 2020). Hence, the joint surfaces were, as far as possible, similarly discretised in 3DEC and FLAC3D. It appears that the differences in the results can mainly be attributed to the differences in the joint contact logic formulations. The zone-joint logic in FLAC3D_9 is, like the contact logic in 3DEC, two-sided and appears to be more robust than the one-sided interface logic (used in FLAC3D_7), particularly when it comes to handle joint plane intersections.

The results from the simulations are summarised in the following list:

- Typically, over 80 % of the joint surface areas included in the models here failed in shear and/or tension.
- Single fracture model (Chapter 2). 3DEC and FLAC3D generated practically identical fracture shear displacement results.
- Thermo-mechanical multiple-fracture model (Chapter 3). The stresses agreed within 1 % and joint displacements within a few percent in most cases. However, differences that could be attributed to issues at joint intersections in FLAC3D_7 (see bullet below) were found in some cases.
- Thermo-mechanical model with openings and fractures (Chapter 4). 3DEC and FLAC3D_9 generated similar results. Differences in stress amounting to a few percent were found in small volumes, mainly along joint planes around the excavations. For instance, at the end of simulation the difference in major principal stress exceeded 1 % in about 1.7 % of the volume surrounding the

joint planes. In the elastic case, only insignificant differences in stress were found. The differences in joint displacements were of the order of 1 %.

- Forsmark earthquake model (Chapter 5). The overall earthquake fault response was very similar in 3DEC and both versions of FLAC3D. Some local anomalies in fault displacement were found at the surface break in FLAC3D_9, though. The relative difference in target fracture displacement between 3DEC and both FLAC3D versions was about 4 %, on average. The difference was less than 6 % on about 80 % of the fractures.
- Large-scale earthquake benchmark model (Chapter 6). In general, the agreement between results generated by FLAC3D_9 and by several other programs can be regarded satisfactory, given the different numerical approaches used. In particular, continuum displacements and shear displacements agree well, with differences within 5 %. Velocities, slip velocities and stresses, which in general are more sensitive to numerical disturbances and hence more difficult to fit, also show satisfactory agreement even though some noise is seen in FLAC3D_9 at the end of the time series.
- As pointed out in the program documentation (Itasca 2019), FLAC3D may encounter problems at intersections between joints when interface elements are used. This was observed in the Multiple_joint case model (Chapter 3). Quite significant anomalies in shear displacement were obtained at some interface intersections in FLAC3D_7. This was reflected in the continuum stresses at some monitoring points. However, the displacement anomalies were local and affected the model response locally. At most other locations, the FLAC3D_7 model response was similar to that of the 3DEC model and the difference in stresses was typically within 2 %.
- The analytical thermal logic in FLAC3D_9 works well and gives identical results when compared to 3DEC. It is noted here that the logic is multithreaded in FLAC3D_9 and hence considerably faster than the single-threaded logic in 3DEC.
- In general, FLAC3D is faster (in many cases much faster) than 3DEC. This holds for the initialisation procedures, e.g. application of properties and stresses, as well as for cycling. During cycling, FLAC3D utilises the hardware much more efficiently than 3DEC. Typically, while 3DEC may use 10–20 % of the processor resources, FLAC3D uses 80–100 %. Both programs are multi-threaded, but the better processor utilisation in FLAC3D indicates that the speed of this program would scale better with increasing number of processor cores in the computer system. For the cases here with only a few joint planes/interfaces, FLAC3D_7 completed the calculation up to 10 times faster than 3DEC. However, when more joints were included, it became less clear which of the programs is the fastest. For instance, in the Multiple_joint case (Chapter 3), with ten joints and several joint intersections, 3DEC was about 20 % faster than FLAC3D_7. FLAC3D_9 was faster than FLAC3D_7, with simulation times shortened 6 to 50 times relative to 3DEC. Notable is that the new zone-joint logic in FLAC3D_9 gives less sensitivity to the number of joints in the model and FLAC3D_9 was faster than 3DEC in all modelling cases considered here.

To summarise, for modelling cases with no or only a few joints, both versions of FLAC3D generate results that are practically identical to those delivered by 3DEC. In cases with several intersecting joint planes, displacement anomalies may arise locally around intersections in the FLAC3D solution when the interface logic is used. Using the new zone-joint logic in FLAC3D_9 gives more reliable and faster solutions than what is obtained in FLAC3D_7. For the modelling cases considered here, FLAC3D_9 generated results that differ a few percent from the corresponding results generated by 3DEC and other codes. Given the different numerical approaches in the codes, this can be regarded satisfactory. Considering this and the considerable speed increases that can be obtained when compared with 3DEC, it appears that FLAC3D_9 with the zone-joint logic could be an attractive alternative to 3DEC for applications with a few intersecting joint planes. The results indicate that both versions of FLAC3D could be an alternative to 3DEC for problems with many joints, but without intersections. (e.g. the Forsmark earthquake model in this study). A problem with many intersecting joints (i.e., a fracture network) has not been tested here.

References

SKB's (Svensk Kärnbränslehantering AB) publications can be found at www.skb.com/publications.

Beeler N M, Tullis T E, Goldsby D L, 2008. Constitutive relationships and physical basis of fault strength due to flash heating. *Journal of Geophysical Research* 113:B01401. <https://doi.org/10.1029/2007JB004988>

Bizzarri A, 2010. How to Promote Earthquake Ruptures: Different Nucleation Strategies in a Dynamic Model with Slip-Weakening Friction. *Bull. Seism. Soc. Am.* 100:3, 923–940. <https://doi.org/10.1785/0120090179>

Cundall P A, 1971. A computer model for simulating progressive large scale movements in blocky rock systems, Paper No. II-8. In *Symposium of the International Society for Rock Mechanics*, 4–6 October, Nancy, 1971. Wuhan: Scientific Research, 128–132.

Fälth B, 2022a. Deformation zone stability and co-seismic secondary fracture displacements at Forsmark. SKB TR-22-13, Svensk Kärnbränslehantering AB.

Fälth B, 2022b. Simulating the thermo-mechanical evolution in the inner section of the Äspö Prototype Repository rock mass. SKB R-22-02, Svensk Kärnbränslehantering AB.

Fälth B, Hökmark H, 2006. Seismically induced slip on rock fractures. Results from dynamic discrete fracture modeling. SKB R-06-48, Svensk Kärnbränslehantering AB.

Fälth B, Hökmark H, Munier R, 2010. Effects of large earthquakes on a KBS-3 repository. Evaluation of modelling results and their implications for layout and design. SKB TR-08-11, Svensk Kärnbränslehantering AB.

Fälth B, Hökmark H, Lund B, Mai P M, Roberts R, Munier R, 2015. Simulating earthquake rupture and off-fault fracture response: Application to the safety assessment of the Swedish nuclear waste repository. *Bulletin of the Seismological Society of America* 105:1. <https://doi.org/10.1785/0120140090>

Fälth B, Hökmark H, Lund B, 2016. Simulation of co-seismic secondary fracture displacements for different earthquake rupture scenarios at the proposed nuclear waste repository site in Forsmark. *International Journal of Rock Mechanics and Mining Sciences* 84, 142–158. <https://doi.org/10.1016/j.ijrmms.2016.02.009>

Gephart J W, Forsyth D W, 1984. An improved method for determining the regional stress tensor using earthquake focal mechanism data: Application to the San Fernando earthquake sequence. *Journal of Geophysical Research* 89:NB11, 9305–9320. <https://doi.org/10.1029/JB089iB11p09305>

Harris R A, Barall M, Archuleta R, Aagaard B, Ampuero J-P, Bhat H, Cruz-Atienza V, Dalguer L, Dawson P, Day S, Duan B, Dunham E, Ely G, Kaneko Y, Kase Y, Lapusta N, Liu Y, Ma S, Oglesby D, Olsen K, Pitarka A, Song S, Templeton E, 2009. The SCEC/USGS Dynamic Earthquake Rupture Code Verification Exercise. *Seismological Research Letters* 80:1, 119–126. <https://doi.org/10.1785/gssrl.80.1.119>

Hökmark H, Fälth B, Wallroth T, 2006. T-H-M couplings in rock. Overview of results of importance to the SR-Can safety assessment. SKB R-06-88, Svensk Kärnbränslehantering AB.

Hökmark H, Lönnqvist M, Kristensson O, Sundberg J, Hellström G, 2009. Strategy for thermal dimensioning of the final repository for spent nuclear fuel. Version 1.0. SKB R-09-04, Svensk Kärnbränslehantering AB.

Hökmark H, Lönnqvist M, Fälth B, 2010. THM-issues in repository rock. Thermal, mechanical, thermo-mechanical and hydro-mechanical evolution of the rock at the Forsmark and Laxemar sites. SKB TR-10-23, Svensk Kärnbränslehantering AB.

Itasca, 2019. *FLAC3D – Fast Lagrangian Analysis of Continua in 3 Dimensions*, version 7. Minneapolis, MN: Itasca Consulting Group, Inc.

Itasca, 2020. *3DEC – 3-Dimensional Distinct Element Code*, version 7. Itasca Consulting Group Inc. Minneapolis, MN: Itasca Consulting Group, Inc.

Itasca, 2021. PFC– Particle Flow Code, version 7. Minneapolis, MN: Itasca Consulting Group, Inc.

Itasca, 2022. FLAC3D – Fast Lagrangian Analysis of Continua in 3 Dimensions, version 9. Minneapolis, MN: Itasca Consulting Group, Inc.

Jaeger J C, Cook N G W, 1979. Fundamentals of rock mechanics. 3rd ed. Science London: Paperbacks/Chapman and Hall.

Lönnqvist M, Hökmark H, 2015. Thermal and thermo-mechanical evolution of the Äspö Prototype Repository rock mass. Modelling and assessment of sensors data undertaken in connection with the dismantling of the outer section. R-13-10, Svensk Kärnbränslehantering AB.

Probert T, Claesson J, 1997. Thermoelastic stress due to a rectangular heat source in a semi-infinite medium. Application for the KBS-3 repository. SKB TR 97-26, Svensk Kärnbränslehantering AB.

Segedin C M, 1951. Note on a penny-shaped crack under shear. Mathematical Proceedings of the Cambridge Philosophical Society 47: 2, 396–400. <https://doi.org/10.1017/S0305004100026736>

Results from multiple-fracture model (Chapter 3)

Single_joint case

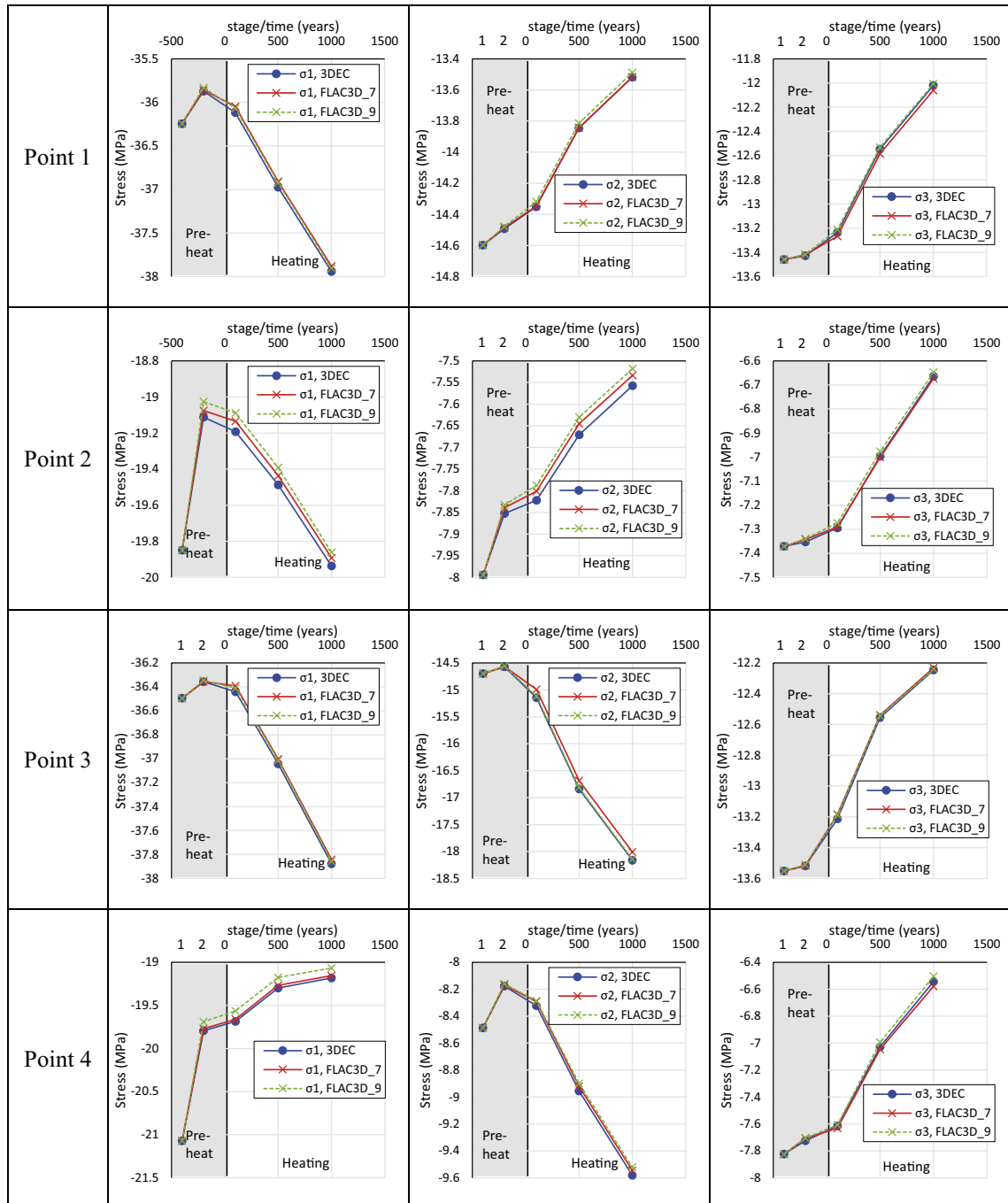


Figure A1-1. Evolution of principal stresses at monitoring points 1 to 4 in the Single_joint case.

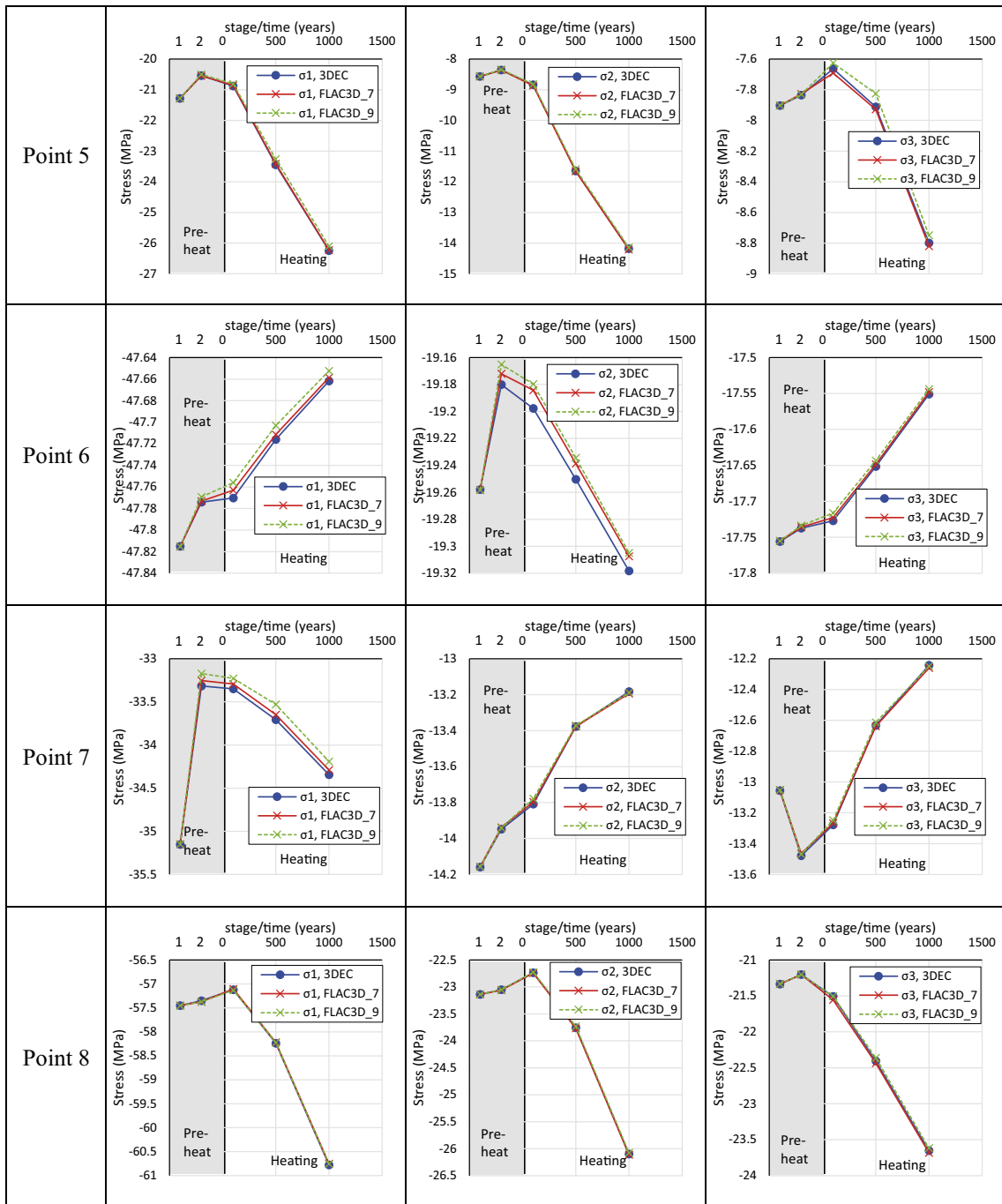


Figure A1-2. Evolution of principal stresses at monitoring points 5 to 8 in the Single joint case.

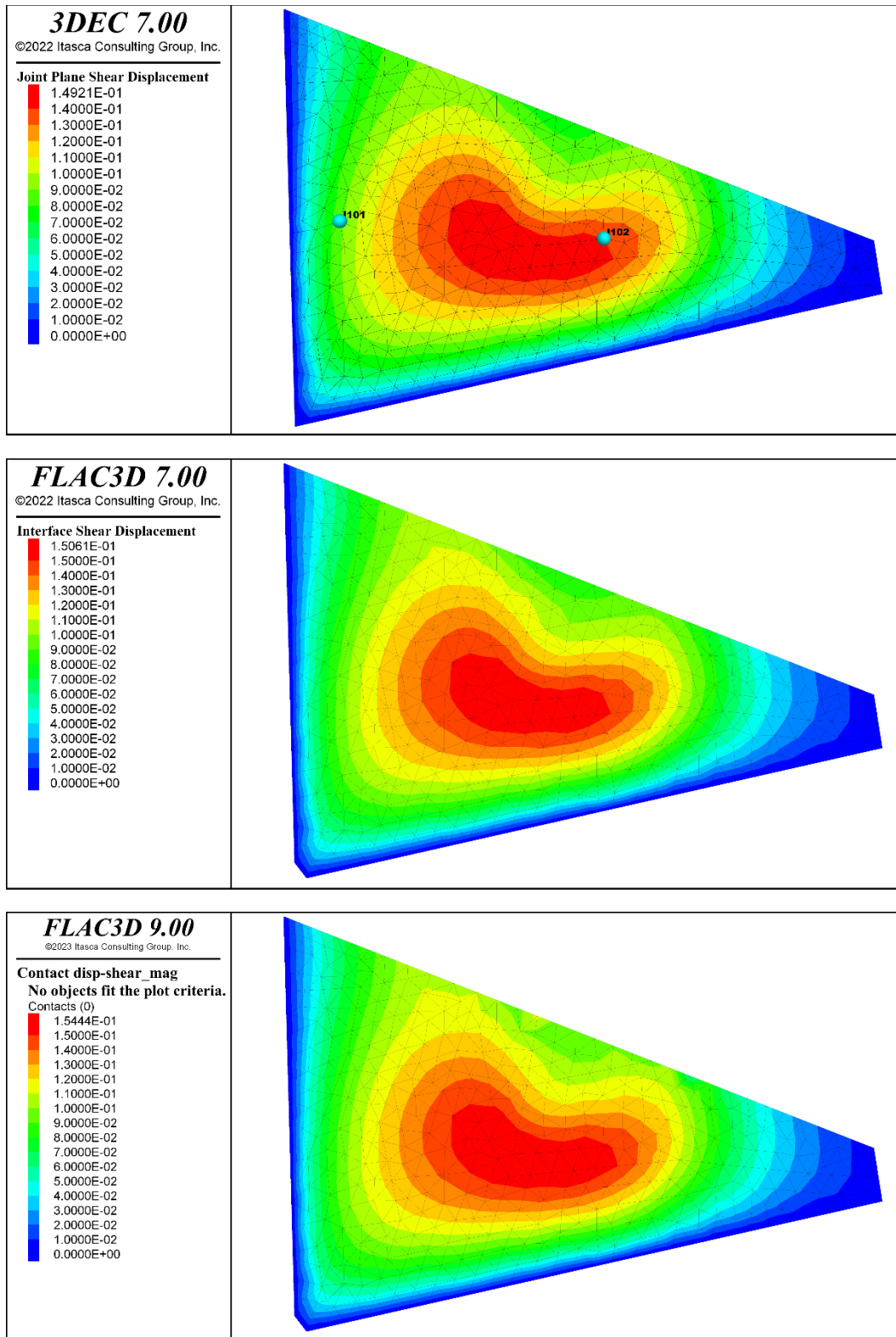


Figure A1-3. Shear displacements on joint 1000 after completed simulation in the Single_joint case. Shear displacement evolution at the two points indicated in the upper plot is shown in Figure A1-5.

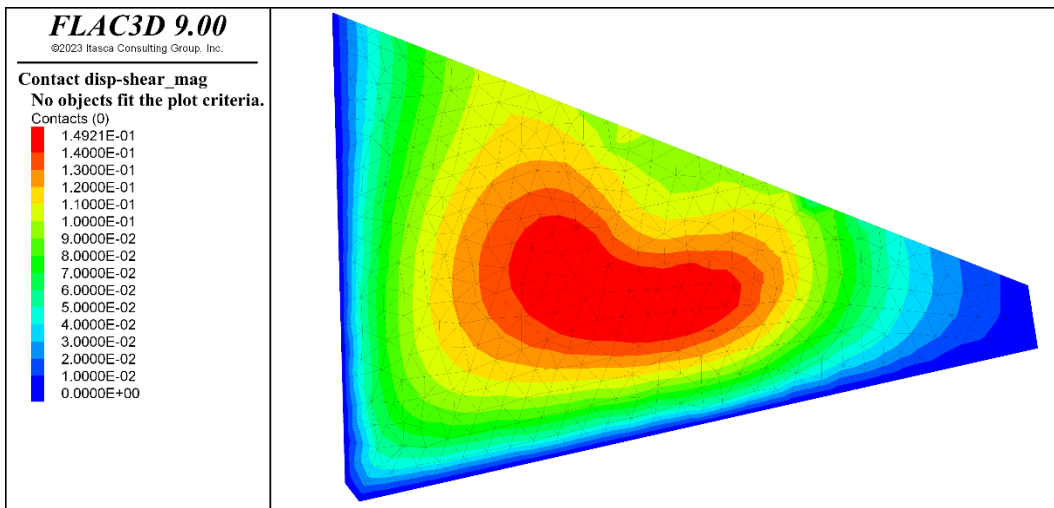
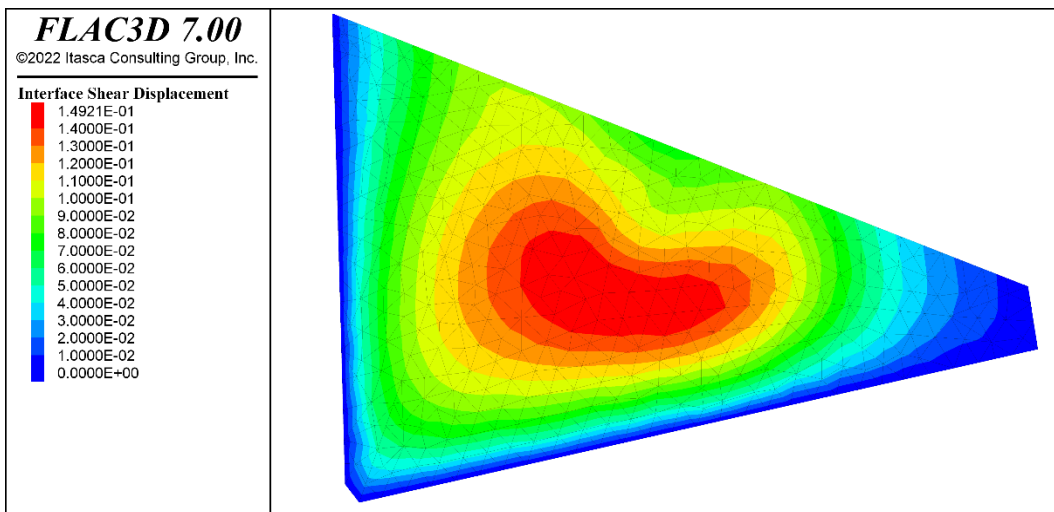
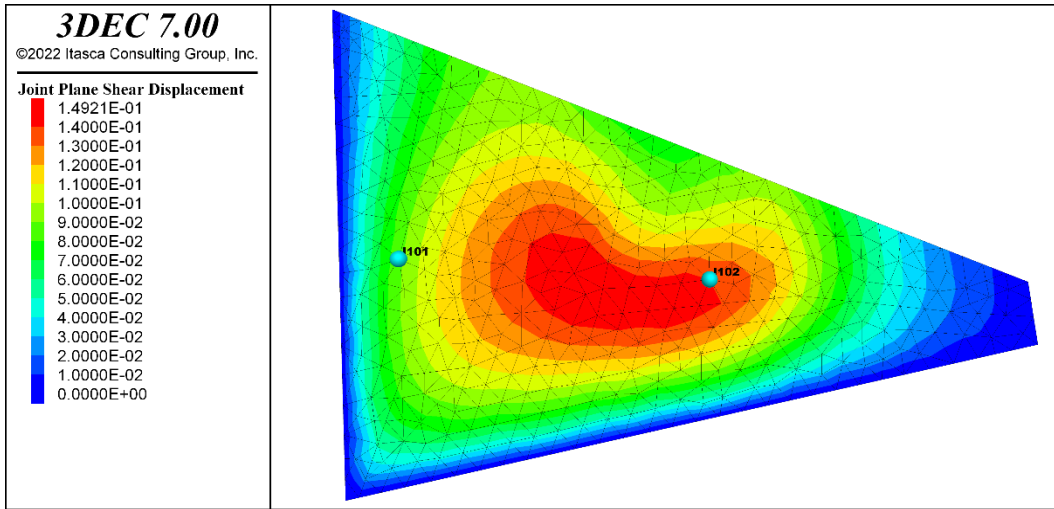


Figure A1-4. Same results as in Figure A1-3 but with same colour scale in all plots.

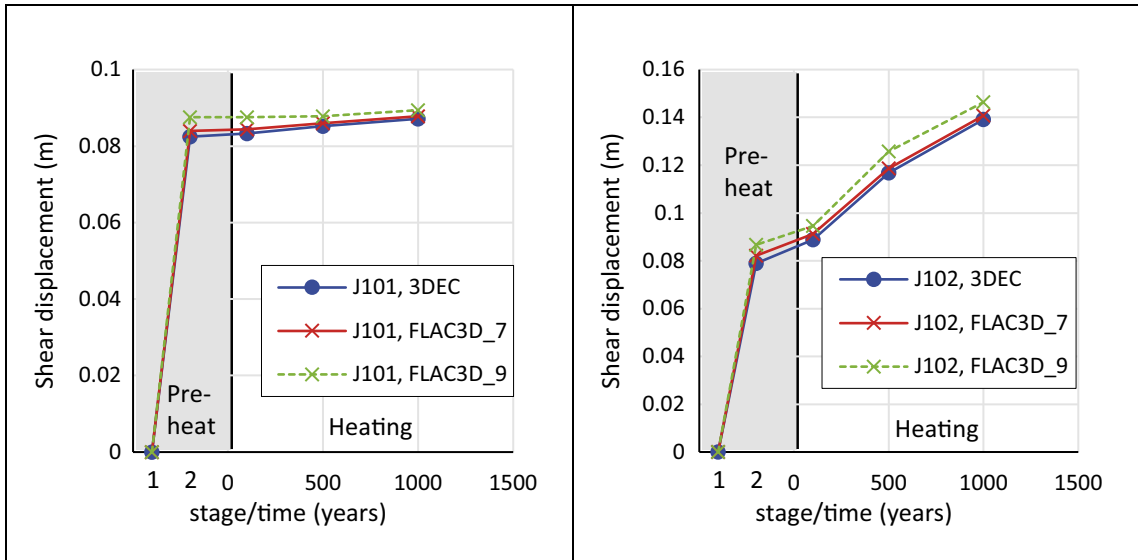


Figure A1-5. Evolution of joint 1000 shear displacement at the two points depicted in the upper plot of Figure A1-3.

Double joint case

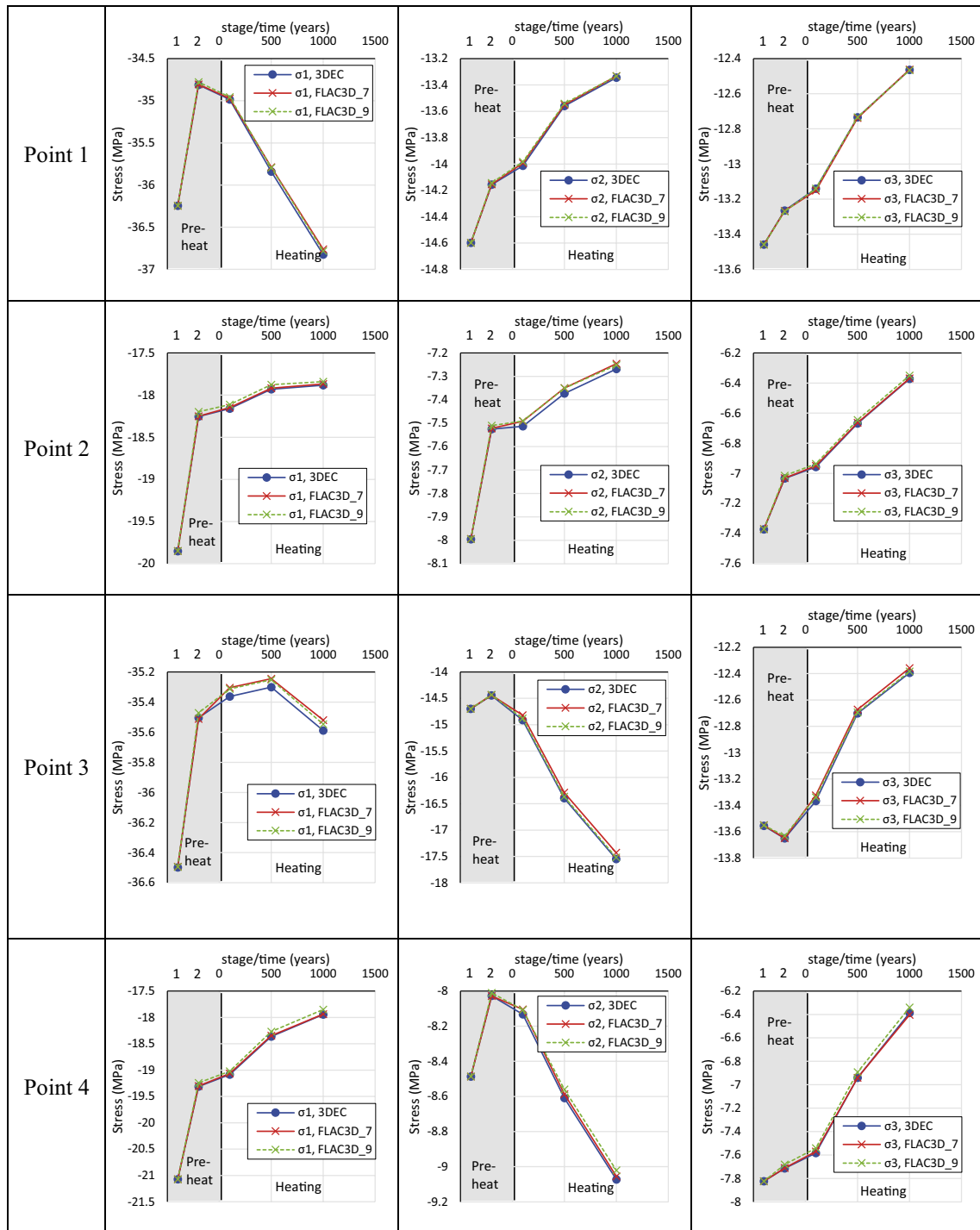


Figure A1-6. Evolution of principal stresses at monitoring points 1 to 4 in the Double joint case.

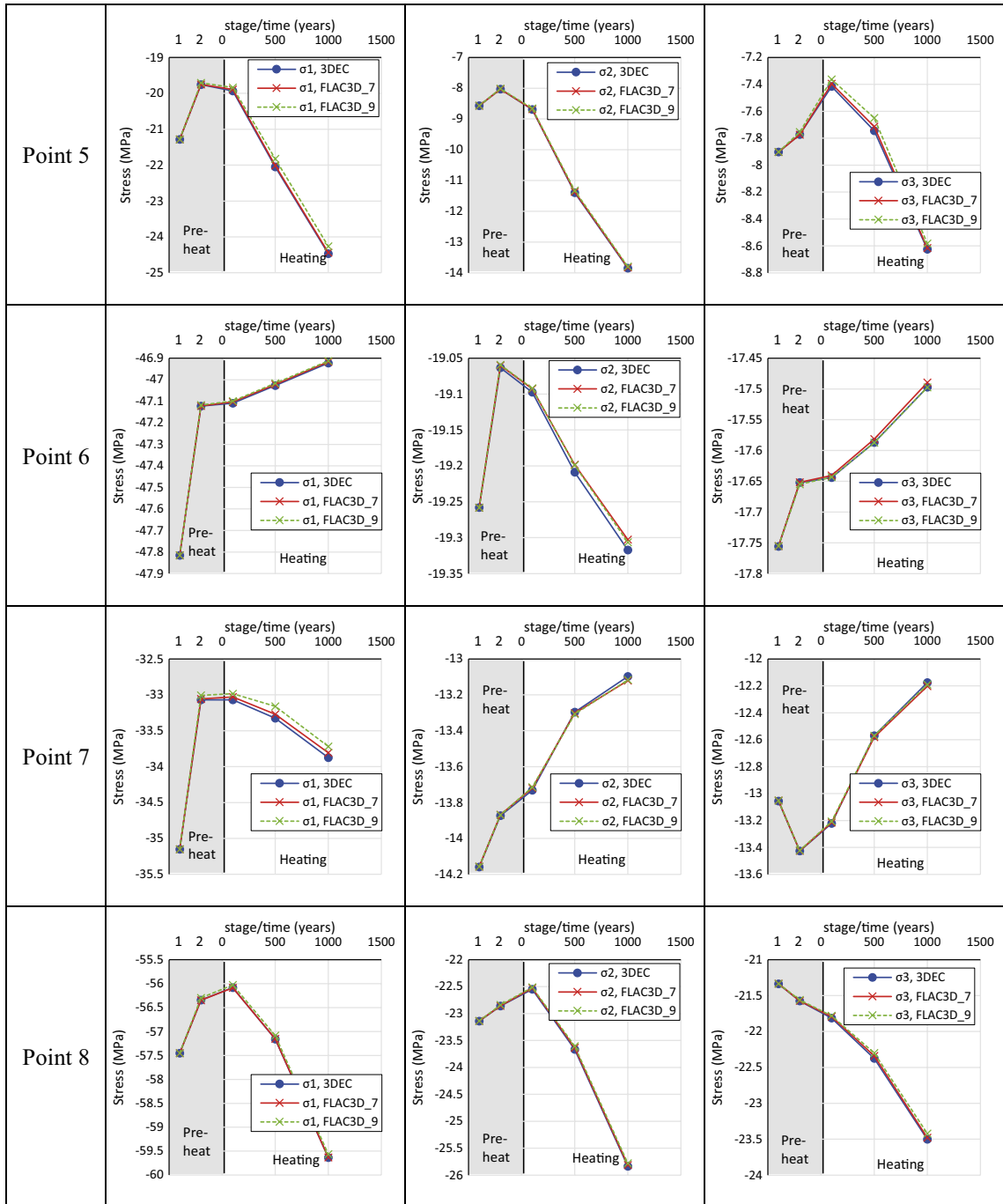


Figure A1-7. Evolution of principal stresses at monitoring points 5 to 8 in the Double joint case.

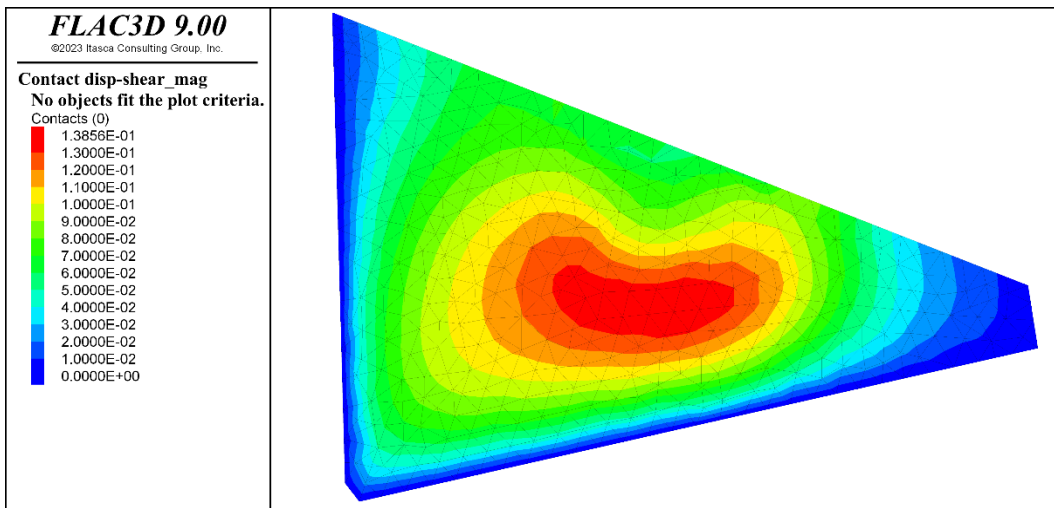
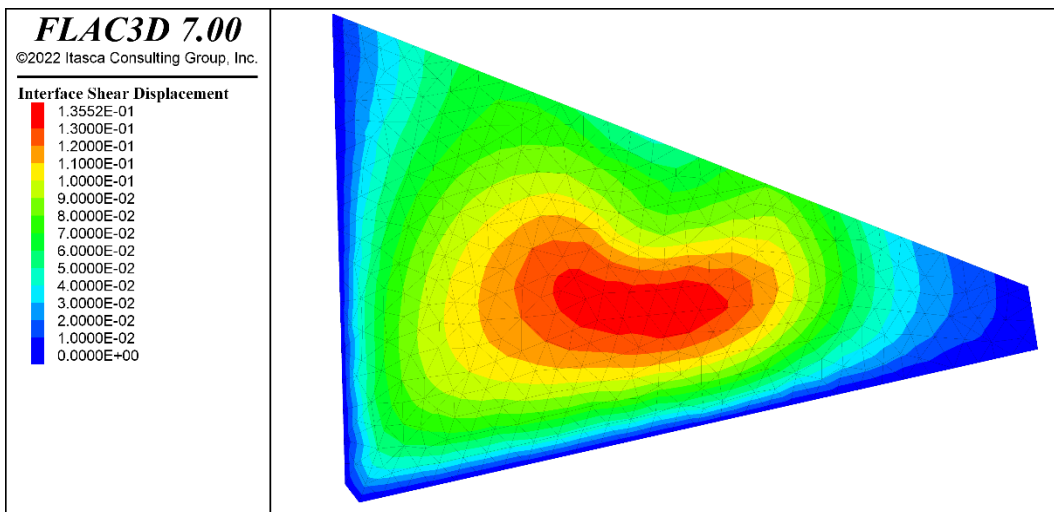
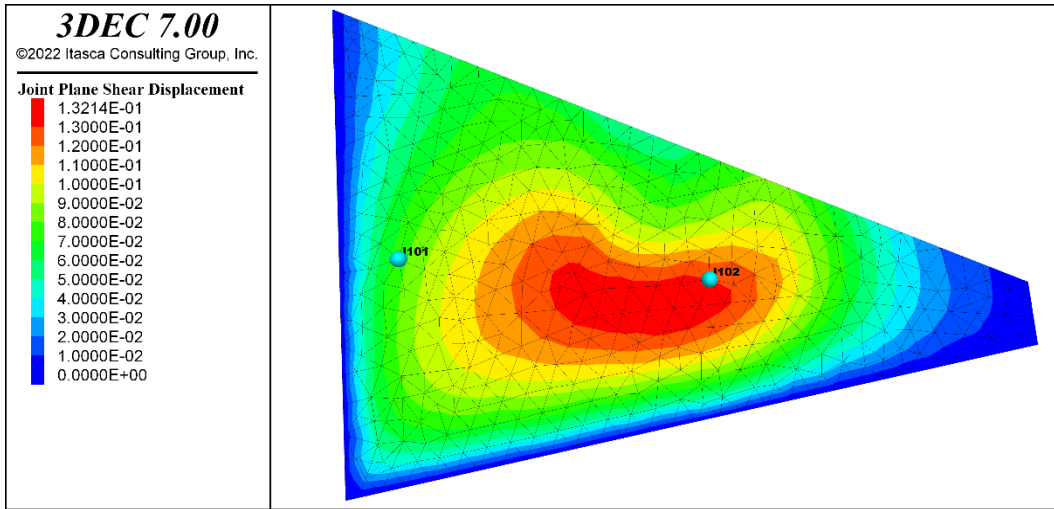


Figure A1-8. Shear displacements on joint 1000 after completed simulation in the Double_joint case. Shear displacement evolution at the two points indicated in the upper plot is shown in Figure A1-12.

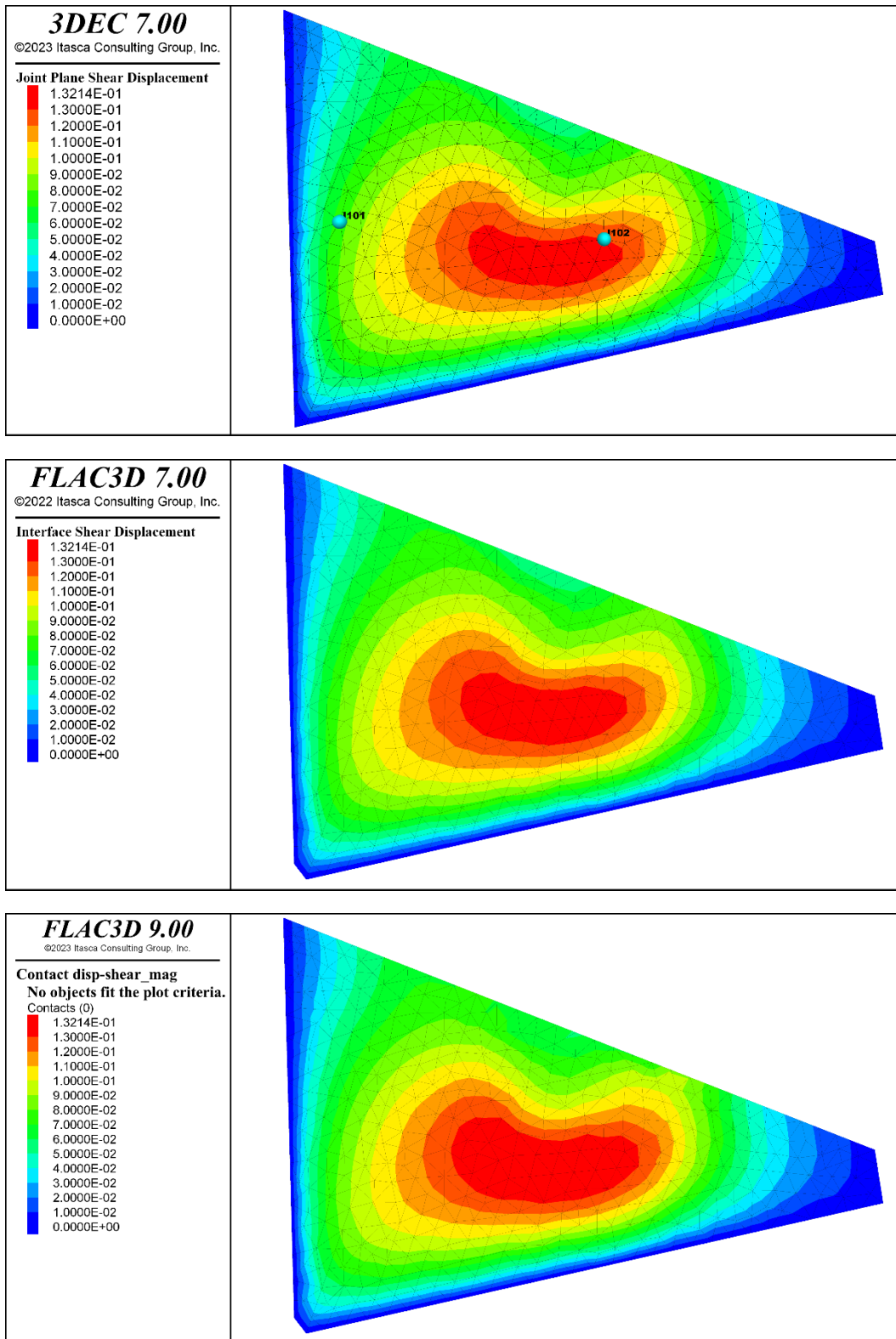


Figure A1-9. Same results as in Figure A1-8 but with same colour scale in all plots.

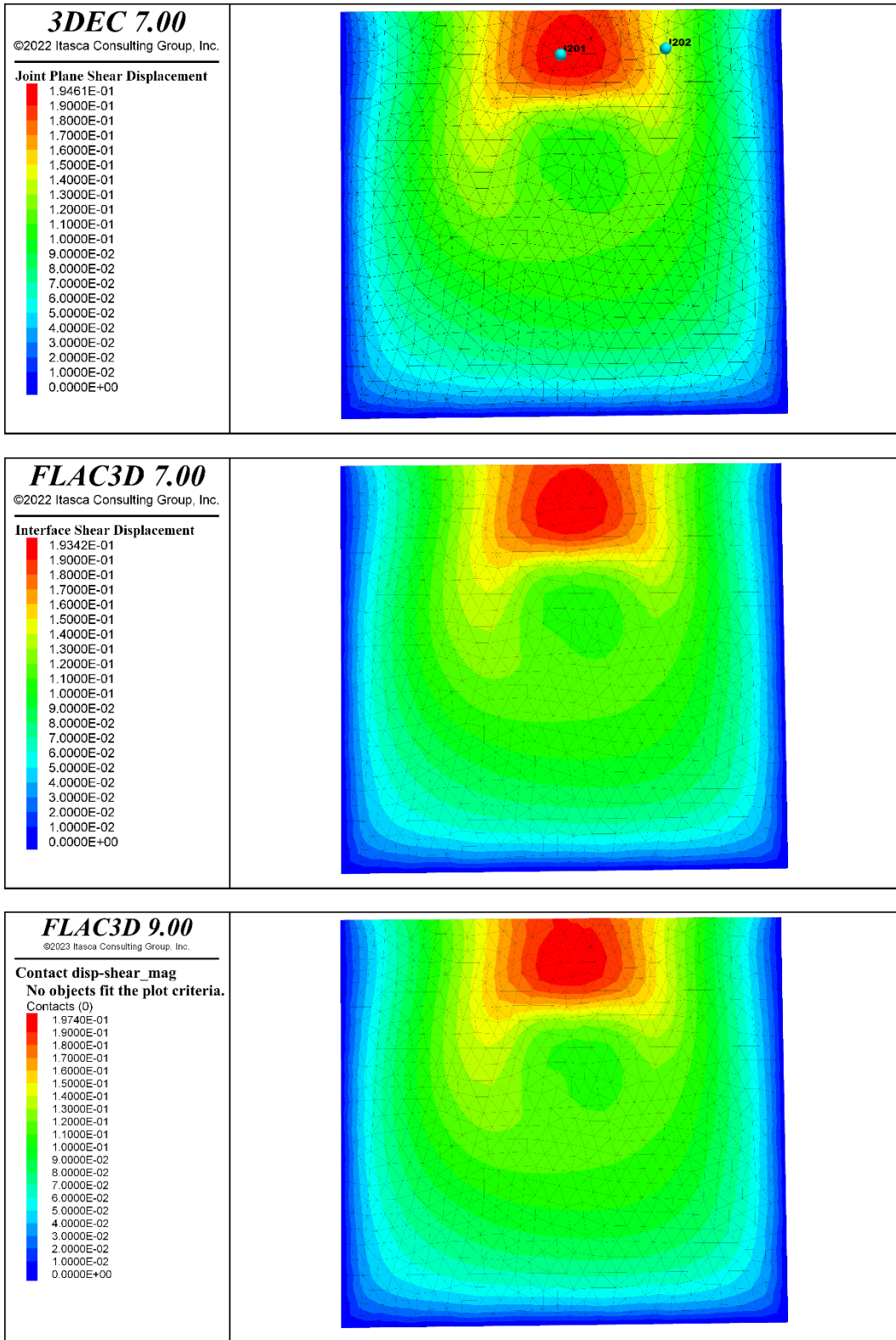


Figure A1-10. Shear displacements on joint 2000 after completed simulation in the Double joint case. Shear displacement evolution at the two points indicated in the upper plot is shown in Figure A1-13.

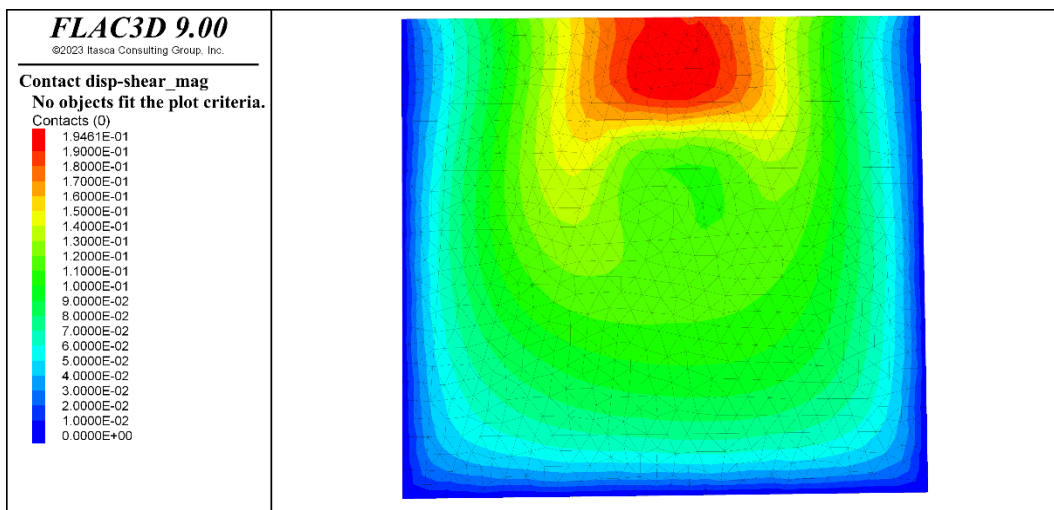
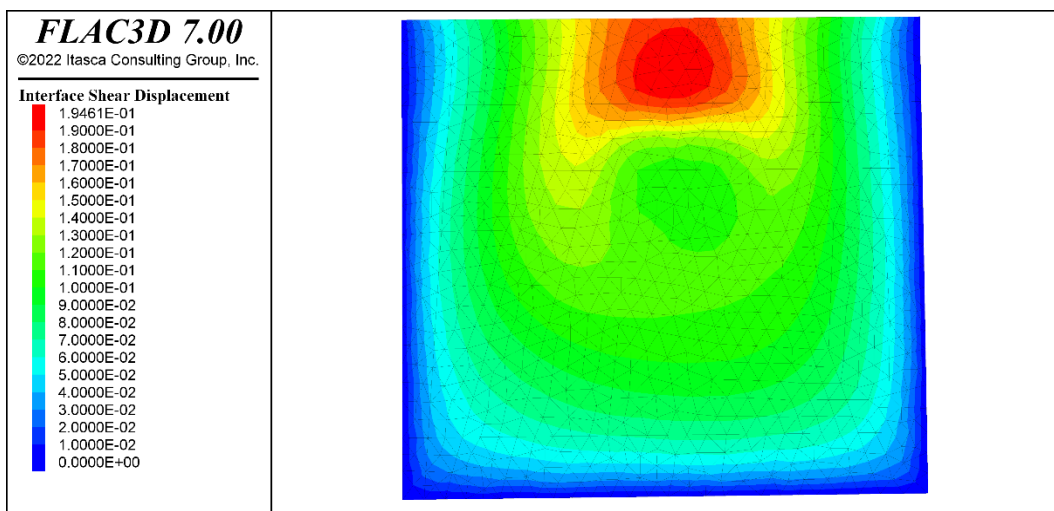
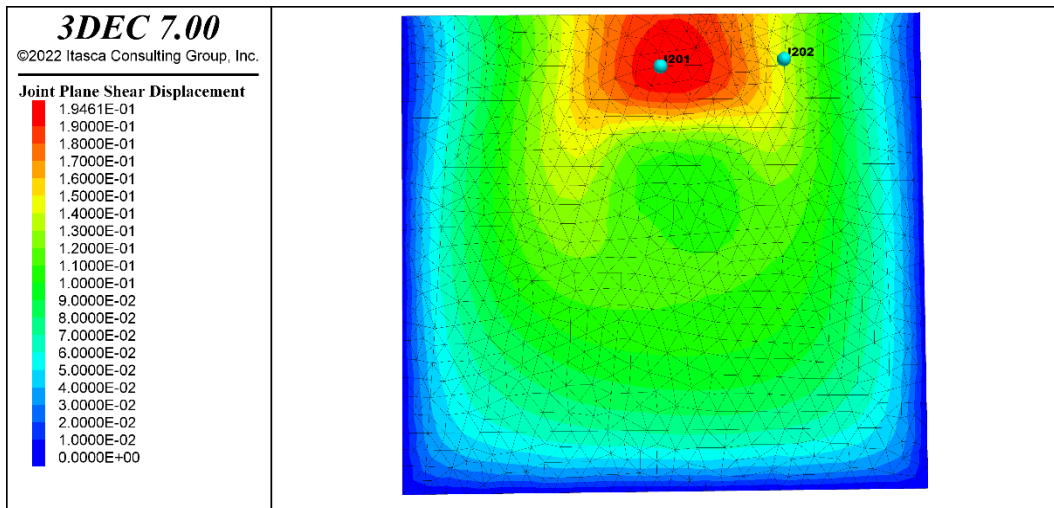


Figure A1-11. Same results as in Figure A1-10 but with same colour scale in all plots.

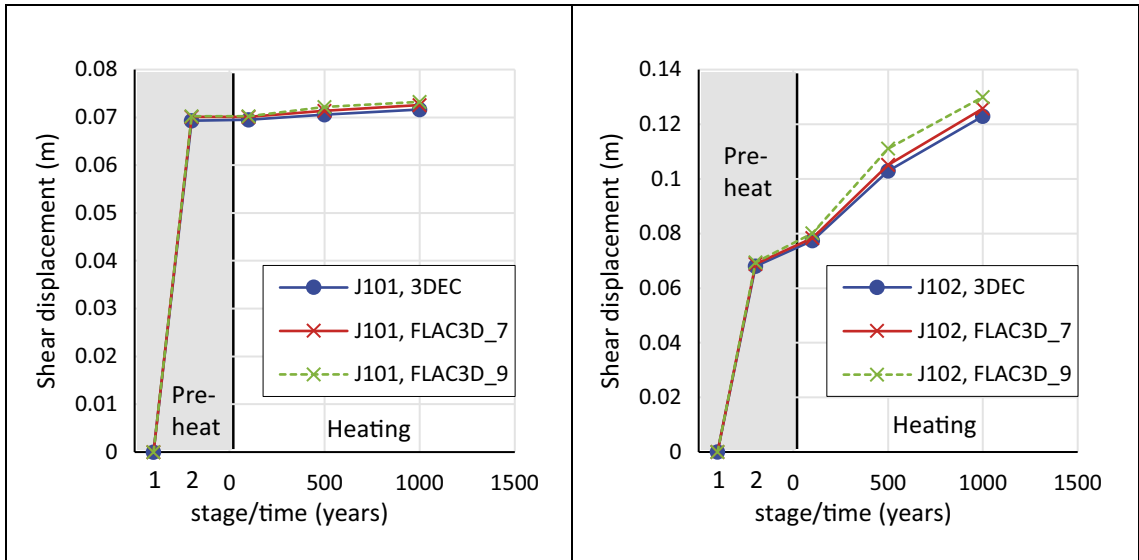


Figure A1-12. Evolution of joint 1000 shear displacement at the two points depicted in the upper plot of Figure A1-8.

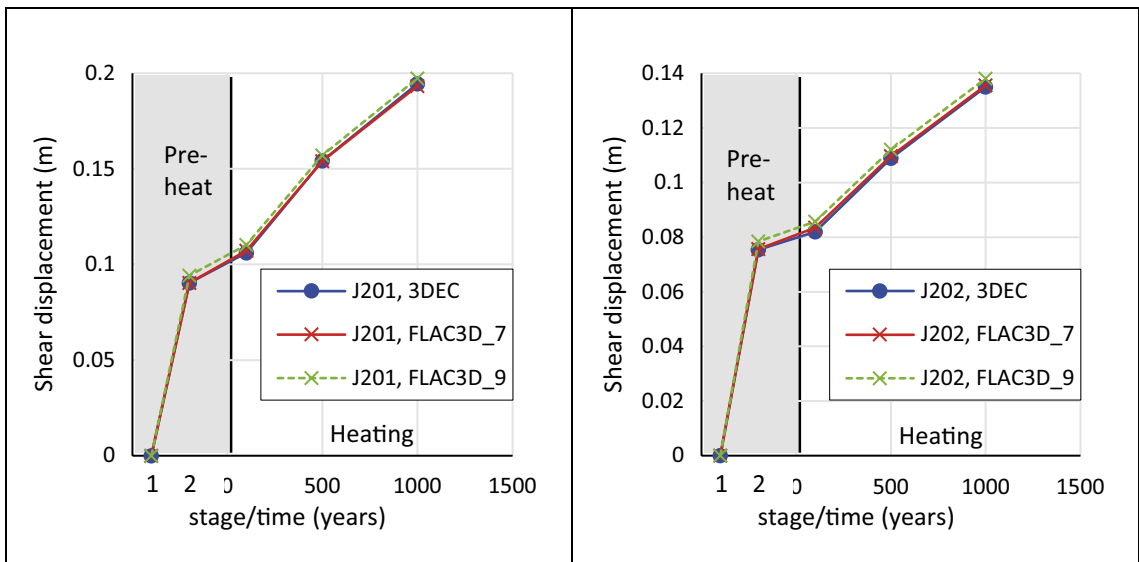


Figure A1-13. Evolution of joint 2000 shear displacement at the two points depicted in the upper plot of Figure A1-10.

Triple_joint case

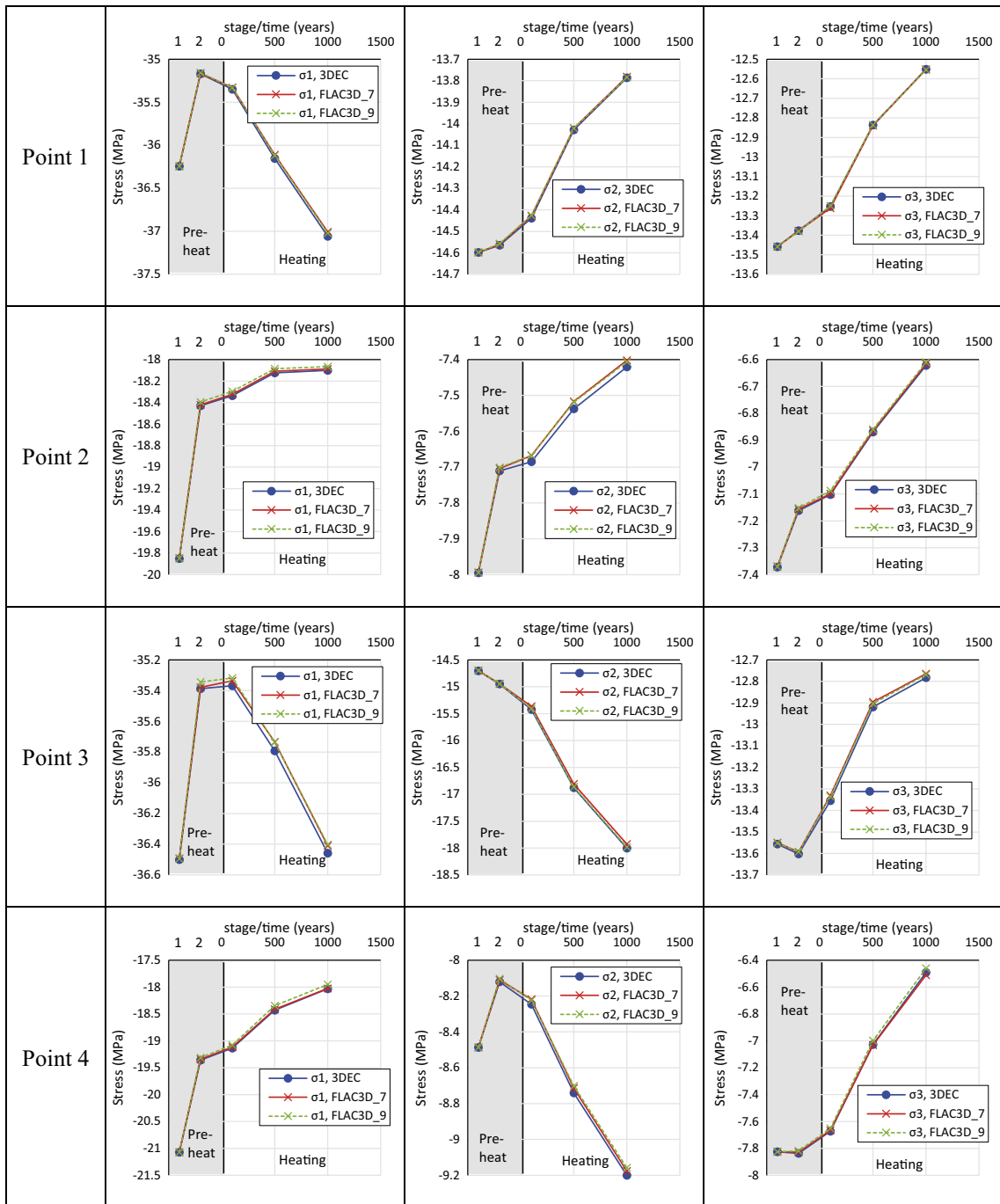


Figure A1-14. Evolution of principal stresses at monitoring points 1 to 4 in the Triple_joint case.

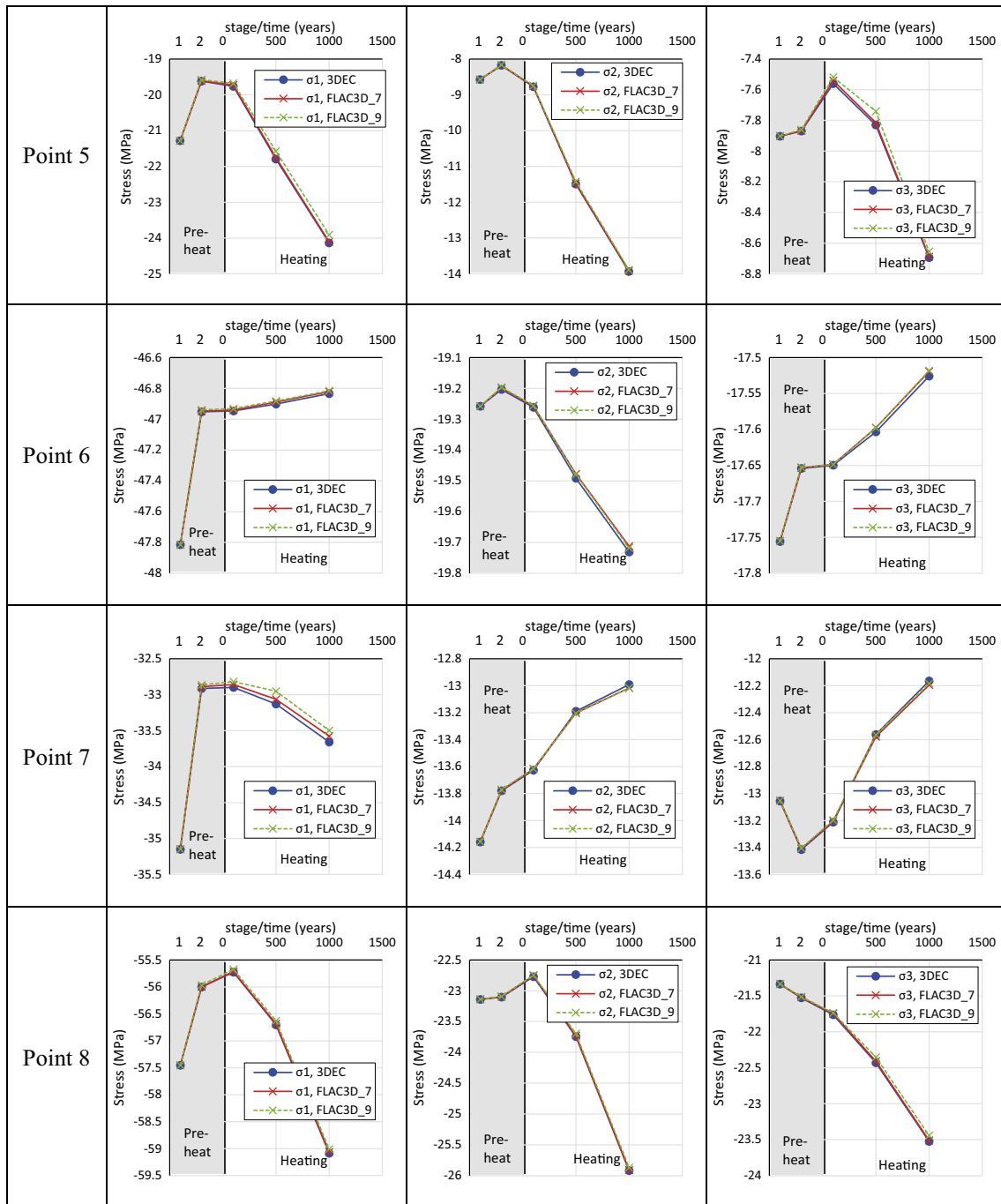


Figure A1-15. Evolution of principal stresses at monitoring points 5 to 8 in the Triple joint case.

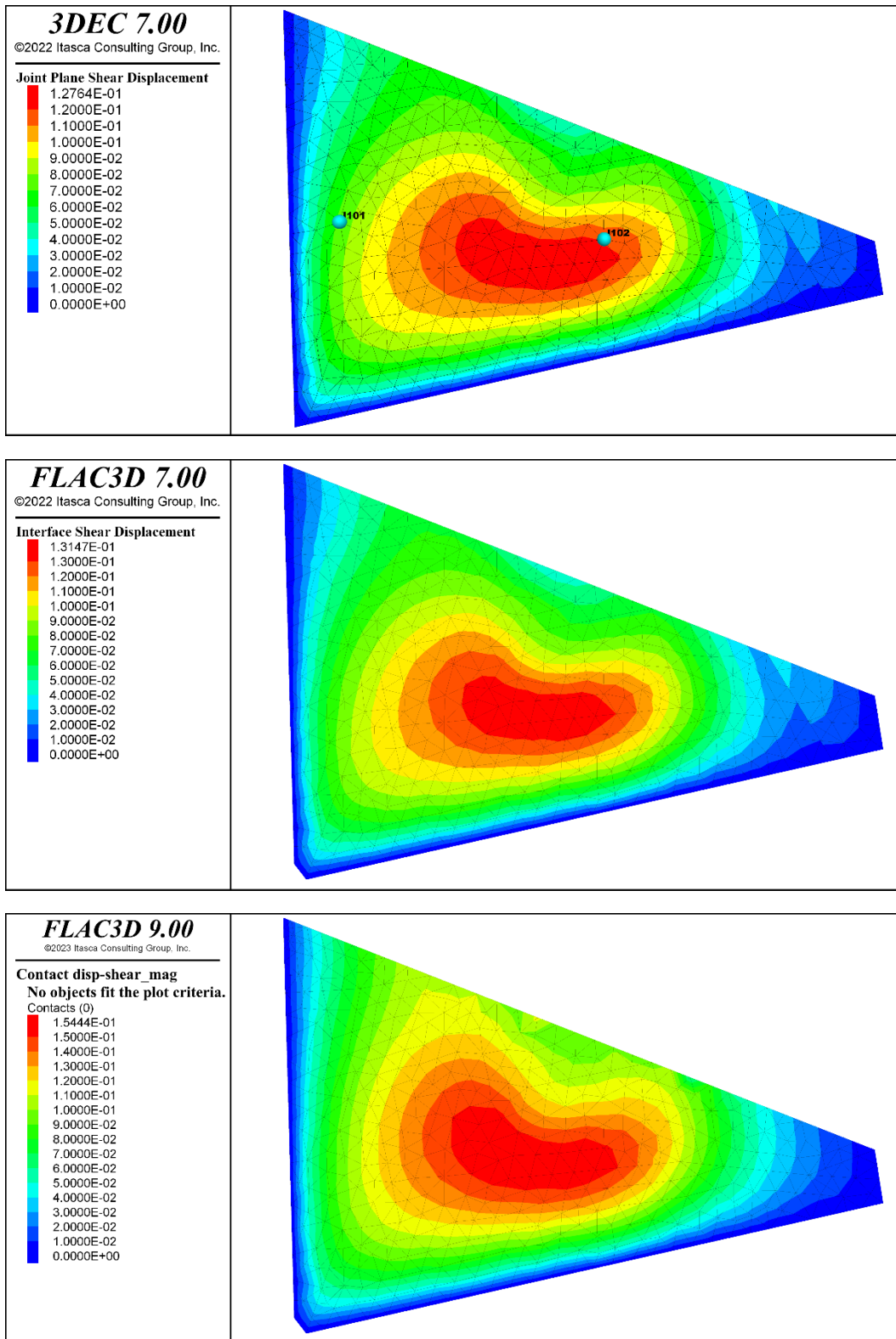


Figure A1-16. Shear displacements on joint 1000 after completed simulation in the Triple_joint case. Shear displacement evolution at the two points indicated in the upper plot is shown in Figure A1-22.

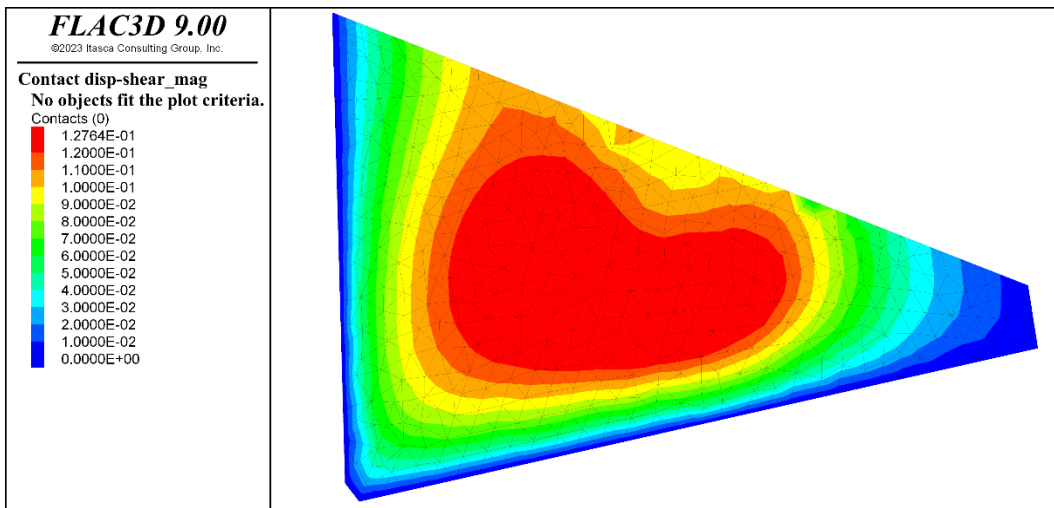
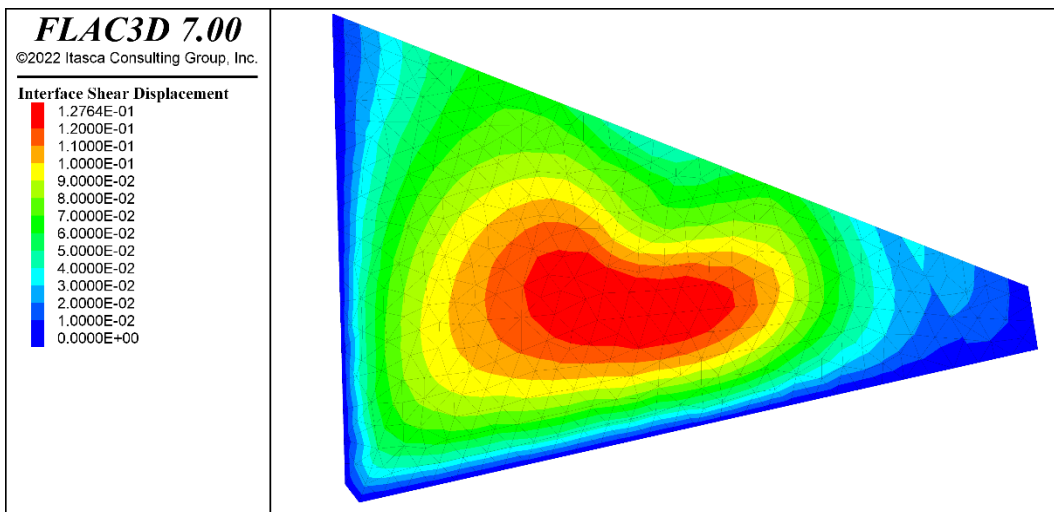
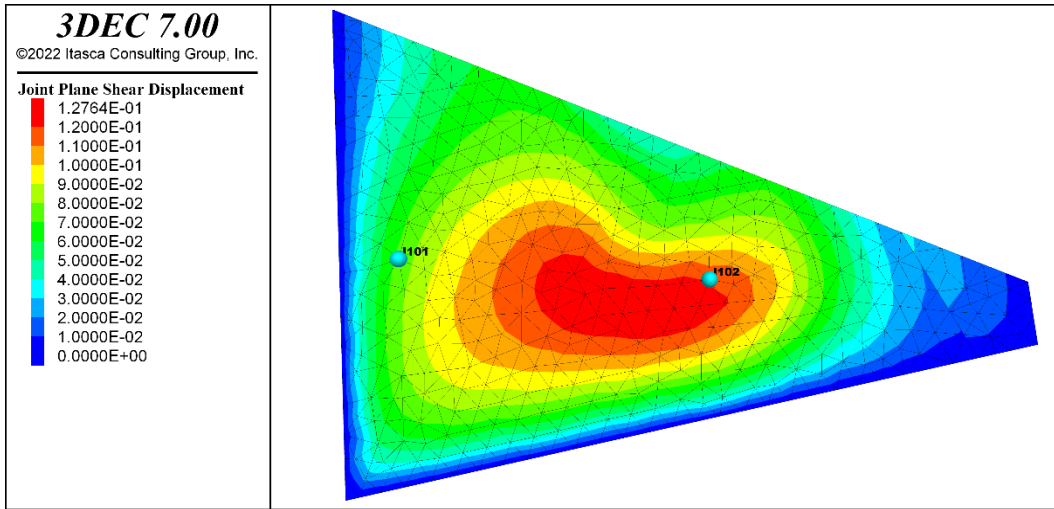


Figure A1-17. Same results as in Figure A1-16 but with same colour scale in all plots.

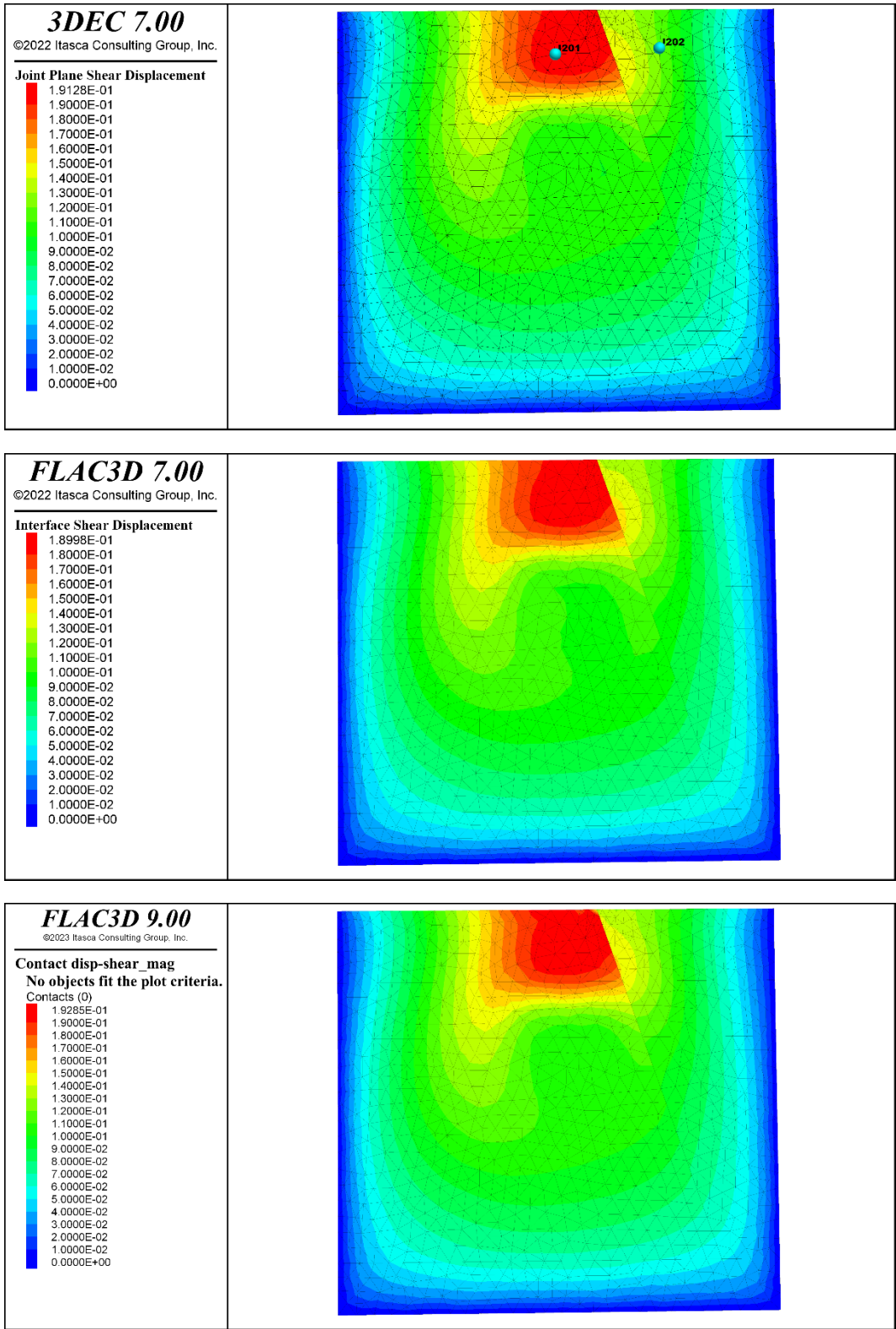


Figure A1-18. Shear displacements on joint 2000 after completed simulation in the Triple_joint case. Shear displacement evolution at the two points indicated in the upper plot is shown in Figure A1-23.

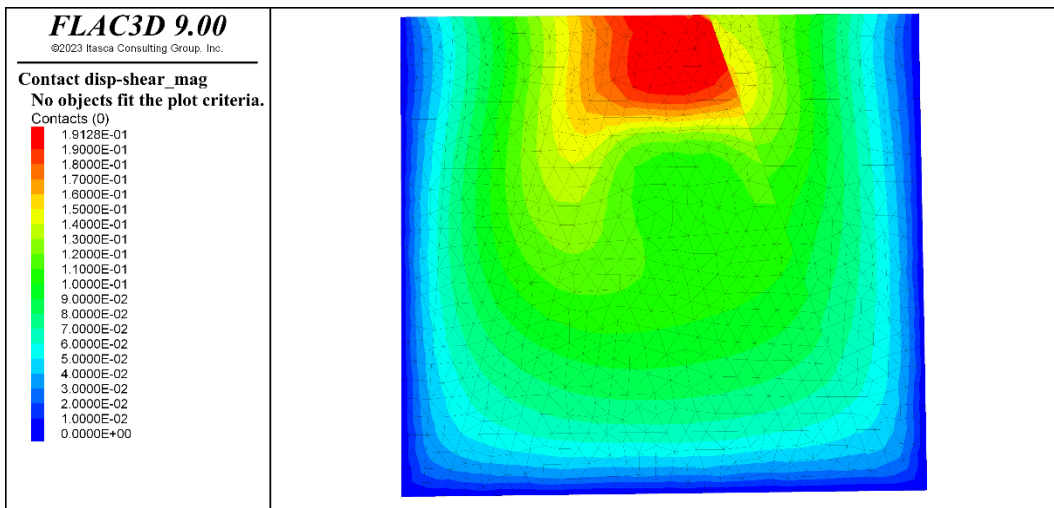
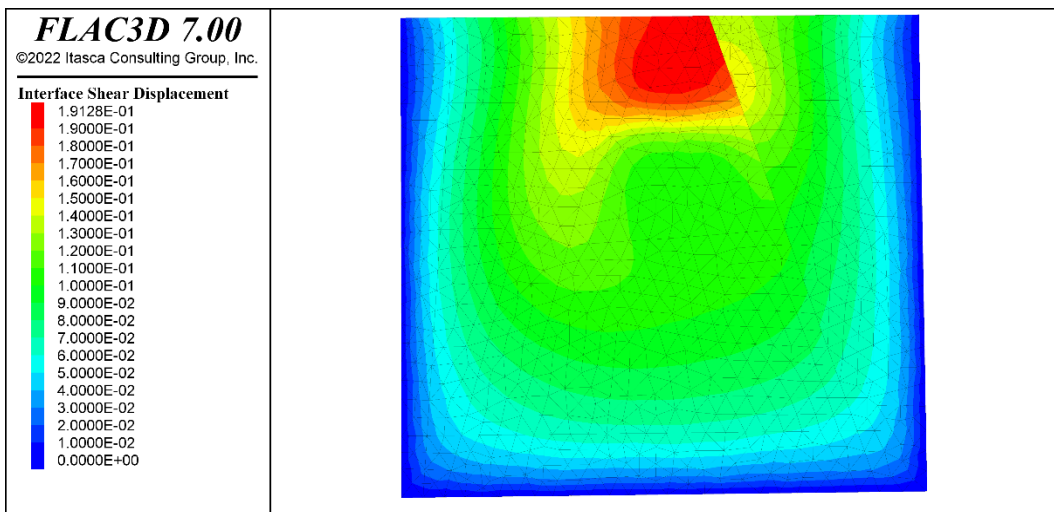
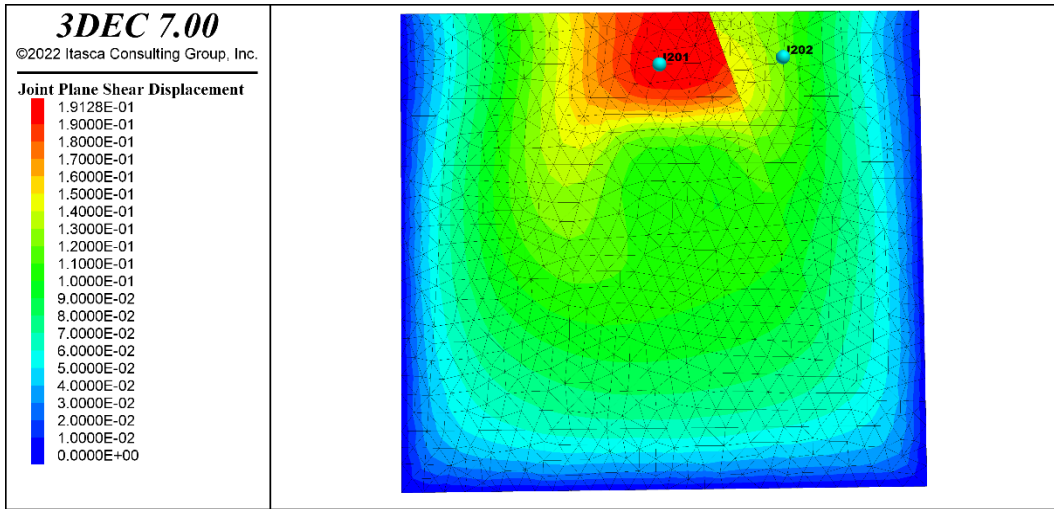


Figure A1-19. Same results as in Figure A1-18 but with same colour scale in all plots.

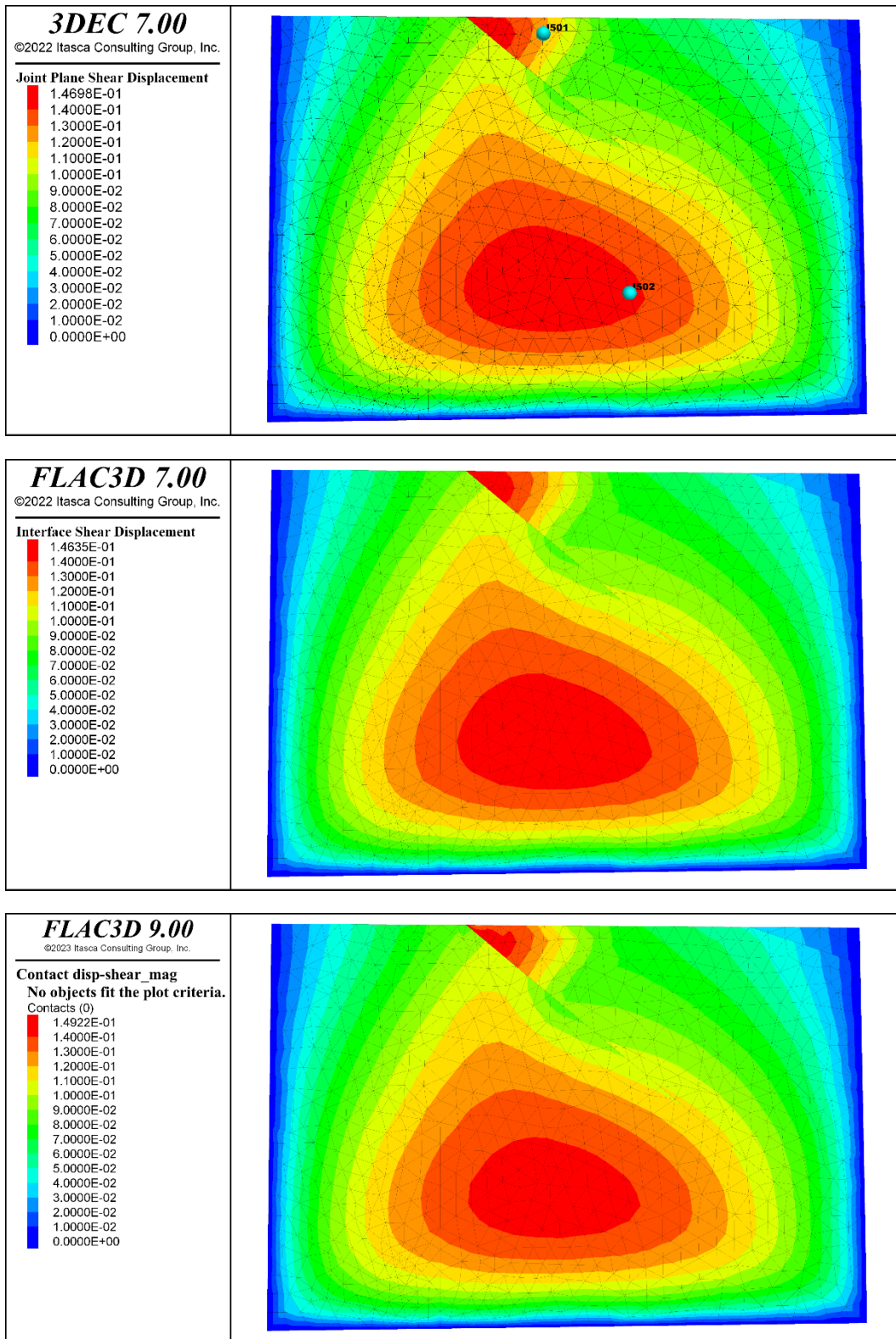


Figure A1-20. Shear displacements on joint 5000 after completed simulation in the Triple_joint case. Shear displacement evolution at the two points indicated in the upper plot is shown in Figure A1-24.

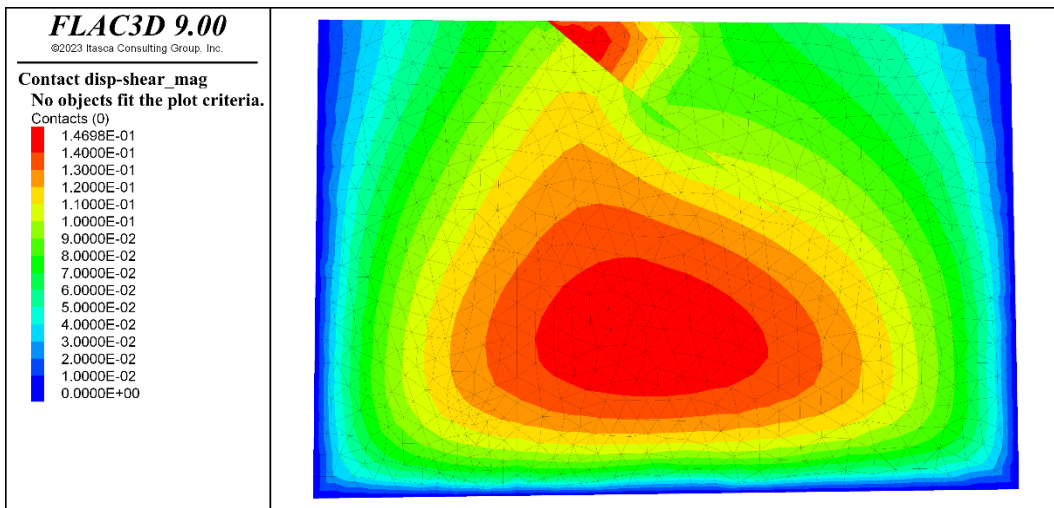
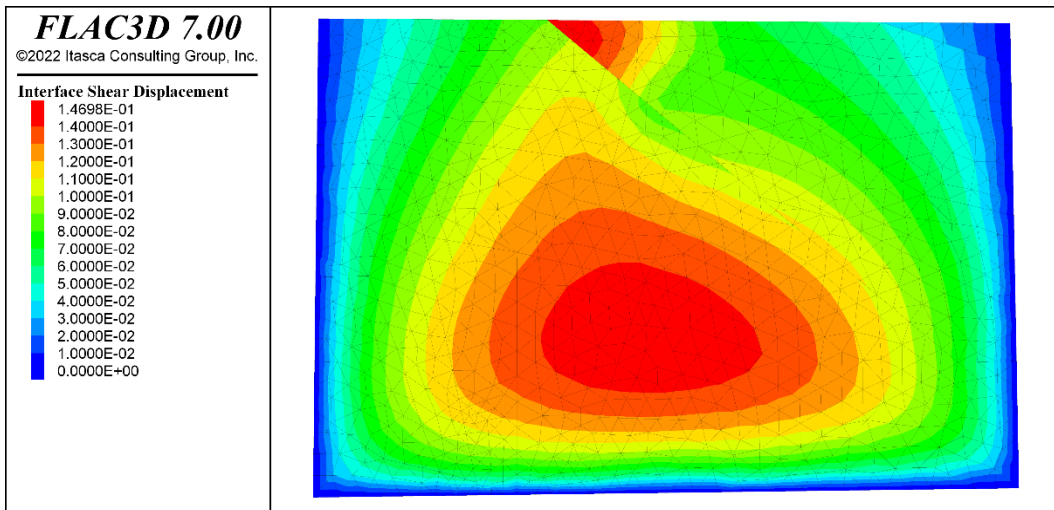
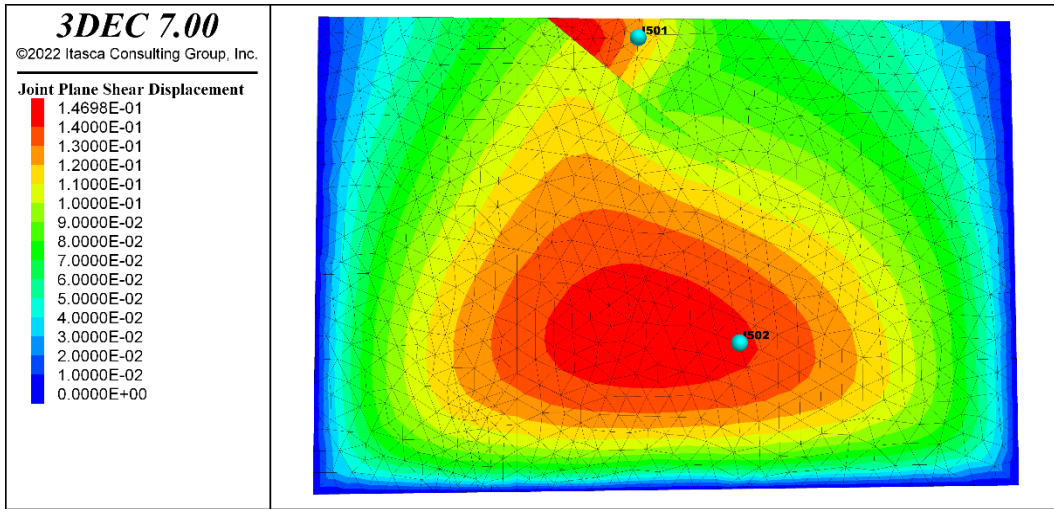


Figure A1-21. Same results as in Figure A1-20 but with same colour scale in all plots.

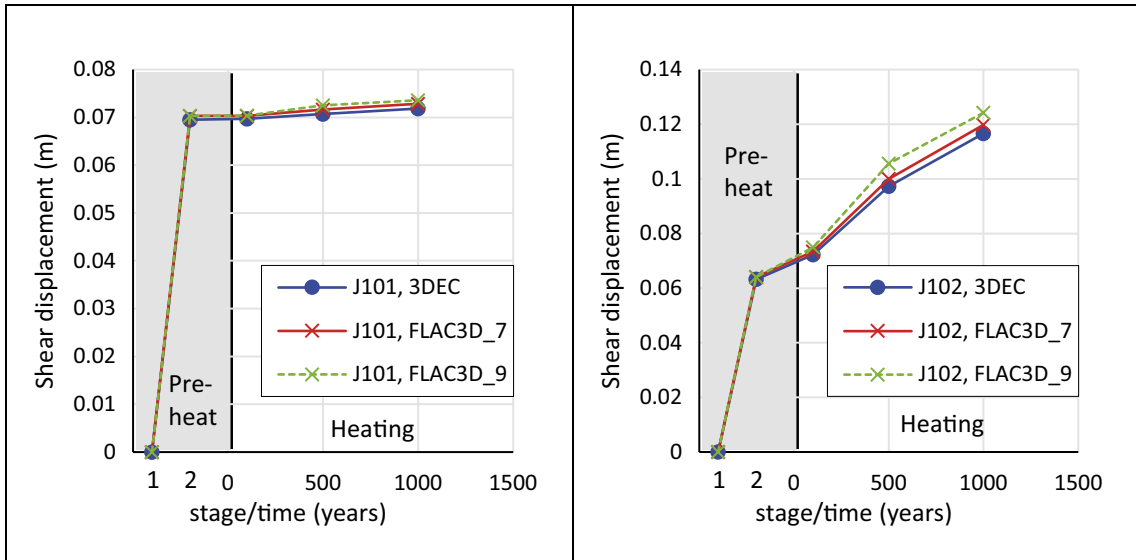


Figure A1-22. Evolution of joint 1000 shear displacement at the two points depicted in the upper plot of Figure A1-16.

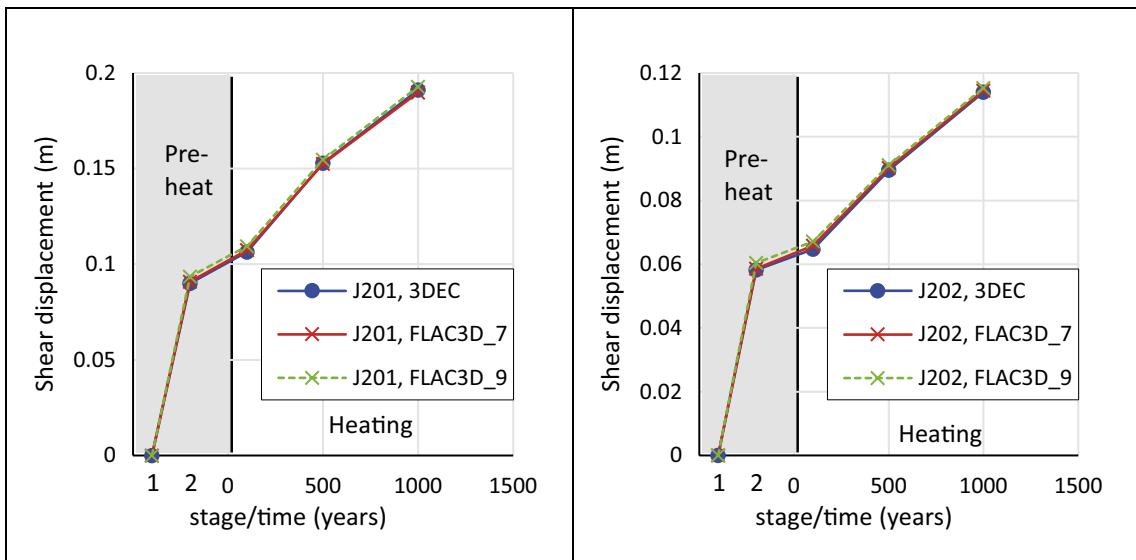


Figure A1-23. Evolution of joint 2000 shear displacement at the two points depicted in the upper plot of Figure A1-18.

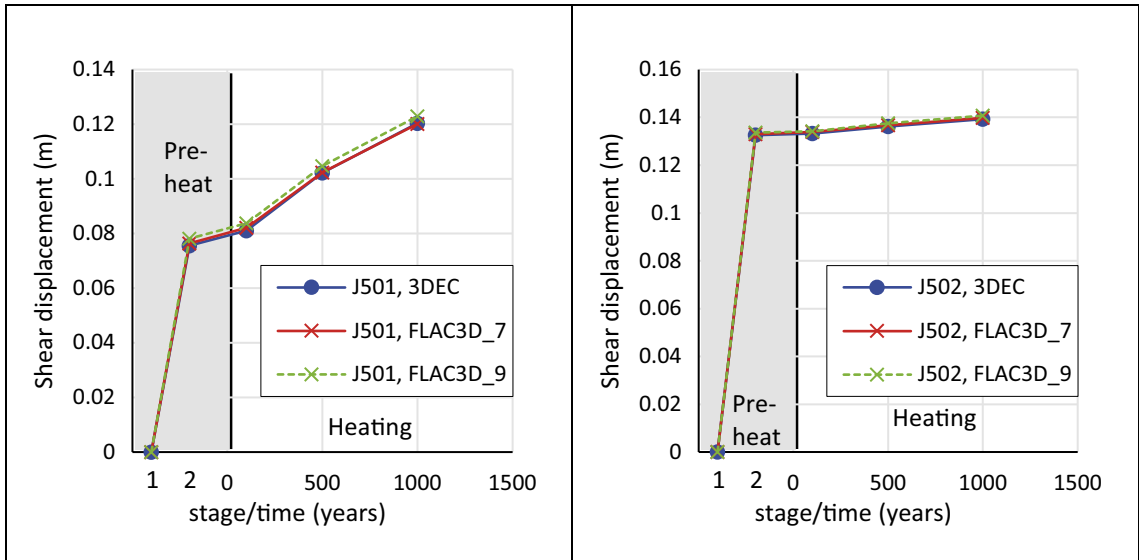


Figure A1-24. Evolution of joint 5000 shear displacement at the two points depicted in the upper plot of Figure A1-20.

Multiple_joint case

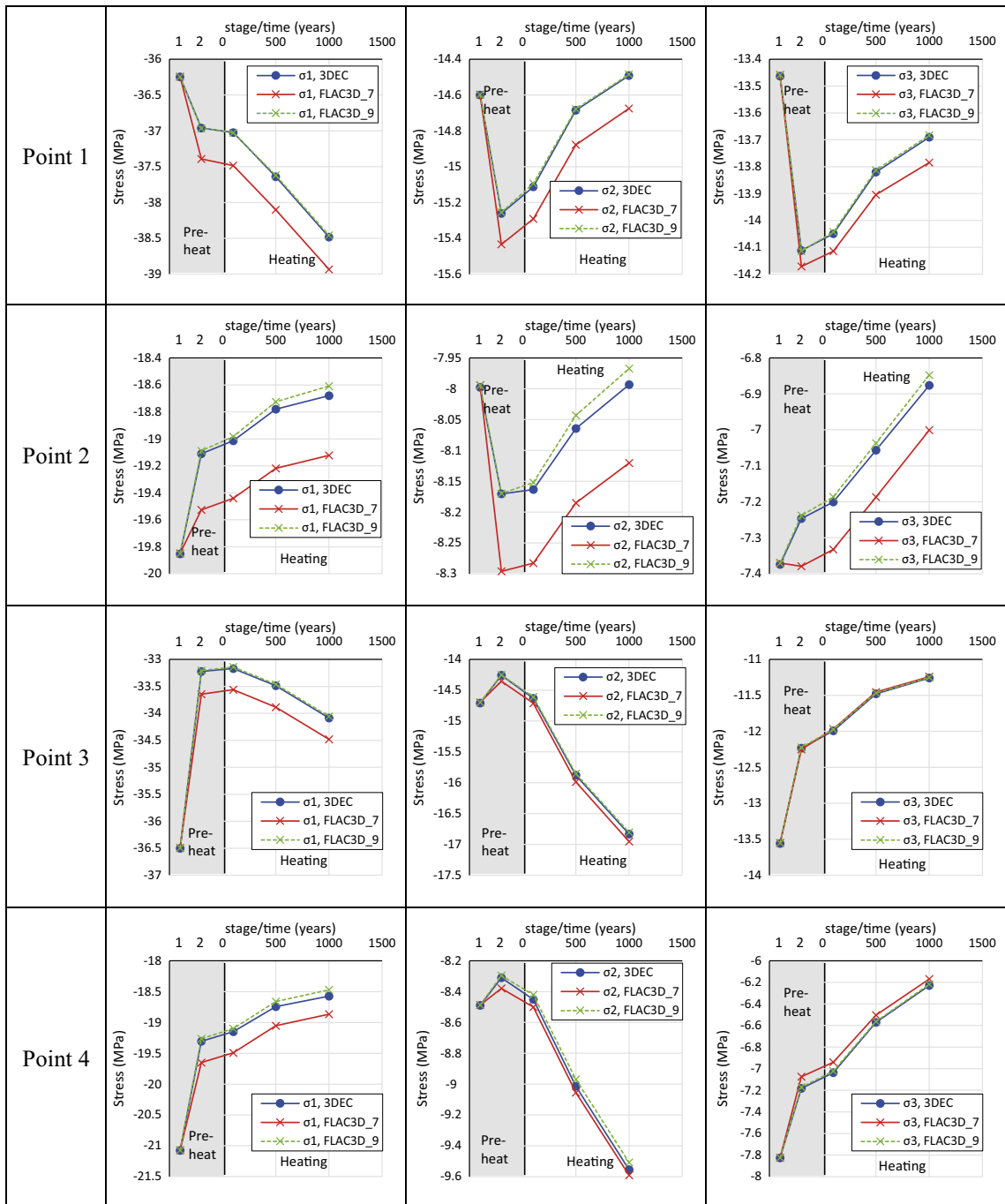


Figure A1-25. Evolution of principal stresses at monitoring points 1 to 4 in the Multiple_joint case.

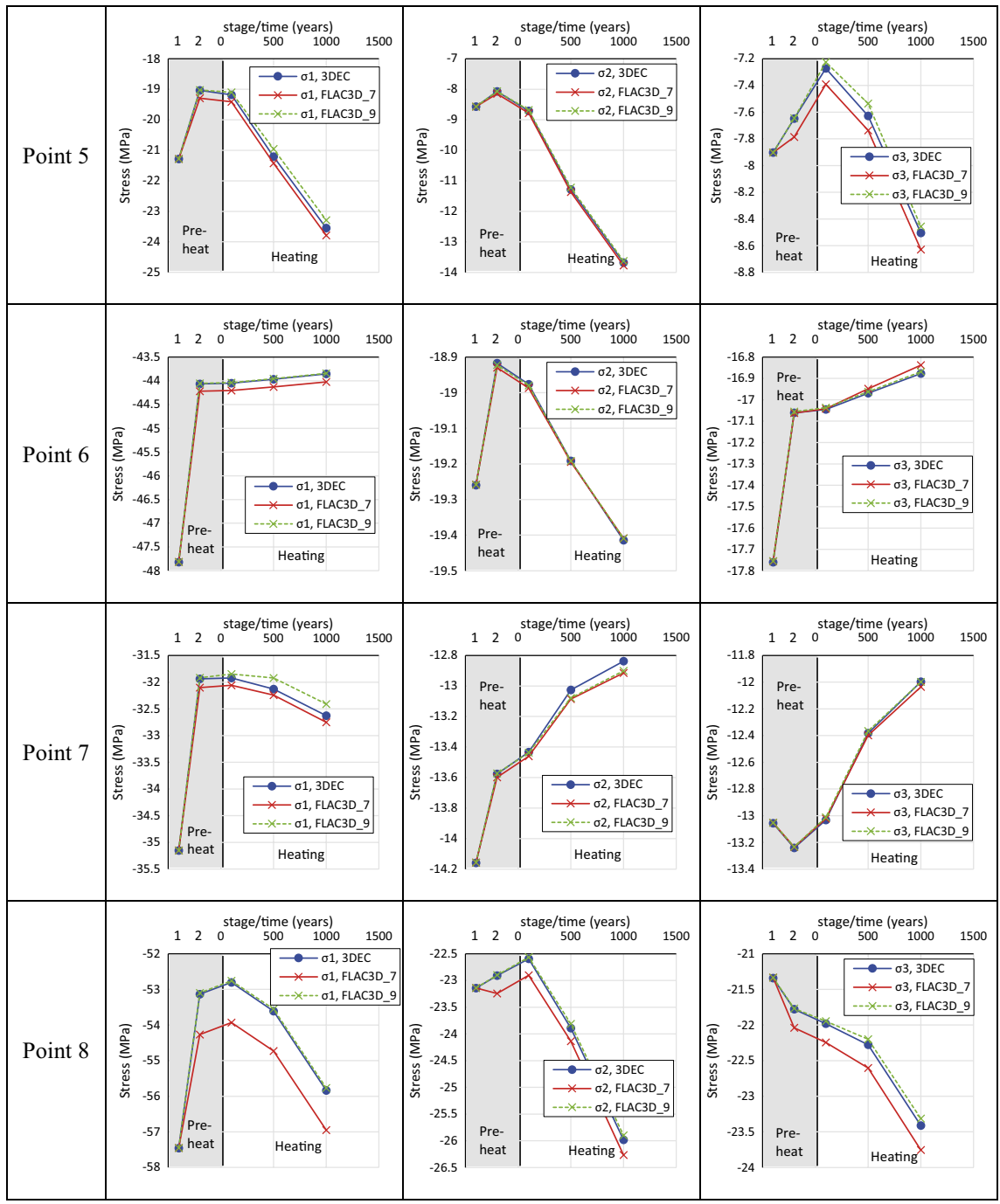


Figure A1-26. Evolution of principal stresses at monitoring points 5 to 8 in the Multiple joint case.

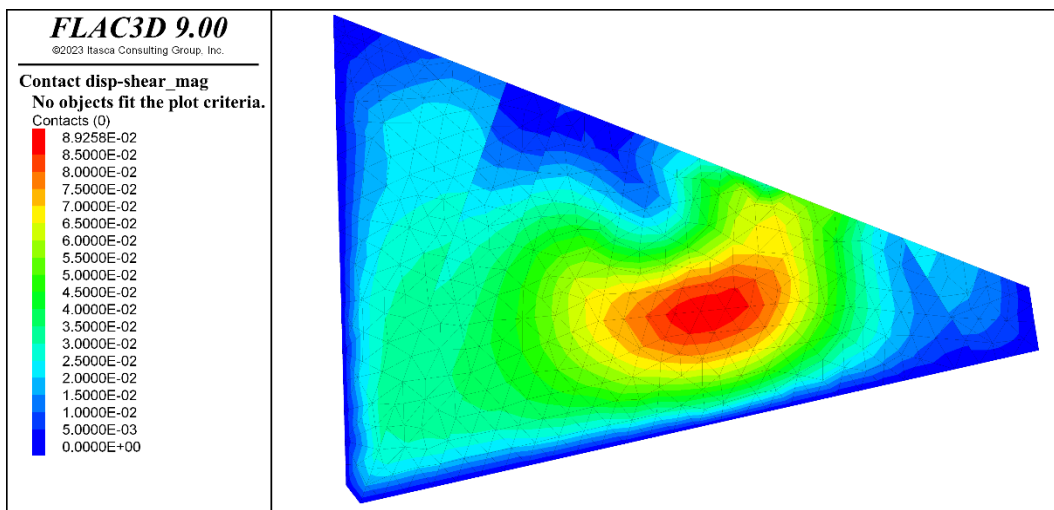
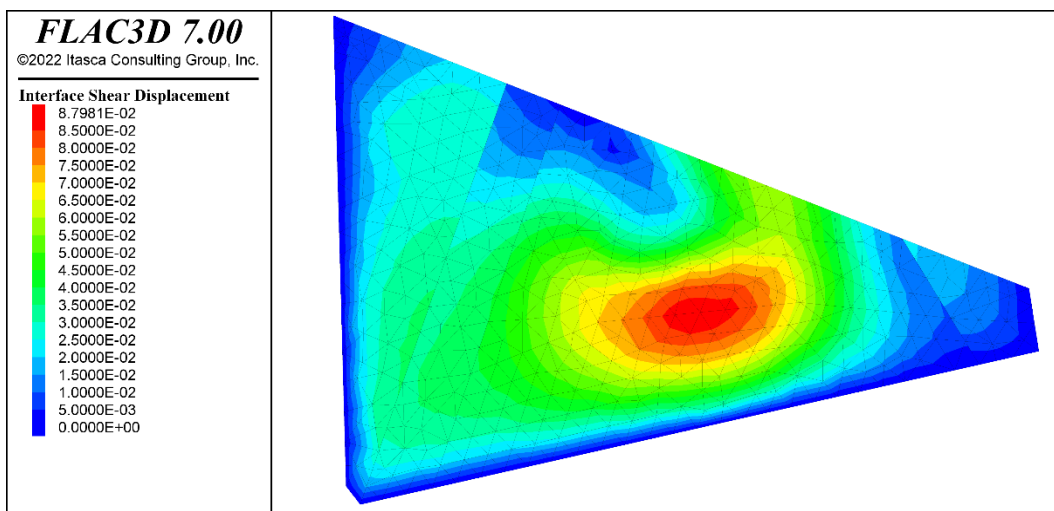
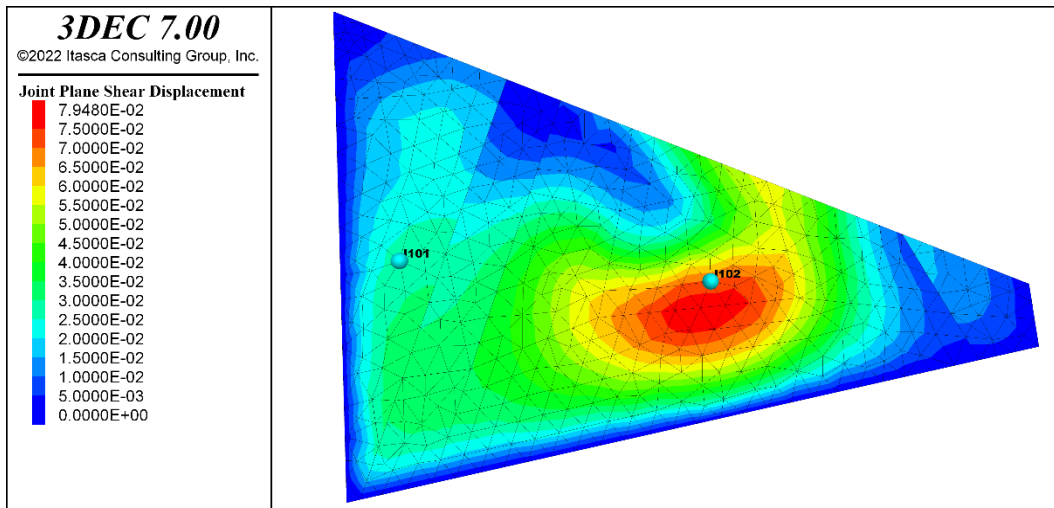


Figure A1-27. Shear displacements on joint 1000 after completed simulation in the Multiple_joint case. Shear displacement evolution at the two points indicated in the upper plot is shown in Figure A1-47.

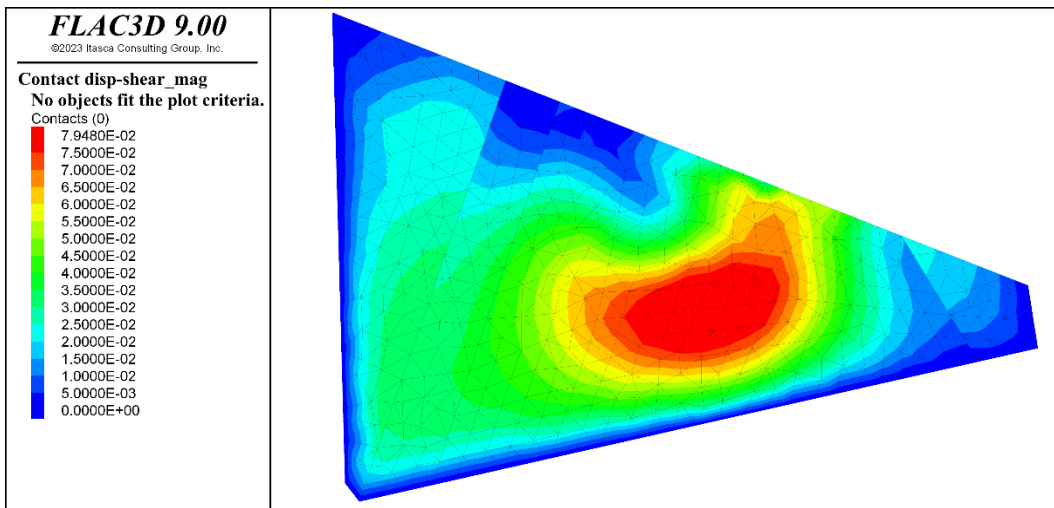
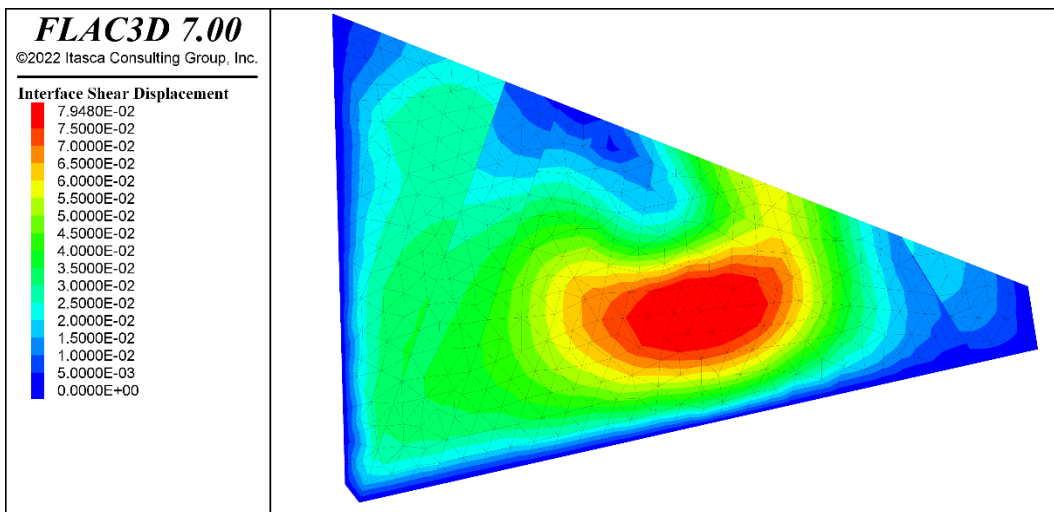
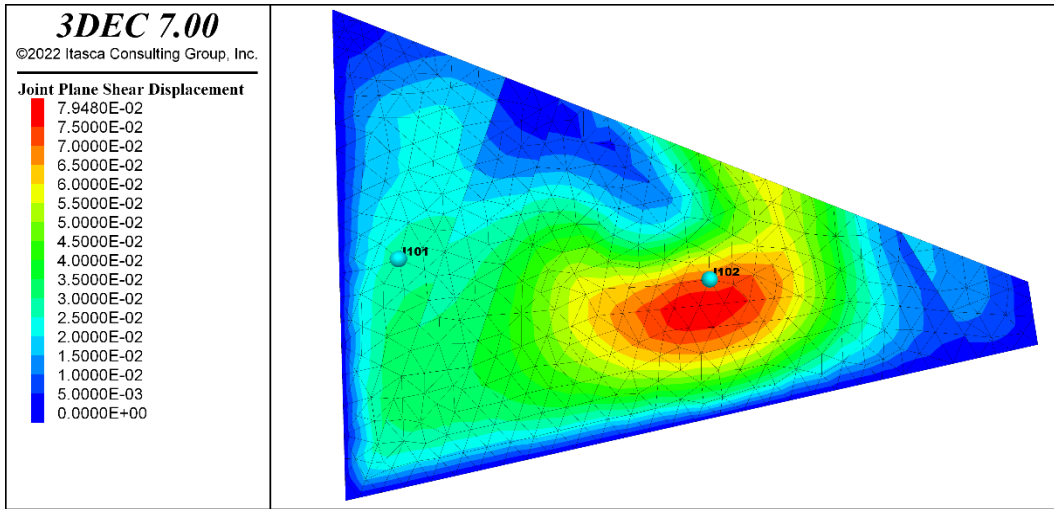


Figure A1-28. Same results as in Figure A1-27 but with same colour scale in all plots.

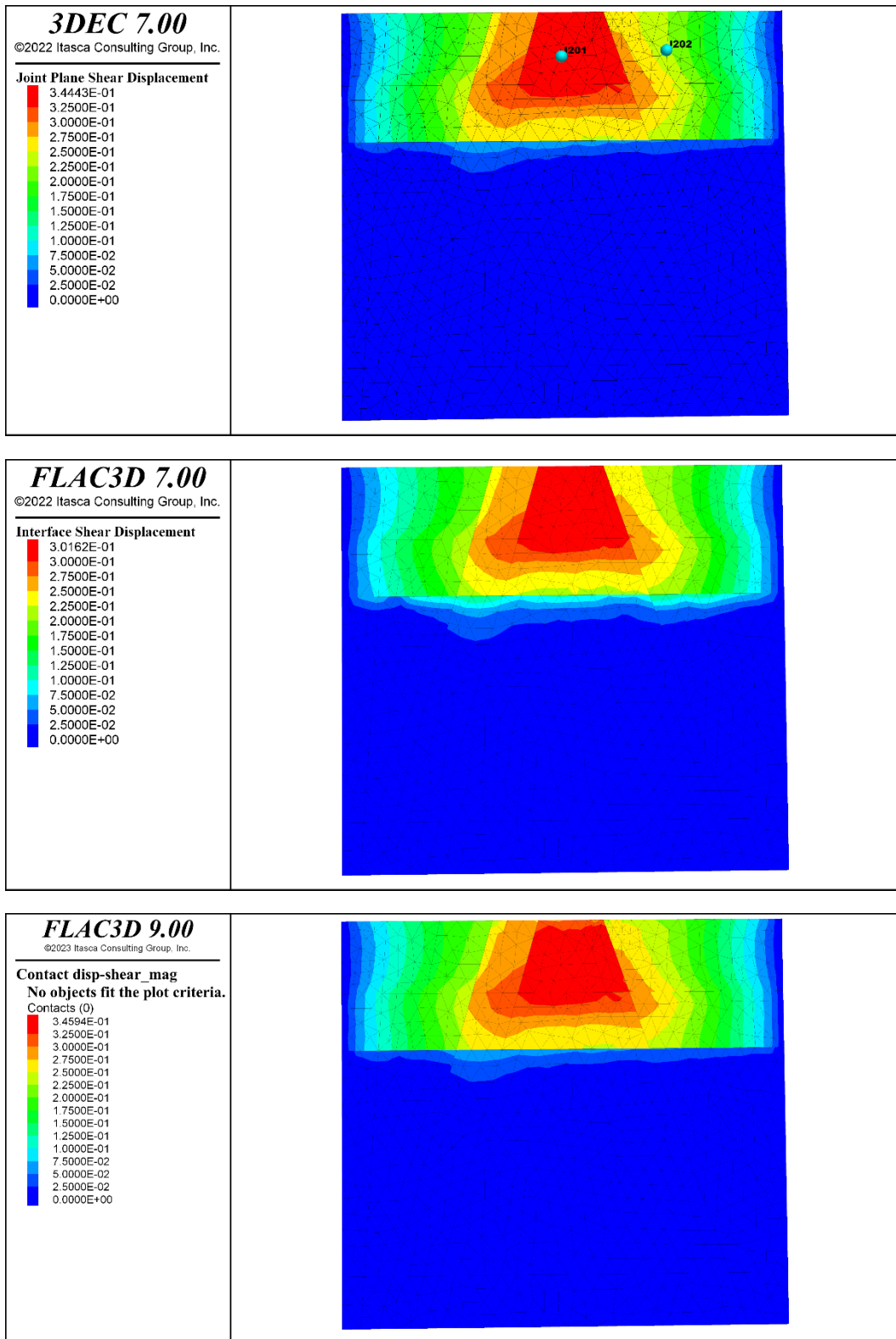


Figure A1-29. Shear displacements on joint 2000 after completed simulation in the Multiple_joint case. Shear displacement evolution at the two points indicated in the upper plot is shown in Figure A1-48.

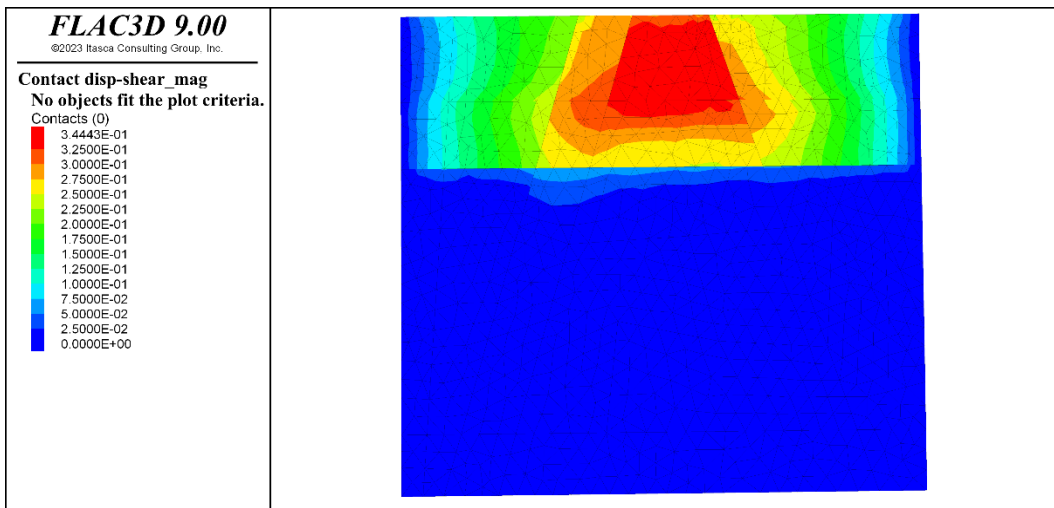
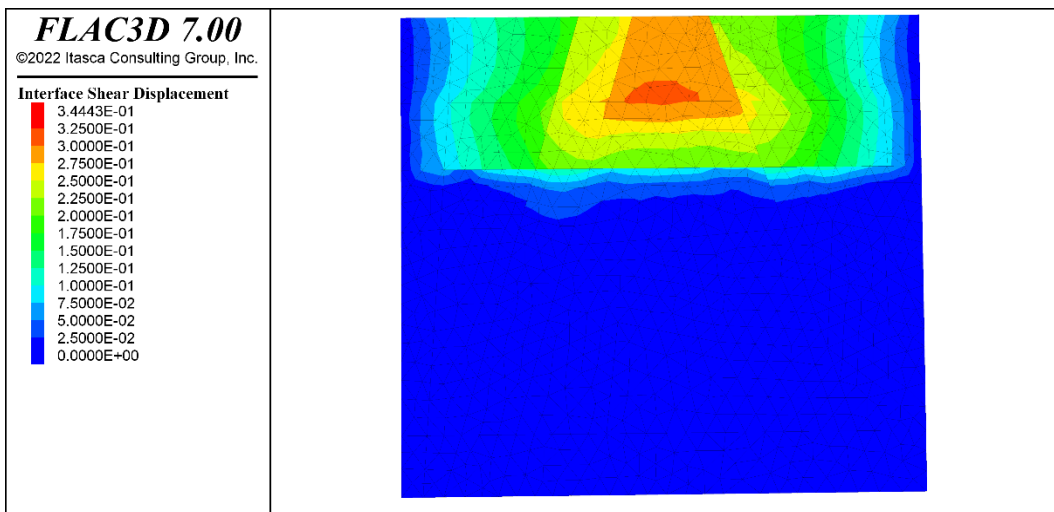
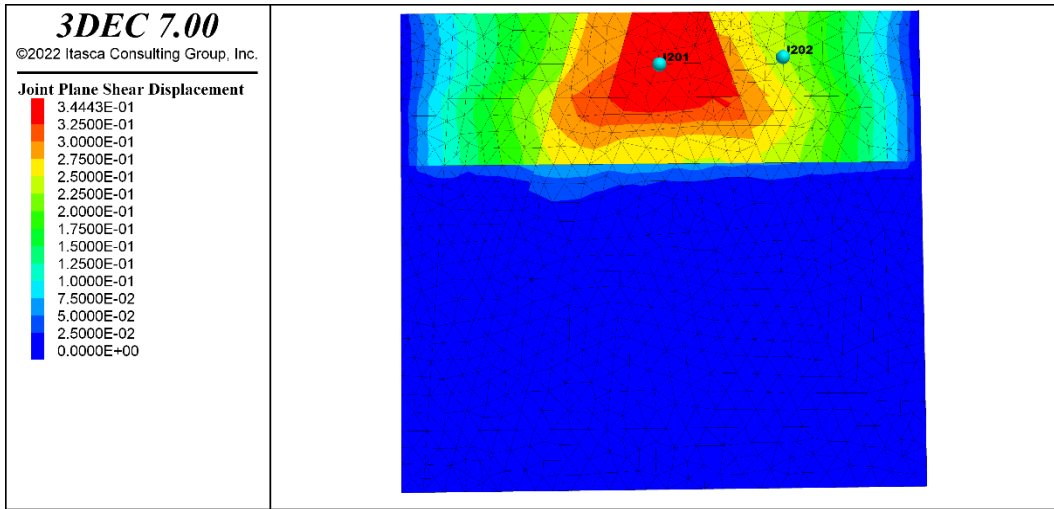


Figure A1-30. Same results as in Figure A1-29 but with same colour scale in all plots.

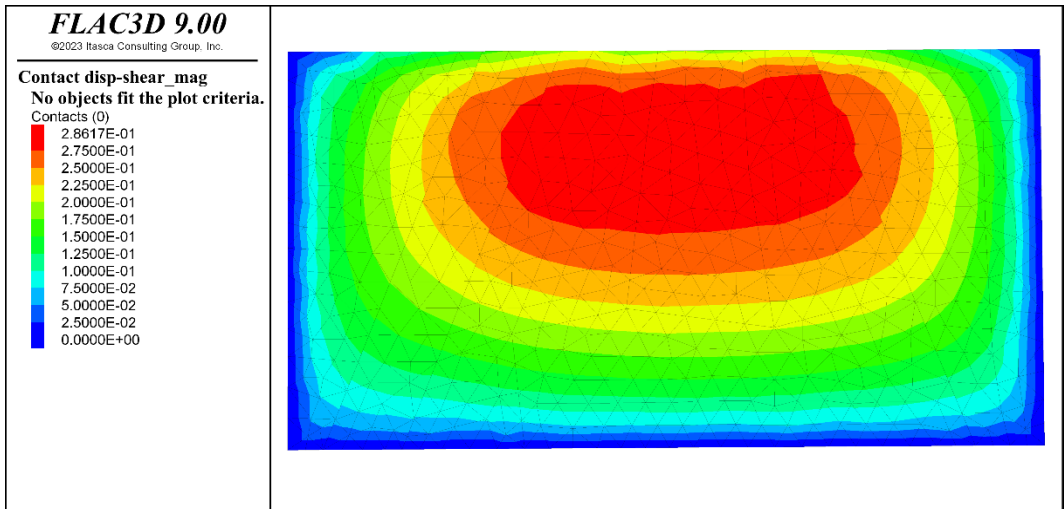
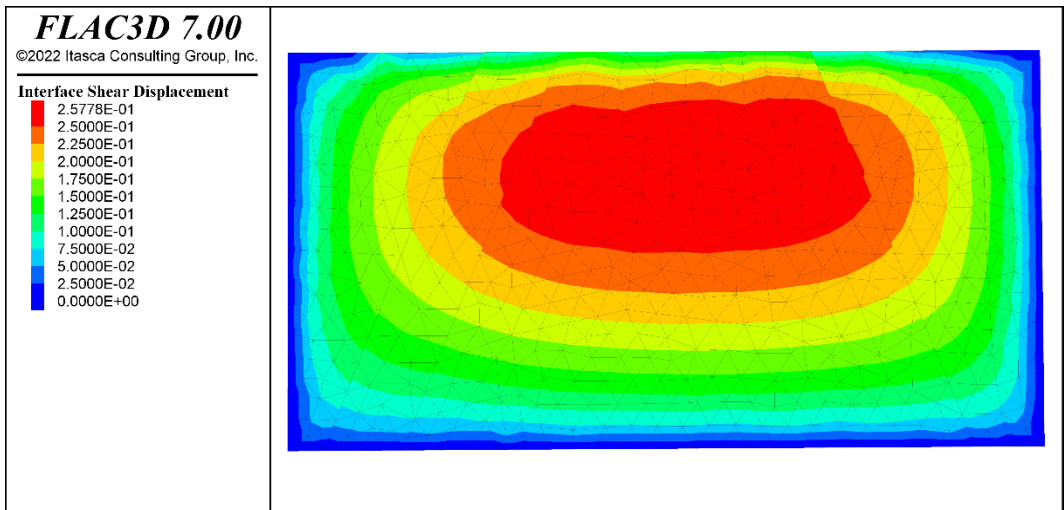
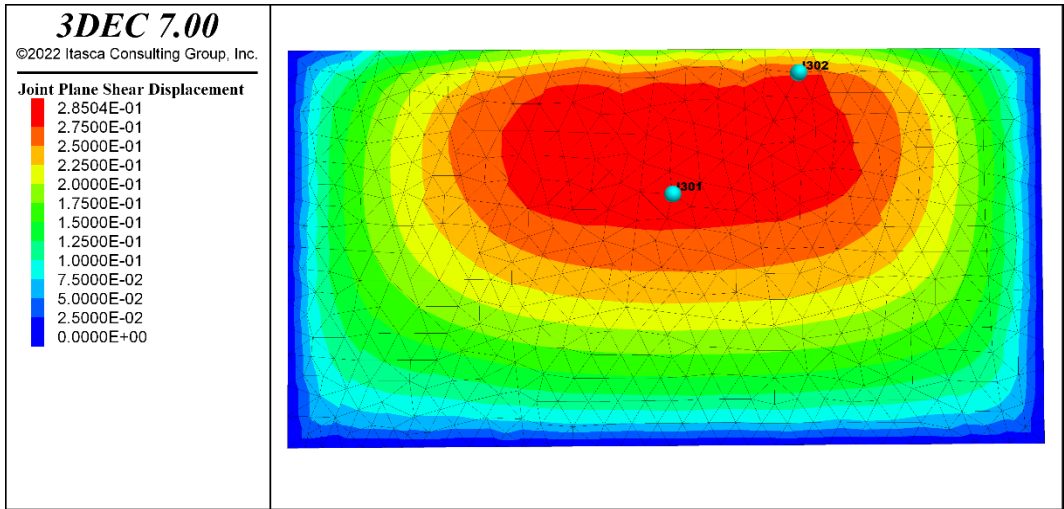


Figure A1-31. Shear displacements on joint 3000 after completed simulation in the Multiple joint case. Shear displacement evolution at the two points indicated in the upper plot is shown in Figure A1-49.

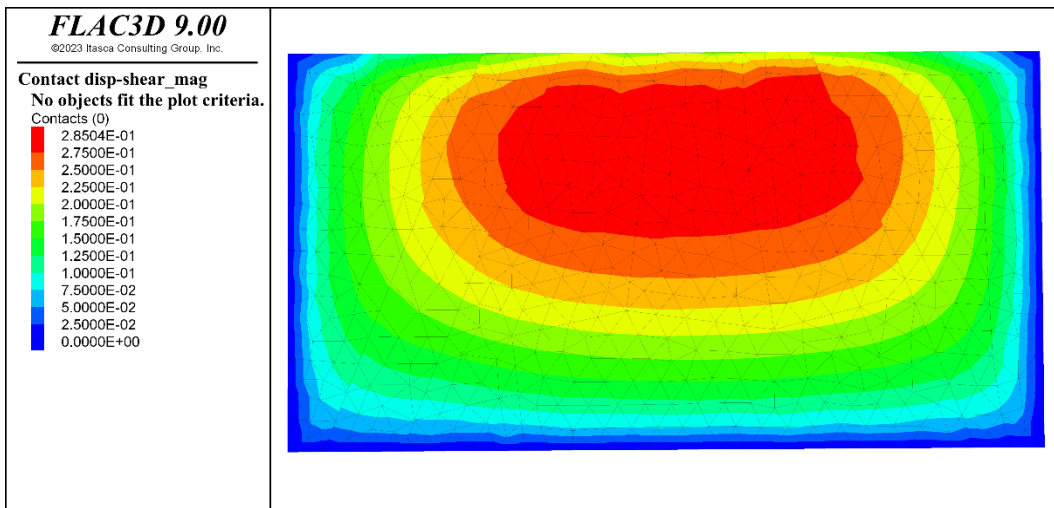
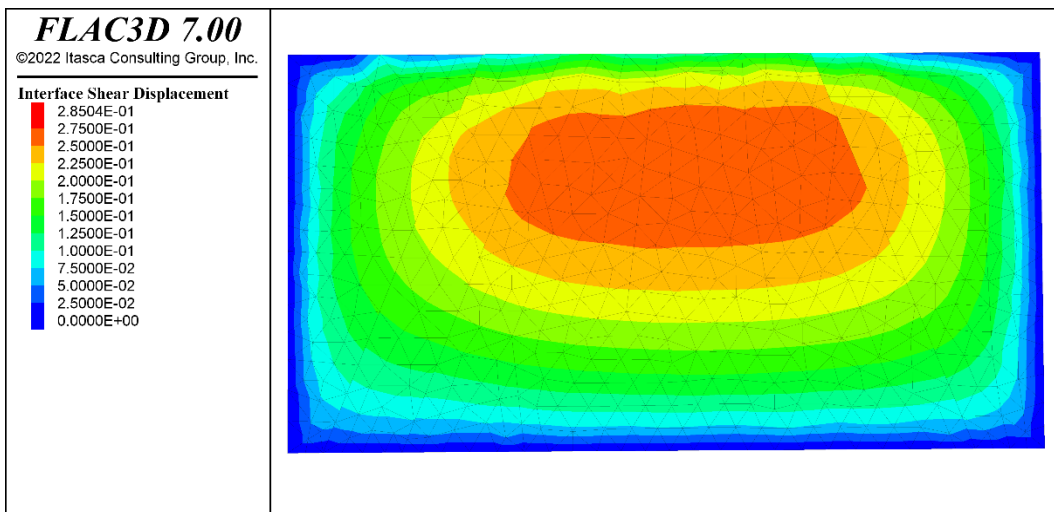
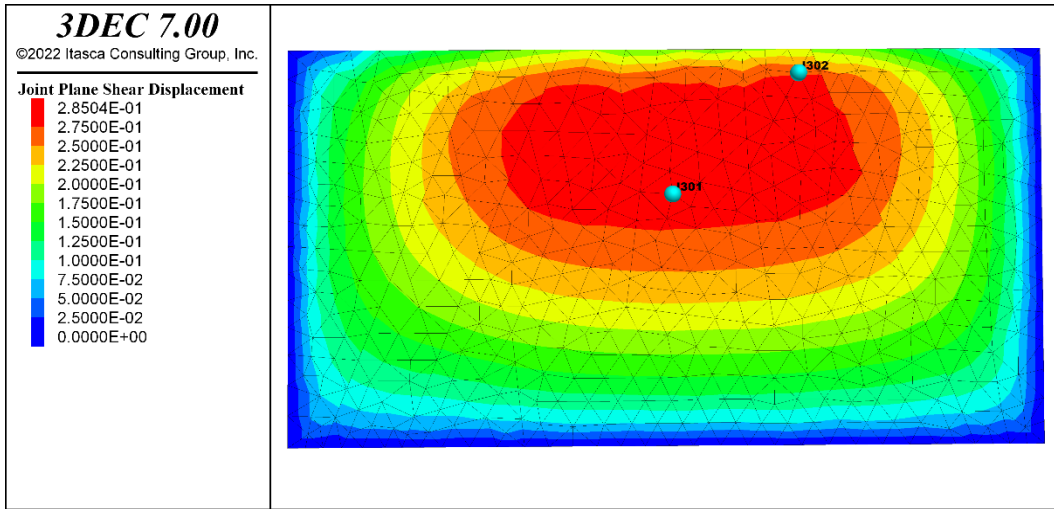


Figure A1-32. Same results as in Figure A1-31 but with same colour scale in all plots.

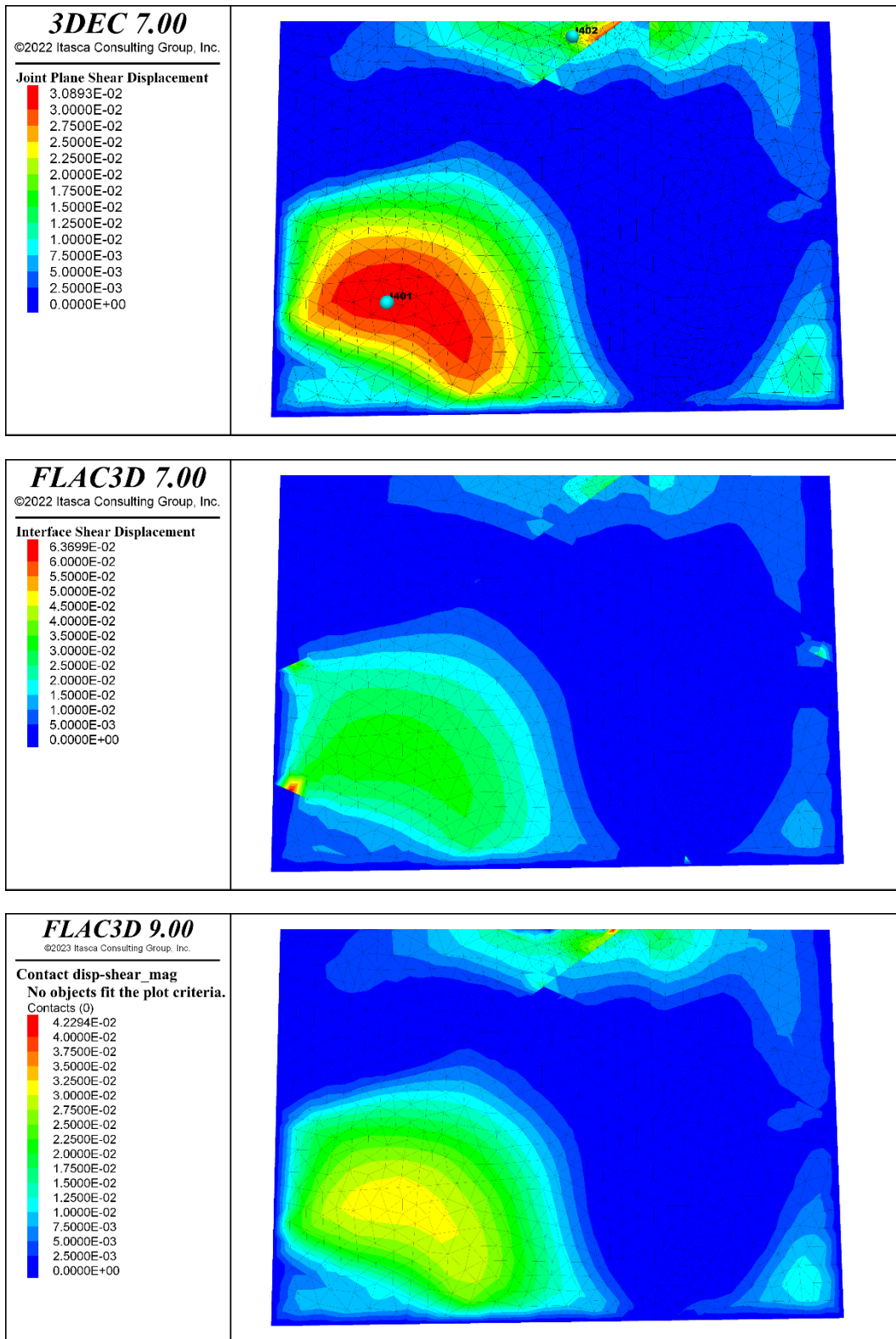


Figure A1-33. Shear displacements on joint 4000 after completed simulation in the Multiple joint case. Shear displacement evolution at the two points indicated in the upper plot is shown in Figure A1-50.

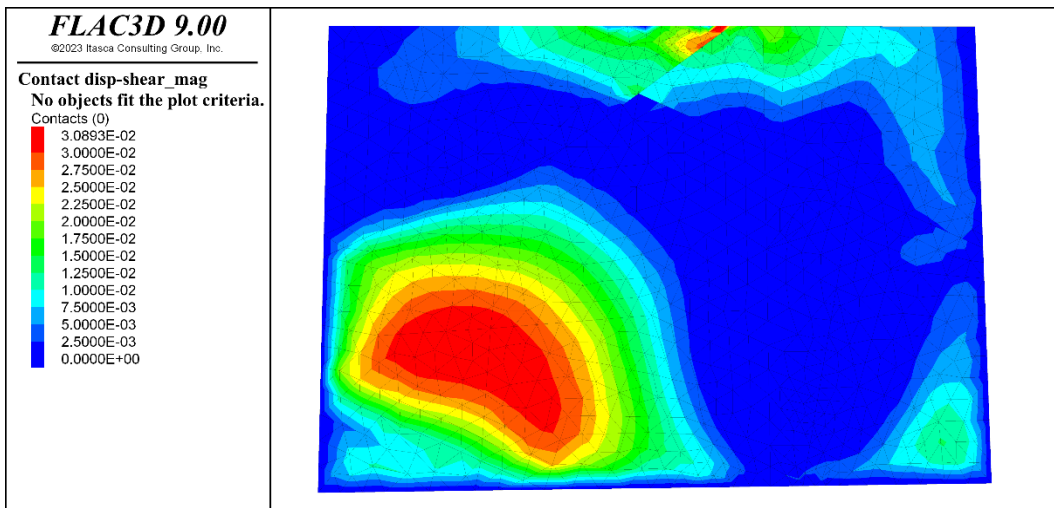
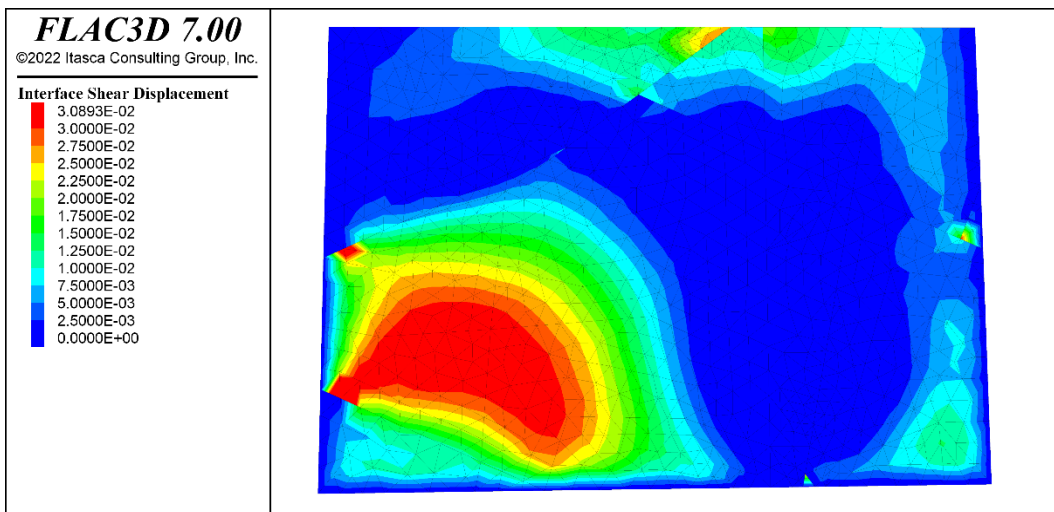
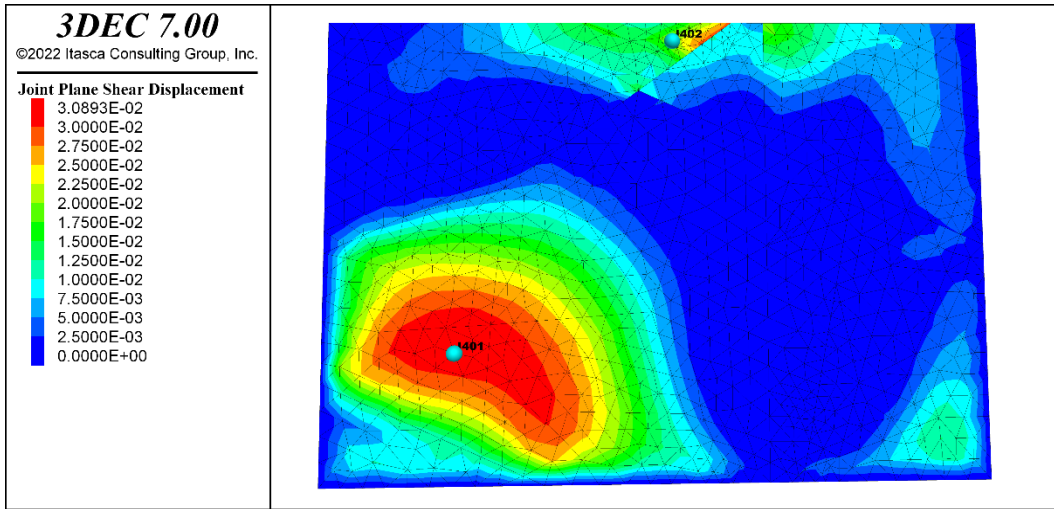


Figure A1-34. Same results as in Figure A1-33 but with same colour scale in all plots.

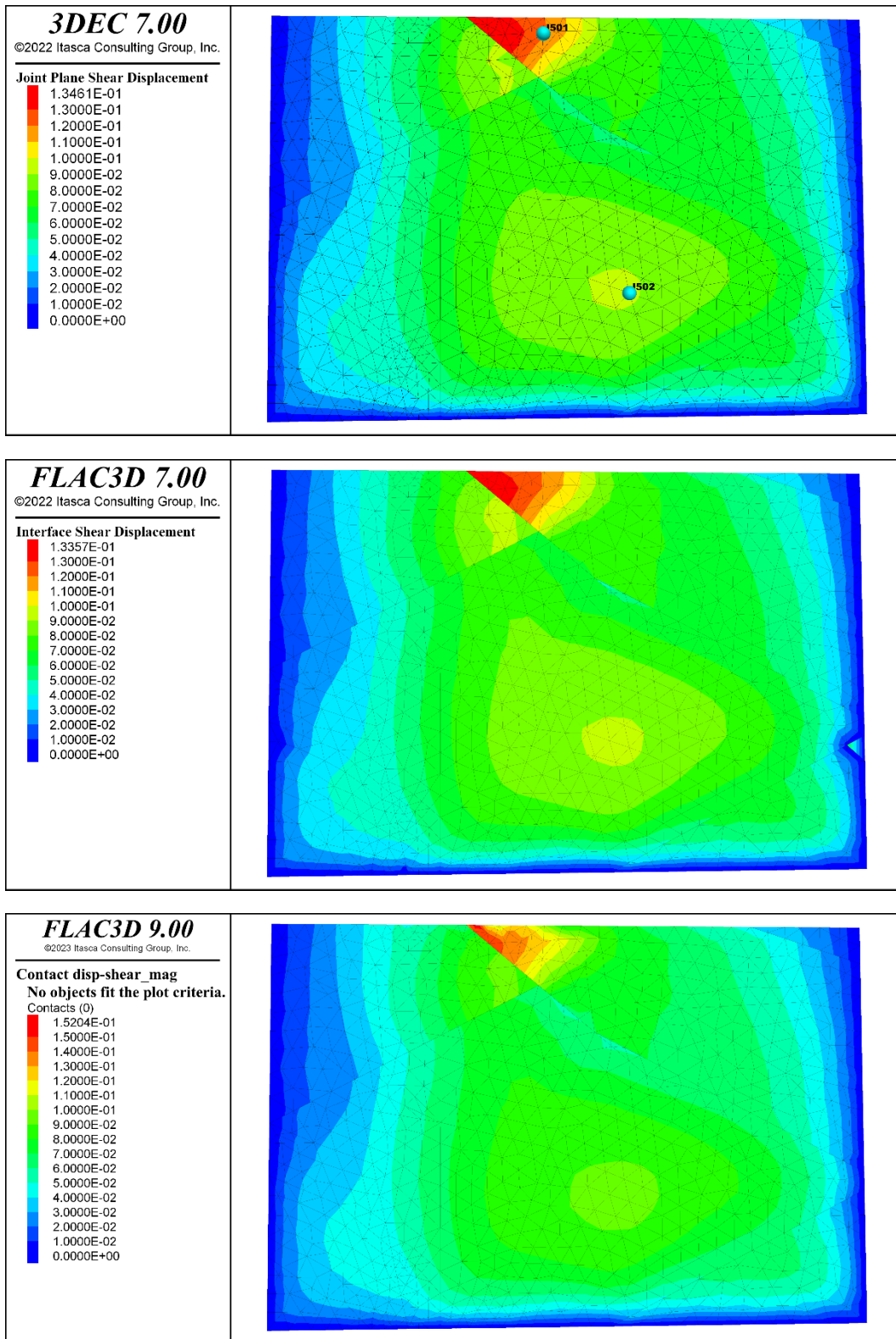


Figure A1-35. Shear displacements on joint 5000 after completed simulation in the Multiple_joint case. Shear displacement evolution at the two points indicated in the upper plot is shown in Figure A1-51.

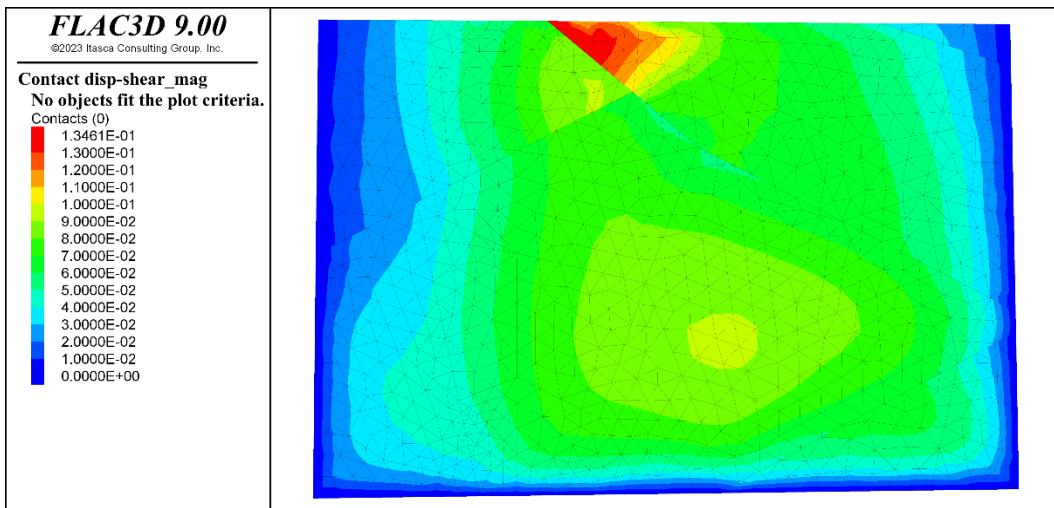
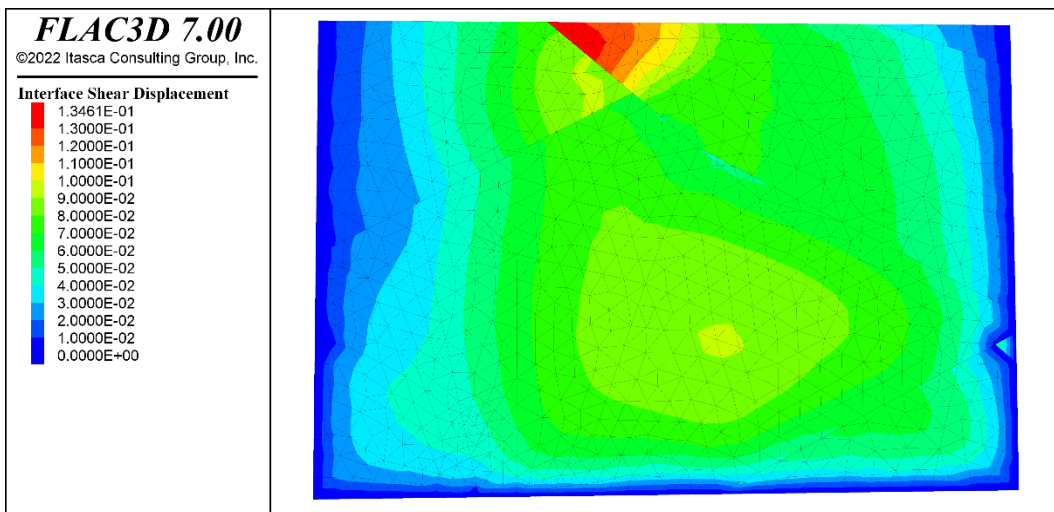
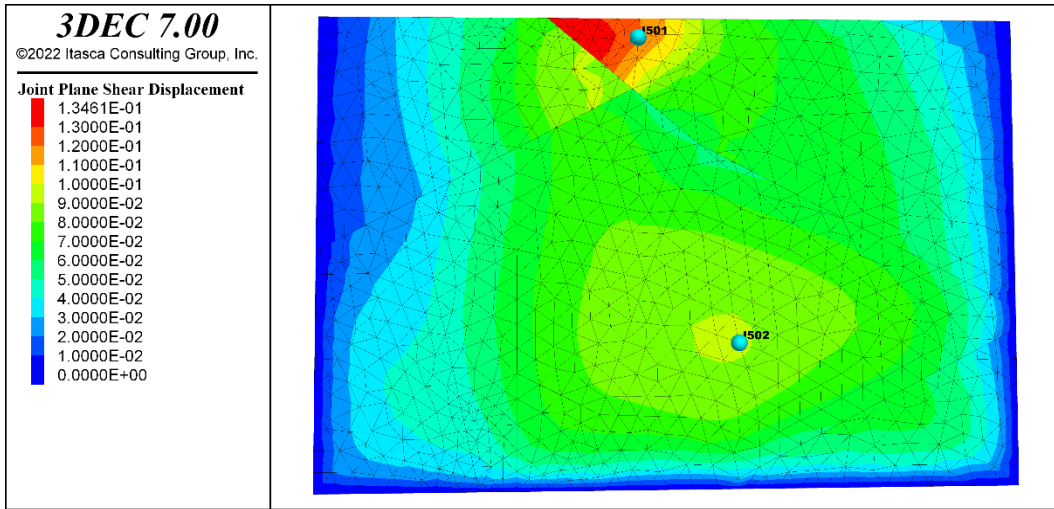


Figure A1-36. Same results as in Figure A1-35 but with same colour scale in all plots.

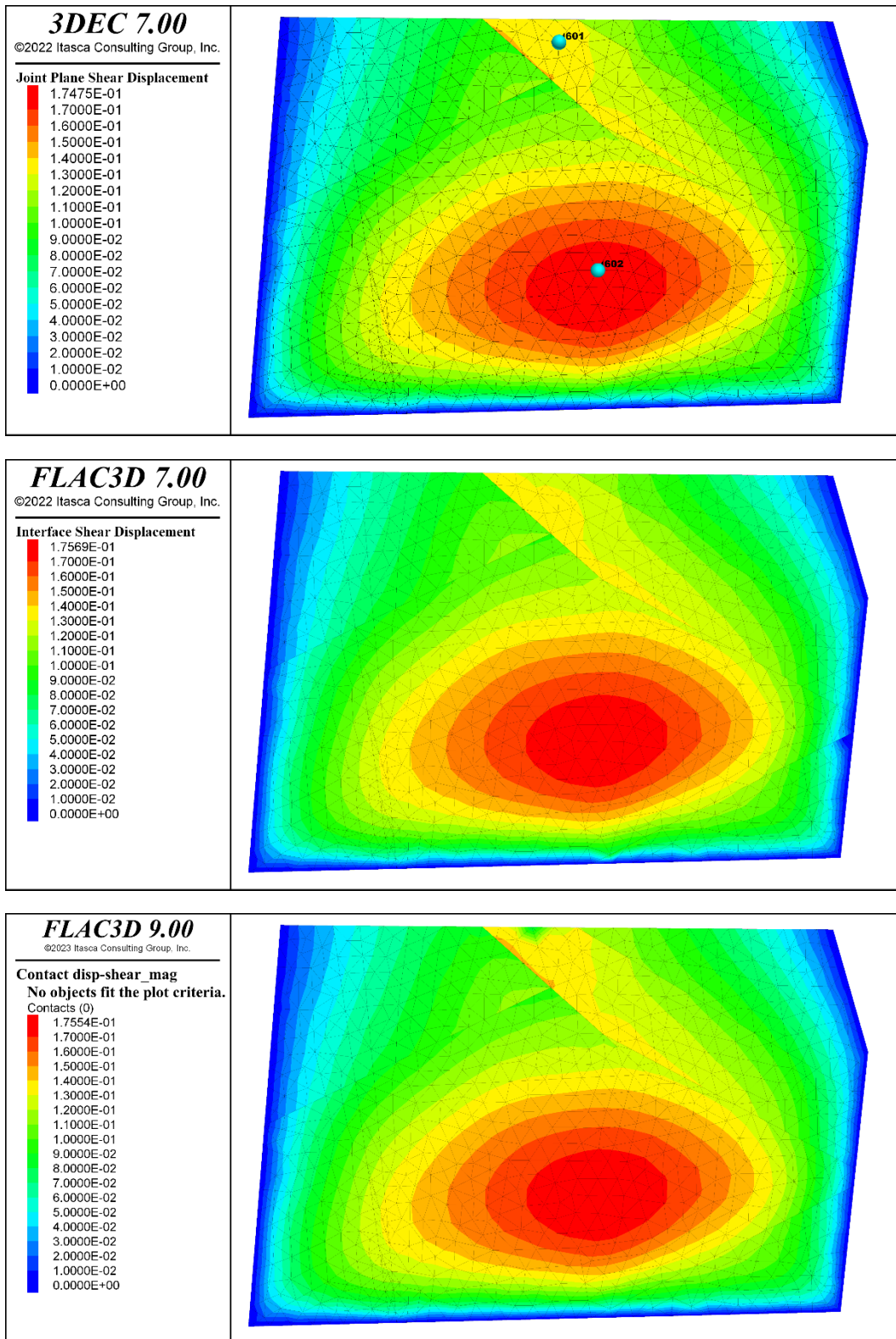


Figure A1-37. Shear displacements on joint 6000 after completed simulation in the Multiple joint case. Shear displacement evolution at the two points indicated in the upper plot is shown in Figure A1-52.

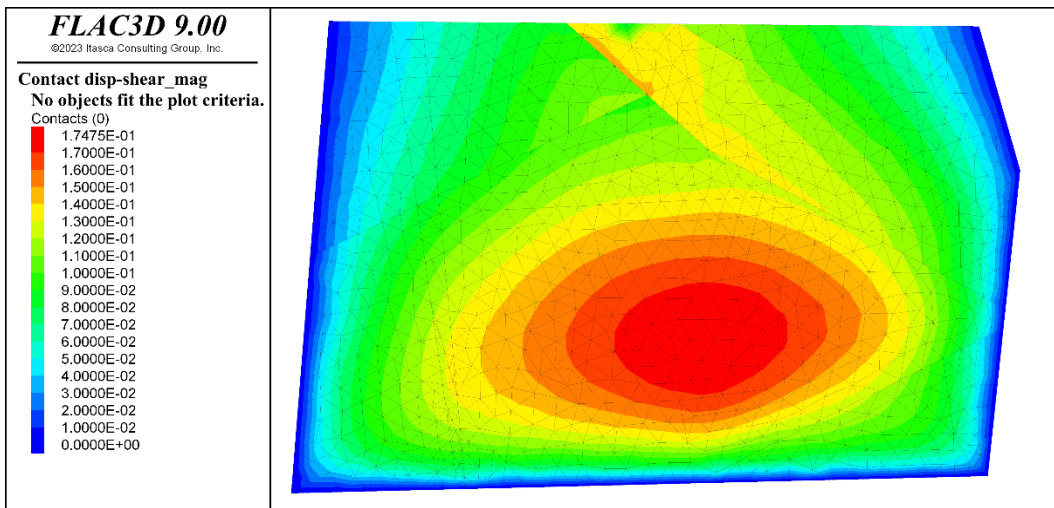
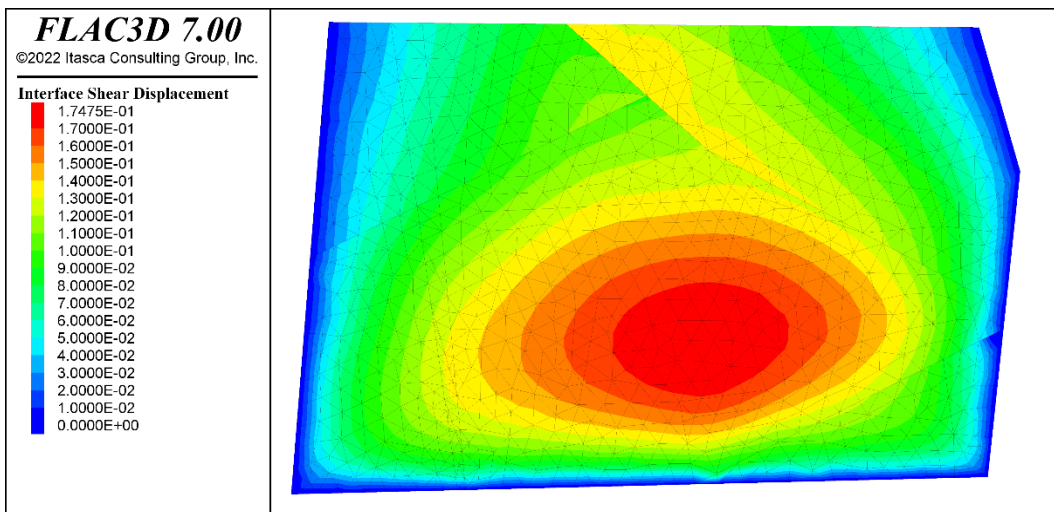
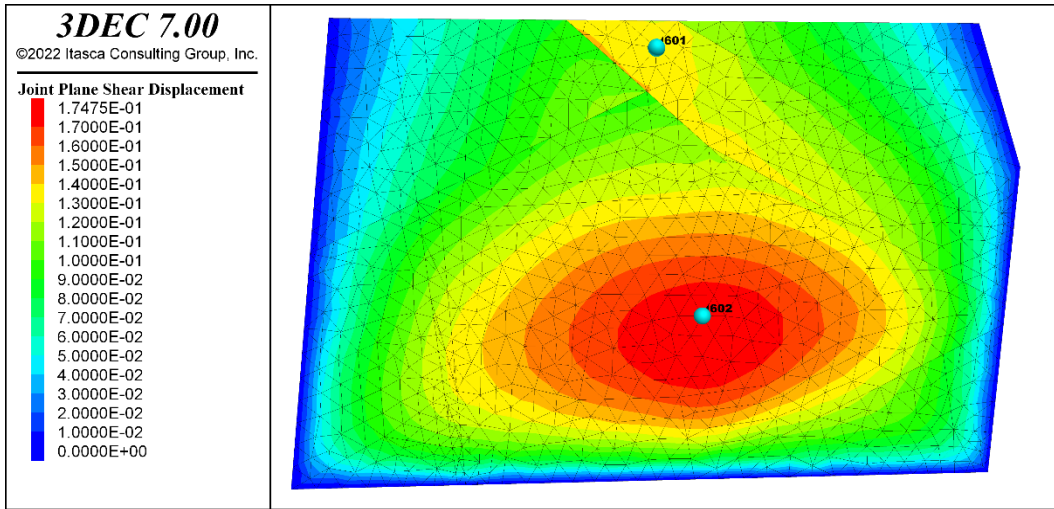


Figure A1-38. Same results as in Figure A1-37 but with same colour scale in all plots.

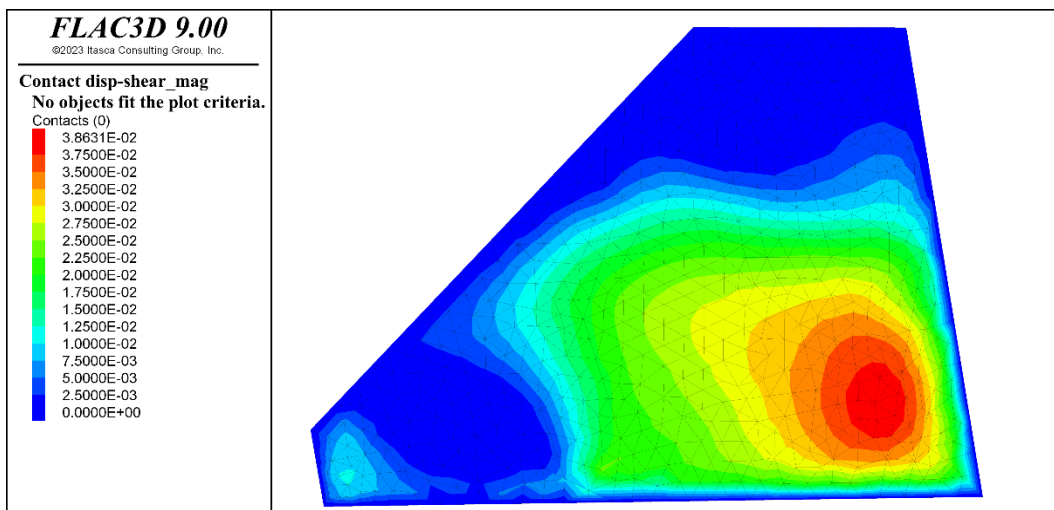
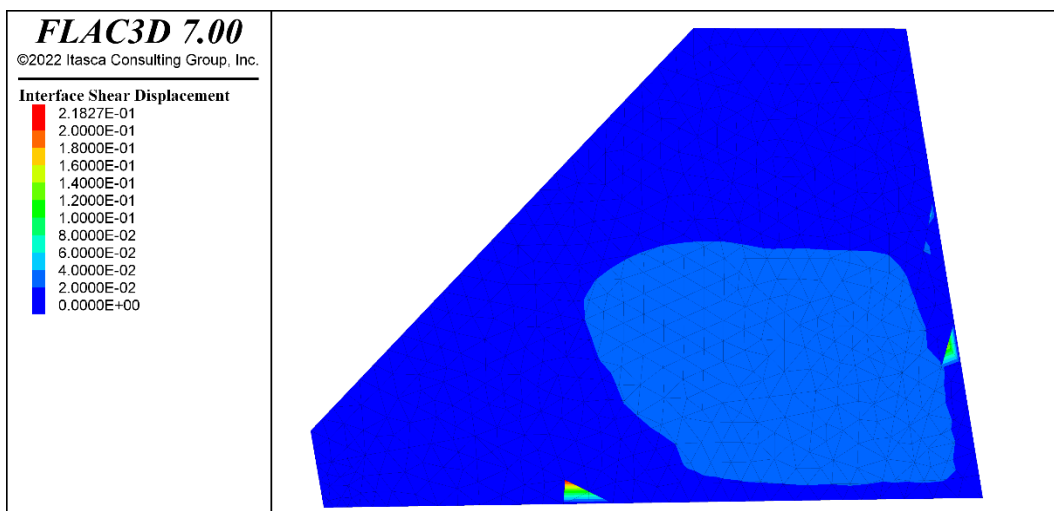
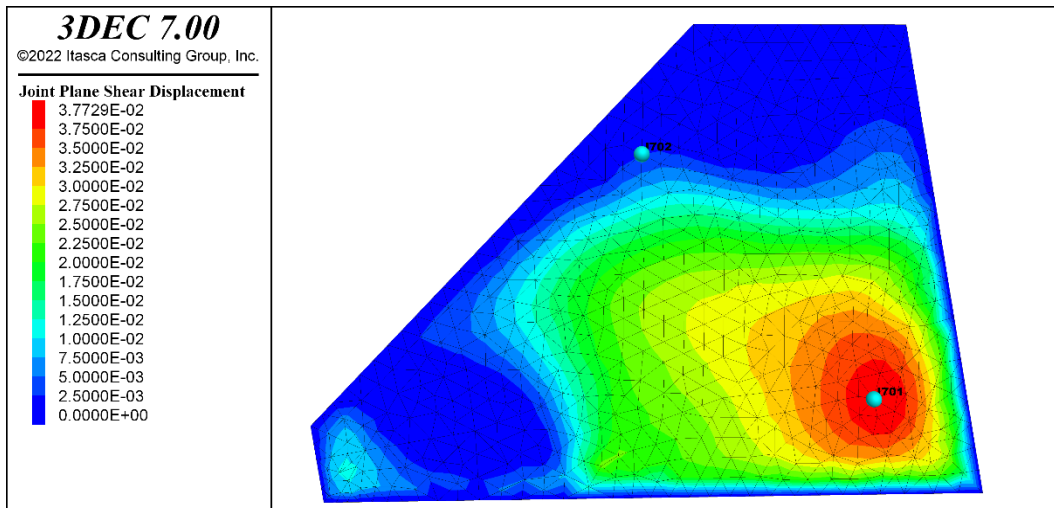


Figure A1-39. Shear displacements on joint 7000 after completed simulation in the Multiple joint case. Shear displacement evolution at the two points indicated in the upper plot is shown in Figure A1-53.

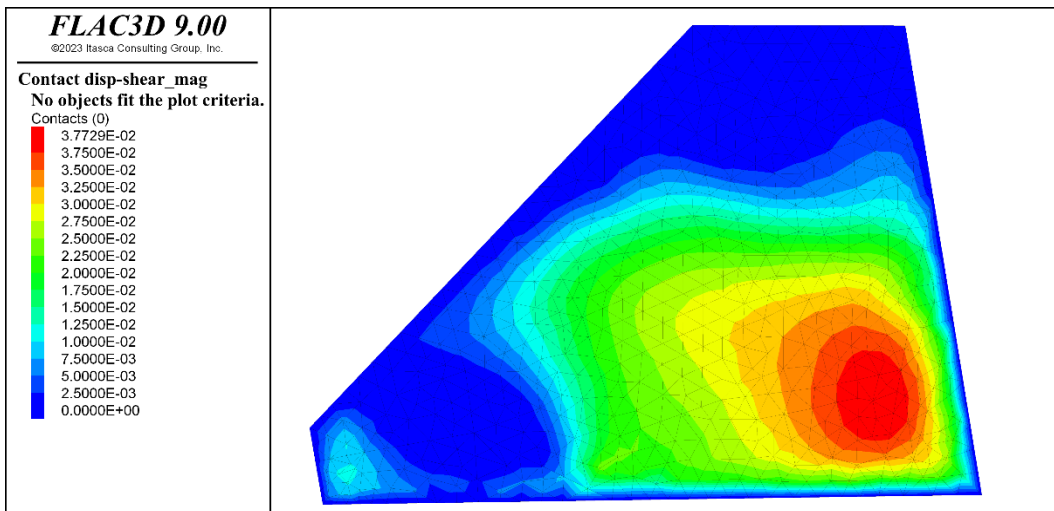
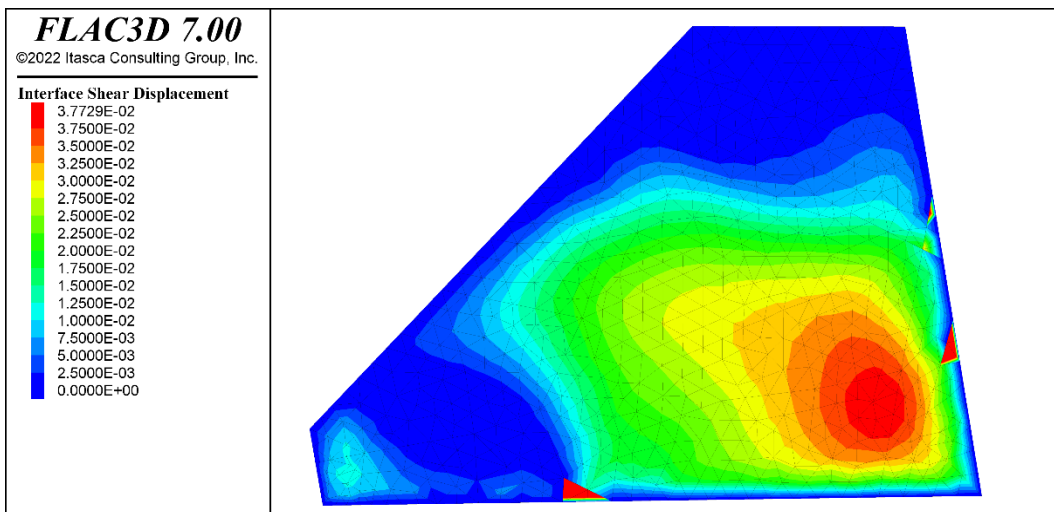
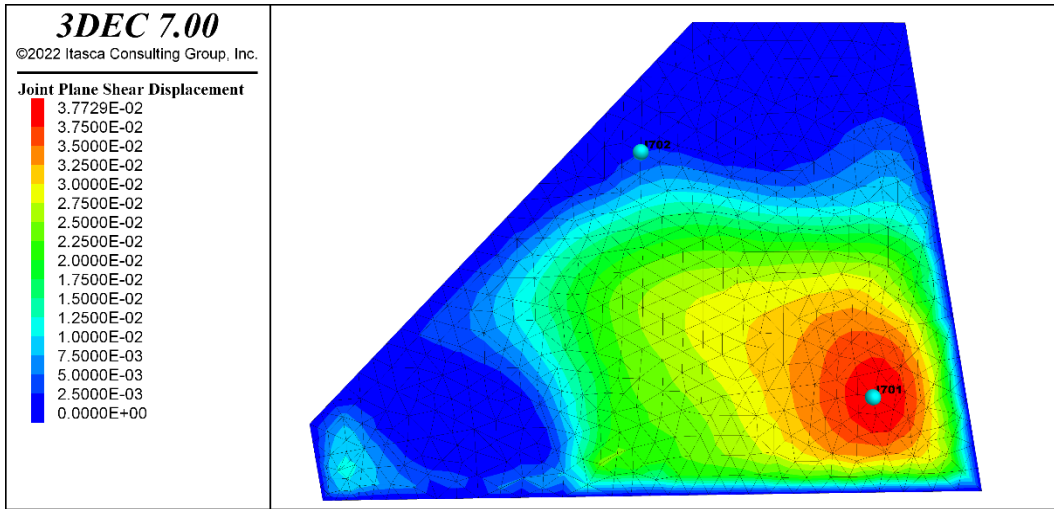


Figure A1-40. Same results as in Figure A1-39 but with same colour scale in all plots.

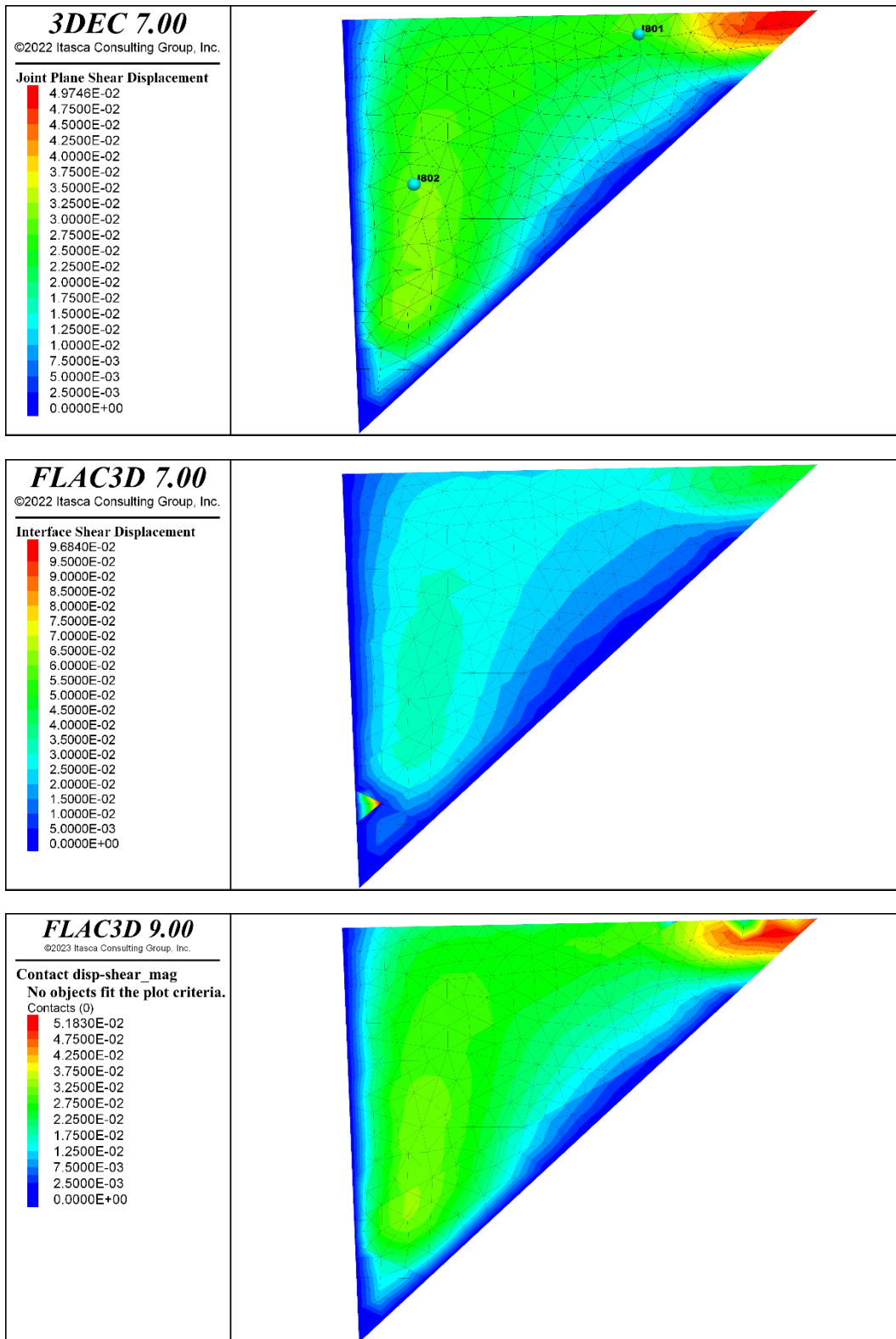


Figure A1-41. Shear displacements on joint 8000 after completed simulation in the Multiple_joint case. Shear displacement evolution at the two points indicated in the upper plot is shown in Figure A1-54.

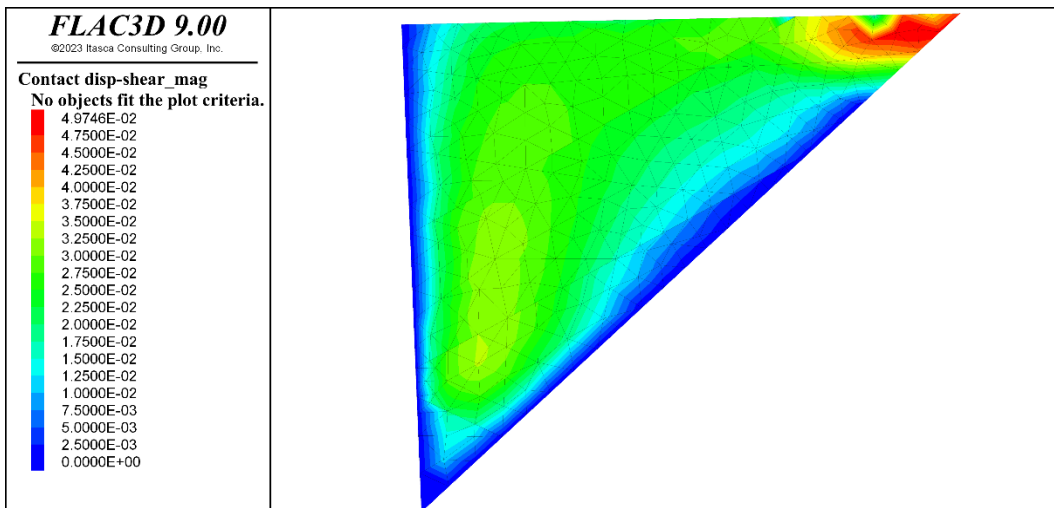
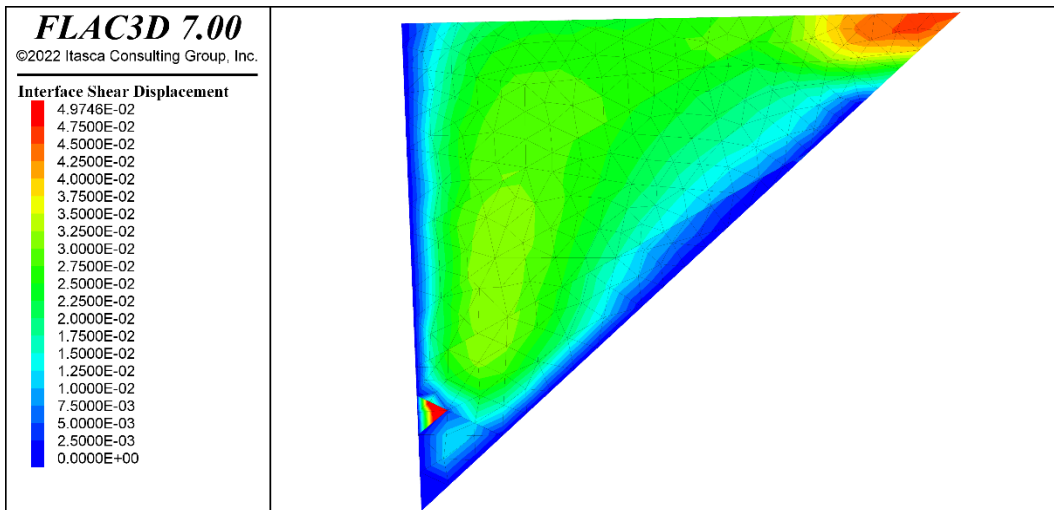
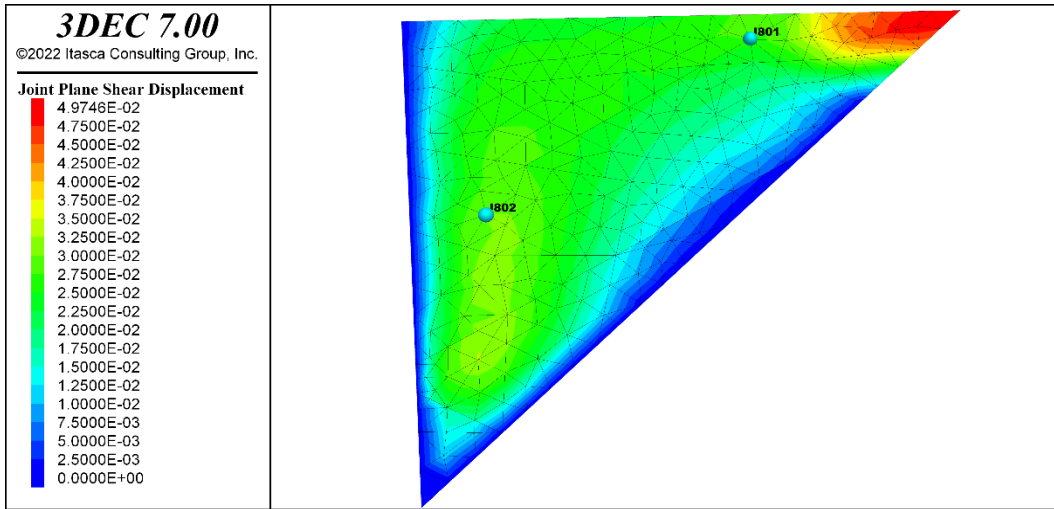


Figure A1-42. Same results as in Figure A1-41 but with same colour scale in all plots.

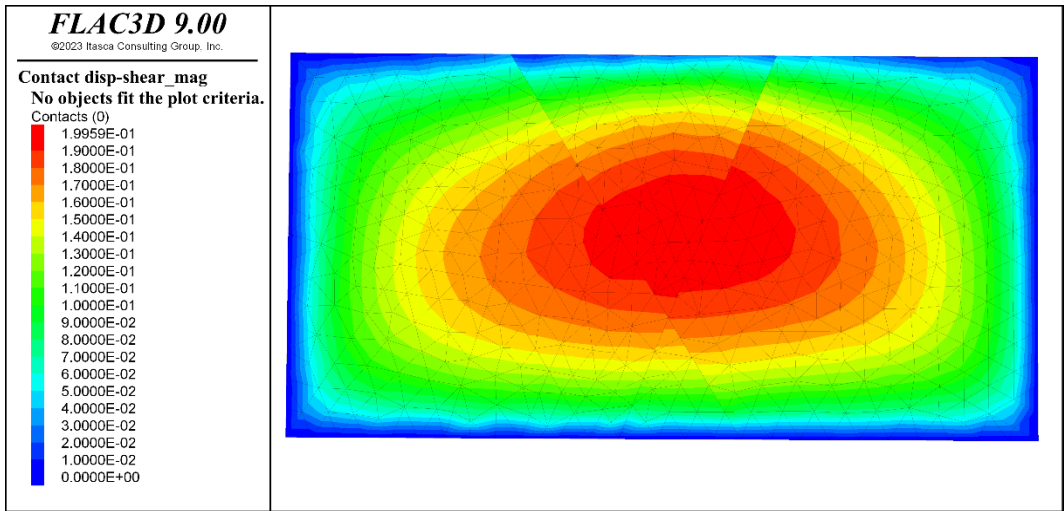
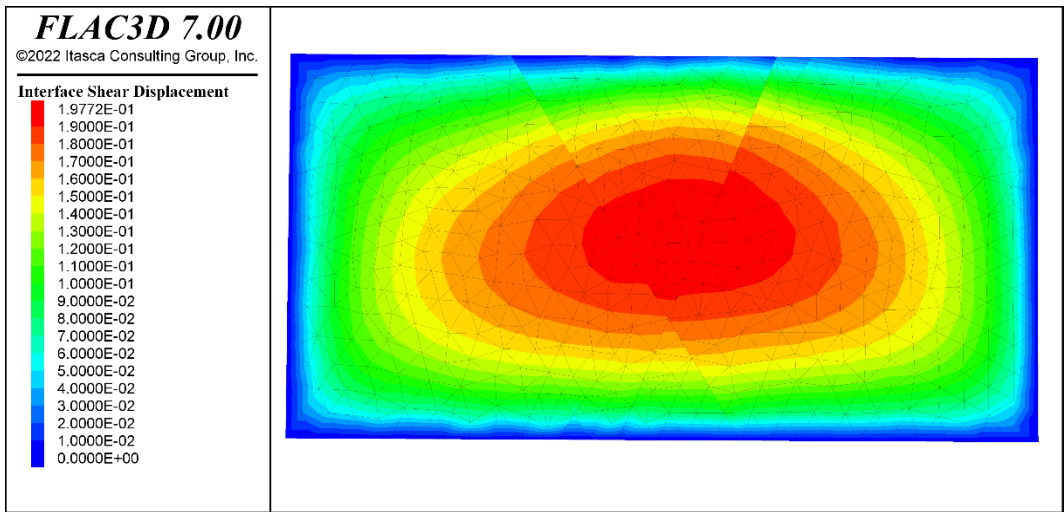
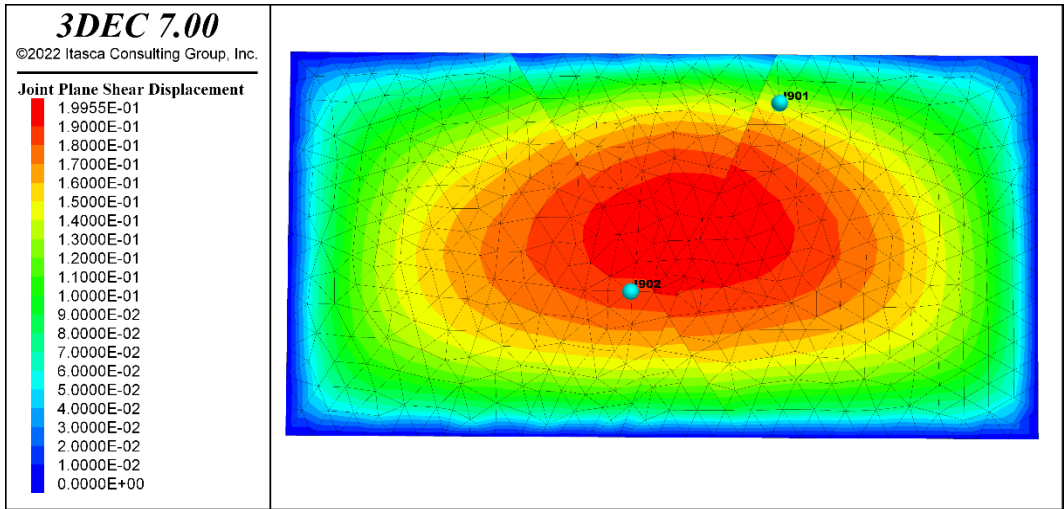


Figure A1-43. Shear displacements on joint 9000 after completed simulation in the Multiple_joint case. Shear displacement evolution at the two points indicated in the upper plot is shown in Figure A1-55.

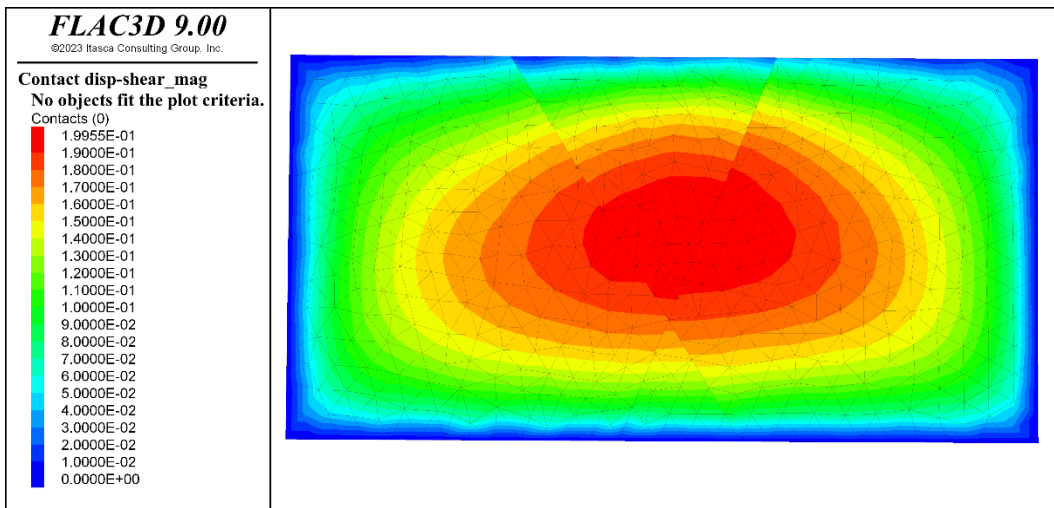
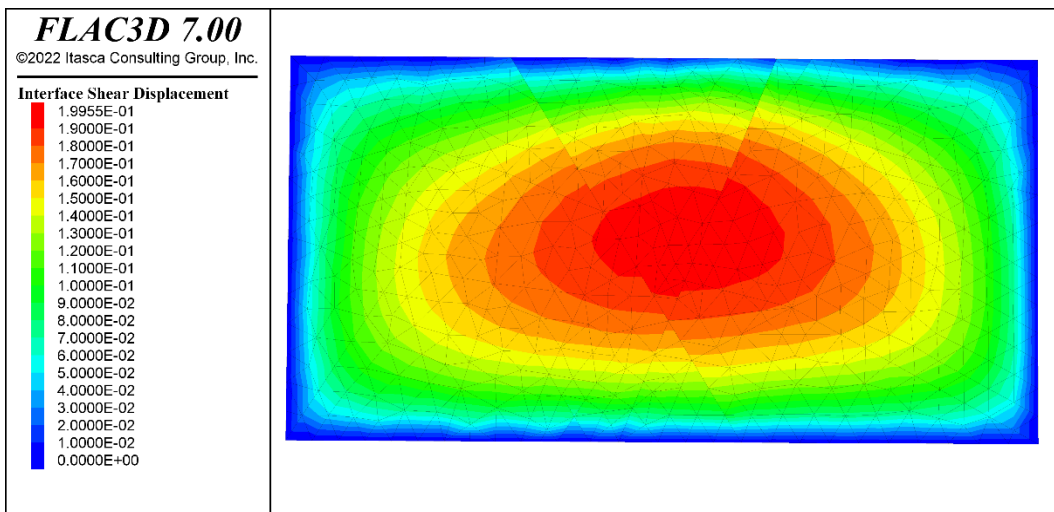
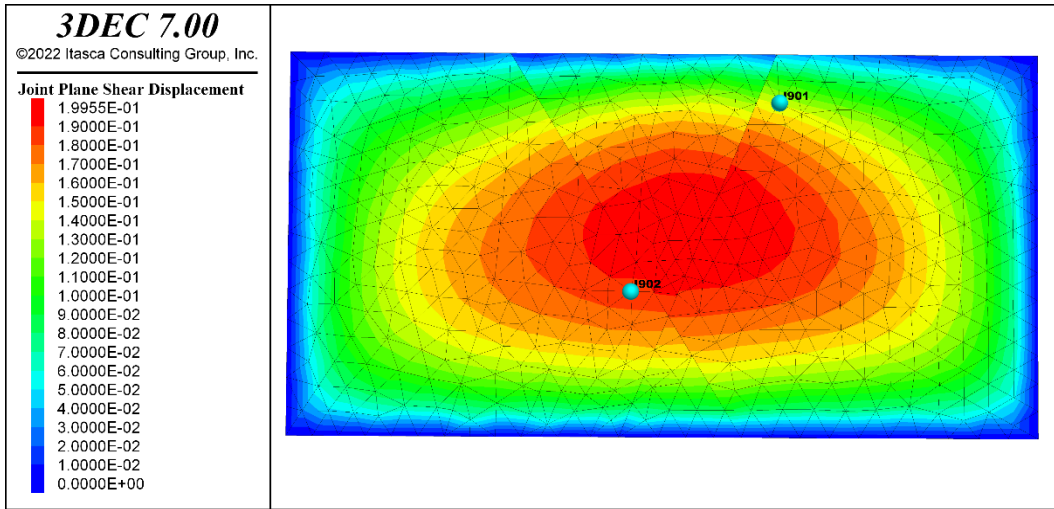


Figure A1-44. Same results as in Figure A1-43 but with same colour scale in all plots.

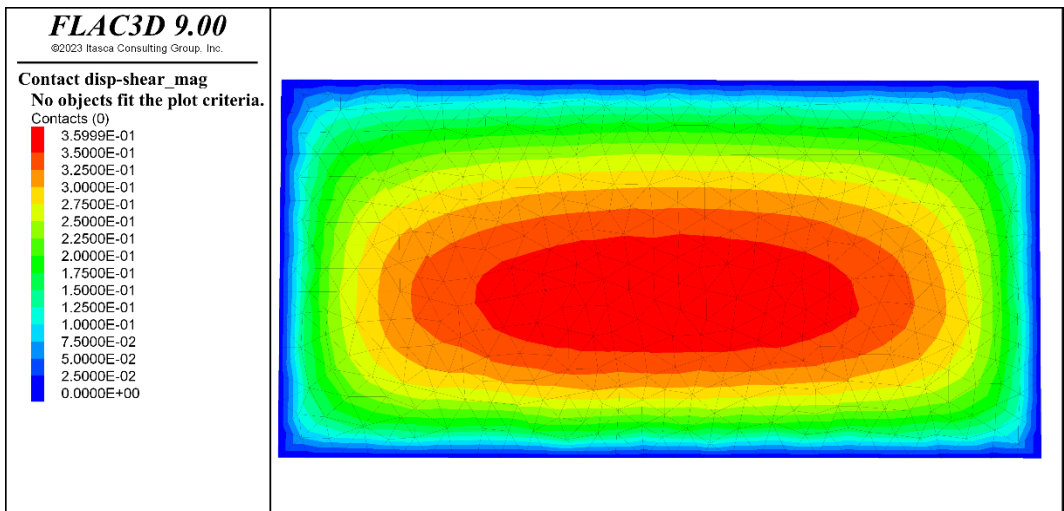
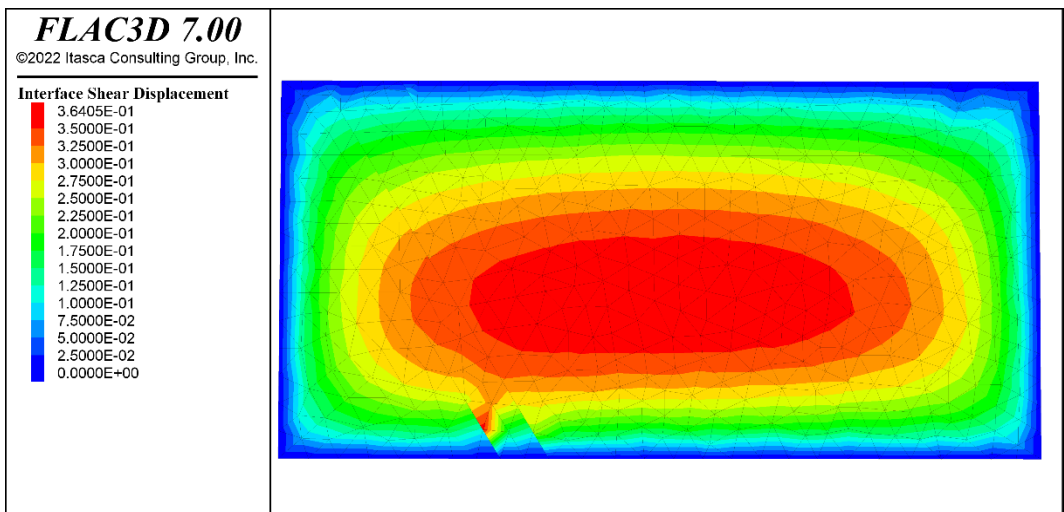
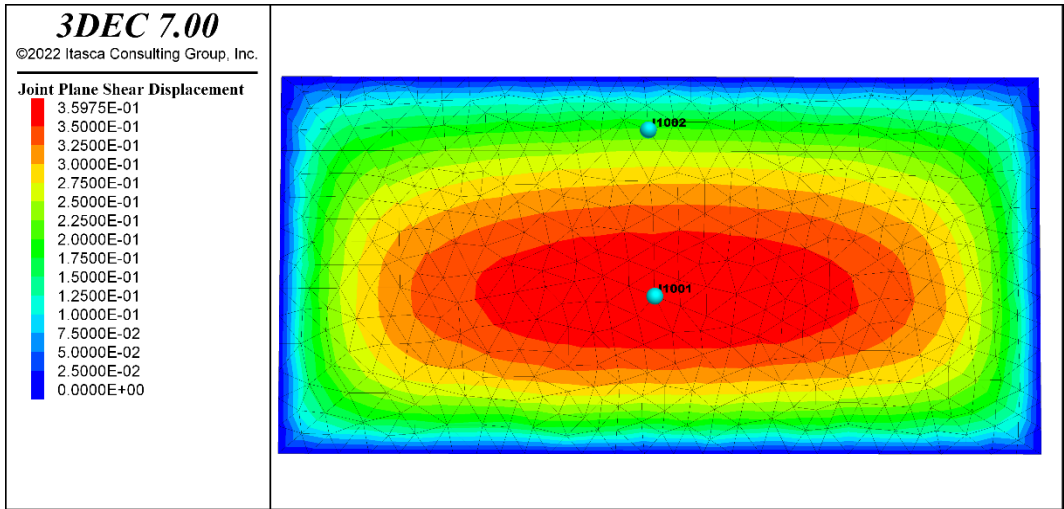


Figure A1-45. Shear displacements on joint 10000 after completed simulation in the Multiple joint case. Shear displacement evolution at the two points indicated in the upper plot is shown in Figure A1-56.

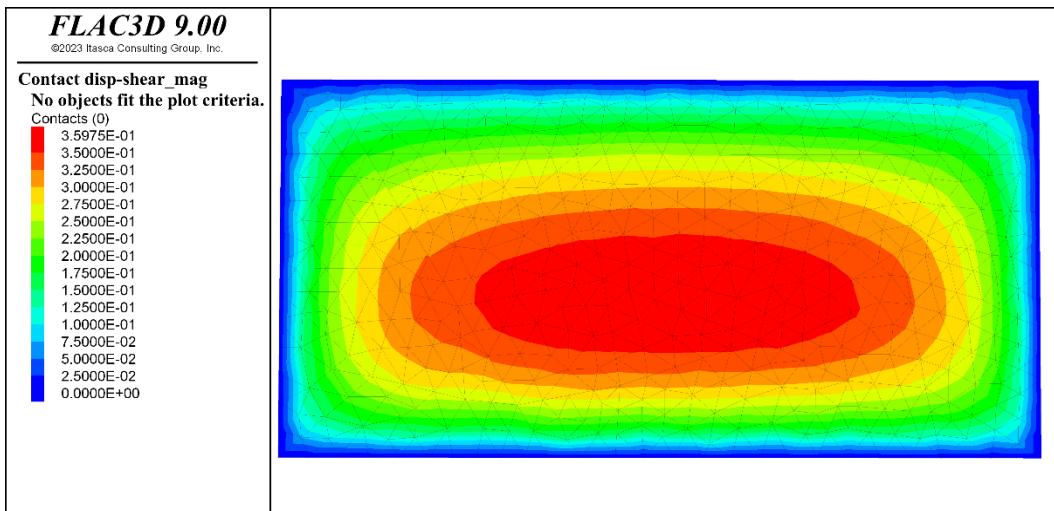
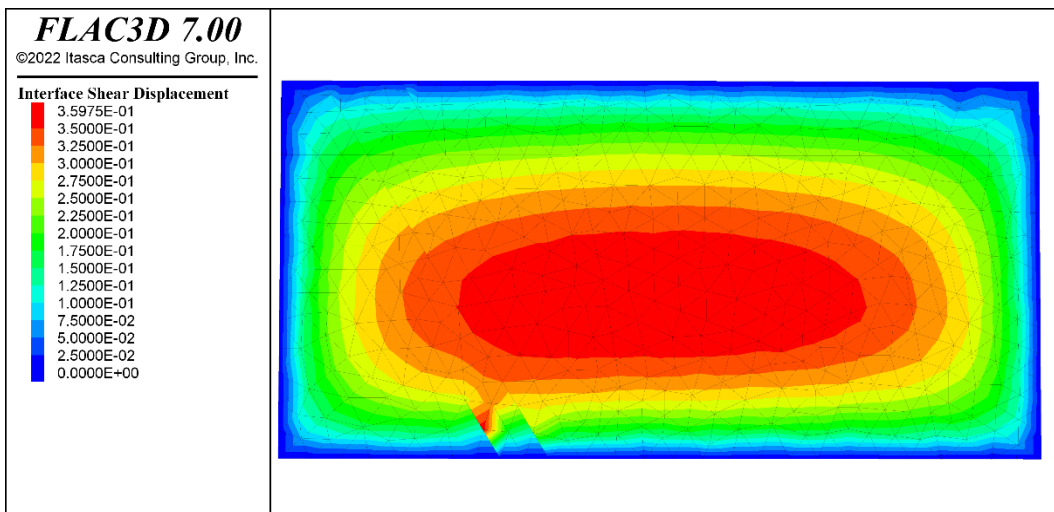
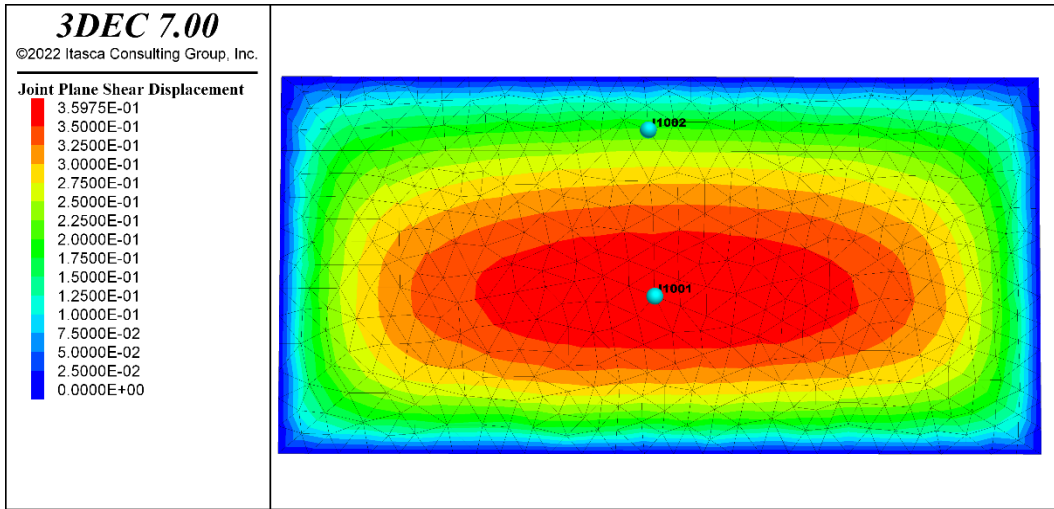


Figure A1-46. Same results as in Figure A1-45 but with same colour scale in all plots.

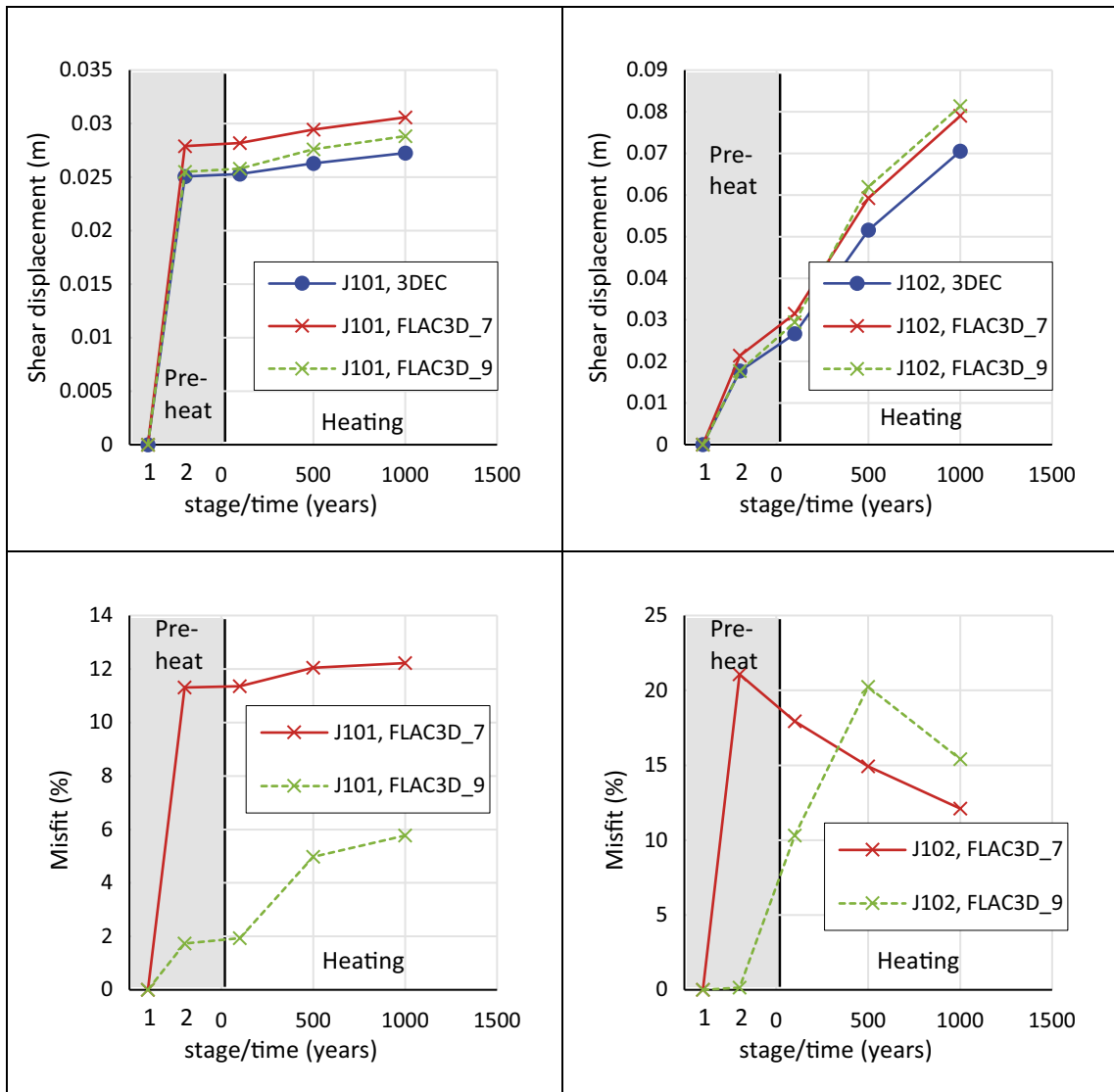


Figure A1-47. Upper: Evolution of joint 1000 shear displacement at the two points depicted in Figure A1-27, upper. Lower: Misfit between the FLAC3D results and the 3DEC results.

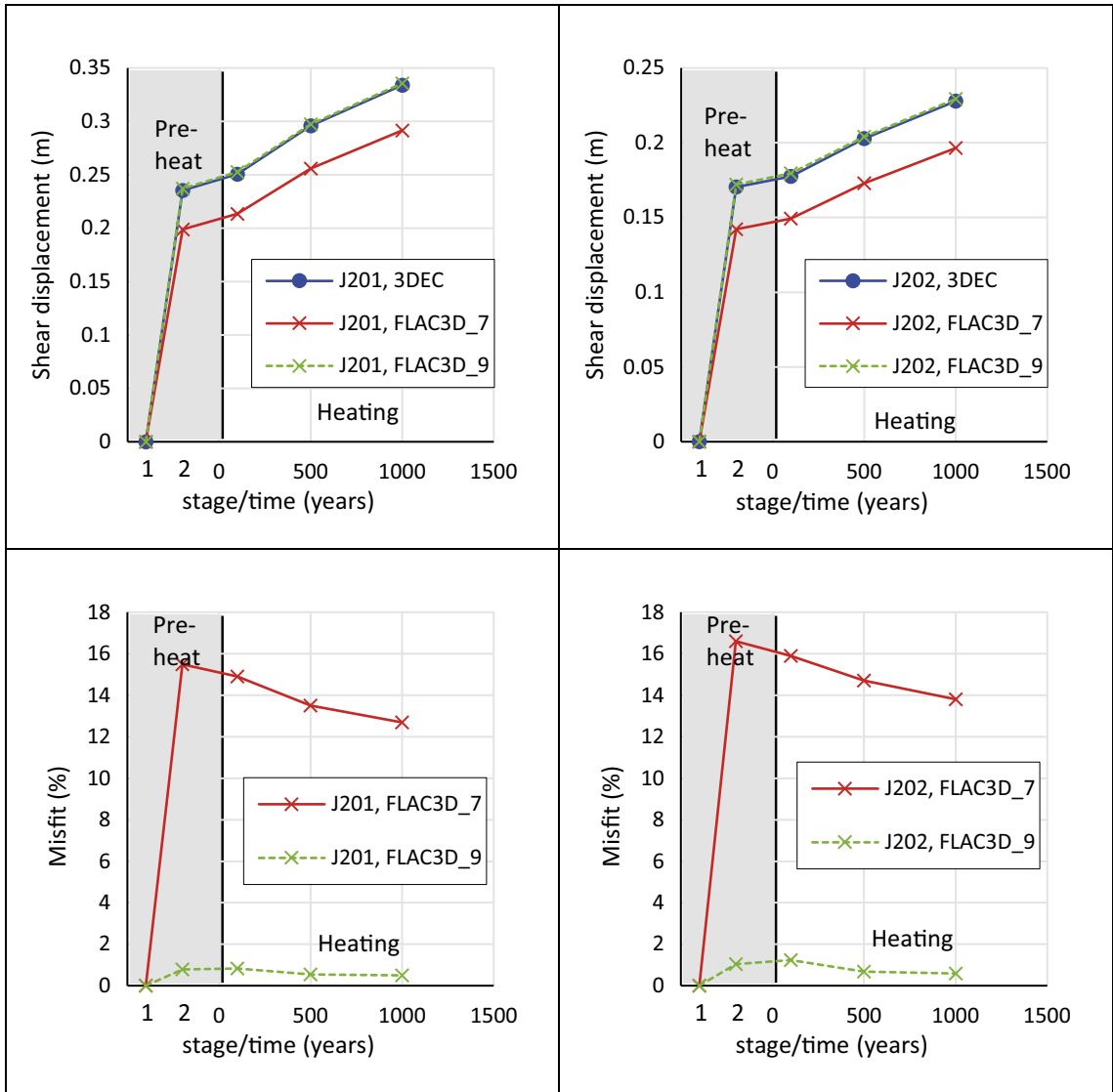


Figure A1-48. Upper: Evolution of joint 2000 shear displacement at the two points depicted in Figure A1-29, upper. Lower: Misfit between the FLAC3D results and the 3DEC results.

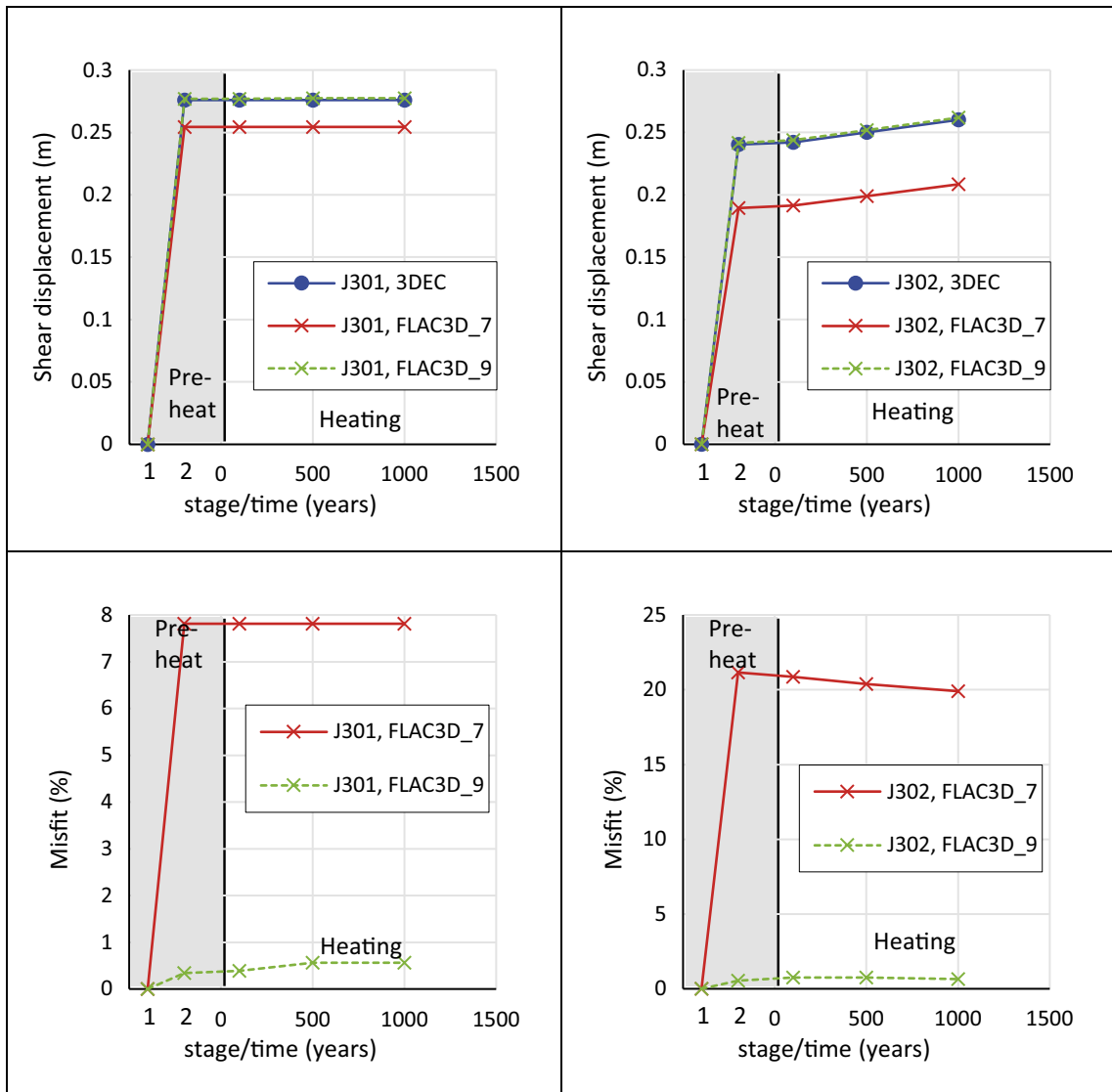


Figure A1-49. Upper: Evolution of joint 3000 shear displacement at the two points depicted in Figure A1-31, upper. Lower: Misfit between the FLAC3D results and the 3DEC results.

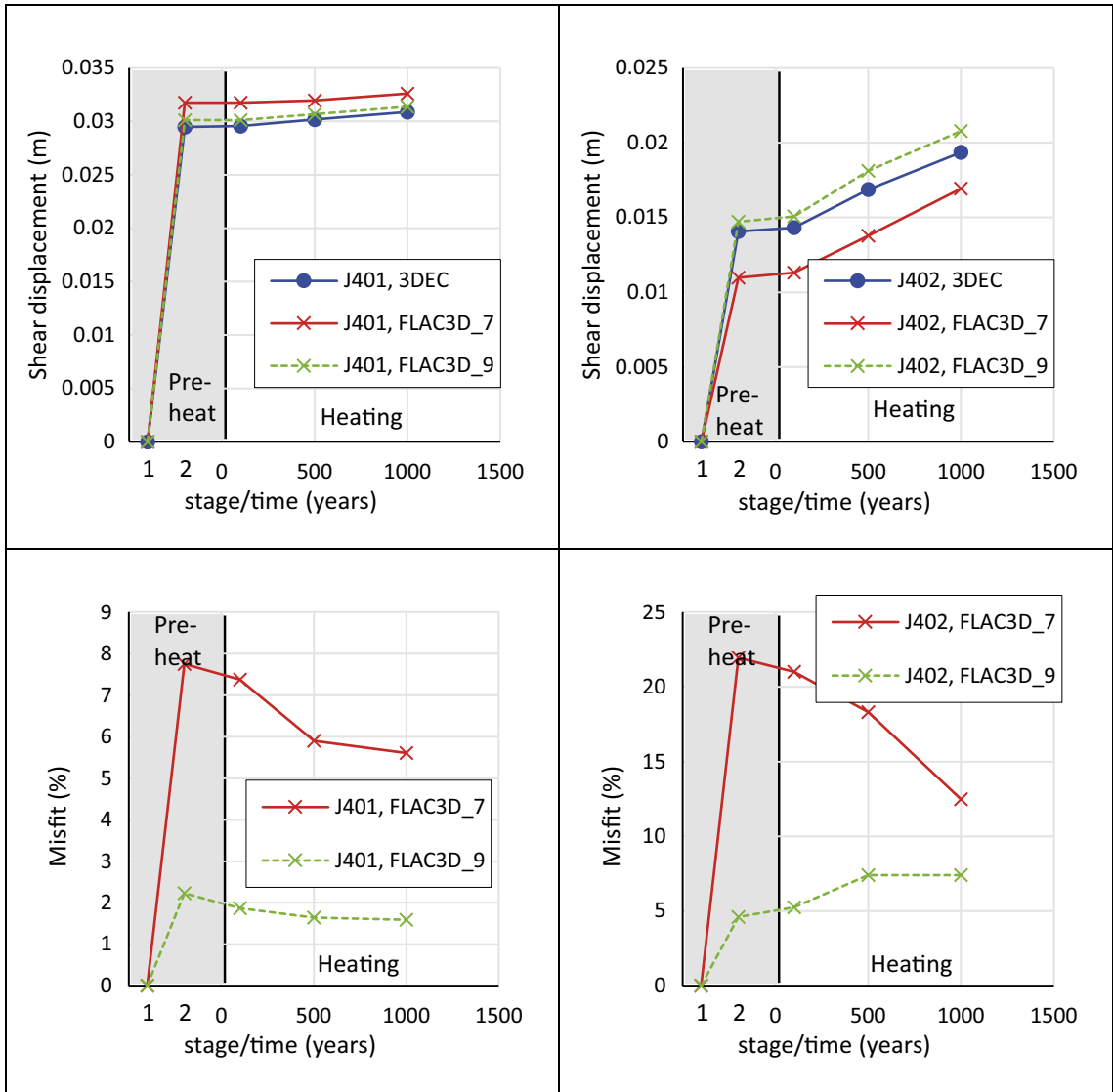


Figure A1-50. Upper: Evolution of joint 4000 shear displacement at the two points depicted in Figure A1-33, upper. Lower: Misfit between the FLAC3D results and the 3DEC results.

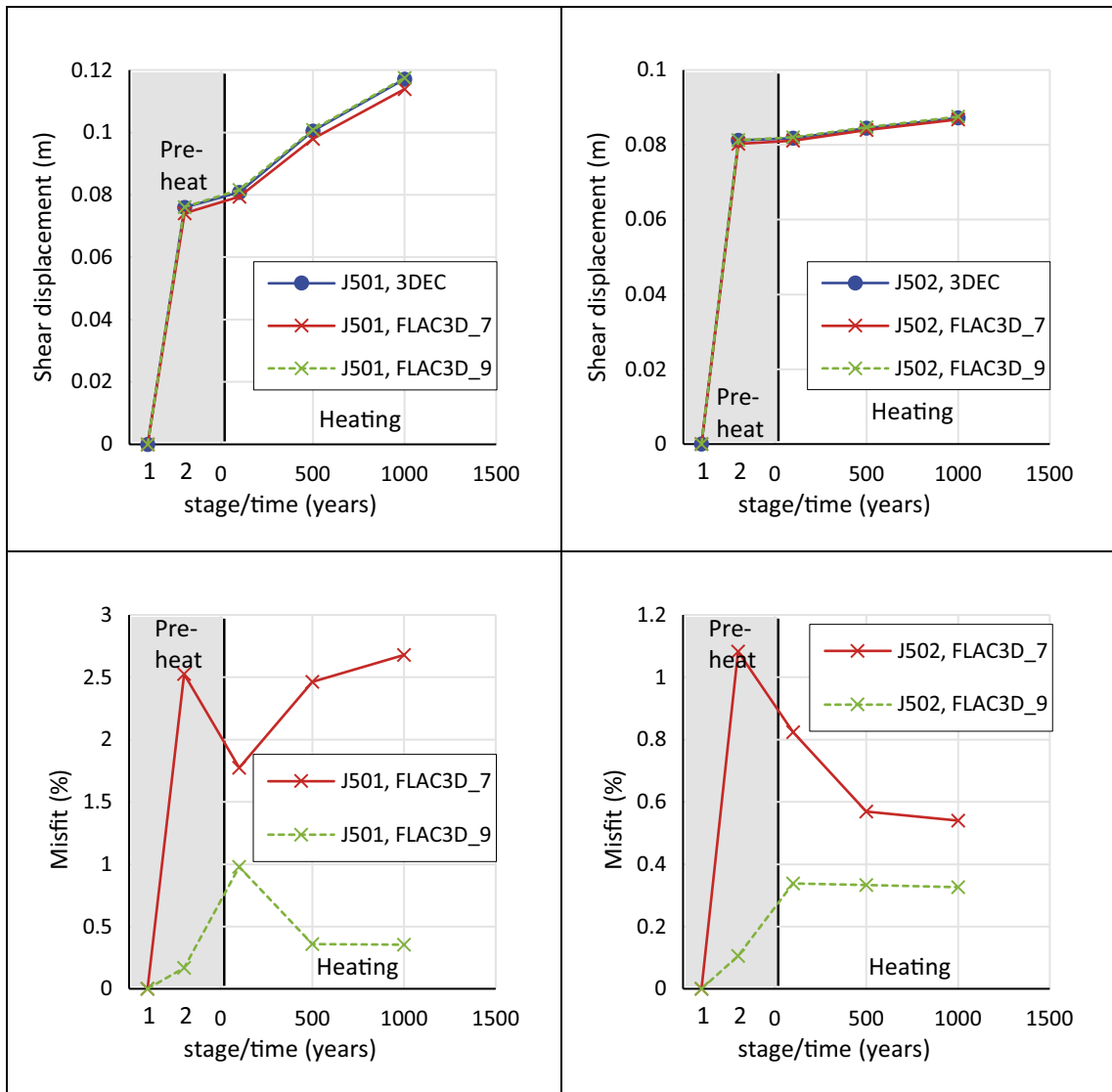


Figure A1-51. Upper: Evolution of joint 5000 shear displacement at the two points depicted in Figure A1-35, upper. Lower: Misfit between the FLAC3D results and the 3DEC results.

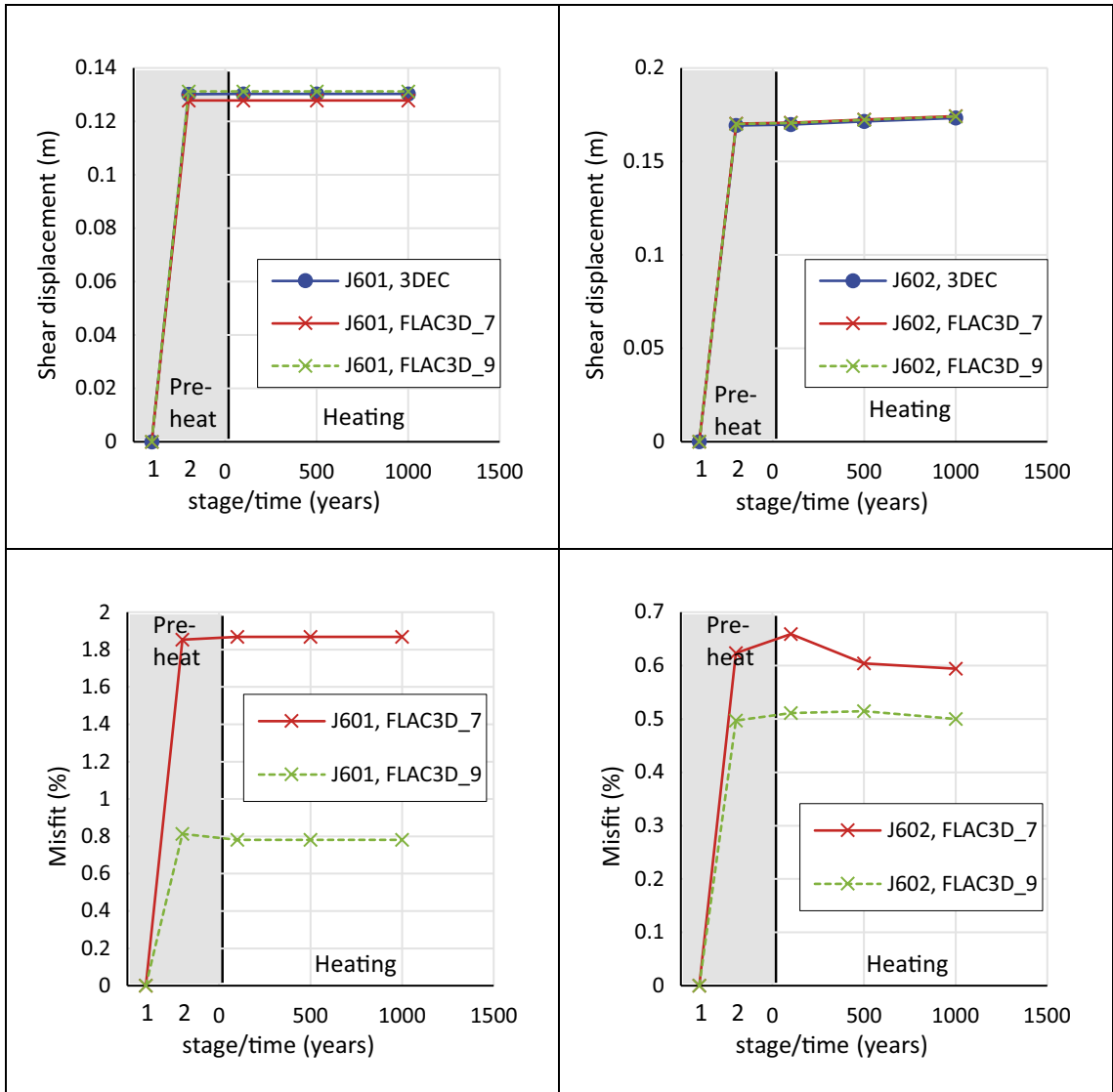


Figure A1-52. Upper: Evolution of joint 6000 shear displacement at the two points depicted in Figure A1-37, upper. Lower: Misfit between the FLAC3D results and the 3DEC results.

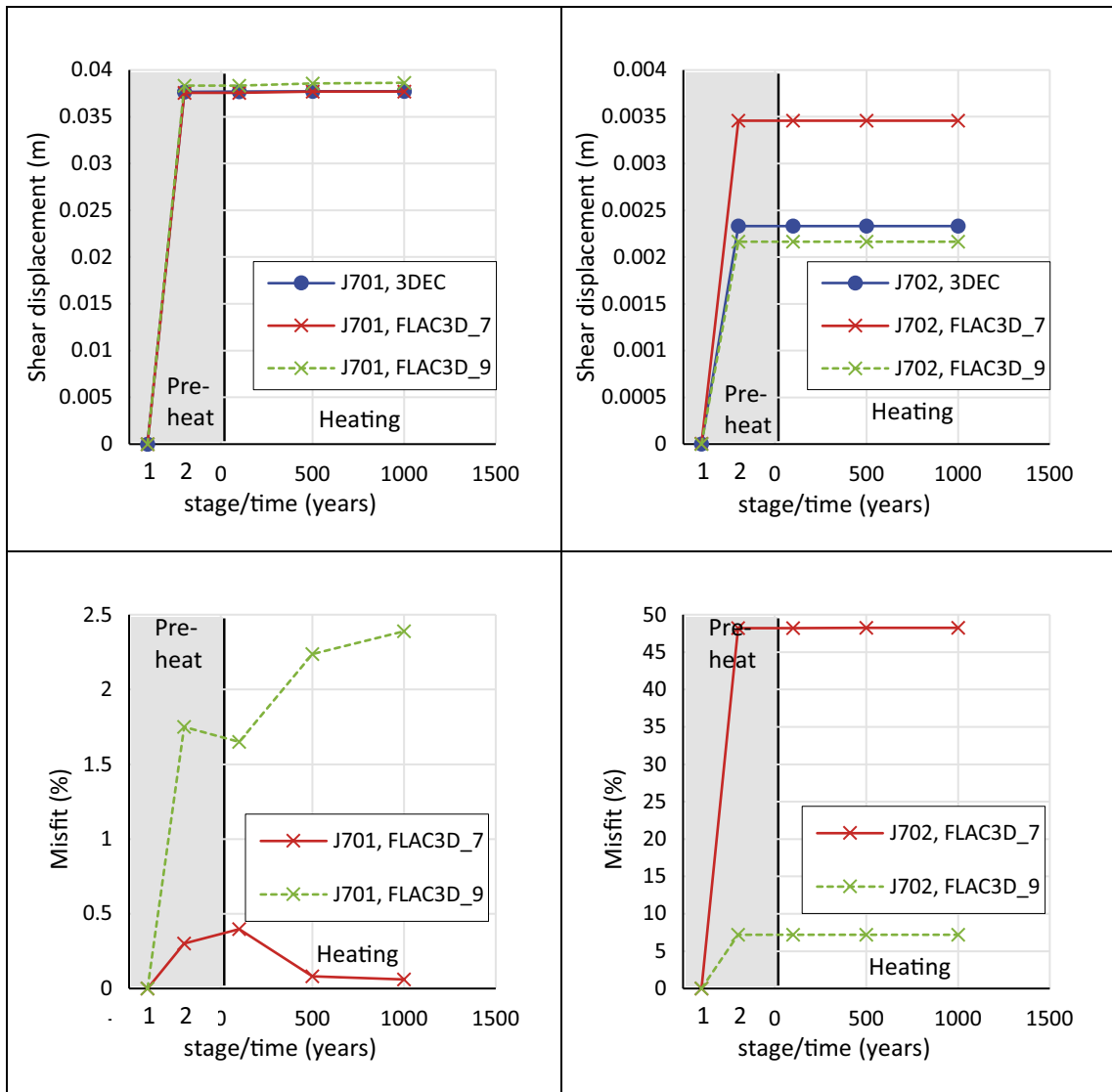


Figure A1-53. Upper: Evolution of joint 7000 shear displacement at the two points depicted in Figure A1-39, upper. Lower: Misfit between the FLAC3D results and the 3DEC results.

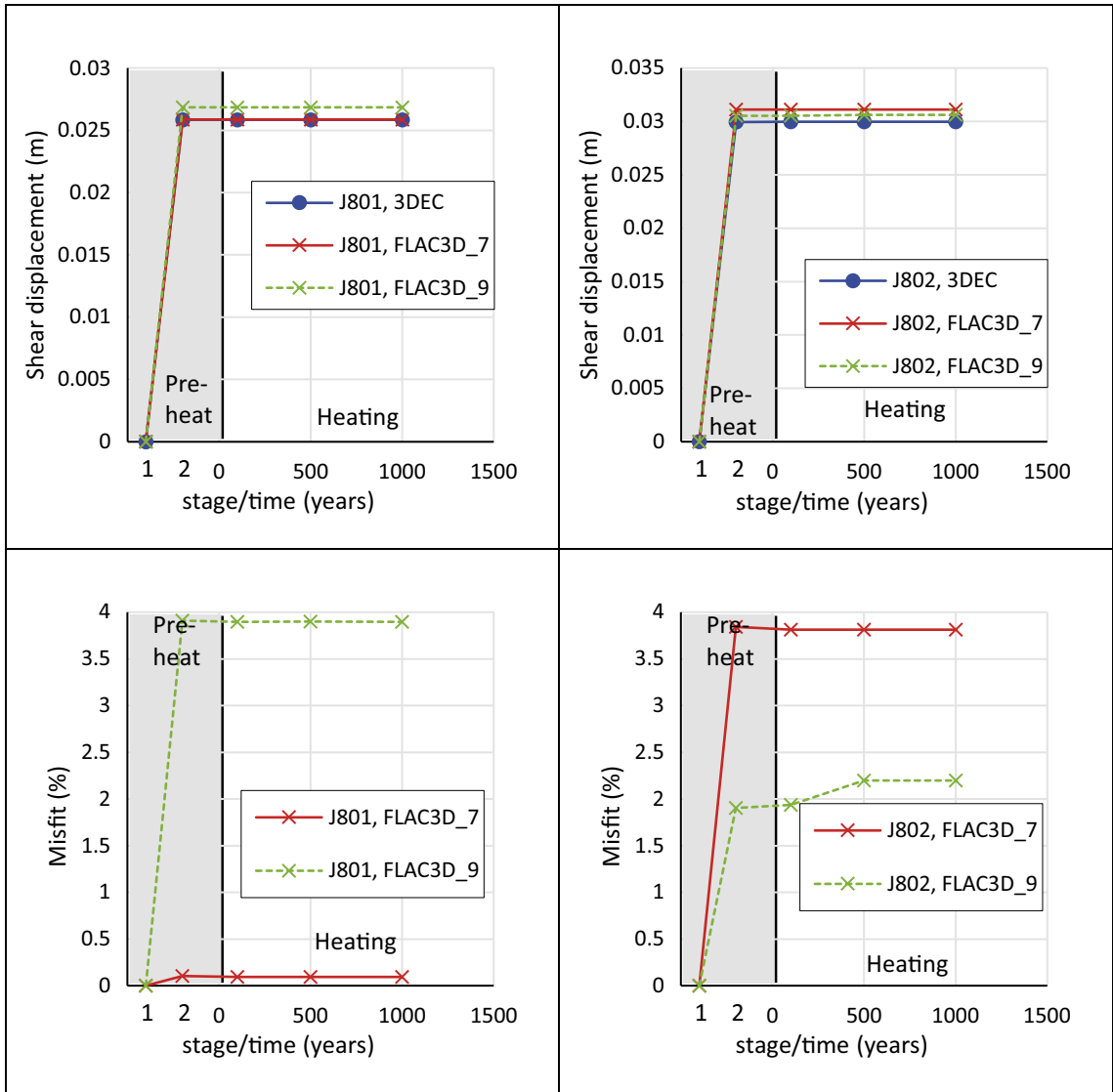


Figure A1-54. Upper: Evolution of joint 8000 shear displacement at the two points depicted in Figure A1-41, upper. Lower: Misfit between the FLAC3D results and the 3DEC results.

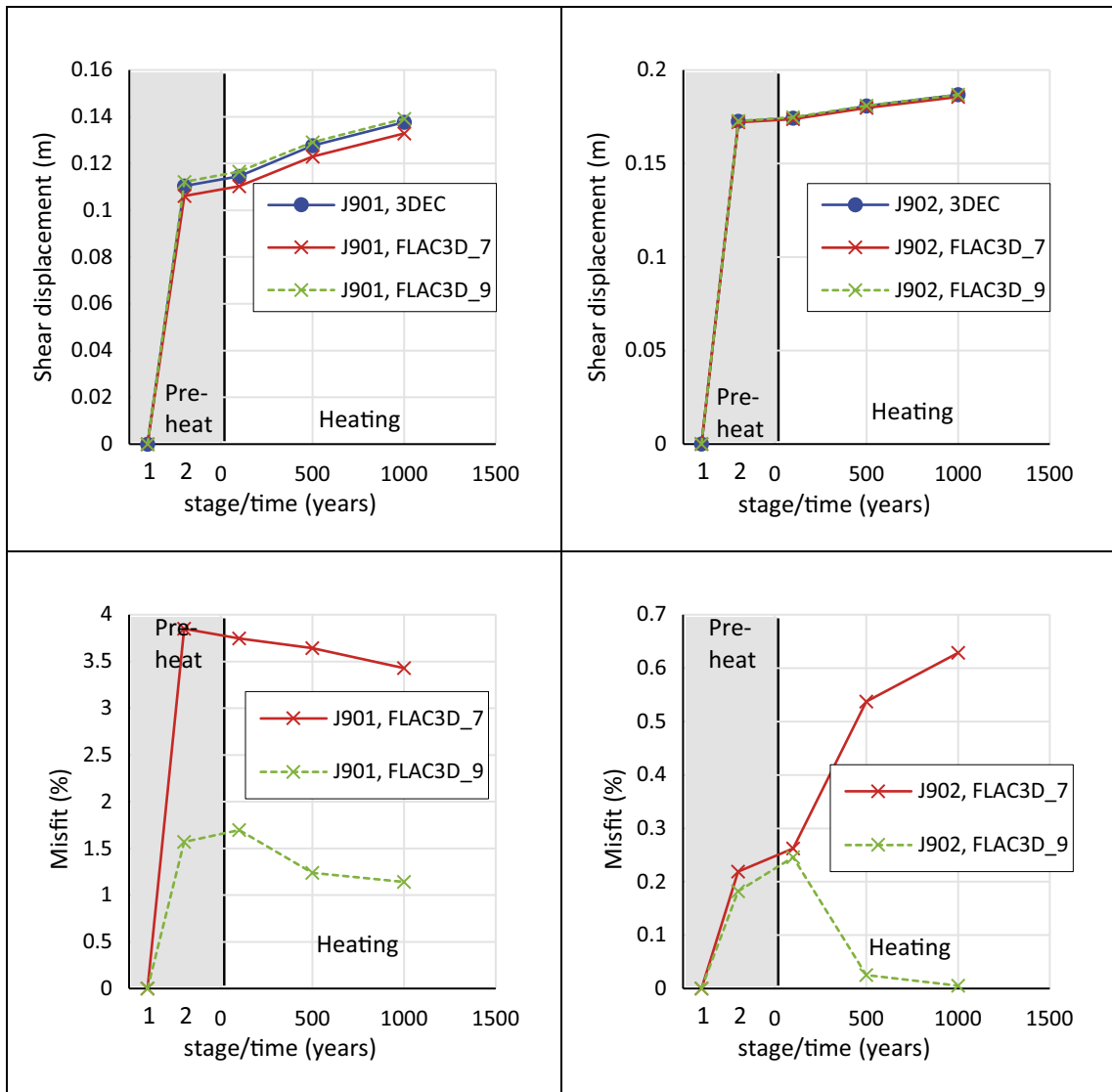


Figure A1-55. Upper: Evolution of joint 9000 shear displacement at the two points depicted in Figure A1-43, upper. Lower: Misfit between the FLAC3D results and the 3DEC results.

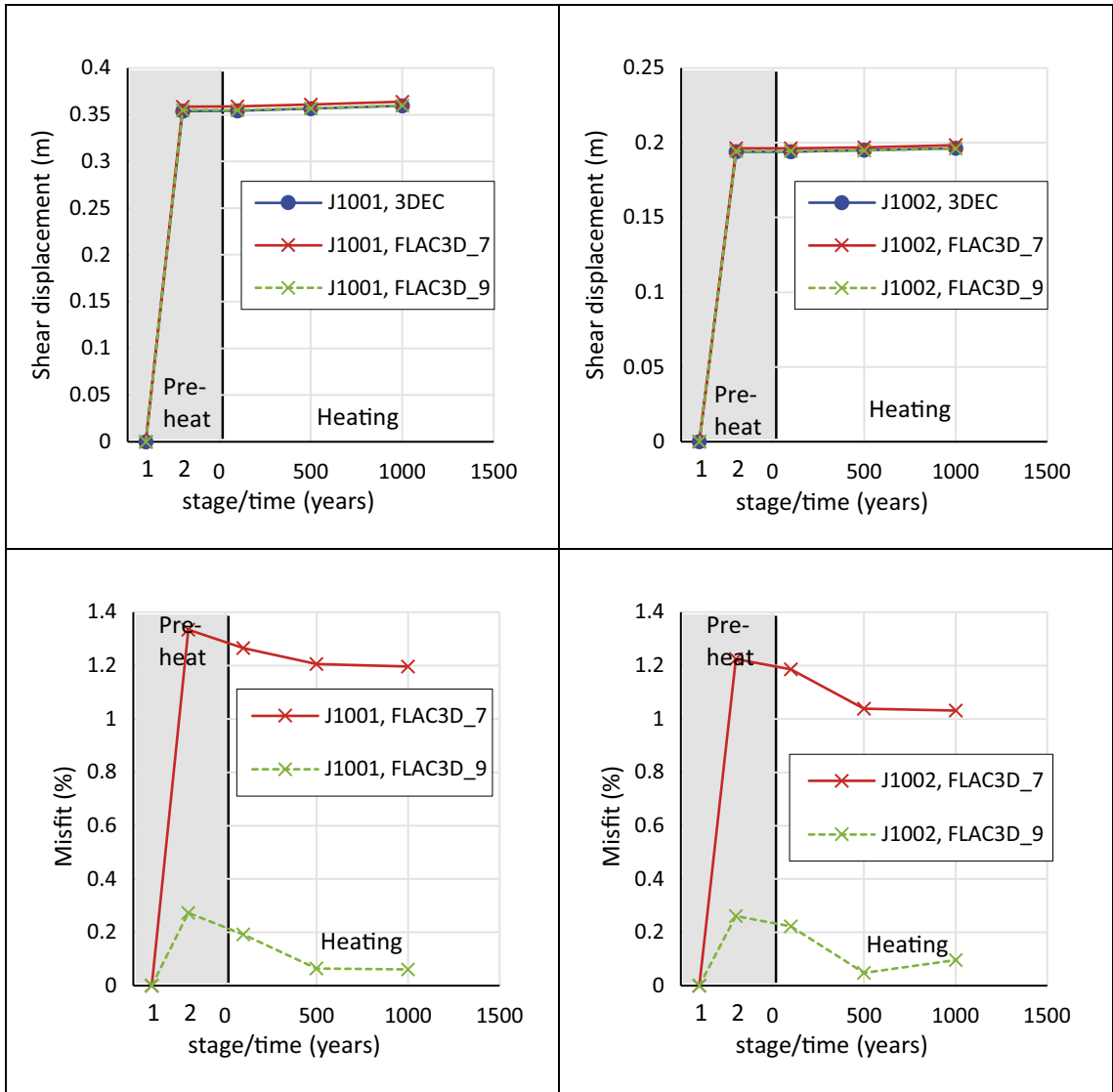


Figure A1-56. Upper: Evolution of joint 10000 shear displacement at the two points depicted in Figure A1-45, upper. Lower: Misfit between the FLAC3D results and the 3DEC results.

Results from thermo-mechanical model with openings and fractures (Chapter 4)

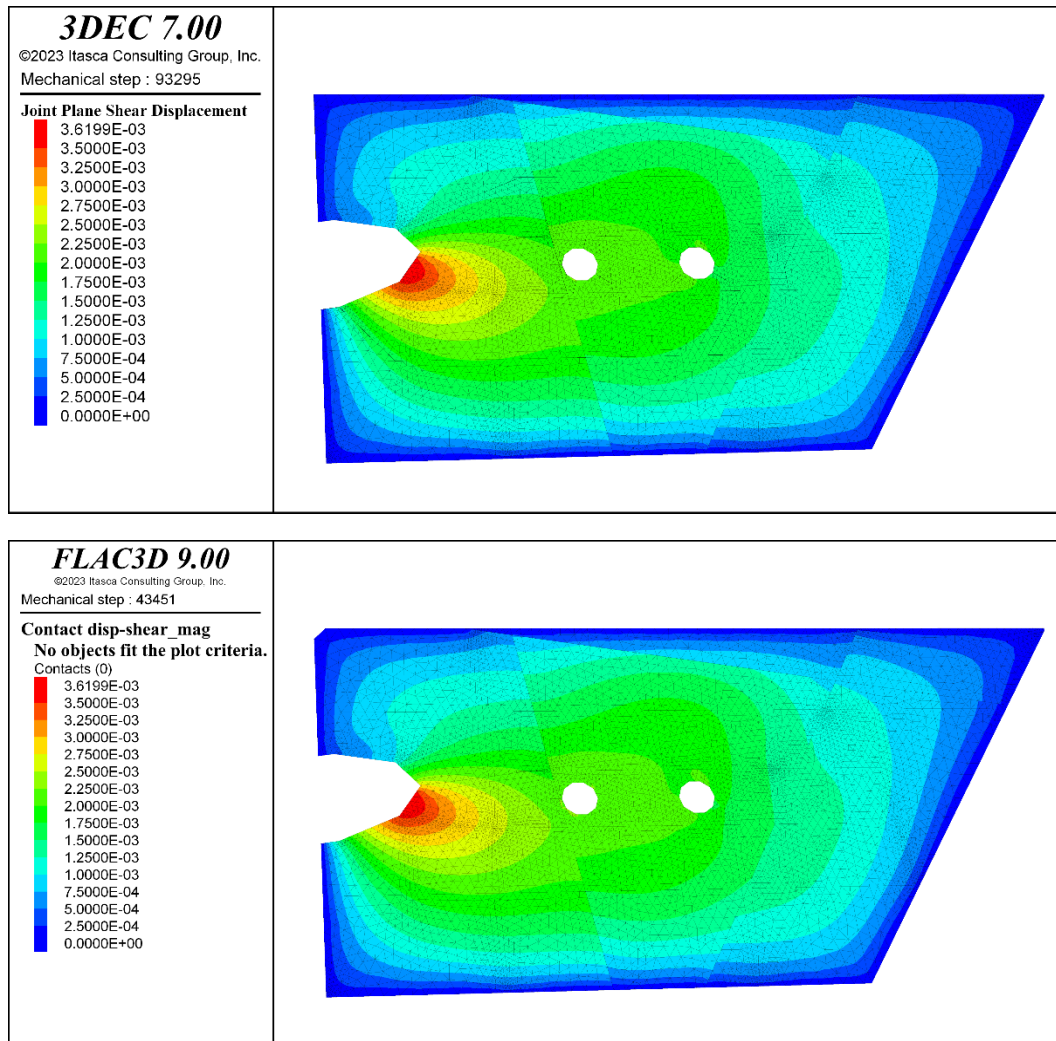


Figure A2-1. Colour scale plots of shear displacement on joint 1046 after completed simulation. To facilitate comparison, the colour scales are set equal.

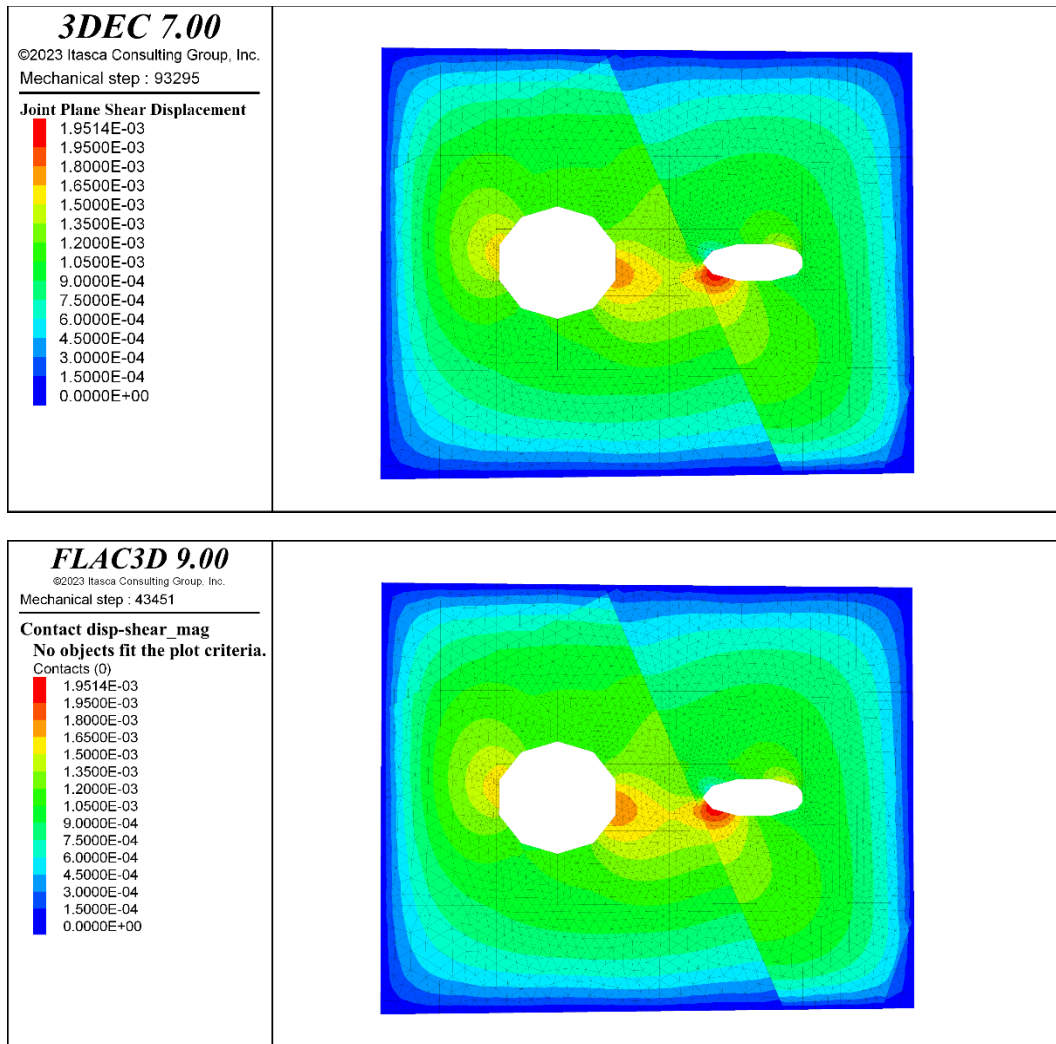


Figure A2-2. Colour scale plots of shear displacement on joint 1061 after completed simulation. To facilitate comparison, the colour scales are set equal.

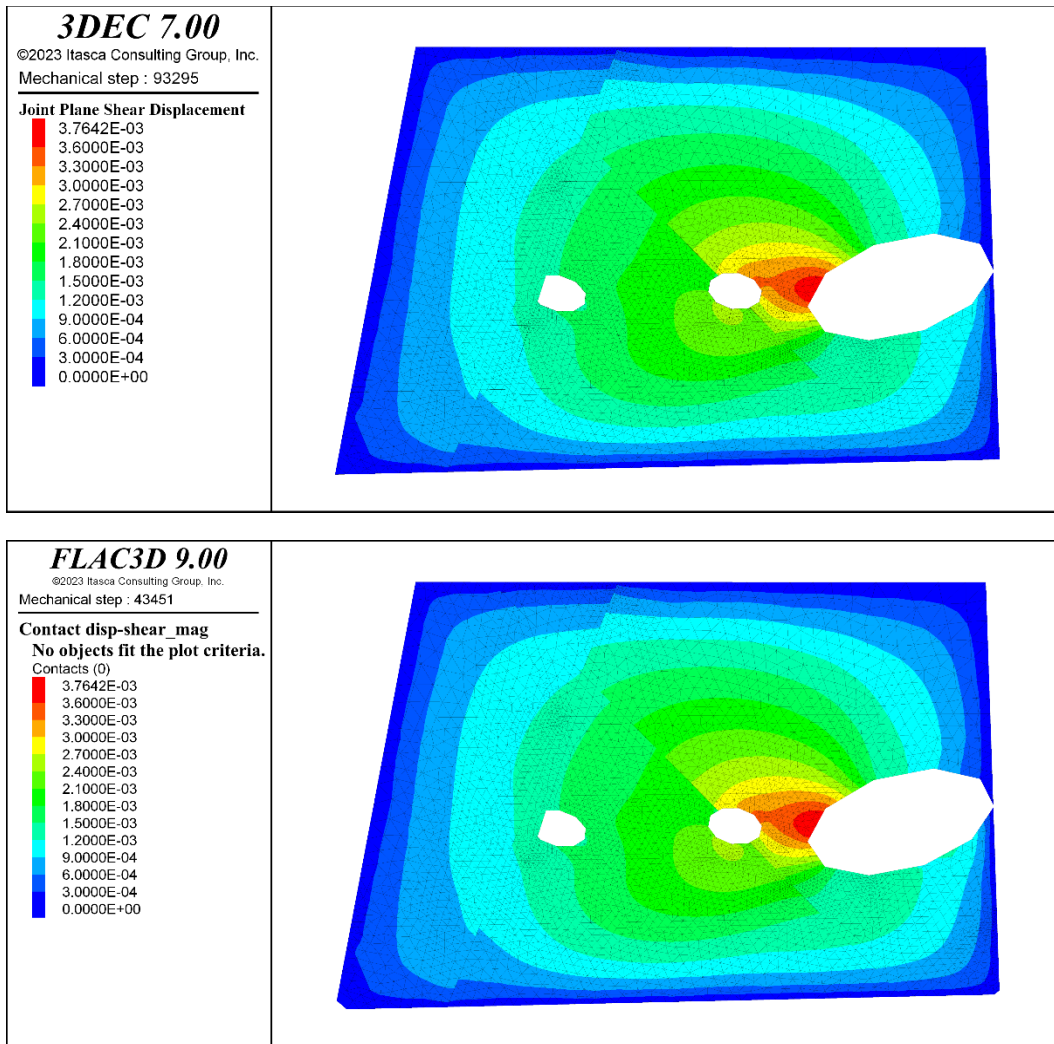


Figure A2-3. Colour scale plots of shear displacement on joint 3075 after completed simulation. To facilitate comparison, the colour scales are set equal.

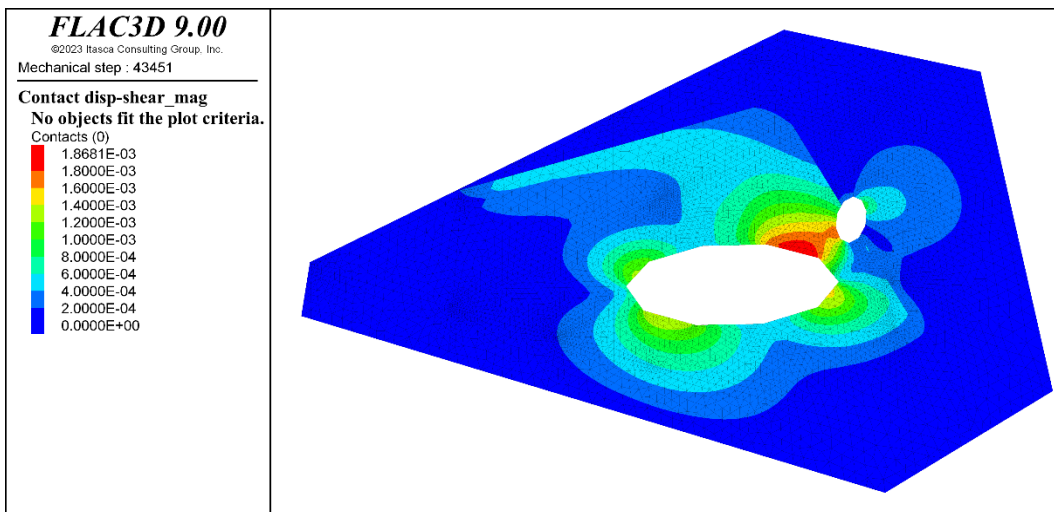
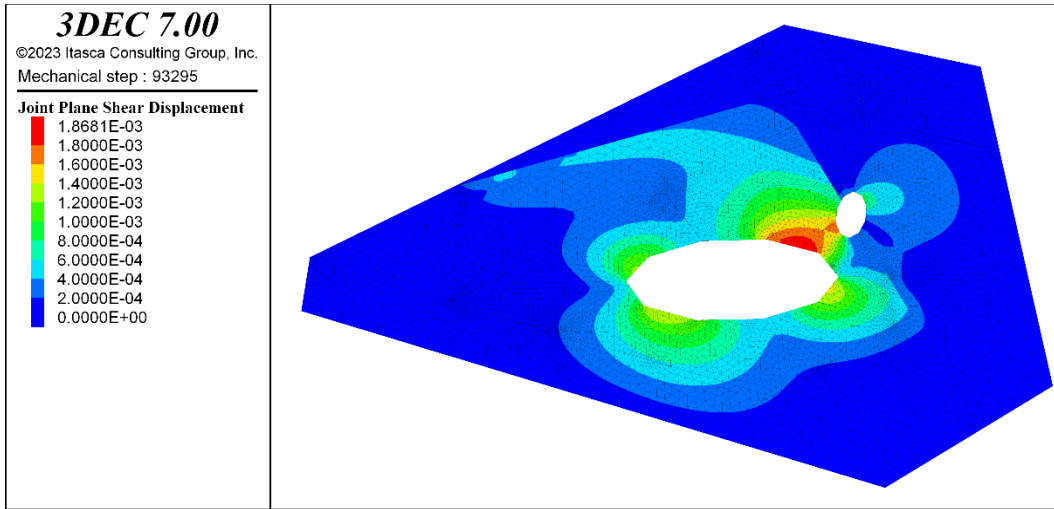


Figure A2-4. Colour scale plots of shear displacement on joint 4019 after completed simulation. To facilitate comparison, the colour scales are set equal.

Results from Forsmark earthquake model (Chapter 5)

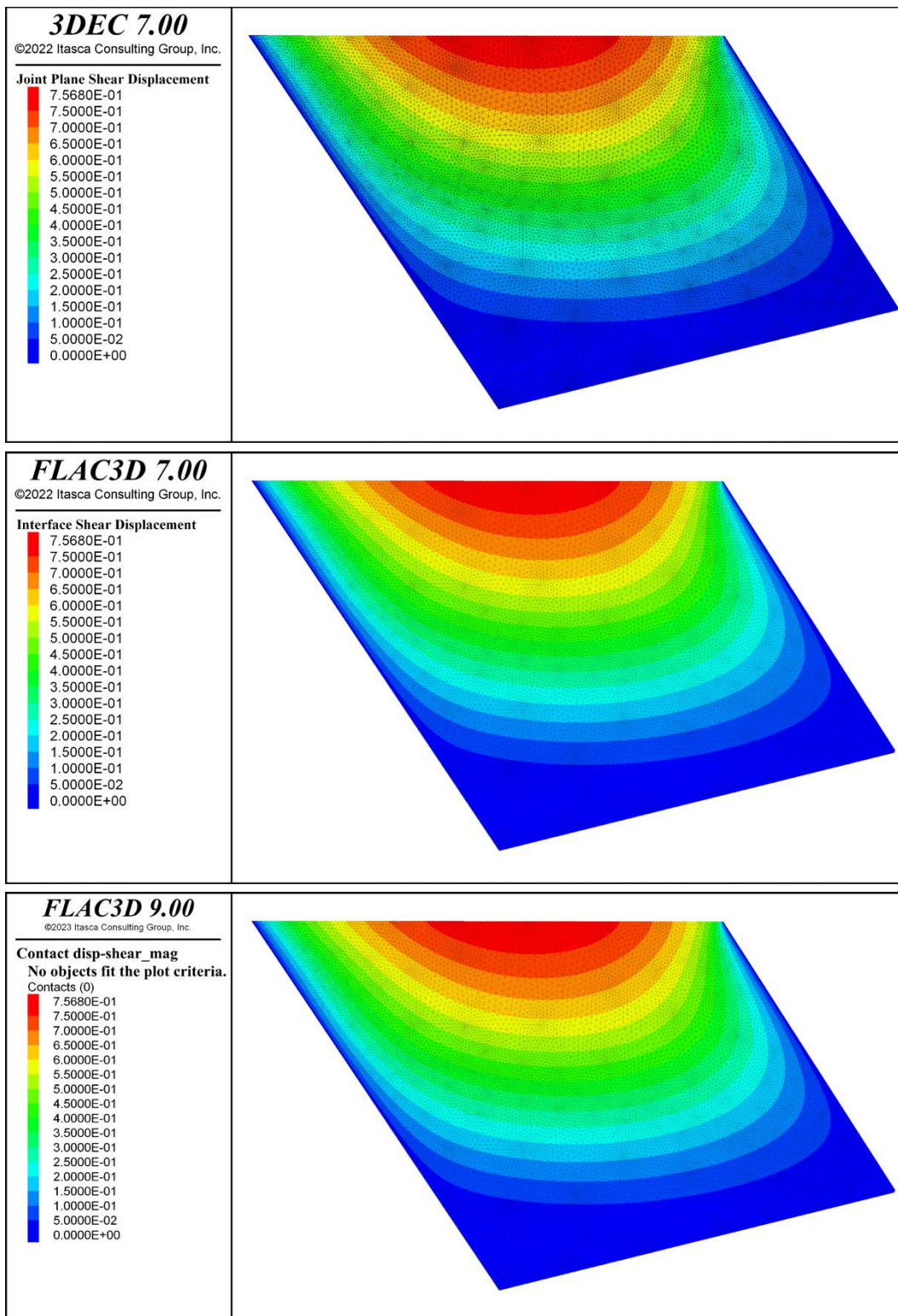


Figure A3-1. ZFMA2 shear displacements generated during the quasi-static calculation step. Upper: 3DEC. Middle: FLAC3D_7. Lower: FLAC3D_9.

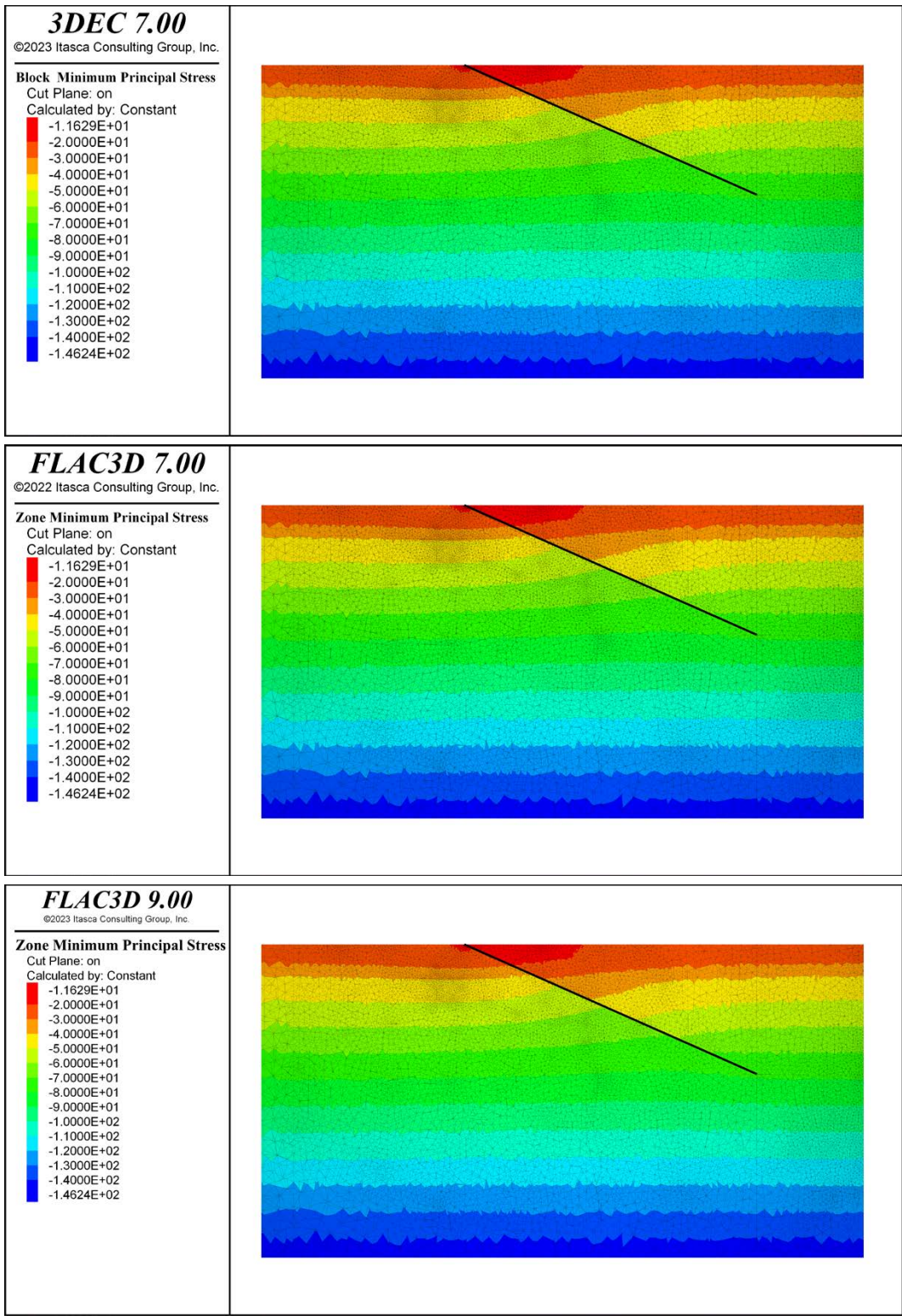


Figure A3-2. Major principal stress (MPa) in the continuum after the quasi-static calculation step. The results are shown on a vertical cross-section plane. The black line indicates the location of the ZFMA2 plane. Upper: 3DEC. Middle: FLAC3D_7. Lower: FLAC3D_9. Note that only a portion of the model volume is shown here.

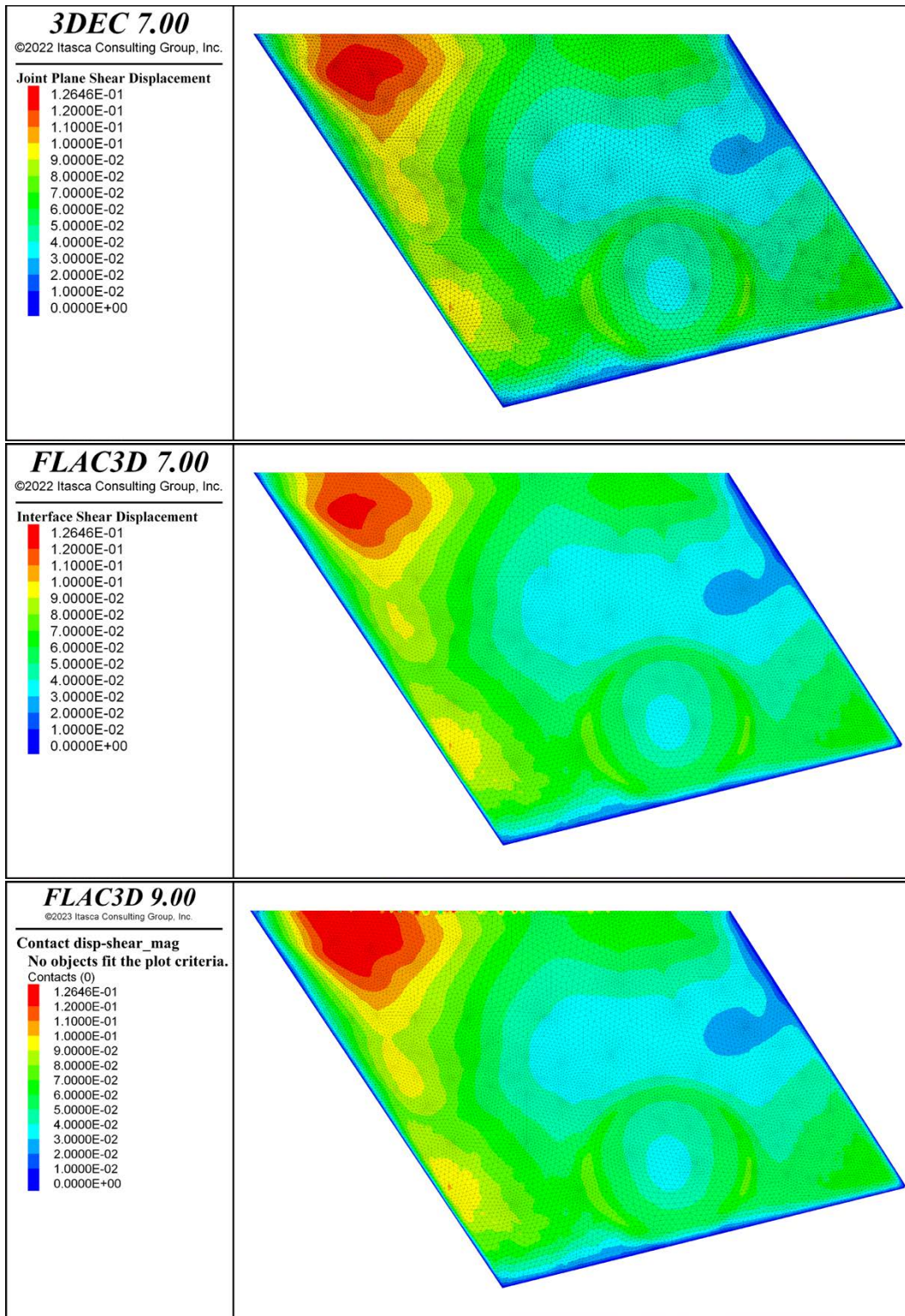


Figure A3-3. ZFMA2 final shear displacement (m) generated during earthquake rupture. Upper: 3DEC. Middle: FLAC3D_7. Lower: FLAC3D_9.

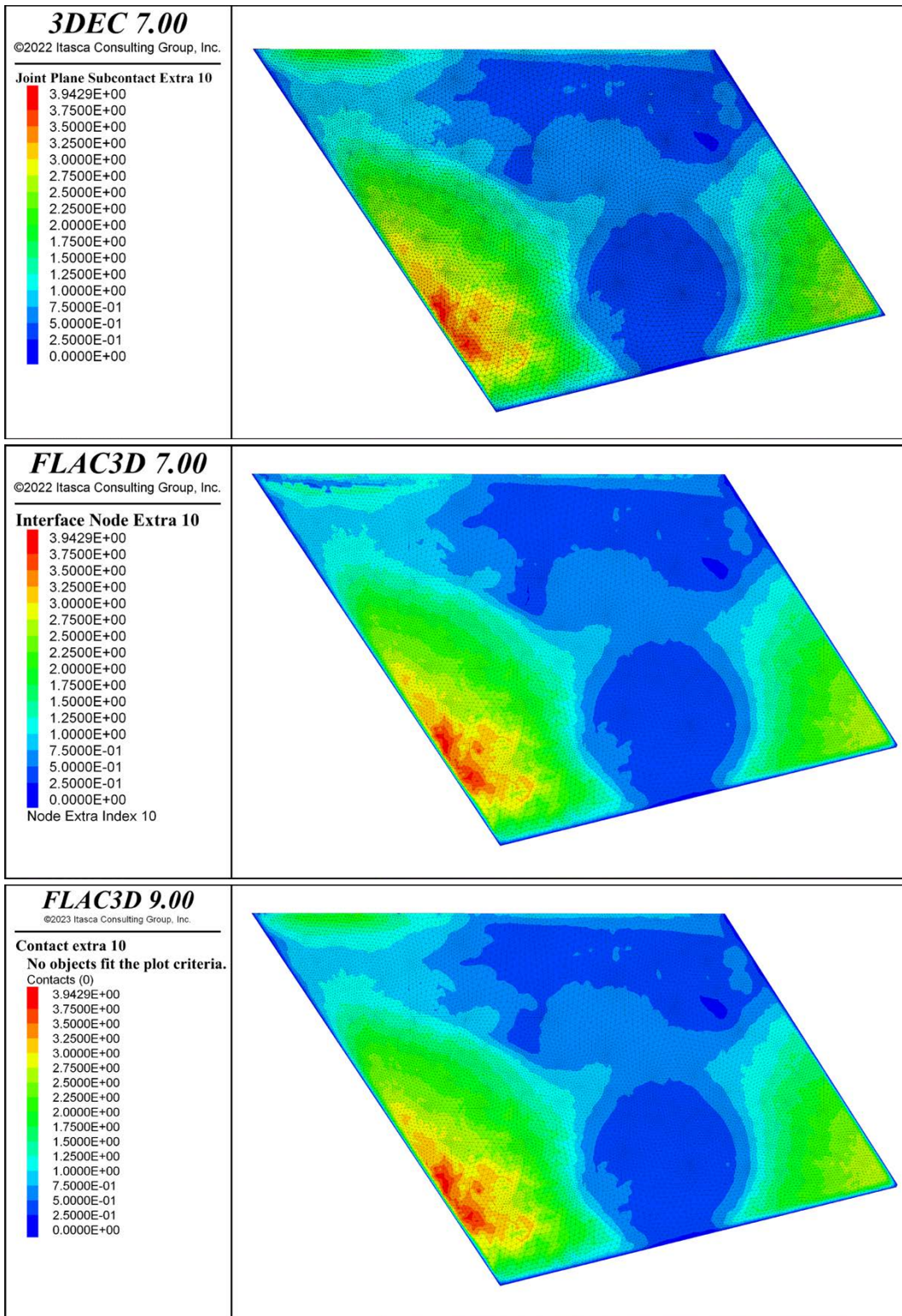


Figure A3-4. ZFMA2 peak slip velocity (m/s) during earthquake rupture. Upper: 3DEC. Middle: FLAC3D_7. Lower: FLAC3D_9.

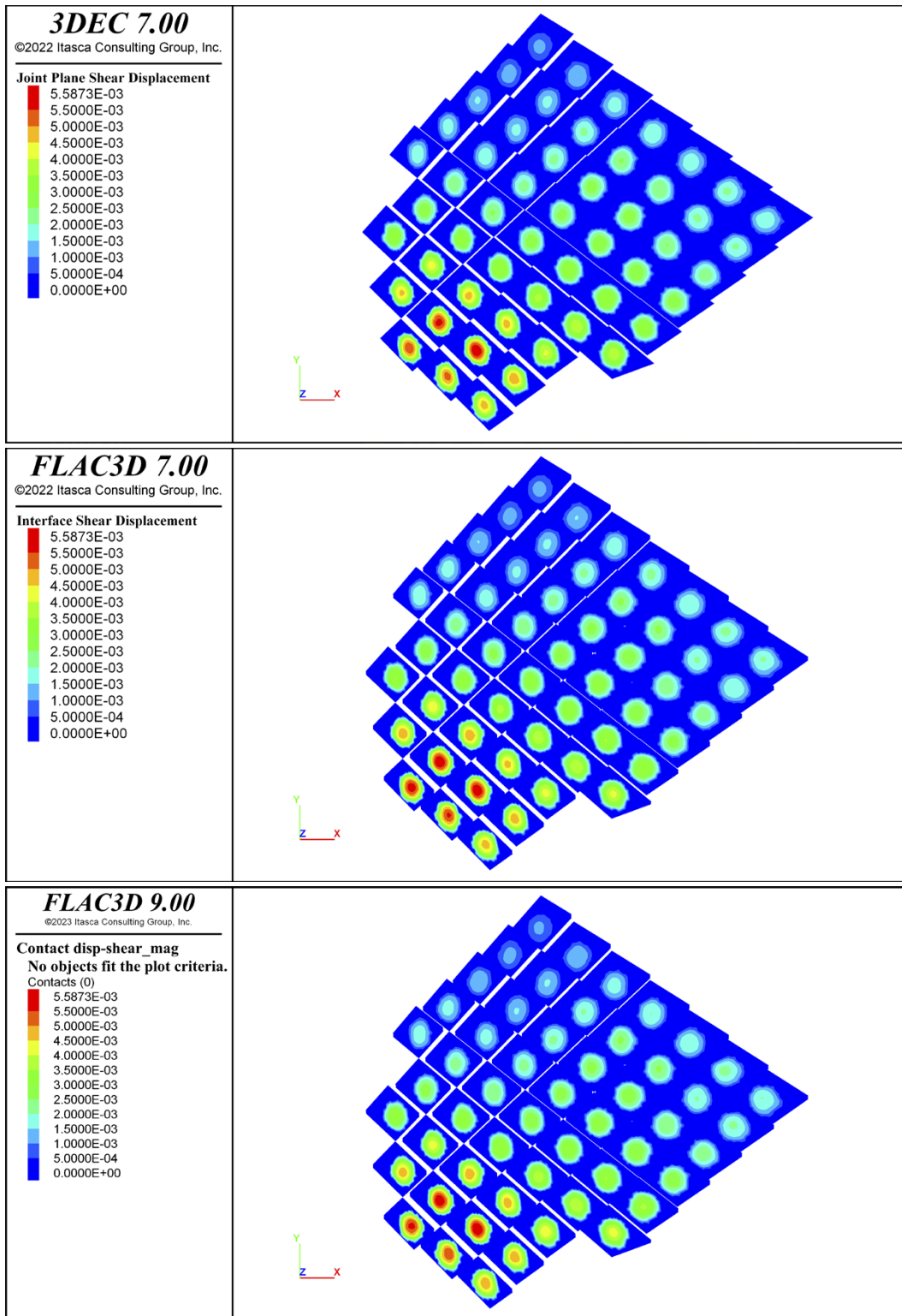


Figure A3-5. Target fracture final shear displacements (m) after earthquake rupture.

Results from large-scale earthquake benchmark case (Chapter 6)

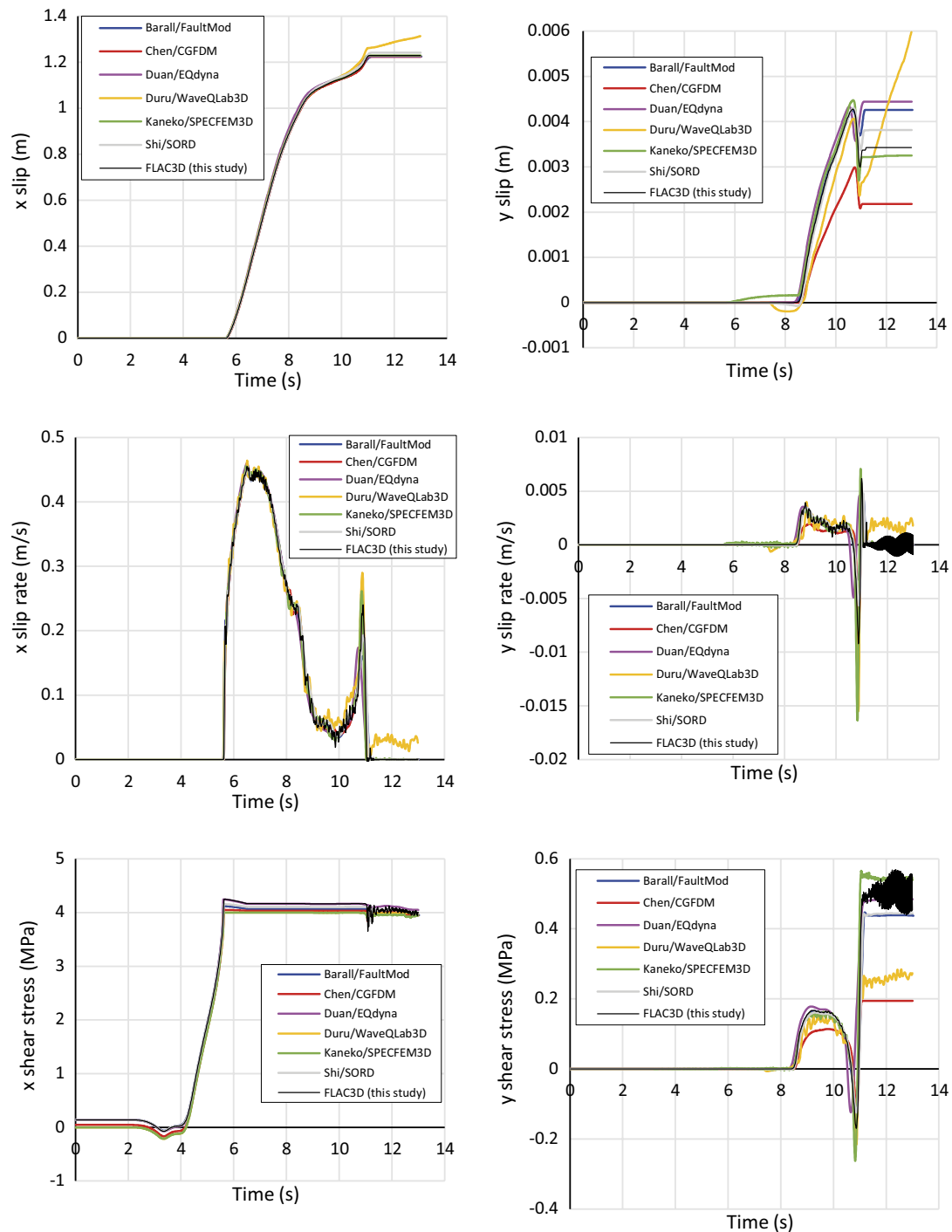


Figure A4-1. Time evolution of slip, slip rate and shear stress at the on-fault monitoring station F-050dp000 (cf. Figure 6-4). Results from FLAC3D_9 (on zone-joint) are plotted along with results from other authors/codes.

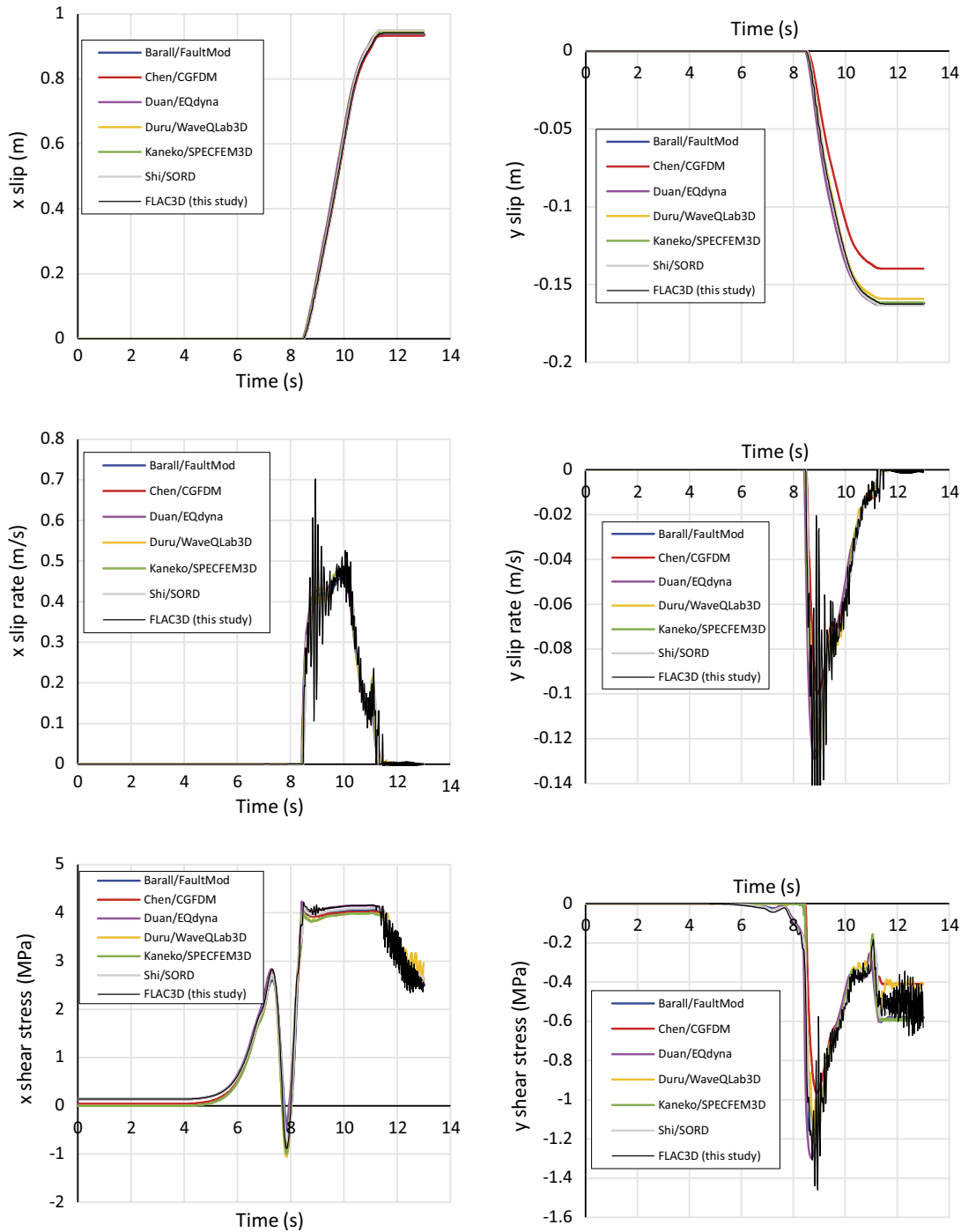


Figure A4-2. Time evolution of slip, slip rate and shear stress at the on-fault monitoring station F150dp000 (cf. Figure 6-4). Results from *FLAC3D_9* (on zone-joint) are plotted along with results from other authors/codes.

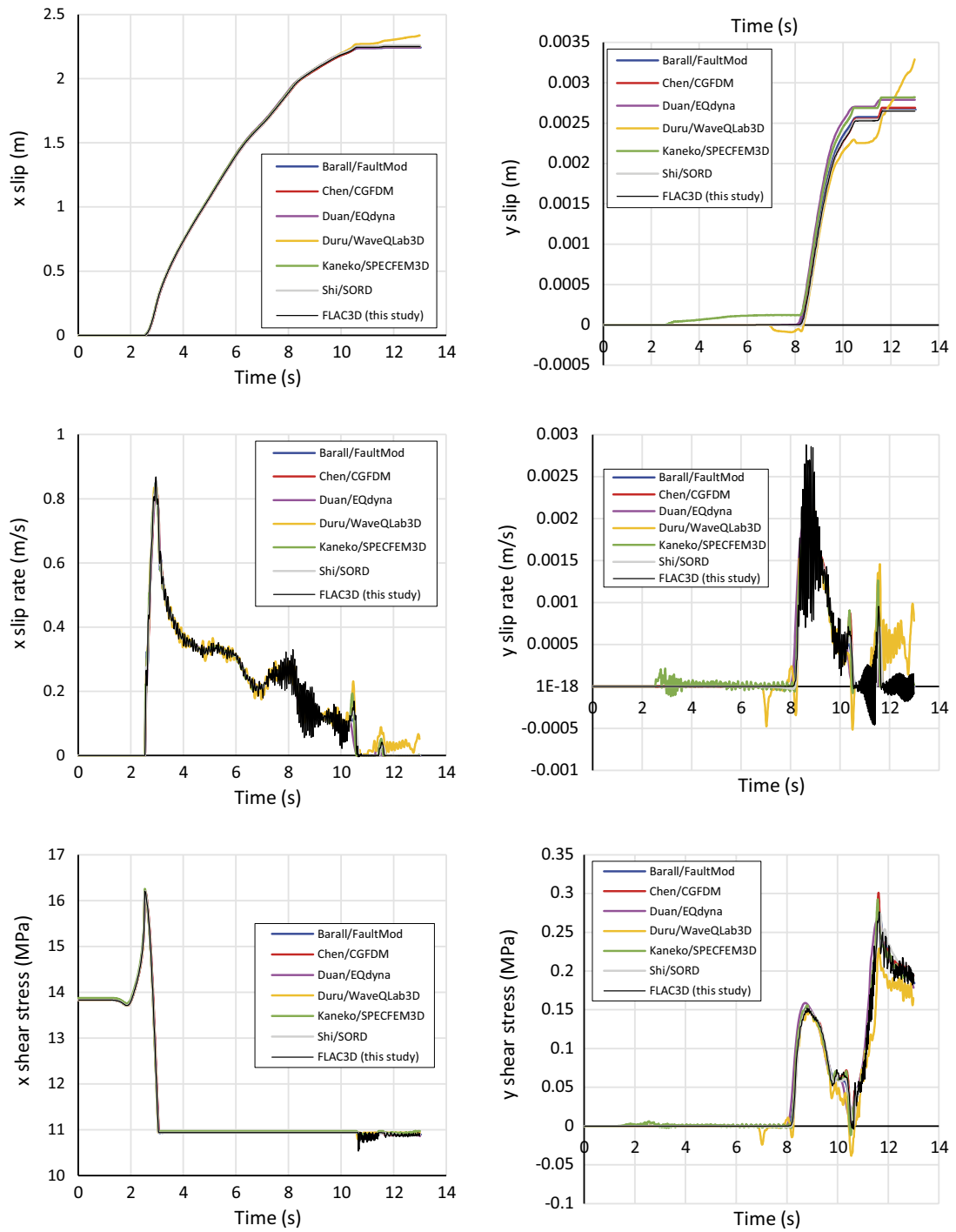


Figure A4-3. Time evolution of slip, slip rate and shear stress at the on-fault monitoring station F-050dp050 (cf. Figure 6-4). Results from FLAC3D_9 (on zone-joint) are plotted along with results from other authors/codes.

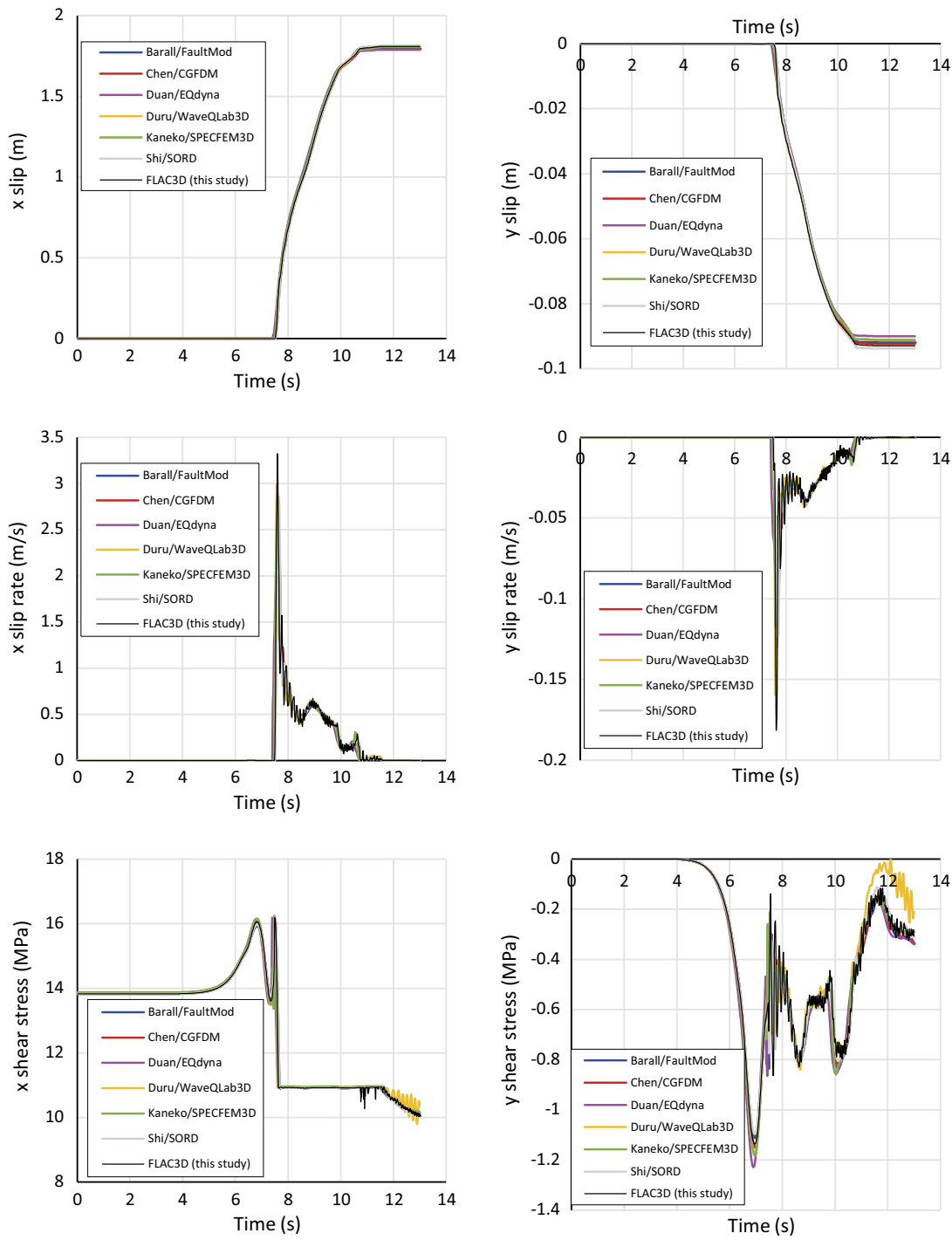


Figure A4-4. Time evolution of slip, slip rate and shear stress at the on-fault monitoring station F150dp050 (cf. Figure 6-4). Results from FLAC3D_9 (on zone-joint) are plotted along with results from other authors/codes.

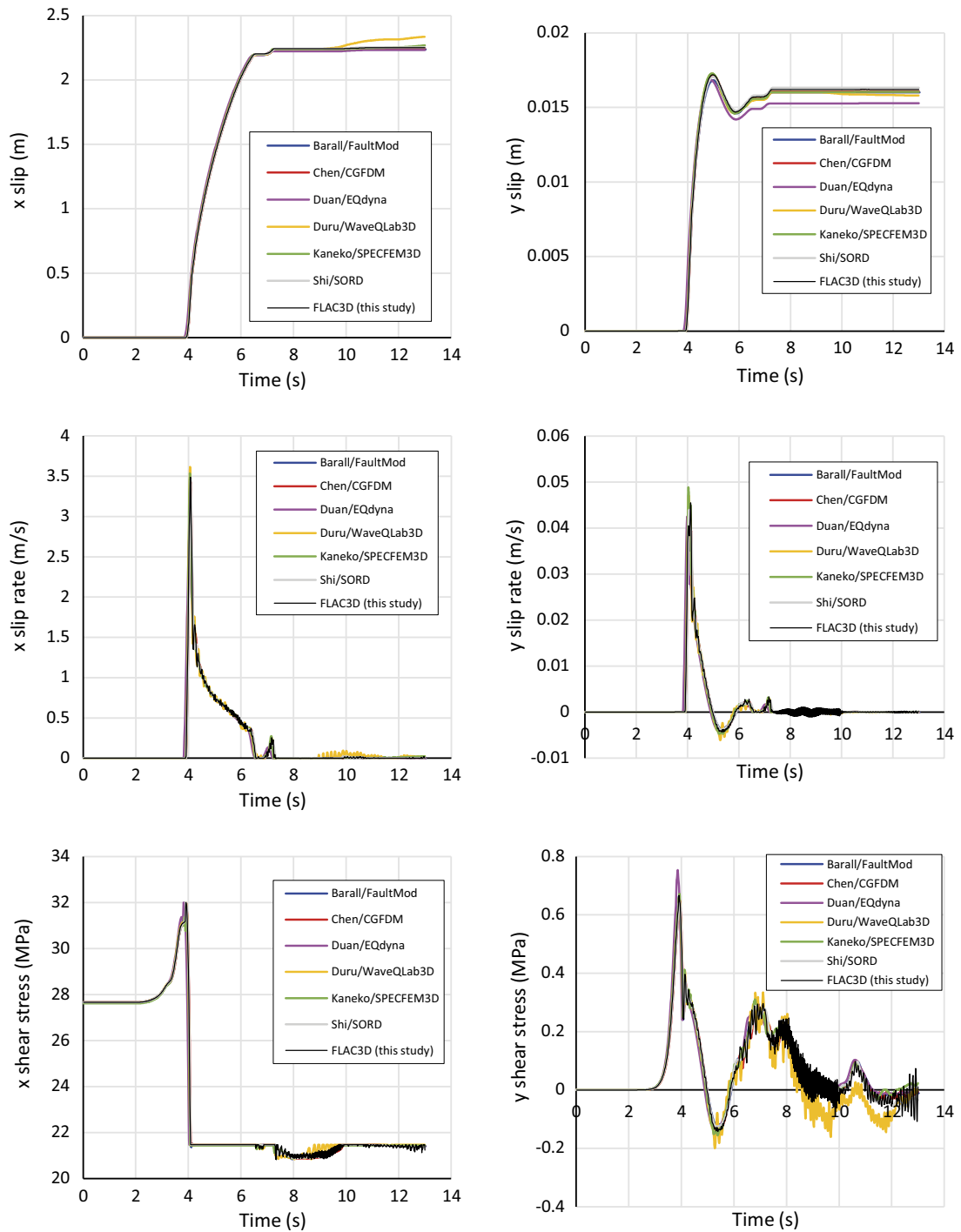


Figure A4-5. Time evolution of slip, slip rate and shear stress at the on-fault monitoring station F-150dp100 (cf. Figure 6-4). Results from *FLAC3D_9* (on zone-joint) are plotted along with results from other authors/codes.

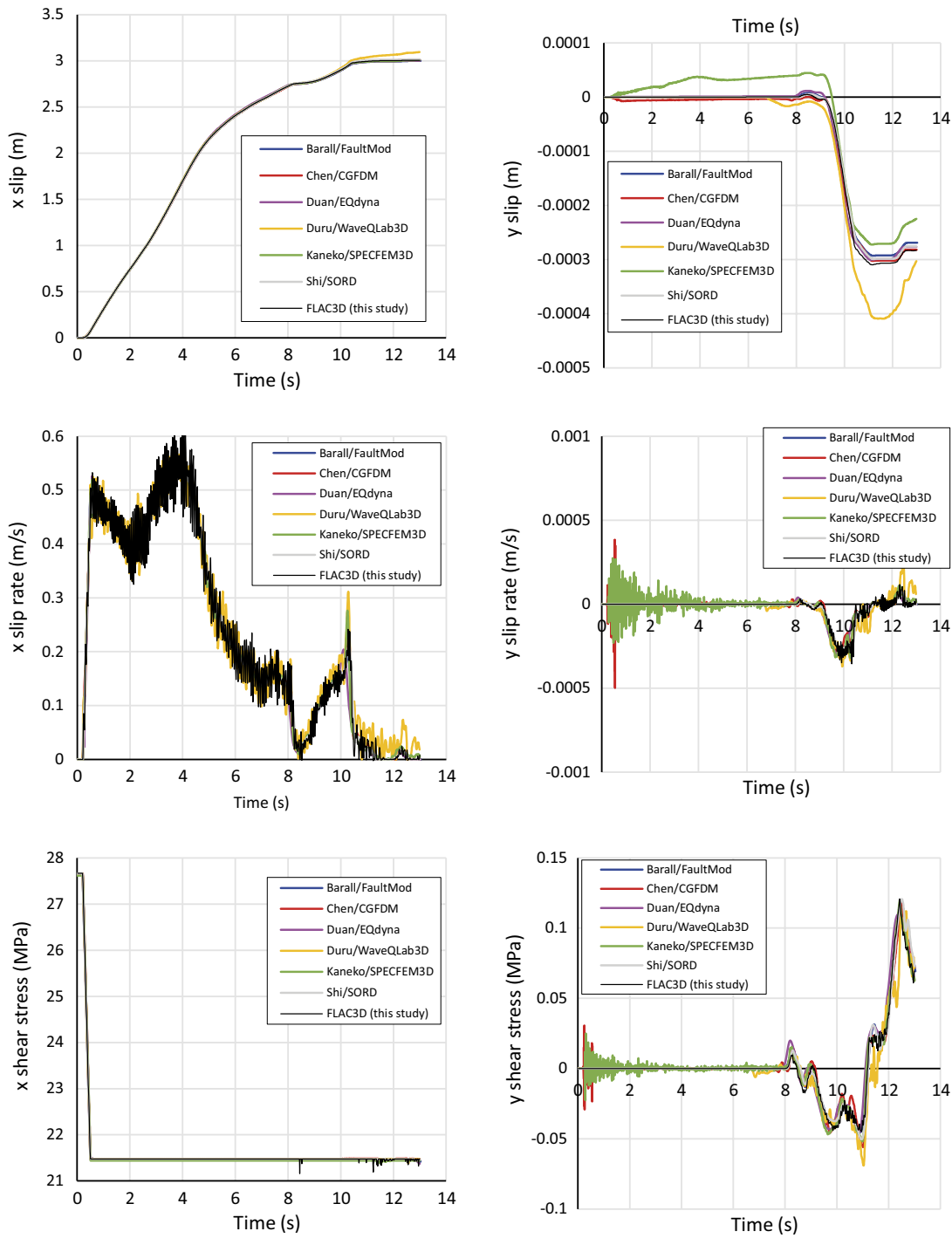


Figure A4-6. Time evolution of slip, slip rate and shear stress at the on-fault monitoring station F-050dp100 (cf. Figure 6-4). Results from *FLAC3D_9* (on zone-joint) are plotted along with results from other authors/codes.

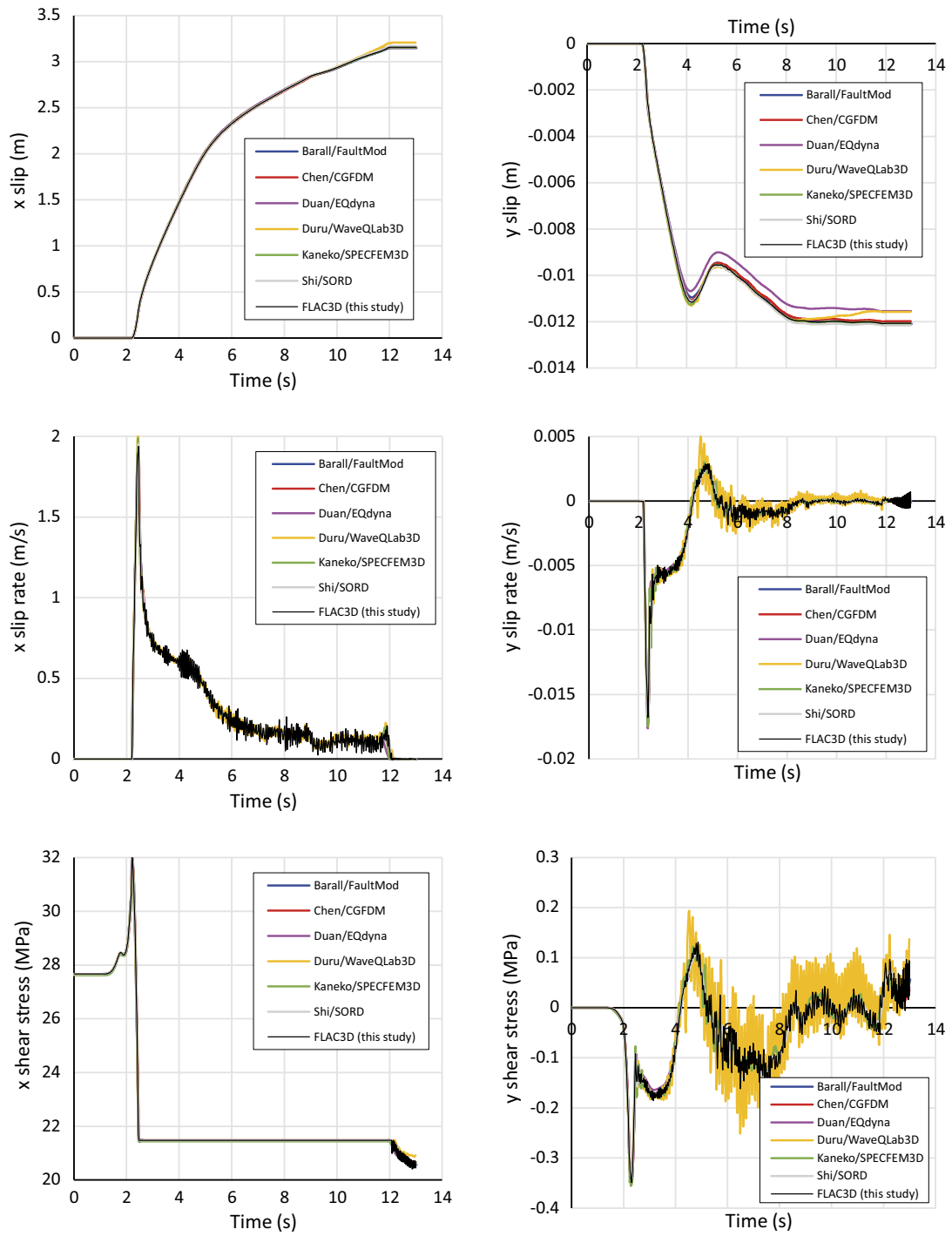


Figure A4-7. Time evolution of slip, slip rate and shear stress at the on-fault monitoring station F000dp100 (cf. Figure 6-4). Results from FLAC3D_9 (on zone-joint) are plotted along with results from other authors/codes.

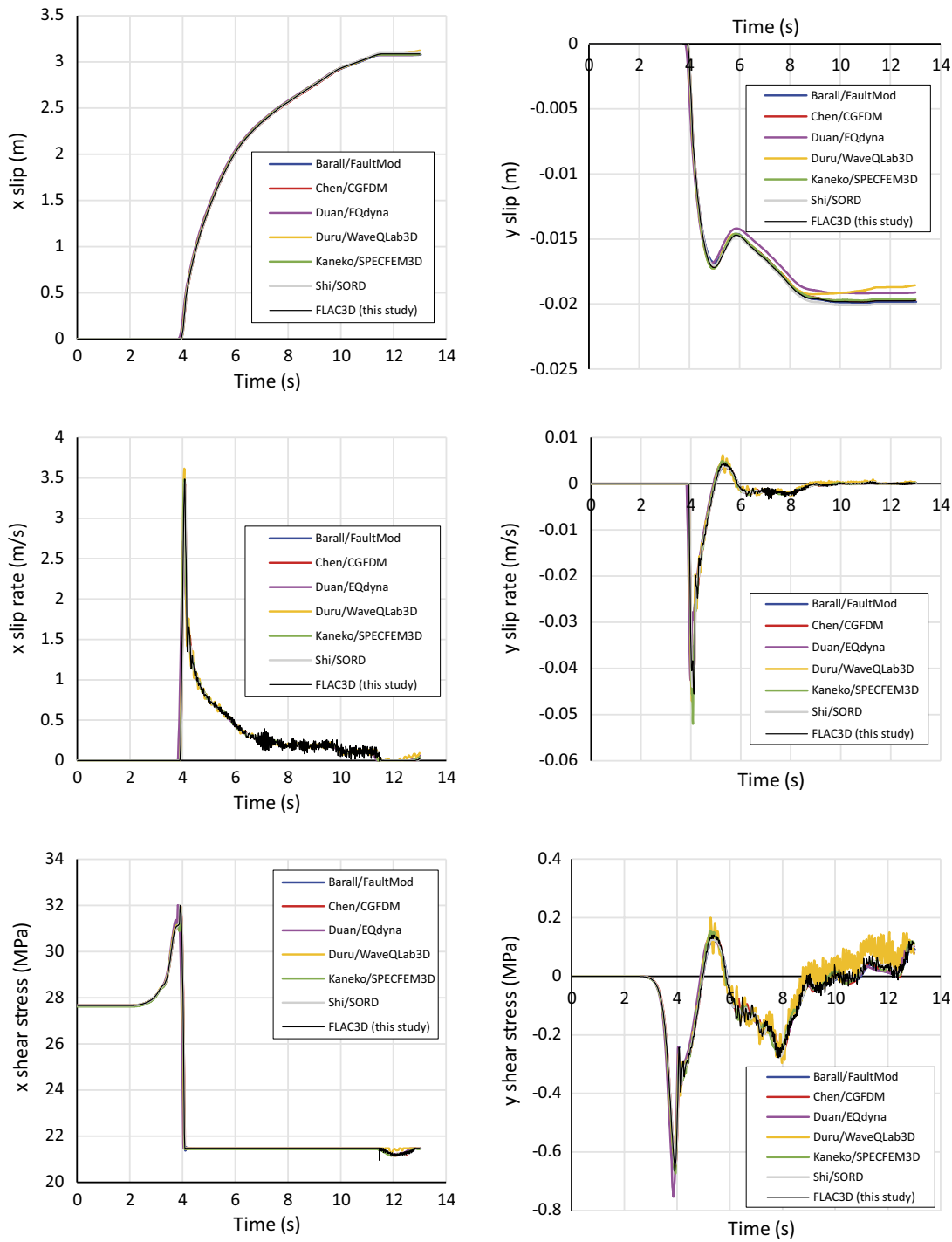


Figure A4-8. Time evolution of slip, slip rate and shear stress at the on-fault monitoring station F050dp100 (cf. Figure 6-4). Results from *FLAC3D_9* (on zone-joint) are plotted along with results from other authors/codes.

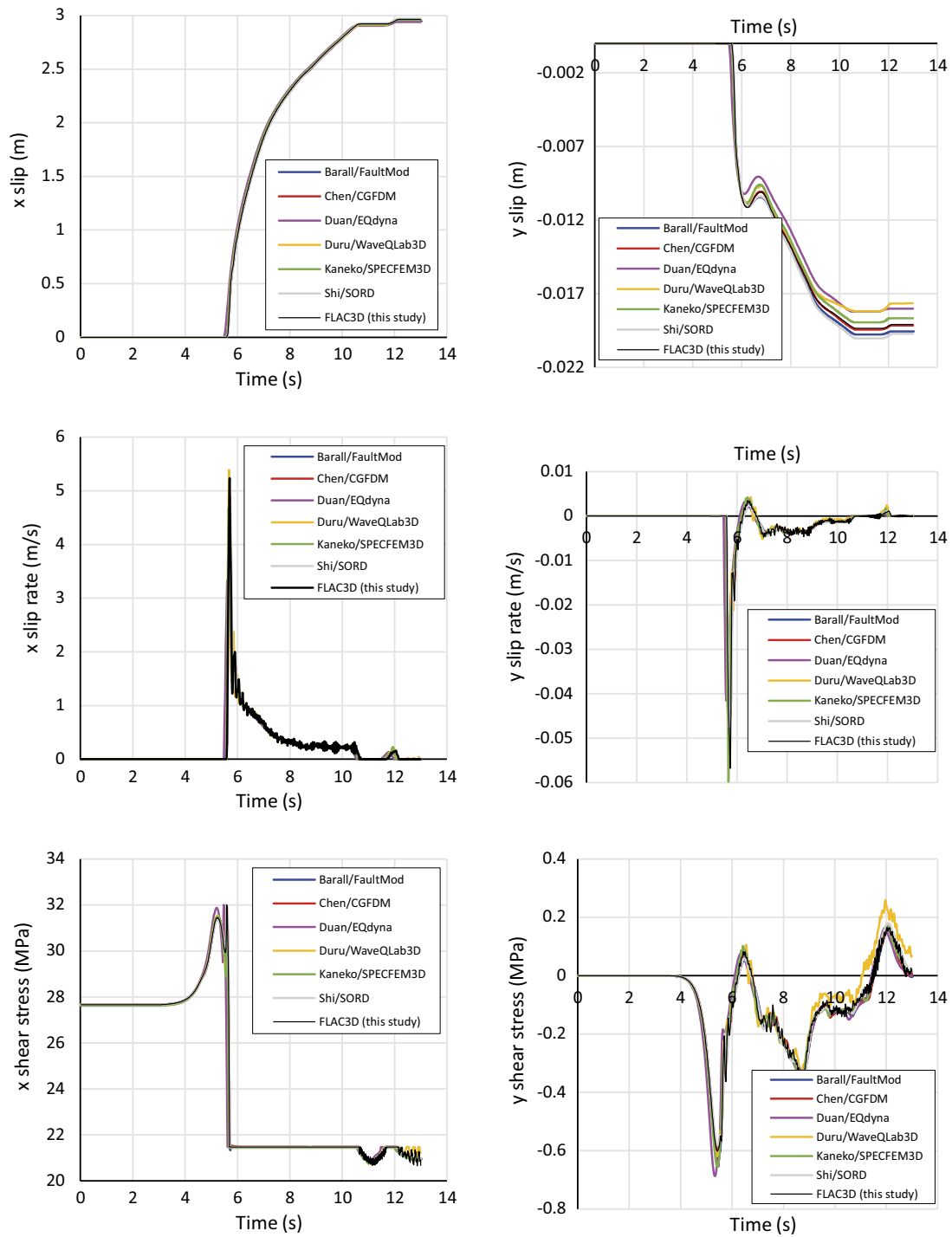


Figure A4-9. Time evolution of slip, slip rate and shear stress at the on-fault monitoring station F100dp100 (cf. Figure 6-4). Results from *FLAC3D_9* (on zone-joint) are plotted along with results from other authors/codes.

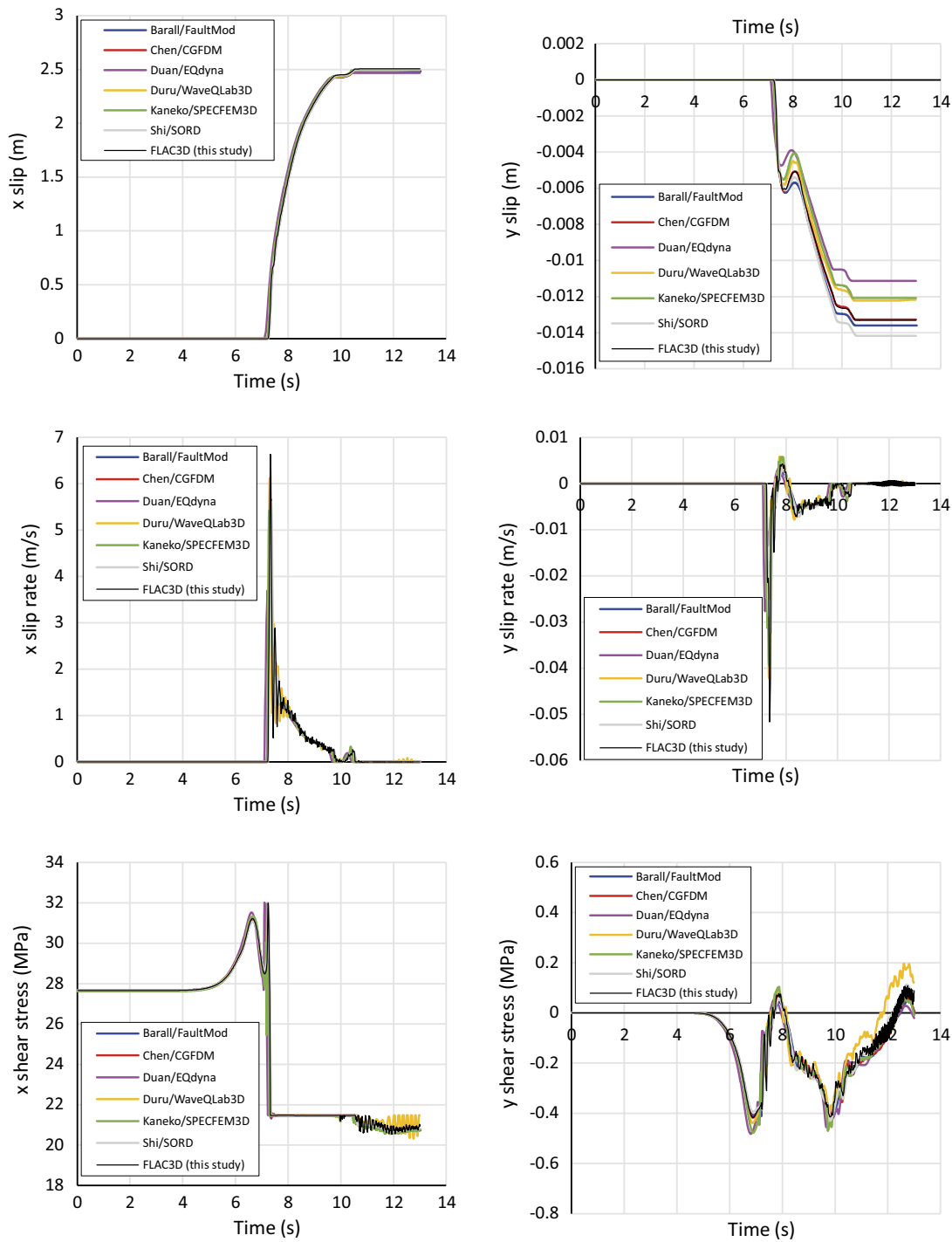


Figure A4-10. Time evolution of slip, slip rate and shear stress at the on-fault monitoring station F150dp100 (cf. Figure 6-4). Results from *FLAC3D_9* (on zone-joint) are plotted along with results from other authors/codes.

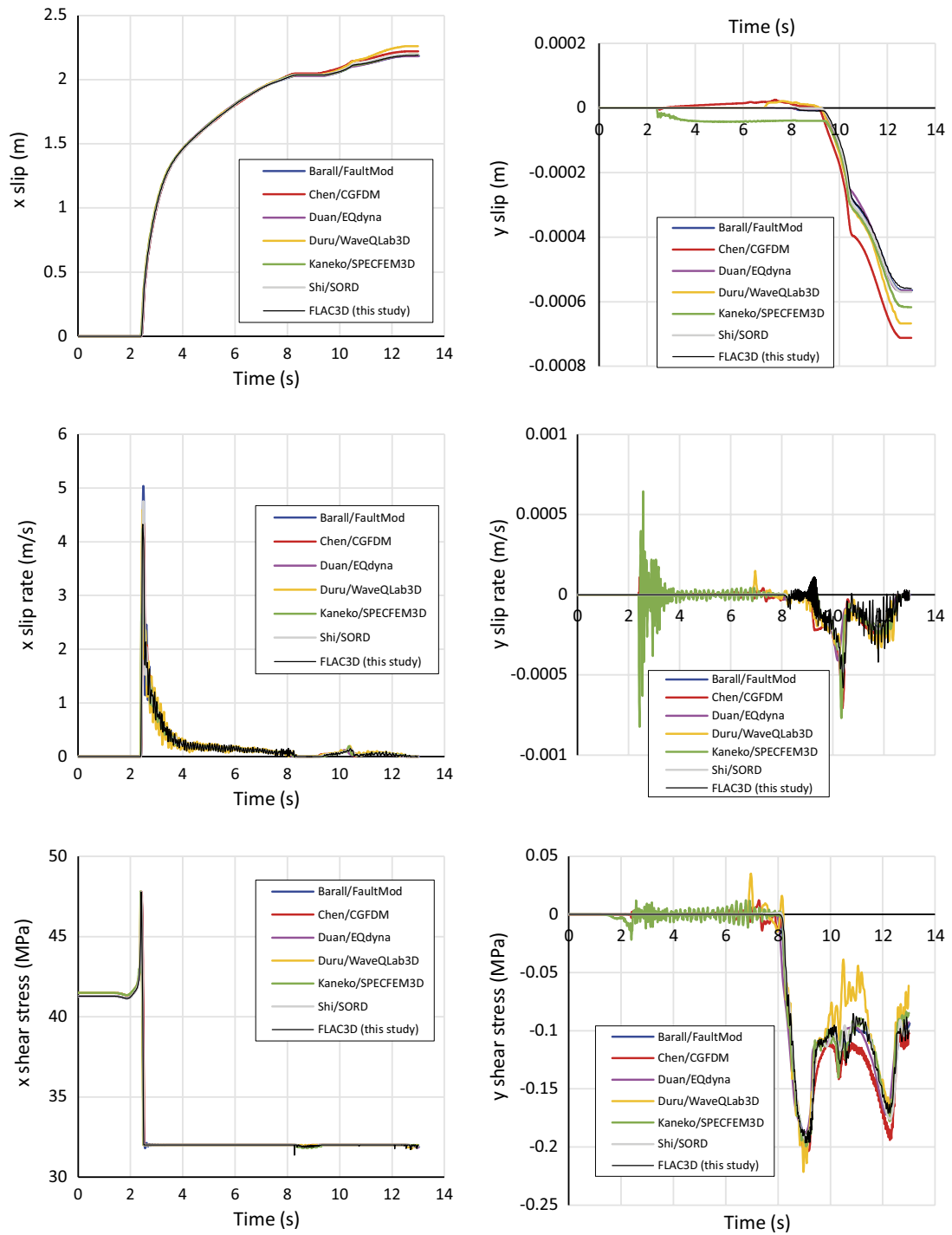


Figure A4-11. Time evolution of slip, slip rate and shear stress at the on-fault monitoring station F-050dp150 (cf. Figure 6-4). Results from FLAC3D₉ (on zone-joint) are plotted along with results from other authors/codes.

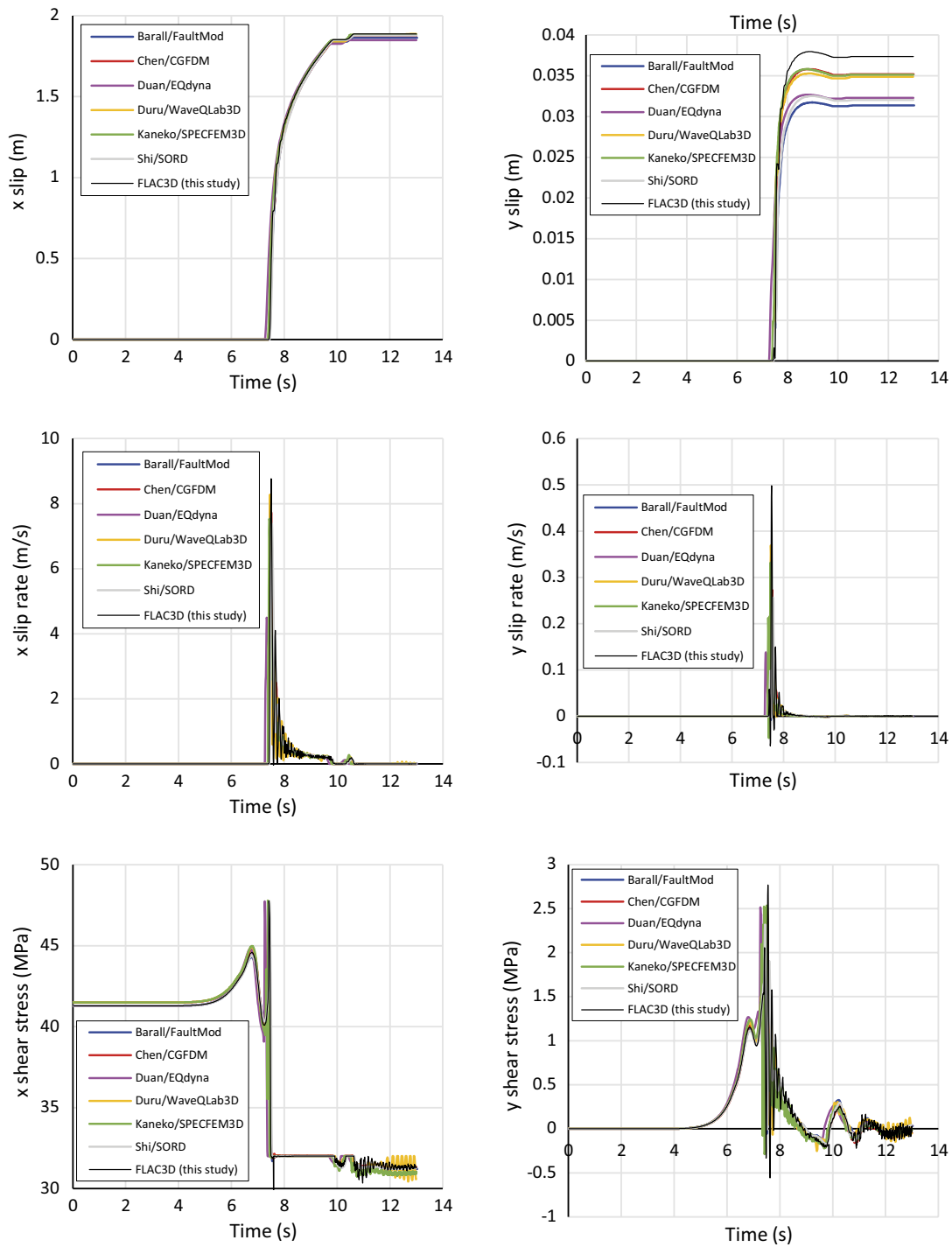


Figure A4-12. Time evolution of slip, slip rate and shear stress at the on-fault monitoring station F150dp150 (cf. Figure 6-4). Results from FLAC3D_9 (on zone-joint) are plotted along with results from other authors/codes.

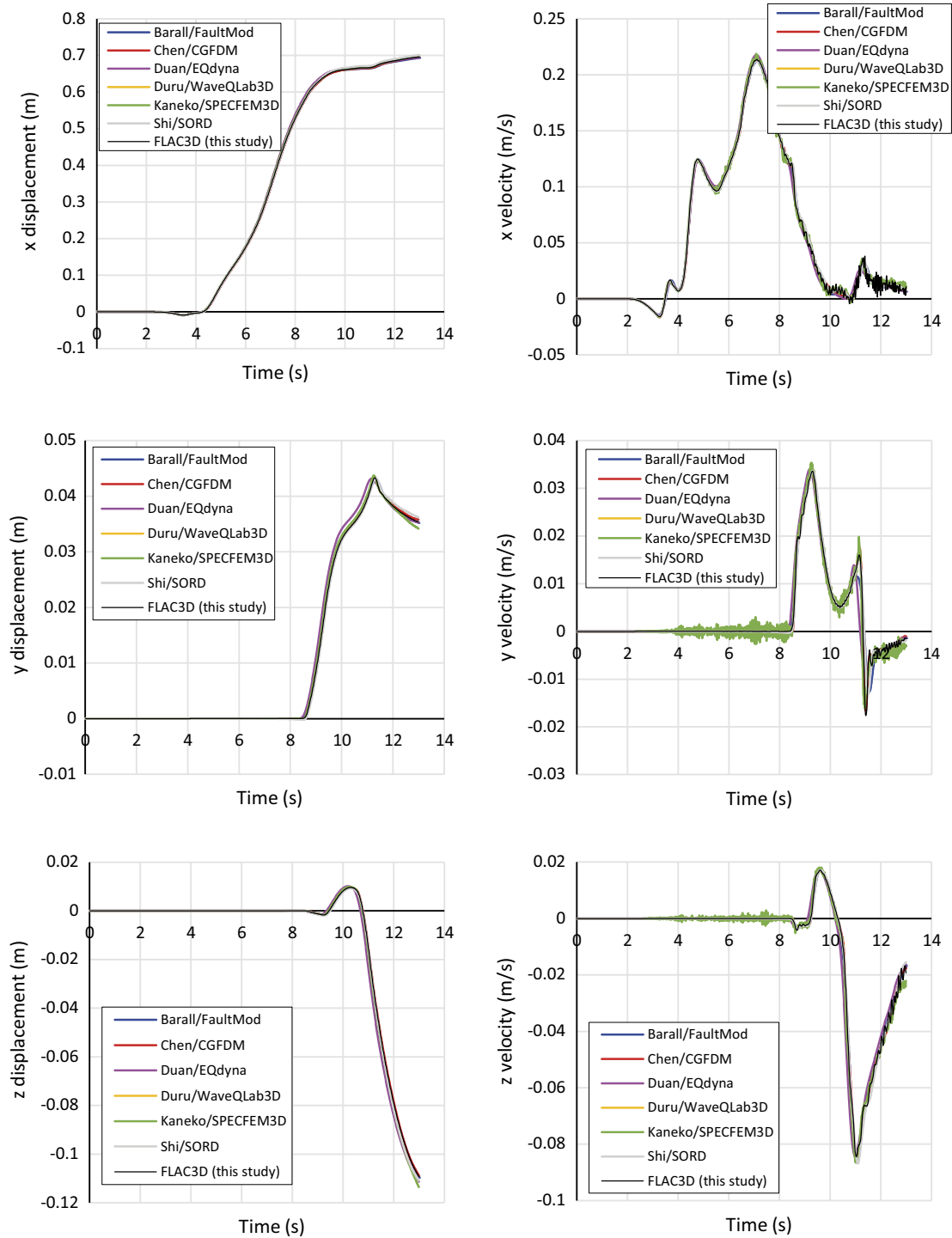


Figure A4-13. Time evolution of displacement and velocity at the off-fault surface monitoring station S030st-050 (cf. Figure 6-5). Results from FLAC3D_9 are plotted along with results from other authors/codes.

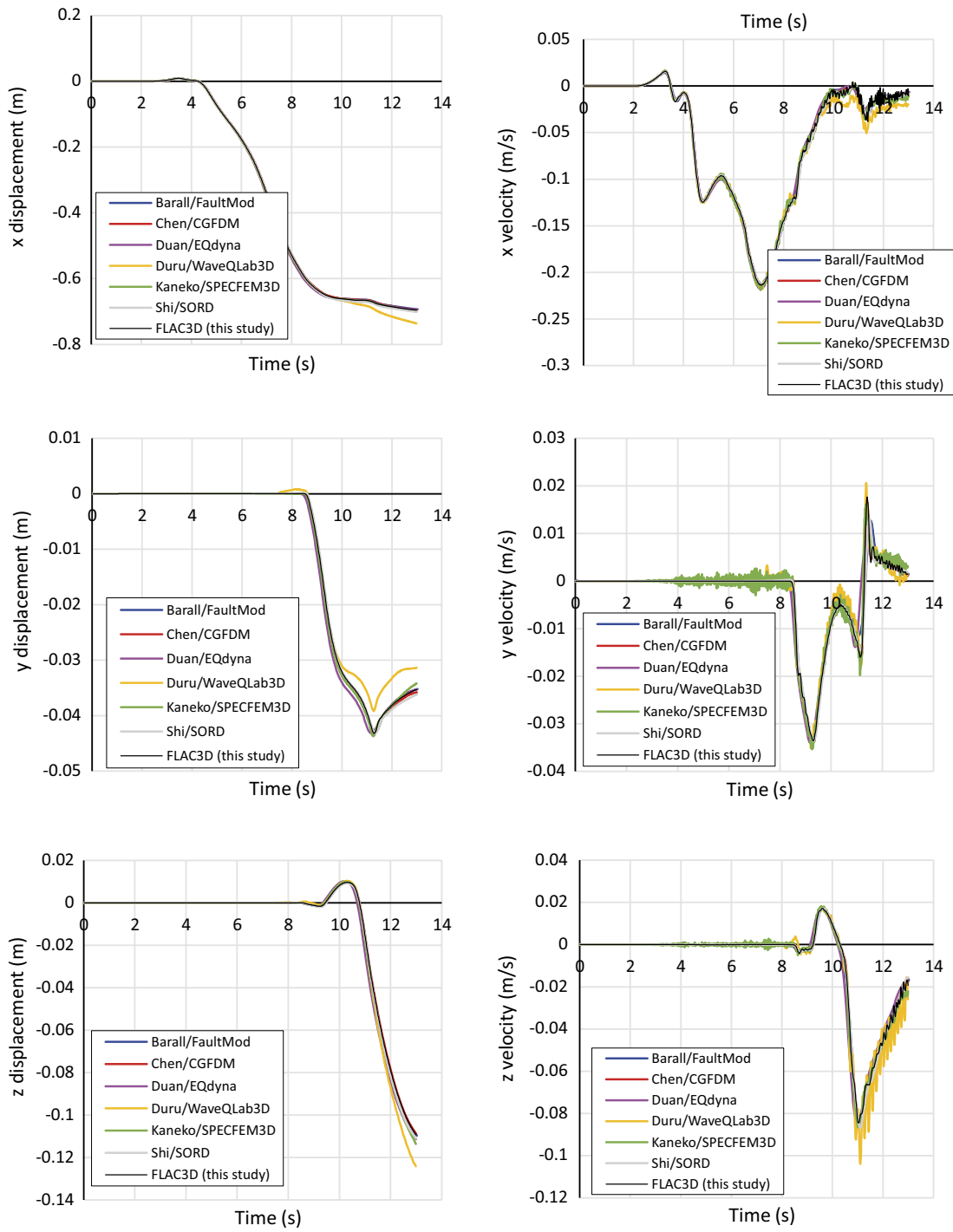


Figure A4-14. Time evolution of displacement and velocity at the off-fault surface monitoring station S-030st-050 (cf. Figure 6-5). Results from `FLAC3D_9` are plotted along with results from other authors/codes.

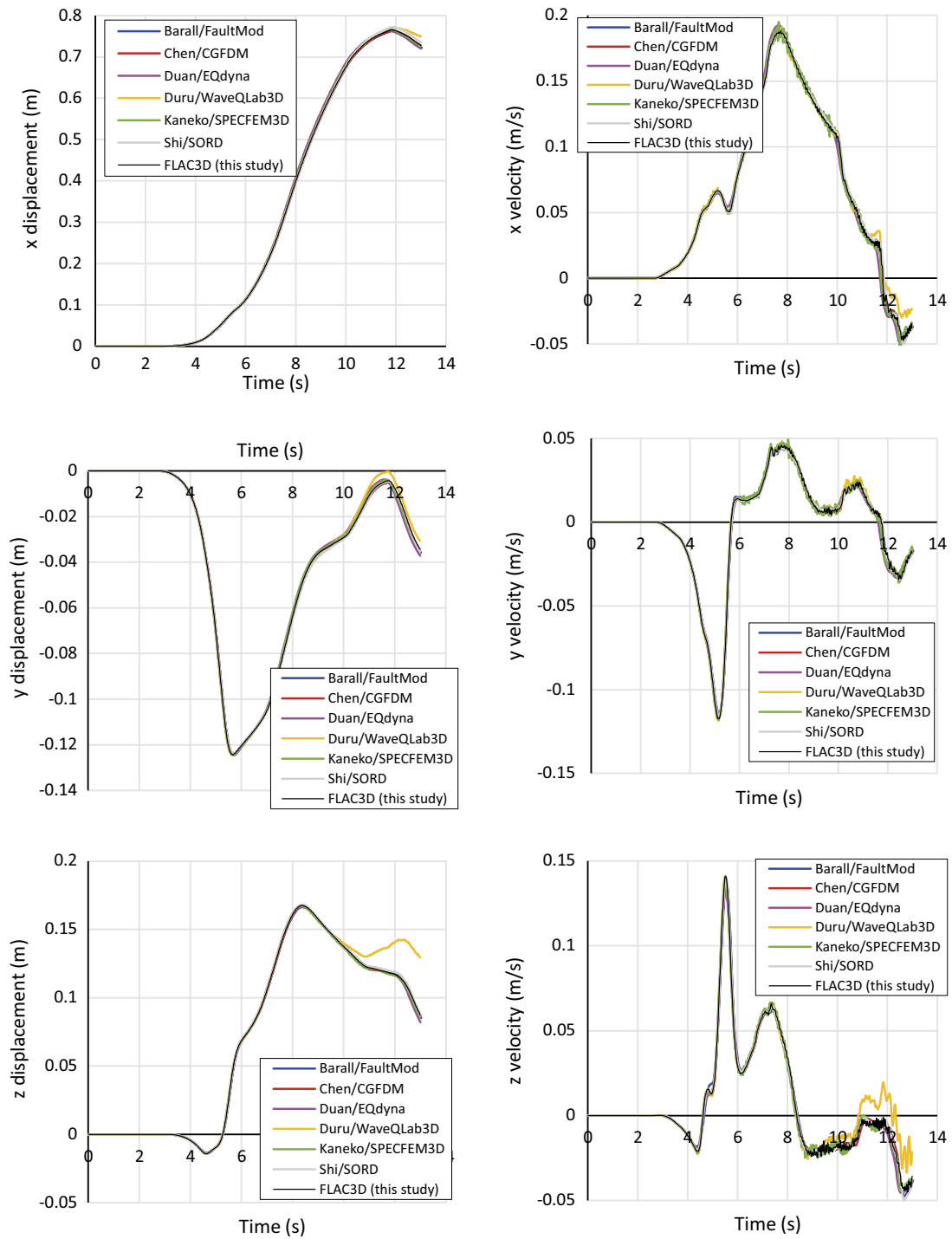


Figure A4-15. Time evolution of displacement and velocity at the off-fault surface monitoring station *s030st050* (cf. Figure 6-5). Results from *FLAC3D_9* are plotted along with results from other authors/codes.

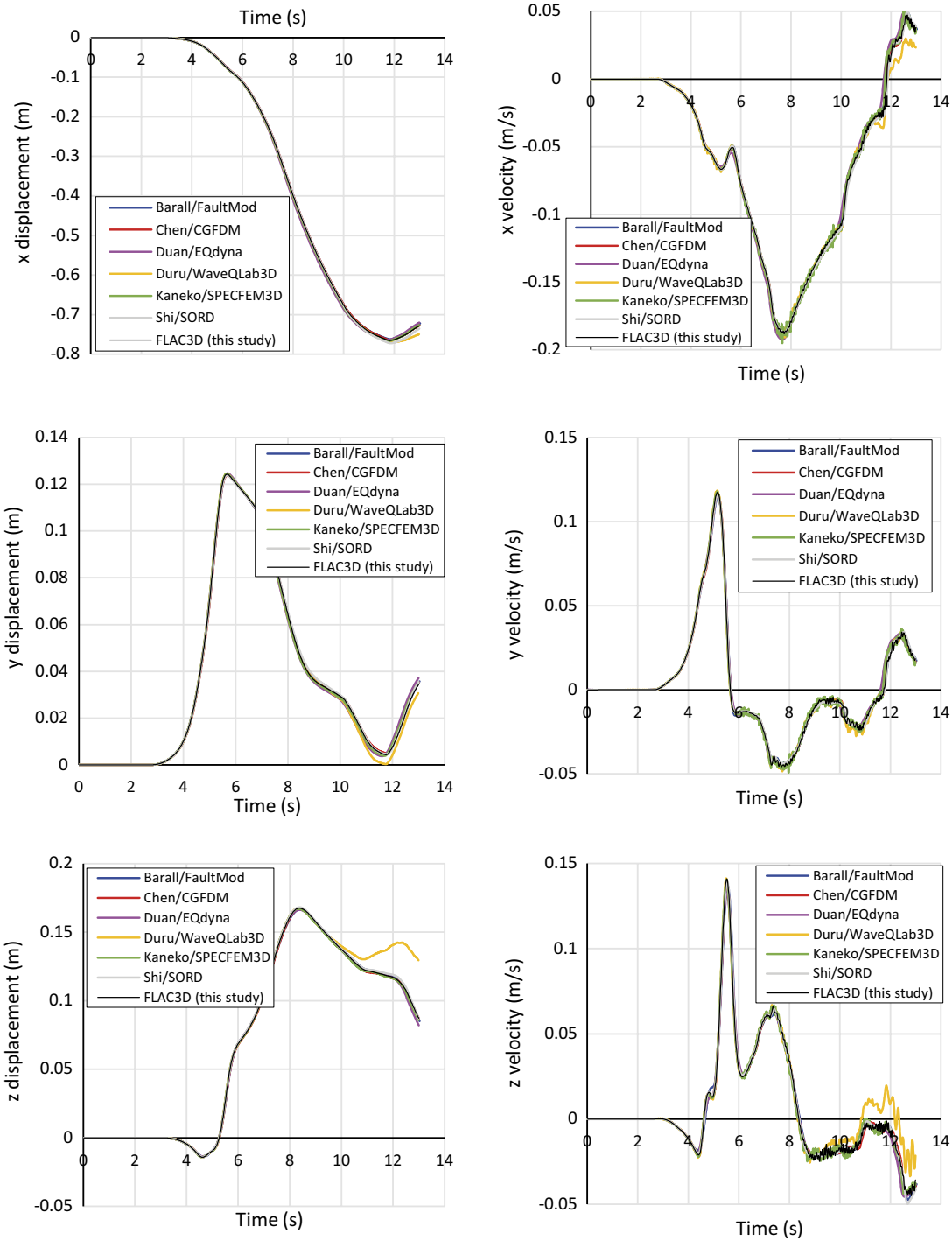


Figure A4-16. Time evolution of displacement and velocity at the off-fault surface monitoring station S-030st050 (cf. Figure 6-5). Results from FLAC3D₉ are plotted along with results from other authors/codes.

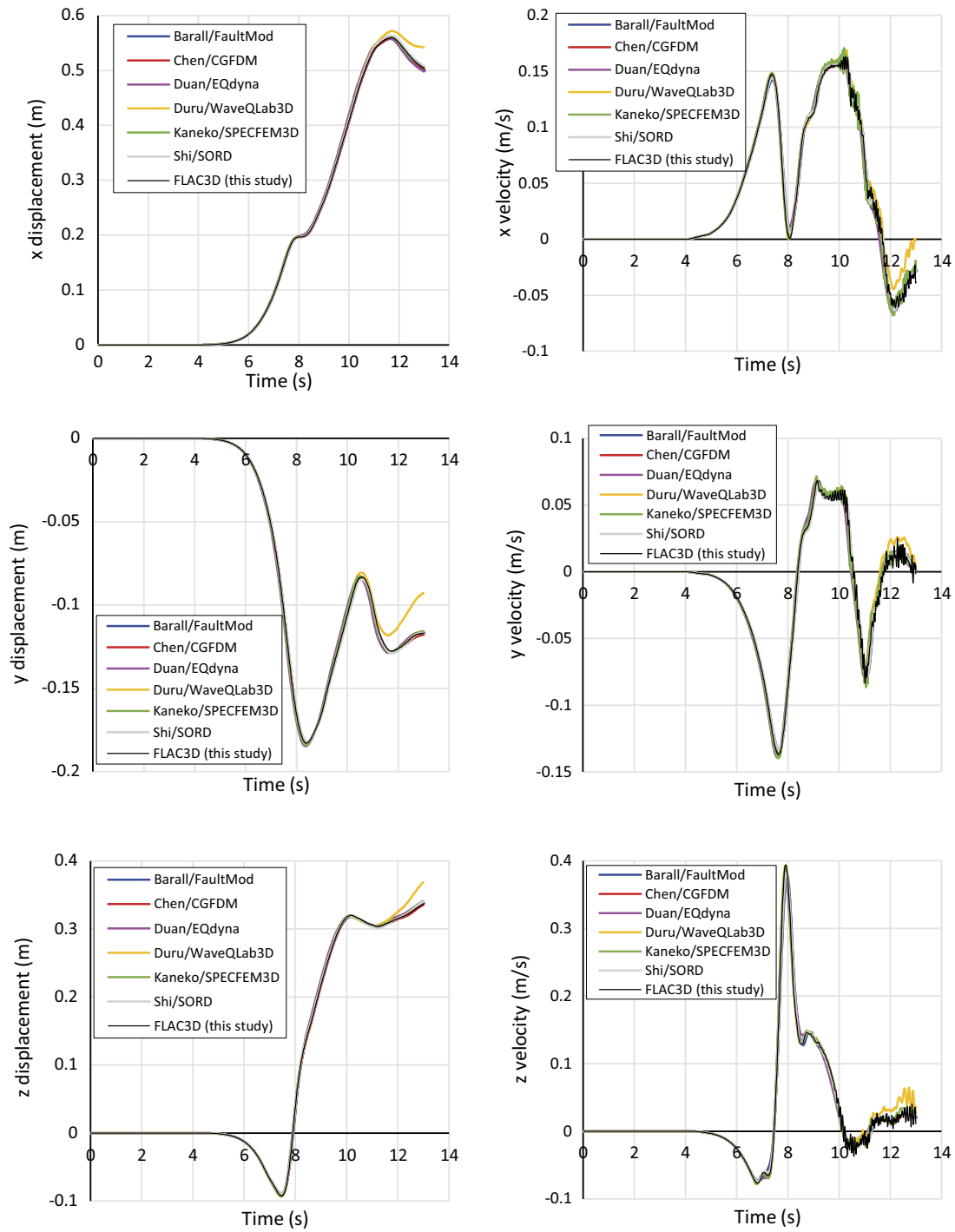


Figure A4-17. Time evolution of displacement and velocity at the off-fault surface monitoring station S030st150 (cf. Figure 6-5). Results from `FLAC3D_9` are plotted along with results from other authors/codes.

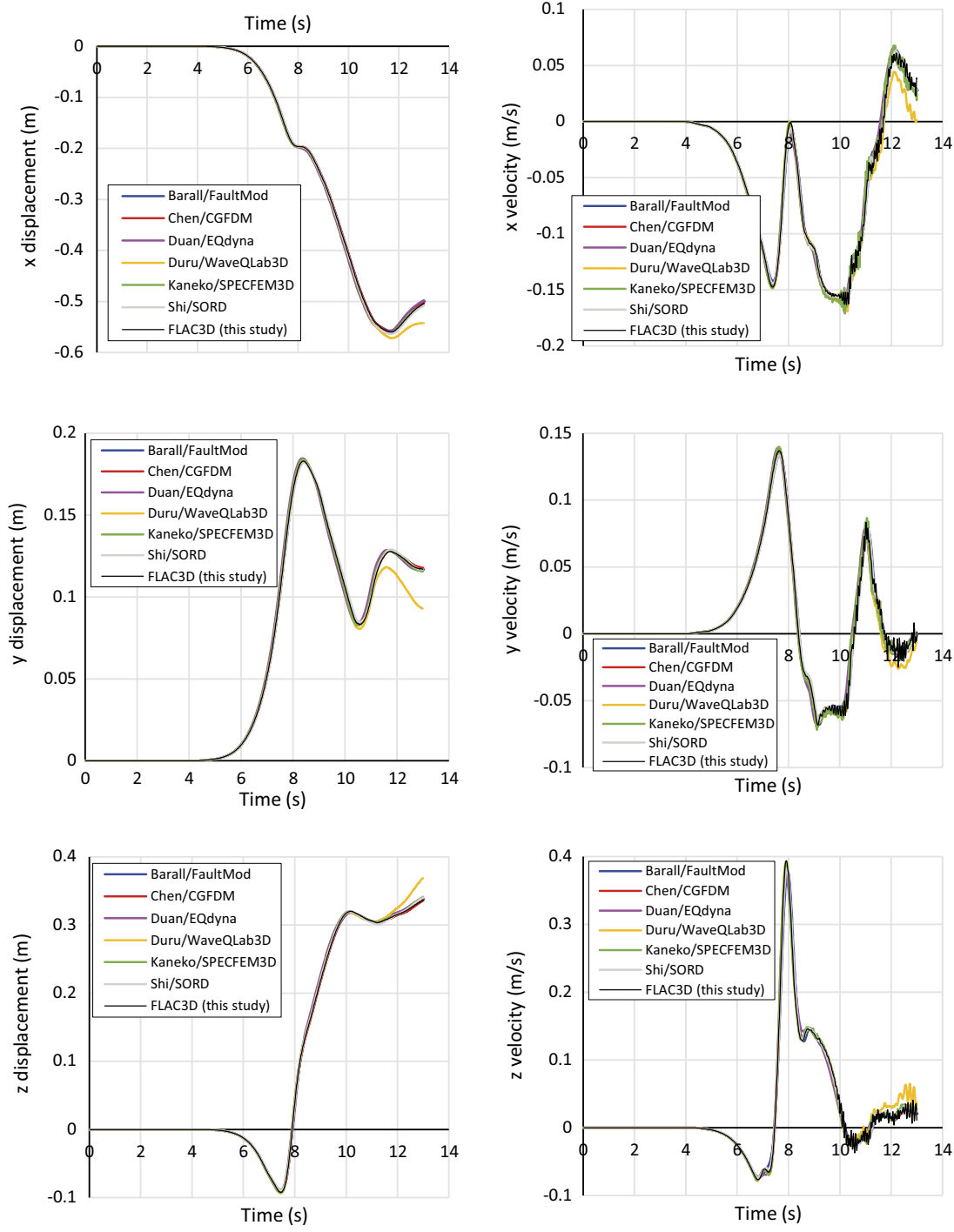


Figure A4-18. Time evolution of displacement and velocity at the off-fault surface monitoring station S-030st150 (cf. Figure 6-5). Results from FLAC3D_9 are plotted along with results from other authors/codes.

Description of TPV26 benchmark case

Downloaded from the homepage of the SCEC/USGS Dynamic Earthquake Rupture Code Verification Exercise project (<https://strike.scec.org/cvws/index.html>) (Harris et al. 2009). Note that only parts of the downloaded content is presented here.

TPV26 and TPV27

Vertical Fault with Viscoplasticity Benchmarks

These 3D benchmarks use a single planar vertical fault in a half-space. We are doing two benchmarks, as shown in the following table.

| Benchmarks | | | |
|------------|-----------|--------------------------------------|------------------------------|
| Benchmark | Dimension | Rupture Type | Material Properties |
| TPV26 | 3D | Right-lateral, vertical strike-slip. | Linear elastic. |
| TPV27 | 3D | Right-lateral, vertical strike-slip. | Drucker-Prager viscoplastic. |

We request that you run each of these two benchmarks using two resolutions: 100 meter resolution, and 50 meter resolution.

Benchmark Summary

- The geometry is a single, vertical, planar, strike-slip fault in a half-space. The fault is 40 km long and 20 km deep.
- Material properties are uniform throughout the model volume. The benchmarks include gravity and fluid pressure. The initial stress tensor varies with depth, and is in static equilibrium.
- The material properties are the only difference between the two benchmarks.
- The benchmarks use linear slip-weakening friction. Friction parameters are uniform over the fault surface, except that there is increased frictional cohesion in the uppermost 5 km to suppress freesurface effects.
- The fault boundary condition is that slip goes to zero at the border of the fault. So, a node which lies precisely on the border of a fault should *not* be permitted to slip. The free surface is not considered to be a border of the fault.
- Nucleation is done using a smoothed forced rupture. The forced rupture is applied over an interval of 0.5 seconds, and the forced rupture velocity decreases with distance from the hypocenter.

1: Considerations for Plastic Benchmarks

Benchmarks with plasticity are more complicated to set up than benchmarks with linear elastic material properties. The following list highlights some special considerations to keep in mind when implementing a benchmark with off-fault plastic yielding.

- **Benchmark TPV27 uses non-associative Drucker-Prager viscoplasticity with yielding in shear.** Benchmark TPV26 uses linear elasticity. We include a detailed description of DruckerPrager viscoplasticity.
- **The initial stress tensor is specified everywhere throughout the entire model volume.** Benchmarks with linear elasticity only need to specify initial shear and normal stresses on the fault surfaces. In TPV26 and TPV27, the initial shear and normal stresses on the faults are implied by resolving the initial stress tensor onto the fault surface.
- **Gravity must be accounted for.** The initial stress increases with depth, so gravitational acceleration is required to balance the gradient in the initial stress tensor.

- **You may need to apply traction forces to the boundary of the model volume.** The initial stresses exert traction forces on the boundary of the model volume. Depending on your implementation, you may need to balance them with externally-applied tractions.
- **Fluid pressure is included in the model.** Fluid pressure is hydrostatic, with water table at the earth's surface. The fluid pressure enters into the plastic constitutive law, and the friction law.
- **Nucleation is done using forced rupture.** Benchmarks with linear elasticity can simply impose higher shear stress near the hypocenter, but that is not possible with plasticity because it would be inconsistent with the initial stress tensor. In TPV26 and TPV27, we nucleate by using a zone of forced rupture surrounding the hypocenter. A detailed description is provided.

TPV26 and TPV27 use a linear slip-weakening friction law.

2: Fault Geometry for TPV26 and TPV27

The model volume is a half-space.

The fault is a rectangle measuring 40 000 m along-strike and 20 000 m deep. The fault is a vertical, planar, strike-slip, right-lateral fault. The fault reaches the earth's surface.

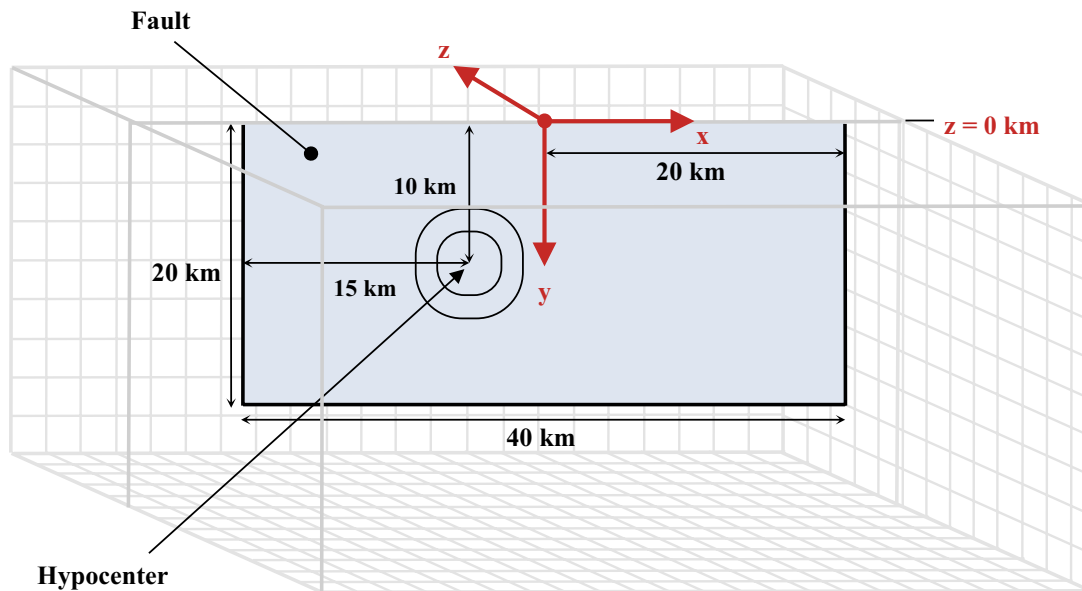
The hypocenter is located 15 km from the left edge of the fault, at a depth of 10 km.

Introduce an (x, y, z) coordinate system, where x increases from left to right, y increases from top to bottom, and z increases from front to back. The origin is on the earth's surface, 20 000 m from the right edge of the fault. In this coordinate system, the fault is:

$$-20\,000\text{ m} \leq x \leq 20\,000\text{ m}$$

$$0\text{ m} \leq y \leq 20\,000\text{ m}$$

$$z = 0\text{ m}$$



3: Description of the 3D Benchmarks

Fault Geometry

Fault geometry for TPV26 and TPV27 is shown in part 2.

The hypocenter is 15 000 m from the left edge of the fault, and 10 000 m deep, at location $(x, y, z) = -5\,000\text{ m}, 10\,000\text{ m}, 0\text{ m}$.

Slip goes to zero at the border of a fault. So, a node which lies precisely on the border of a fault should not be permitted to slip. The free surface is not considered to be a border of the fault.

Material Properties

In TPV26, the entire model volume is a linear elastic material, with the following parameters.

- Density $\rho = 2\,670\text{ kg/m}^3$
- Shear-wave velocity $V_s = 3\,464\text{ m/s}$
- Pressure-wave velocity $V_p = 6\,000\text{ m/s}$

In TPV27, the entire model volume is a non-associative Drucker-Prager viscoplastic material that yields in shear, with the following parameters. Drucker-Prager viscoplasticity is described later, in part 6.

- Density $\rho = 2\,670\text{ kg/m}^3$
- Shear-wave velocity $V_s = 3\,464\text{ m/s}$
- Pressure-wave velocity $V_p = 6\,000\text{ m/s}$
- Cohesion $c = 1.36\text{ MPa}$
- Bulk friction $\nu = 0.1934\text{ MPa}$
- Viscoplastic relaxation time $T_v = 0.03\text{ s}$

The material properties are the only difference between the elastic benchmark (TPV26), and the viscoplastic benchmark (TPV27).

Initial Stress Tensor

In an inelastic calculation, the initial stress tensor needs to be specified throughout the medium. The total (time-varying) stress, which equals the initial stress plus the stress change, is used in the plastic yield calculation. The (time-varying) normal and shear stresses acting on the fault surface are implied by the stress tensor in the adjacent rock.

For TPV26 and TPV27, the initial stress tensor varies only with depth. The components of the stress tensor are defined in the following table.

| Stress Tensor Components | |
|--------------------------|---|
| Component | Definition |
| σ_{22} | Compressive stress in the vertical direction. Negative values denote compression. |
| σ_{11} | Compressive stress in the direction parallel to the fault. Negative values denote compression. |
| σ_{33} | Compressive stress in the direction perpendicular to the fault. Negative values denote compression. This equals the negative of the total normal stress on the fault. |
| σ_{13} | Shear stress in the horizontal plane. Positive values denote right-lateral shear stress on the fault. This equals the horizontal shear stress on the fault. |
| σ_{23} | Shear stress in a vertical plane perpendicular to the fault. |
| σ_{12} | Shear stress in a vertical plane parallel to the fault. |

The stress tensor components can vary with time during the simulation.

Fluid pressure P_f is hydrostatic with water table at the surface. It varies with depth, but is constant in time.

For these 3D benchmarks, the fluid pressure and the initial values of the stress tensor are:

$$P_f = (1\,000 \text{ kg/m}^3)(9.8 \text{ m/s}^2)(\text{depth in meters})$$

$$\sigma_{22} = -(2\,670 \text{ kg/m}^3)(9.8 \text{ m/s}^2)(\text{depth in meters})$$

$$\sigma_{11} = \Omega(\text{depth})(b_{11}(\sigma_{22} + P_f) - P_f) + (1 - \Omega(\text{depth}))\sigma_{22}$$

$$\sigma_{33} = \Omega(\text{depth})(b_{33}(\sigma_{22} + P_f) - P_f) + (1 - \Omega(\text{depth}))\sigma_{22}$$

$$\sigma_{13} = \Omega(\text{depth})(b_{13}(\sigma_{22} + P_f))$$

$$\sigma_{23} = 0$$

$$\sigma_{12} = 0$$

The tapering coefficient $\Omega(\text{depth})$ causes the deviatoric component of stress to taper down to zero at depths between 15 000 m and 20 000 m.

$$\Omega(\text{depth}) = \begin{cases} 1, & \text{if depth} \leq 15\,000 \text{ m} \\ (20\,000 \text{ m} - \text{depth})/(5\,000 \text{ m}), & \text{if } 15\,000 \text{ m} \leq \text{depth} \leq 20\,000 \text{ m} \\ 0, & \text{if depth} \geq 20\,000 \text{ m} \end{cases}$$

The coefficients b_{11} , b_{33} , and b_{13} are given in the following table.

| Coefficient | Value for TPV26 and TPV27 |
|-------------|---------------------------|
| b_{11} | 0.926793 |
| b_{33} | 1.073206 |
| b_{13} | -0.169029 |

Note that we have chosen the gravitational acceleration g to be *exactly* 9.8 m/s^2 . Do not substitute a “more accurate” value of g .

Note that the initial axis of intermediate compressive stress is vertical, and its initial value is lithostatic. The initial axes of maximum and minimum compressive stress are horizontal, and their average value is lithostatic. For TPV27, the initial deviatoric stress at hypocenter depth is 93 % of the plastic yield stress.

Note that we defined the stress tensor components σ_{ij} to be the **total** stress tensor, which includes both elastic stress and fluid pressure. To obtain the **effective** stress tensor, which includes only elastic stress, you need to add the fluid pressure P_f to the diagonal components. This can be shown as:

$$\text{Total stress tensor} = \begin{pmatrix} \sigma_{11} & \sigma_{12} & \sigma_{13} \\ \sigma_{12} & \sigma_{22} & \sigma_{23} \\ \sigma_{13} & \sigma_{23} & \sigma_{33} \end{pmatrix}$$

$$\text{Effective stress tensor} = \begin{pmatrix} \sigma_{11} + P_f & \sigma_{12} & \sigma_{13} \\ \sigma_{12} & \sigma_{22} + P_f & \sigma_{23} \\ \sigma_{13} & \sigma_{23} & \sigma_{33} + P_f \end{pmatrix}$$

Friction Parameters and Nucleation

We use a linear slip-weakening friction law, which has the following six parameters.

| Friction Parameters | | |
|---------------------|-----------------------------------|---------------|
| Symbol | Parameter | Unit |
| μ_s | Static coefficient of friction. | Dimensionless |
| μ_d | Dynamic coefficient of friction. | Dimensionless |
| d_0 | Slip-weakening critical distance. | Meter |
| C_0 | Frictional cohesion. | Pascal |
| T | Time of forced rupture. | Second |
| t_0 | Forced rupture decay time. | Second |

The operation of the slip-weakening friction law is described in detail later, in part 4.

The friction parameter values are as follows, where r denotes distance to the hypocenter:

$$\mu_s = 0.18$$

$$\mu_d = 0.12$$

$$d_0 = 0.30 \text{ m}$$

$$C_0 = \begin{cases} 0.40 \text{ MPa} + (0.00072 \text{ MPa/m})(5000 \text{ m} - \text{depth}), & \text{if depth} \leq 5000 \text{ m} \\ 0.40 \text{ MPa}, & \text{if depth} \geq 5000 \text{ m} \end{cases}$$

$$r_{\text{crit}} = 4000 \text{ m}$$

$$T = \begin{cases} \frac{r}{0.7 V_S} + \frac{0.081 r_{\text{crit}}}{0.7 V_S} \left(\frac{1}{1 - (r/r_{\text{crit}})^2} - 1 \right), & \text{if } r < r_{\text{crit}} \\ 1.0\text{E}+9, & \text{if } r \geq r_{\text{crit}} \end{cases}$$

$$t_0 = 0.50 \text{ s}$$

The variation in the value of T near the hypocenter causes the rupture to nucleate, in a manner that is described later, in part 5.

The frictional cohesion C_0 (not to be confused with the plastic cohesion c) is 4.00 MPa at the earth's surface. It is 0.40 MPa at depths greater than 5000 m, and is linearly tapered in the uppermost 5000 m.

Running Time, Node Spacing, and Results

Run the model for times from **0.0 to 13.0 seconds after nucleation**.

Please submit results for two resolutions:

- Using **100 m node spacing** on the fault plane.
- Using **50 m node spacing** on the fault plane.

If you are unable to run the simulation with 50 m node spacing, then it is OK to omit the 50 m case. However, we strongly suggest that you run the simulation with 50 m resolution if at all possible.

The requested output files are:

- **On-fault time-series files**, which give slips, slip rates, and stresses for each on-fault station at each time step. These files are described in part 8.
- **Off-fault time-series files**, which give displacements and velocities for each off-fault station at each time step. These files are described in part 9.
- **A contour-plot file** which, for each node on the fault, gives the time at which the slip rate first changes from 0 to greater than 0.001 m/s. This file is described in part 10.

4: Linear Slip-Weakening Friction

Benchmarks TPV26 and TPV27 use linear slip-weakening friction, with frictional cohesion and forced rupture. This friction law has the following parameters and variables:

| Friction Parameters | | |
|---------------------|-----------------------------------|---------------|
| Symbol | Parameter | Unit |
| μ_s | Static coefficient of friction. | Dimensionless |
| μ_d | Dynamic coefficient of friction. | Dimensionless |
| d_0 | Slip-weakening critical distance. | Meter |
| C_0 | Frictional cohesion. | Pascal |
| T | Time of forced rupture. | Second |
| t_0 | Forced rupture decay time. | Second |

| Friction Variables | | |
|--------------------|--|--------|
| Symbol | Parameter | Unit |
| σ_n | Total normal stress acting on the fault, taken to be positive in compression. | Pascal |
| τ | Shear stress acting on the fault. | Pascal |
| P_f | Fluid pressure (which is assumed to be constant in time). | Pascal |
| $\sigma_n - P_f$ | Effective normal stress acting on the fault, which is positive in compression. | Pascal |

When the fault is sliding, the shear stress τ at a given point on the fault is given by:

$$\tau = C_0 + \mu \max(0, \sigma_n - P_f)$$

The time-varying coefficient of friction μ is given by the following formulas, where D is the total distance the node has slipped, and t is the time since the start of the simulation:

$$\mu = \mu_s + (\mu_d - \mu_s) \max(f_1, f_2)$$

$$f_1 = \begin{cases} D/d_0, & \text{if } D < d_0 \\ 1, & \text{if } D \geq d_0 \end{cases}$$

$$f_2 = \begin{cases} 0, & \text{if } t < T \\ (t - T)/t_0, & \text{if } T \leq t < T + t_0 \\ 1, & \text{if } t \geq T + t_0 \end{cases}$$

The distance D that the node has slipped is path-integrated. For example, if the node slips 0.4 m in one direction and then 0.1 m in the opposite direction, the value of D is 0.5 m (and not 0.3 m).

The time of forced rupture T is used to nucleate the rupture, as described in part 5. At time $t = T$, the coefficient of friction begins to decrease, reaching its final dynamic value at time $t = T + t_0$. So, the node is forced to begin sliding somewhere in the interval $T < t < T + t_0$. Notice that because of the expression $\max(f_1, f_2)$, forcing has no effect if friction has already weakened due to the accumulated slip. If a given node does not undergo forced rupture, then the value of T is 1.0E9.

Tension on the fault: If you encounter tension on the fault, you should **treat tension on the fault the same as if the effective normal stress equals zero**. This is shown in the above formulas by the expression $\max(0, \sigma_n - P_f)$.

You should **constrain the motion of the node so that the fault cannot open (that is, only permit sliding parallel to the fault), even when the fault is in tension**. During the time the fault is in tension, continue to accumulate the slip distance D as usual.

In your time-series files, where you are asked to report “normal stress,” you should report the effective normal stress which is defined to be $\sigma_n - P_f$.

5: Nucleation

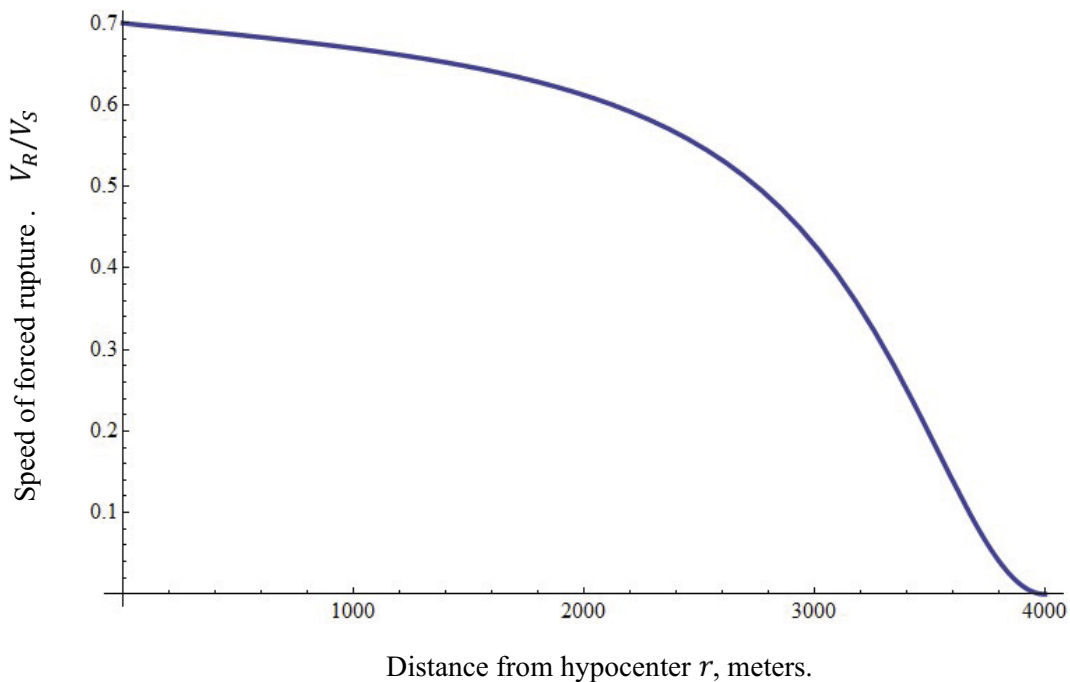
Nucleation is performed by forcing the fault to rupture, within a circular zone surrounding the hypocenter. Forced rupture is achieved by artificially reducing the friction coefficient, beginning at a specified time T . The parameter t_0 specifies how long it takes for the friction coefficient to be artificially reduced from its static value to its dynamic value. So, the friction coefficient reaches its dynamic value at time $T + t_0$. We reduce the friction coefficient gradually, over an interval of time, in order to smooth the nucleation process and reduce unwanted oscillations.

Recall that we selected $t_0 = 0.5$ s, and that the time of forced rupture is defined to be

$$T = \begin{cases} \frac{r}{0.7 V_S} + \frac{0.081 r_{\text{crit}}}{0.7 V_S} \left(\frac{1}{1 - (r/r_{\text{crit}})^2} - 1 \right), & \text{if } r < r_{\text{crit}} \\ 1.0\text{E}+9, & \text{if } r \geq r_{\text{crit}} \end{cases}$$

where r is distance from the hypocenter, and where $r_{\text{crit}} = 4000$ m is the radius of the nucleation zone. At the hypocenter, $T = 0$. The value of T then increases with distance from the hypocenter, which creates an expanding circular region of forced rupture.

The time T is computed so that the forced rupture expands at a variable speed. Near the hypocenter, the forced rupture expands at a speed of $0.7 V_S$. The speed decreases with increasing distance from the hypocenter, finally reaching a speed of zero at a distance of 4000 m from the hypocenter. The variable speed allows for a smooth transition between forced rupture and spontaneous rupture, because the spontaneous rupture should gradually overtake the ever-slowing forced rupture. The graph below shows the forced rupture speed $V_R \equiv dr/dT$ as a function of distance from the hypocenter.



6: On-Fault Stations, and Time-Series File Format

The benchmarks use 12 stations on the fault, which are listed below. A diagram of station locations is given following the table. You need to supply one time-series file for each station.

| On-Fault Stations, for TPV26 and TPV27 | |
|--|--|
| Station Name | Location |
| faultst-050dp000 | On fault, -5.0 km along strike, 0 km down-dip. |
| faultst150dp000 | On fault, 15.0 km along strike, 0 km down-dip. |
| faultst-050dp050 | On fault, -5.0 km along strike, 5.0 km down-dip. |
| faultst150dp050 | On fault, 15.0 km along strike, 5.0 km down-dip. |
| faultst-150dp100 | On fault, -15.0 km along strike, 10.0 km down-dip. |
| faultst-050dp100 | On fault, -5.0 km along strike, 10.0 km down-dip (hypocenter). |
| faultst000dp100 | On fault, 0 km along strike, 10.0 km down-dip. |
| faultst050dp100 | On fault, 5.0 km along strike, 10.0 km down-dip. |
| faultst100dp100 | On fault, 10.0 km along strike, 10.0 km down-dip. |
| faultst150dp100 | On fault, 15.0 km along strike, 10.0 km down-dip. |
| faultst-050dp150 | On fault, -5.0 km along strike, 15.0 km down-dip. |
| faultst150dp150 | On fault, 15.0 km along strike, 15.0 km down-dip. |

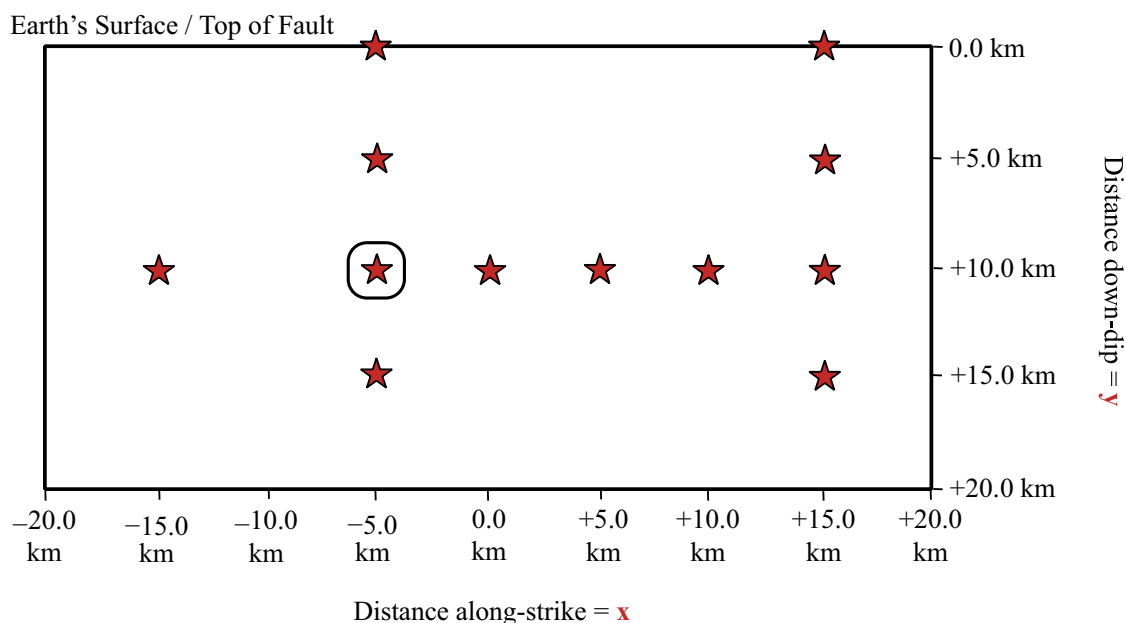
If you do not have a node at the location of a station, there are two options: (1) you can move the station to the nearest node, or (2) you can interpolate the data values from nodes near the station location.

Note: Location along-strike is measured relative to the origin of the (x, y, z) coordinate system. Positive locations are to the right of the origin.

Station Locations on the Fault

There are 12 stations:

- -5.0 km and +15.0 km along-strike, and 0 km down-dip distance.
- -5.0 km and +15.0 km along-strike, and 5.0 km down-dip distance.
- -15.0 km, -5.0 km, 0.0 km, +5.0 km, +10 km, and +15.0 km along-strike, and 10.0 km down-dip distance.
- -5.0 km and +15.0 km along-strike, and 15.0 km down-dip distance.



Note that location along-strike is measured relative to the origin of the (x, y, z) coordinate system. Positive locations are to the right of the origin.

Each time series file is an ASCII file that contains 8 data fields, as follows.

On-Fault Time Series Data Fields for TPV26 and TPV27

| <i>Field Name</i> | <i>Description, Units, and Sign Convention</i> |
|-------------------|--|
| t | Time (s). |
| h-slip | Horizontal slip along-strike (m). Sign convention: Positive means right lateral slip. |
| h-slip-rate | Horizontal slip rate along-strike (m/s). Sign convention: Positive means right lateral motion. |
| h-shear-stress | Horizontal shear stress along-strike (MPa). Sign convention: Positive means shear stress that tends to cause right lateral slip. |
| v-slip | Vertical along-dip slip (m). Sign convention: Positive means downward slip (that is, the far side of the fault moving downward relative to the near side of the fault). |
| v-slip-rate | Vertical along-dip slip rate (m/s). Sign convention: Positive means downward motion (that is, the far side of the fault moving downward relative to the near side of the fault). |
| v-shear-stress | Vertical along-dip shear stress (MPa). Sign convention: Positive means shear stress that tends to cause downward slip (that is, the far side of the fault moving downward relative to the near side of the fault). |
| n-stress | Normal stress (MPa). Note: You should report effective normal stress , which is defined to be total normal stress minus fluid pressure. Sign convention: Positive means extension . |

The **near side** of a fault is in the front of the diagram (the $-z$ side of the fault).

The **far side** of a fault is in the back of the diagram (the $+z$ side of the fault).

The on-fault time series file consists of three sections, as follows.

On-Fault Time Series File Format for TPV26 and TPV27

| <i>File Section</i> | <i>Description</i> |
|---------------------|---|
| File Header | A series of lines, each beginning with a # symbol, that gives the following information: <ul style="list-style-type: none"> – Benchmark problem (TPV26 or TPV27) <ul style="list-style-type: none"> • Author • Date • Code • Code version • Node spacing or element size • Time step • Number of time steps in file • Station location • Descriptions of data columns (7 lines) • Anything else you think is relevant |
| Field List | A single line , which lists the names of the 8 data fields, in column order, separated by spaces. It should be: <pre>t h-slip h-slip-rate h-shear-stress v-slip v-slip-rate v-shear-stress n-stress</pre> <p>(all on one line). The server examines this line to check that your file contains the correct data fields.</p> |

On-Fault Time Series File Format for TPV26 and TPV27

| <i>File Section</i> | <i>Description</i> |
|---------------------|--|
| Time History | <p>A series of lines. Each line contains 8 numbers, which give the data values for a single time step. The lines must appear in order of increasing time.</p> <p>C/C++ users: For all data fields except the time, we recommend using 14.6E or 14.6e floating-point format. For the time field, we recommend using 20.12E or 20.12e format (but see the note on the next page).</p> <p>Fortran users: For all data fields except the time, we recommend using E15.7 or 1PE15.6 floating-point format. For the time field, we recommend using E21.13 or 1PE21.12 format (but see the note on the next page).</p> <p>The server accepts most common numeric formats. If the server cannot understand your file, you will see an error message when you attempt to upload the file.</p> |

Note: We recommend higher precision for the time field so the server can tell that your time steps are all equal. (If the server thinks your time steps are not all equal, it will refuse to apply digital filters to your data.) If you use a “simple” time step value like 0.01 seconds or 0.005 seconds, then there is no need for higher precision, and you can write the time using the same precision as all the other data fields. When you upload a file, the server will warn you if it thinks your time steps are not all equal.

Here is an example of an on-fault time-series file. This is an invented file, not real modeling data.

```
# Example on-fault time-series file.
#
# This is the file header:
# problem = TPV26
# author = A.Modeler
# date = 2014/01/23
# code = MyCode
# code_version = 3.7
# element_size = 100 m
# time_step = 0.008
# num_time_steps = 1625
# location= on fault, 5.0 km along strike, 10.0 km down-dip
# Column #1 = Time (s)
# Column #2 = horizontal slip (m)
# Column #3 = horizontal slip rate (m/s)
# Column #4 = horizontal shear stress (MPa)
# Column #5 = vertical slip (m)
# Column #6 = vertical slip rate (m/s)
# Column #7 = vertical shear stress (MPa)
# Column #8 = normal stress (MPa)
#
# The line below lists the names of the data fields:
t h-slip h-slip-rate h-shear-stress v-slip v-slip-rate v-shear-stress n-stress
#
# Here is the time-series data.
# There should be 8 numbers on each line, but this page is not wide enough
# to show 8 numbers on a line, so we only show the first five.
0.000000E+00 0.000000E+00 0.000000E+00 7.000000E+01 0.000000E+00 ...
5.000000E-03 0.000000E+00 0.000000E+00 7.104040E+01 0.000000E+00 ...
1.000000E-02 0.000000E+00 0.000000E+00 7.239080E+01 0.000000E+00 ...
1.500000E-02 0.000000E+00 0.000000E+00 7.349000E+01 0.000000E+00 ...
2.000000E-02 0.000000E+00 0.000000E+00 7.440870E+01 0.000000E+00 ...
2.500000E-02 0.000000E+00 0.000000E+00 7.598240E+01 0.000000E+00 ... #
... and so on.
```

7: Off-Fault Stations, and Time-Series File Format

The benchmarks use the 6 off-fault stations listed below. All stations are at the earth's surface.

Refer to the next page for a diagram of station locations. You need to supply one time-series file for each station.

| Off-Fault Stations for TPV26 and TPV27 | |
|--|--|
| Station Name | Location |
| body030st-050dp000 | 3.0 km off fault (far side), -5.0 km along strike, 0 km depth. |
| body-030st-050dp000 | -3.0 km off fault (near side), -5.0 km along strike, 0 km depth. |
| body030st050dp000 | 3.0 km off fault (far side), 5.0 km along strike, 0 km depth. |
| body-030st050dp000 | -3.0 km off fault (near side), 5.0 km along strike, 0 km depth. |
| body030st150dp000 | 3.0 km off fault (far side), 15.0 km along strike, 0 km depth. |
| body-030st150dp000 | -3.0 km off fault (near side), 15.0 km along strike, 0 km depth. |

In the station names, the first number is the horizontal perpendicular distance from the station to the fault. A positive number means that the station is located on the **far side** of the fault.

If you do not have a node at the location of a station, there are two options: (1) you can move the station to the nearest node, or (2) you can interpolate the data values from nodes near the station location.

Off-Fault Station Locations

The diagram shows the earth's surface, looking downwards.

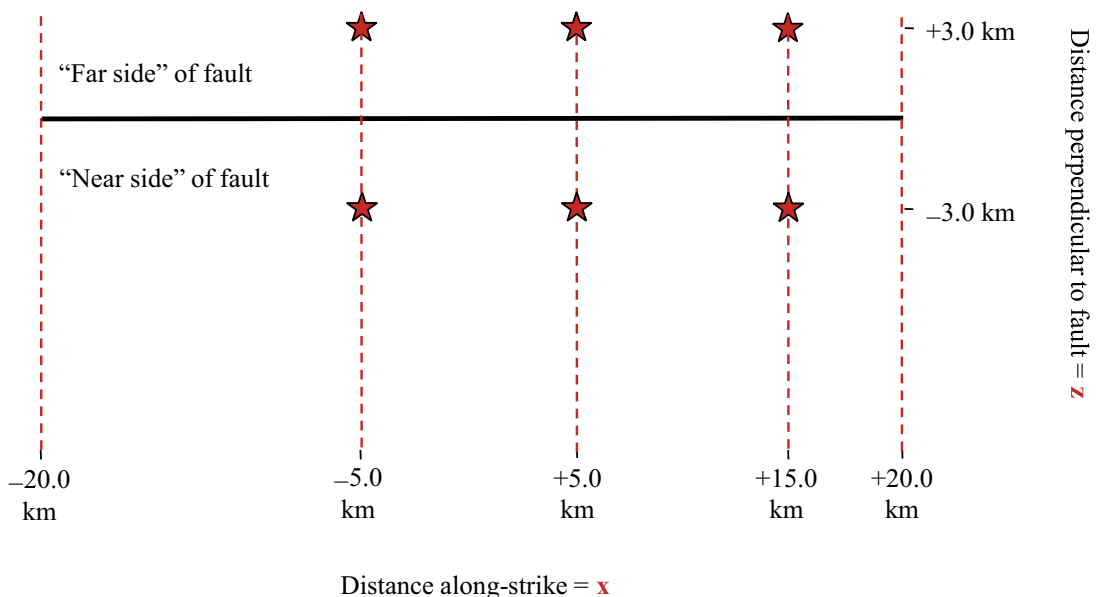
There are 6 stations at the earth's surface:

- -5.0 km, +5.0 km, and +15.0 km along-strike, and +3.0 km perpendicular distance from the fault trace.
- -5.0 km, +5.0 km, and +15.0 km along-strike, and -3.0 km perpendicular distance from the fault trace.

The **near side** of the fault is in the front of the diagram (the $-z$ side of the fault).

The **far side** of the fault is in the back of the diagram (the $+z$ side of the fault).

Positive perpendicular distance from the fault means that the station is on the **far side**.



Each time series file is an ASCII file that contains 7 data fields, as follows.

Off-Fault Time Series Data Fields for TPV26 and TPV27

| <i>Field Name</i> | <i>Description, Units, and Sign Convention</i> |
|-------------------|---|
| t | Time (s). |
| h-disp | Horizontal displacement, parallel to the fault strike (m). Sign convention: Positive means displacement to the right relative to the station's initial position (that is, in the +x direction). |
| h-vel | Horizontal velocity, parallel to the fault strike (m/s). Sign convention: Positive means motion to the right (that is, in the +x direction). |
| v-disp | Vertical displacement (m). Sign convention: Positive means displacement downward relative to the station's initial position (that is, in the +y direction). |
| v-vel | Vertical velocity (m/s). Sign convention: Positive means motion downward (that is, in the +y direction). |
| n-disp | Horizontal displacement, perpendicular to the fault strike (m). Sign convention: Positive means displacement away from the viewer, into the paper (away from near side of the fault and toward the far side of the fault) relative to the station's initial position. In other words, displacement in the +z direction. |
| n-vel | Horizontal velocity, perpendicular to the fault strike (m/s). Sign convention: Positive means motion away from the viewer, into the paper (that is, away from near side of the fault and toward the far side of the fault). In other words, motion in the +z direction. |

The **near side** of the fault is in the front of the diagram (the -z side of the fault).

The **far side** of the fault is in the back of the diagram (the +z side of the fault).

The off-fault time series file consists of three sections, as follows.

Off-Fault Time Series File Format for TPV26 and TPV27

| <i>File Section</i> | <i>Description</i> |
|---------------------|---|
| File Header | A series of lines, each beginning with a # symbol, that gives the following information: <ul style="list-style-type: none"> - Benchmark problem (TPV26 or TPV27) <ul style="list-style-type: none"> • Author • Date • Code • Code version • Node spacing or element size • Time step • Number of time steps in file • Station location • Descriptions of data columns (7 lines) • Anything else you think is relevant |
| Field List | A single line , which lists the names of the 7 data fields, in column order, separated by spaces. It should be: <pre>t h-disp h-vel v-disp v-vel n-disp n-vel</pre> <p>(all on one line). The server examines this line to check that your file contains the correct data fields.</p> |

Time History A series of lines. Each line contains 7 numbers, which give the data values for a single time step. The lines must appear in order of increasing time.

C/C++ users: For all data fields except the time, we recommend using 14.6E or 14.6e floating-point format. For the time field, we recommend using 20.12E or 20.12e format (but see the note on the next page).

Fortran users: For all data fields except the time, we recommend using E15.7 or 1PE15.6 floating-point format. For the time field, we recommend using E21.13 or 1PE21.12 format (but see the note on the next page).

The server accepts most common numeric formats. If the server cannot understand your file, you will see an error message when you attempt to upload the file.

Note: We recommend higher precision for the time field so the server can tell that your time steps are all equal. (If the server thinks your time steps are not all equal, it will refuse to apply digital filters to your data.) If you use a "simple" time step value like 0.01 seconds or 0.005 seconds, then there is no need for higher precision, and you can write the time using the same precision as all the other data fields. When you upload a file, the server will warn you if it thinks your time steps are not all equal.

Here is an example of an off-fault time-series file. This is an invented file, not real modeling data.

```
# Example off-fault time-series file.
#
# This is the file header:
# problem = TPV26
# author = A.Modeler
# date = 2014/01/23
# code = MyCode
# code_version = 3.7
# element_size = 100 m
# time_step = 0.008
# num_time_steps = 1625
# location= 3.0 km off fault, 5.0 km along strike, 0.0 km depth
# Column #1 = Time (s)
# Column #2 = horizontal displacement (m)
# Column #3 = horizontal velocity (m/s)
# Column #4 = vertical displacement (m)
# Column #5 = vertical velocity (m/s)
# Column #6 = normal displacement (m)
# Column #7 = normal velocity (m/s)
#
# The line below lists the names of the data fields:
t h-disp h-vel v-disp v-vel n-disp n-vel
#
# Here is the time-series data.
# There should be 7 numbers on each line, but this page is not wide enough
# to show 7 numbers on a line, so we only show the first five.
0.000000E+00 0.000000E+00 0.000000E+00 0.000000E+00 0.000000E+00 ...
5.000000E-03 -2.077270E-85 -2.575055E-83 -2.922774E-86 -3.623018E-84 ...
1.000000E-02 -1.622118E-82 -2.005817E-80 -1.387778E-83 -1.713249E-81 ...
1.500000E-02 -9.020043E-80 -1.114231E-77 -4.402893E-81 -5.424313E-79 ...
2.000000E-02 -1.201684E-77 -1.467704E-75 -4.549845E-79 -5.533119E-77 ...
2.500000E-02 -1.528953E-75 -1.866265E-73 -4.126064E-77 -5.004886E-75 ... #
... and so on.
```


SKB is responsible for managing spent nuclear fuel and radioactive waste produced by the Swedish nuclear power plants such that man and the environment are protected in the near and distant future.

skb.se